

THE PRIMARY CREEP BEHAVIOR OF SINGLE CRYSTAL, NICKEL BASE  
SUPERALLOYS PWA 1480 AND PWA 1484

By

BRANDON CHARLES WILSON

A DISSERTATION PRESENTED TO THE GRADUATE SCHOOL  
OF THE UNIVERSITY OF FLORIDA IN PARTIAL FULFILLMENT  
OF THE REQUIREMENTS FOR THE DEGREE OF  
DOCTOR OF PHILOSOPHY

UNIVERSITY OF FLORIDA

2008

© 2008 Brandon Charles Wilson

In memory of Richard “Doc” Connell, Ph.D.

## ACKNOWLEDGMENTS

This work would not have been successful without the help of many great and wonderful people. First, I must thank my family and friends that have supported and loved me through this process. These are the people that were there to give me advice when I needed it, to help me focus when I needed to, to help me relax when I needed to, and to pray for me always. So much of what brings a Ph.D. to completion happens outside of the lab and away from a computer and I am incredibly thankful for the love and care directed towards my wife and me while we were in graduate school.

My research hinged on the kindness of several strangers (at the time) during the early stages of my work. Three engineers at Pratt & Whitney Aircraft Engines (East Hartford, CT) deserve to be mentioned for their gift of a combined total of 47 single crystal test bars. Alan Cetel and Dilip Shaw supplied the original 12 bars along with some journal articles of note to get me started. Later, Samuel Krotzer supplied 11 bars of PWA 1480, 12 bars of PWA 1484, and even agreed to make a special heat of PWA 1480 with 3wt.% rhenium added free of charge. Without their help, this project would not have gone very far. I also need to recognize Rick Black and Bill Kumrow of Satec (a division of Instron, Norwood, MA) for their help in diagnosing and repairing electrical and software failures on the M-3 creep system used for most of the data presented here.

Additionally, the hard work of several members of the Major Analytical Instrumentation Center (MAIC) at the University of Florida (Gainesville, FL) and the Advanced Materials Processing and Analysis Center (AMPAC) at the University of Central Florida (Orlando, FL) contributed to several aspects of this investigation. Specifically, Wayne Acree, Ben Pletcher, Jung Hun Jang, Valentine Craciun, Gerald Bourne, and Kerry Siebein of MAIC and Kirk Scammon and Helge Heinrich of AMPAC were instrumental in training and helping me with the

various analytical techniques utilized for this research. Mike Kaufman and Anantha Puthicode, formerly of the University of North Texas (Denton, TX), deserve to be recognized for their help with generating the Local Electrode Atom Probe (LEAP) data presented herein as well.

Within the University of Florida, I would like to acknowledge my advisor and mentor, Dr. Gerhard Fuchs. Without his help and direction I would have been lost in the enormity of the task at hand. Former graduate student Slade Stotlz also deserves to be mentioned for his here-to-fore unacknowledged SEM work during my undergraduate research. In addition to Slade's help, I am indebted to my fellow students in the High Temperature Alloys Laboratory (HTAL) for their advice, encouragement, and humor while I have been a student. From the Particle Engineering Research Center (PERC) at UF, I thank Nate Stevens, Ph.D. who is a great friend that volunteered to proof read this dissertation in various stages of completion. I am also thankful for the quick and responsive work of several support staff members between the academic, payroll, finance, and secretary offices. Without their help nothing that is done in the department would ever be completed and I am thankful for their help in spite of the difficulties I often presented them. Finally, I need to recognize my wife, Krista Renner Wilson, Ph.D., for her constant support and encouragement. Whether I was frustrated or nervous or unsure of what to do next, she would gently, lovingly guide my hand and my thoughts in the right direction. Without her help, I would not have completed this project.

## TABLE OF CONTENTS

	<u>page</u>
ACKNOWLEDGMENTS .....	4
LIST OF TABLES .....	9
LIST OF FIGURES .....	10
ABSTRACT .....	23
CHAPTER	
1 INTRODUCTION .....	25
2 BACKGROUND .....	29
Overview .....	29
The Rhenium Effect .....	30
Secondary $\gamma'$ Precipitates .....	33
Lattice Mismatch .....	34
Modern Superalloys .....	35
The Challenge of High Temperature Service .....	37
Tensile Behavior .....	38
Creep Behavior .....	41
Summary .....	43
3 EXPERIMENTAL PROCEDURES .....	44
Materials .....	44
Heat Treatment .....	46
Heat Treatment Development .....	46
Differential Thermal Analysis .....	48
Furnaces .....	49
Characterization .....	50
Preparing Samples for Metallography .....	51
Preparing Samples for TEM .....	52
Preparing Samples for LEAP .....	53
Preparing Samples for X-Ray Diffraction .....	55
JMatPro Thermodynamic Prediction .....	57
Mechanical Behavior .....	57
Tensile Testing .....	58
Creep Testing .....	60
4 RESULTS: ALLOY MICROSTRUCTURES .....	62
Phase Descriptions .....	62

	The $\gamma$ Phase.....	62
	The $\gamma'$ Phase.....	64
	Primary $\gamma'$ .....	65
	Secondary $\gamma'$ .....	66
	The $\gamma/\gamma'$ Eutectic.....	68
	The Carbides.....	69
	The Topologically Close Packed (TCP) Phases.....	70
	Changes Following Primary Creep.....	72
5	RESULTS: TENSILE BEHAVIOR.....	91
6	RESULTS: CREEP BEHAVIOR.....	113
	Full Length Tests.....	114
	PWA 1480 .....	114
	PWA 1480+.....	116
	PWA 1484 .....	118
	Interrupted Tests.....	120
	Transmission Electron Microscopy (TEM).....	121
	PWA 1480 .....	121
	PWA 1480+.....	122
	PWA 1484 .....	123
7	RESULTS: ADDITIONAL CHARACTERIZATION.....	140
	Local Electrode Atom Probe (LEAP).....	140
	PWA 1484 LT .....	143
	Reconstruction (solution HT).....	143
	Composition profile (solution HT).....	143
	PWA 1484 HT.....	145
	Reconstruction (age HT).....	145
	Composition profile (age HT).....	145
	Reconstruction (solution HT).....	146
	Composition profile (solution HT).....	146
	Secondary $\gamma'$ Concentrations .....	147
	X-Ray Diffraction (XRD).....	148
8	DISCUSSION.....	163
	Microstructure.....	164
	$\gamma/\gamma'$ Morphology .....	164
	Carbides.....	168
	Topologically Close Packed Phases.....	168
	Tensile Behavior.....	169
	Secondary $\gamma'$ .....	170
	$\gamma$ Channel Thickness.....	172
	Lattice Misfit.....	173

Stacking Fault Energy .....	173
Anti-Phase Boundary Energy .....	174
Tensile Results.....	175
Creep Behavior .....	176
Tertiary Creep.....	177
Rafting .....	178
Primary Creep.....	180
Creep Results.....	182
Modeling Primary Creep .....	186
Lattice Misfit .....	189
Secondary $\gamma'$ .....	191
Composition .....	193
Concluding Remarks .....	195
9 CONCLUSION.....	199
Conclusions.....	199
Future Directions .....	200
APPENDIX	
A DIFFERENTIAL THERMAL ANALYSIS .....	201
B XRD PEAK DECONVOLUTION .....	208
LIST OF REFERENCES .....	292
BIOGRAPHICAL SKETCH .....	297

## LIST OF TABLES

<u>Table</u>	<u>page</u>
2-1	Compositions in weight percent of several common Nickel-based superalloys.....36
3-1	Laue orientation data and original heat treatments for PWA 1480 .....44
3-2	Laue orientation data and original heat treatments for PWA 1484 .....45
3-3	Laue orientation data and original heat treatments for PWA 1480+ .....45
3-4	Heat treatments used in this study .....47
3-5	DTA results for all three alloys.....49
3-6	Tensile test matrix with sample identification .....59
3-7	Creep test matrix with sample identification .....61
5-1	Tensile results at 700°C and 815°C for all three alloys.....101
5-2	Elastic modulus calculations from creep loads.....104
5-3	Creep loads vs. yield strength for all three alloys.....111
6-1	Primary creep and creep rates from interrupted creep tests.....125
6-2	Rupture lives and total creep elongation from full-length creep tests .....127
7-1	Composition (wt%) of secondary $\gamma'$ precipitates.....160
7-2	Net changes in secondary $\gamma'$ concentration with increasing precipitate size .....160
7-3	Lattice misfit (%) for the (002) plane following heat treatments at 1080°C .....161
B-1	PWA 1480 (002) peak lattice misfit calculations .....211
B-2	PWA 1480+ (002) peak lattice misfit calculations .....212
B-3	PWA 1484 (002) peak lattice misfit calculations .....213
B-4	PWA 1480 (004) peak lattice misfit calculations .....214
B-5	PWA 1480+ (004) peak lattice misfit calculations .....215
B-6	PWA 1484 (004) peak lattice misfit calculations .....216

## LIST OF FIGURES

<u>Figure</u>	<u>page</u>
2-1 Idealized creep curve with the three creep stages labeled .....	32
3-1 Flow-chart of heat treatments for LEAP samples.....	54
3-2 SEM micrograph of the tip of a LEAP specimen .....	55
3-3 Creep and tensile specimen geometry and dimensions.....	58
3-4 Three Type K thermocouples attached to a creep specimen.....	61
4-1 $\gamma/\gamma'$ microstructure of PWA 1480 HT3 .....	73
4-2 $\gamma/\gamma'$ microstructure of PWA 1480+ HT3.....	73
4-3 $\gamma/\gamma'$ microstructure of PWA 1484 HT3 .....	74
4-4 Composition of the $\gamma$ phase of PWA 1480 as a function of temperature.....	74
4-5 Composition of the $\gamma$ phase of PWA 1480+ as a function of temperature.....	75
4-6 Composition of the $\gamma$ phase of PWA 1484 as a function of temperature.....	75
4-7 Composition of the $\gamma'$ phase of PWA 1480 as a function of temperature .....	76
4-8 Composition of the $\gamma'$ phase of PWA 1480+ as a function of temperature .....	76
4-9 Composition of the $\gamma'$ phase of PWA 1484 as a function of temperature .....	77
4-10 The $\gamma'$ phase in PWA 1480 near a retained eutectic .....	77
4-11 Irregular $\gamma'$ phase in PWA 1480 near a partially solutioned eutectic region .....	78
4-12 $\gamma/\gamma'$ eutectic region in PWA 1480+ during the early stages of solutioning .....	78
4-13 The $\gamma'$ structure of as-cast PWA 1484 .....	79
4-14 The $\gamma'$ volume fraction vs. temperature for all three alloys.....	79
4-15 Secondary $\gamma'$ in the $\gamma$ matrix of PWA 1480 following an interrupted creep test .....	80
4-16 Secondary $\gamma'$ in the $\gamma$ matrix of PWA 1480 following an interrupted creep test .....	80
4-17 Secondary $\gamma'$ in the matrix of PWA 1480+ following an interrupted creep test.....	81

4-18	Three dimensional LEAP compositional map (18wt.% Al iso-surface).....	82
4-19	$\gamma/\gamma'$ eutectics in as-cast PWA 1480.....	83
4-20	$\gamma/\gamma'$ eutectics in the vicinity of primary carbides in PWA 1480+.....	83
4-21	Close-up of a eutectic in as-cast PWA 1480+.....	84
4-22	Close-up of a retained eutectic in PWA 1480+.....	84
4-23	Carbide phase in PWA 1480+ (HT1A).....	85
4-24	Carbide phase in PWA 1480+ (as-cast, longitudinal section).....	85
4-25	Local carbide network in PWA 1480.....	86
4-26	Carbide phase in PWA 1484.....	86
4-27	A possible carbide that dissolved during solution heat treatment.....	87
4-28	TCP phase formation in PWA 1480+ during interrupted creep testing.....	87
4-29	TCP phase formation in PWA 1480+ during interrupted creep testing.....	88
4-30	$\gamma$ phase elongation in the [110] direction in PWA 1484.....	88
4-31	$\gamma$ phase elongation in the [110] direction in PWA 1484.....	89
4-32	$\gamma'$ phase shear along (111) planes in PWA 1484.....	89
4-33	$\gamma'$ phase shear along (111) planes in PWA 1484.....	44
5-1	Tensile results for PWA 1480.....	100
5-2	Tensile results for PWA 1480+.....	100
5-3	Tensile results for PWA 1484.....	101
5-4	Comparison of tensile results for all three alloys with the LT age (700°C).....	102
5-5	Comparison of tensile results for all three alloys with the LT age (815°C).....	102
5-6	Comparison of tensile results for all three alloys with the HT age (700°C).....	103
5-7	Comparison of tensile results for all three alloys with the HT age (815°C).....	103
5-8	Plastic deformation behavior of PWA 1480 LT at 700°C.....	104
5-9	Plastic deformation behavior of PWA 1480 HT at 700°C.....	105

5-10	Plastic deformation behavior of PWA 1484 LT at 700°C .....	105
5-11	Plastic deformation behavior of PWA 1484 HT at 700°C.....	106
5-12	Plastic deformation behavior of PWA 1480+ LT at 700°C.....	106
5-13	Plastic deformation behavior of PWA 1480+ HT at 700°C .....	107
5-14	Tensile behavior of PWA 1480 LT at both temperatures.....	107
5-15	Tensile behavior of PWA 1480 HT at both temperatures.....	108
5-16	Tensile behavior of PWA 1480+ LT at both temperatures.....	108
5-17	Tensile behavior of PWA 1480+ HT at both temperatures .....	109
5-18	Tensile behavior of PWA 1484 LT at both temperatures.....	109
5-19	Tensile behavior of PWA 1484 HT at both temperatures.....	110
5-20	Yield strength as a function of temperature for all three alloys.....	110
5-21	Ultimate Tensile Strength as a function of temperature for all three alloys.....	111
5-22	True Failure Stress as a function of temperature for all three alloys .....	112
6-1	Creep at 704°C/862 MPa of all three alloys .....	125
6-2	Creep at 760°C/690 MPa of all three alloys .....	126
6-3	Creep at 815°C/621 MPa of all three alloys .....	126
6-4	Primary creep of PWA 1480.....	128
6-5	Primary creep of PWA 1480+ .....	128
6-6	Primary creep of PWA 1484.....	129
6-7	Creep at 704°C/862 MPa of PWA 1484.....	129
6-8	Primary creep comparison at 704°C/862 MPa for all three alloys .....	130
6-9	Primary creep comparison at 704°C/862 MPa for all three alloys .....	130
6-10	Primary creep comparison at 815°C/621 MPa for all three alloys .....	131
6-11	Bright field(a)/Dark field(b) pair of deformation in PWA 1480 .....	132
6-12	Bright field(a)/Dark field(b) pair of deformation in PWA 1480 .....	133

6-13	Bright field TEM image of dislocation networks in PWA 1480 .....	134
6-14	Stacking fault and dislocation shear of PWA 1480 .....	134
6-15	A stacking fault in PWA 1480 .....	135
6-16	Secondary $\gamma'$ precipitates (marked by arrows) in PWA 1480.....	135
6-17	Stacking fault interactions following primary creep in PWA 1480+ .....	136
6-18	Stacking fault interactions and a dislocation network in PWA 1480+ .....	136
6-19	Short range stacking fault shear of PWA 1480+ .....	137
6-20	Bright field TEM image of PWA 1484 LT (704°C).....	137
6-21	Stacking fault shear of $\gamma'$ precipitates in PWA 1484 .....	138
6-22	Interfacial dislocation networks present in PWA 1484 .....	139
7-1	Schematic illustrating the basic function of the LEAP system.....	151
7-2	LEAP specimens before, (a), and after, (b), the final polishing step.....	152
7-3	Iso surfaces created with the LEAP system (PWA 1484 LT with solution HT) .....	153
7-4	Magnified (SEM) view of the tip analyzed in Figure 7-3.....	154
7-5	Composition profile from the specimen in Figure 7-3.....	154
7-6	The distribution of all recorded ions for PWA 1484 HT .....	155
7-7	Iso surfaces created with the LEAP system (PWA 1484 HT no solution HT).....	155
7-8	Composition profile from the specimen in Figure 7-7.....	156
7-9	Iso surface (18% Aluminum) created with the LEAP system .....	157
7-10	LEAP results with only Al, Ta, Cr, and Mo ions represented .....	158
7-11	Composition profile from the specimen in Figures 7-9 and 7-10.....	159
7-12	Illustration of the data selected for the profile shown in Figure 7-11.....	159
7-13	An example of the deconvolution process .....	161
7-14	Lattice misfit vs. heat treatment from from both the (002) and (004) peaks .....	162
A-1	DTA trace for PWA 1480 in the HT1 condition.....	202

A-2	DTA trace for PWA 1484 in the HT1 condition.....	203
A-3	DTA trace for PWA 1480+ in the HT0 condition .....	204
A-4	DTA trace for PWA 1480 in the HT2 condition.....	205
A-5	DTA trace for PWA 1484 in the HT2 condition.....	206
A-6	DTA trace for PWA 1480+ in the HT2 condition .....	207
B-1	XRD deconvolution of PWA 1480 (4hr. 1080°C, skewed, 6.28% error).....	217
B-2	XRD deconvolution of PWA 1480 (4hr. 1080°C, skewed, 14.81% error).....	218
B-3	XRD deconvolution of PWA 1480 (4hr. 1080°C, unskewed, 6.63% error).....	219
B-4	XRD deconvolution of PWA 1480 (4hr. 1080°C, unskewed, 12.58% error).....	220
B-5	XRD deconvolution of PWA 1480 (10hr. 1080°C, unskewed, 7.94% error).....	221
B-6	XRD deconvolution of PWA 1480 (10hr. 1080°C, skewed, 5.63% error).....	222
B-7	XRD deconvolution of PWA 1480 (100hr. 1080°C, unskewed, 6.94% error).....	223
B-8	XRD deconvolution of PWA 1480 (100hr. 1080°C, skewed, 6.82% error).....	224
B-9	XRD deconvolution of PWA 1480 (100hr. 1080°C, unskewed, 5.20% error).....	225
B-10	XRD deconvolution of PWA 1480 (1000hr. 1080°C, unskewed, 5.93% error).....	226
B-11	XRD deconvolution of PWA 1480 (1000hr. 1080°C, skewed, 4.61% error).....	227
B-12	XRD deconvolution of PWA 1480 (1000hr. 1080°C, skewed, 5.45% error).....	228
B-13	XRD deconvolution of PWA 1480 (4hr. 1080°C, unskewed, 5.58% error).....	229
B-14	XRD deconvolution of PWA 1480 (4hr. 1080°C, unskewed, 7.77% error).....	230
B-15	XRD deconvolution of PWA 1480 (4hr. 1080°C, skewed, 4.99% error).....	231
B-16	XRD deconvolution of PWA 1480 (4hr. 1080°C, skewed, 1.70% error).....	232
B-17	XRD deconvolution of PWA 1480 (10hr. 1080°C, unskewed, 5.79% error).....	233
B-18	XRD deconvolution of PWA 1480 (10hr. 1080°C, skewed, 1.41% error).....	234
B-19	XRD deconvolution of PWA 1480 (1000hr. 1080°C, unskewed, 3.17% error).....	235

B-20	XRD deconvolution of PWA 1480 (1000hr. 1080°C, unskewed, 1.77% error).....	236
B-21	XRD deconvolution of PWA 1480 (1000hr. 1080°C, unskewed, 1.75% error).....	237
B-22	XRD deconvolution of PWA 1480 (1000hr. 1080°C, skewed, 3.14% error).....	238
B-23	XRD deconvolution of PWA 1480 (1000hr. 1080°C, skewed, 1.71% error).....	239
B-24	XRD deconvolution of PWA 1480 (1000hr. 1080°C, skewed, 1.71% error).....	240
B-25	XRD deconvolution of PWA 1484 (4hr. 1080°C, unskewed, 13.36% error).....	241
B-26	XRD deconvolution of PWA 1484 (1000hr. 1080°C, unskewed, 6.30% error).....	242
B-27	XRD deconvolution of PWA 1484 (10hr. 1080°C, unskewed, 4.61% error).....	243
B-28	XRD deconvolution of PWA 1484 (1000hr. 1080°C, unskewed, 5.85% error).....	244
B-29	XRD deconvolution of PWA 1484 (10hr. 1080°C, unskewed, 4.45% error).....	245
B-30	XRD deconvolution of PWA 1484 (4hr. 1080°C, skewed, 11.71% error).....	246
B-31	XRD deconvolution of PWA 1484 (1000hr. 1080°C, skewed, 3.71% error).....	247
B-32	XRD deconvolution of PWA 1484 (1000hr. 1080°C, skewed, 3.20% error).....	248
B-33	XRD deconvolution of PWA 1484 (10hr. 1080°C, skewed, 4.07% error).....	249
B-34	XRD deconvolution of PWA 1484 (10hr. 1080°C, skewed, 4.03% error).....	250
B-35	XRD deconvolution of PWA 1484 (1000hr. 1080°C, unskewed, 4.15% error).....	251
B-36	XRD deconvolution of PWA 1484 (1000hr. 1080°C, unskewed, 3.24% error).....	252
B-37	XRD deconvolution of PWA 1484 (1000hr. 1080°C, unskewed, 4.35% error).....	253
B-38	XRD deconvolution of PWA 1484 (1000hr. 1080°C, skewed, 3.09% error).....	254
B-39	XRD deconvolution of PWA 1484 (1000hr. 1080°C, skewed, 2.07% error).....	255
B-40	XRD deconvolution of PWA 1480+ (4hr. 1080°C, unskewed, 5.07% error) .....	256
B-41	XRD deconvolution of PWA 1480+ (4hr. 1080°C, unskewed, 10.42% error) .....	257
B-42	XRD deconvolution of PWA 1480+ (4hr. 1080°C, unskewed, 10.33% error) .....	258
B-43	XRD deconvolution of PWA 1480+ (10hr. 1080°C, unskewed, 9.55% error) .....	259

B-44	XRD deconvolution of PWA 1480+ (10hr. 1080°C, unskewed, 5.73% error) .....	260
B-45	XRD deconvolution of PWA 1480+ (10hr. 1080°C, unskewed, 4.87% error) .....	261
B-46	XRD deconvolution of PWA 1480+ (1000hr. 1080°C, unskewed, 4.41% error) .....	262
B-47	XRD deconvolution of PWA 1480+ (1000hr. 1080°C, unskewed, 4.37% error) .....	263
B-48	XRD deconvolution of PWA 1480+ (4hr. 1080°C, skewed, 5.05% error) .....	264
B-49	XRD deconvolution of PWA 1480+ (4hr. 1080°C, skewed, 6.91% error) .....	265
B-50	XRD deconvolution of PWA 1480+ (4hr. 1080°C, skewed, 6.85% error) .....	266
B-51	XRD deconvolution of PWA 1480+ (10hr. 1080°C, skewed, 9.54% error) .....	267
B-52	XRD deconvolution of PWA 1480+ (100hr. 1080°C, skewed, 5.42% error) .....	268
B-53	XRD deconvolution of PWA 1480+ (100hr. 1080°C, skewed, 4.13% error) .....	269
B-54	XRD deconvolution of PWA 1480+ (1000hr. 1080°C, skewed, 4.30% error) .....	270
B-55	XRD deconvolution of PWA 1480+ (1000hr. 1080°C, skewed, 4.28% error) .....	271
B-56	XRD deconvolution of PWA 1480+ (4hr. 1080°C, unskewed, 2.38% error) .....	272
B-57	XRD deconvolution of PWA 1480+ (10hr. 1080°C, unskewed, 9.32% error) .....	273
B-58	XRD deconvolution of PWA 1480+ (10hr. 1080°C, unskewed, 7.96% error) .....	274
B-59	XRD deconvolution of PWA 1480+ (10hr. 1080°C, unskewed, 3.84% error) .....	275
B-60	XRD deconvolution of PWA 1480+ (10hr. 1080°C, unskewed, 3.89% error) .....	276
B-61	XRD deconvolution of PWA 1480+ (10hr. 1080°C, unskewed, 3.37% error) .....	277
B-62	XRD deconvolution of PWA 1480+ (10hr. 1080°C, unskewed, 3.38% error) .....	278
B-63	XRD deconvolution of PWA 1480+ (1000hr. 1080°C, unskewed, 2.83% error) .....	279
B-64	XRD deconvolution of PWA 1480+ (1000hr. 1080°C, unskewed, 1.49% error) .....	280
B-65	XRD deconvolution of PWA 1480+ (1000hr. 1080°C, unskewed, 1.49% error) .....	281
B-66	XRD deconvolution of PWA 1480+ (4hr. 1080°C, skewed, 2.36% error) .....	282
B-67	XRD deconvolution of PWA 1480+ (10hr. 1080°C, skewed, 3.77% error) .....	283

B-68	XRD deconvolution of PWA 1480+ (10hr. 1080°C, skewed, 7.19% error) .....	284
B-69	XRD deconvolution of PWA 1480+ (10hr. 1080°C, skewed, 8.42% error) .....	285
B-70	XRD deconvolution of PWA 1480+ (10hr. 1080°C, skewed, 7.04% error) .....	286
B-71	XRD deconvolution of PWA 1480+ (10hr. 1080°C, skewed, 3.28% error) .....	287
B-72	XRD deconvolution of PWA 1480+ (10hr. 1080°C, skewed, 3.31% error) .....	288
B-73	XRD deconvolution of PWA 1480+ (1000hr. 1080°C, skewed, 2.79% error) .....	289
B-74	XRD deconvolution of PWA 1480+ (1000hr. 1080°C, skewed, 1.18% error) .....	290
B-75	XRD deconvolution of PWA 1480+ (1000hr. 1080°C, skewed, 1.18% error) .....	291

## LIST OF ABBREVIATIONS

AC:	Air cooled (following a heat treatment)
AIM:	Advanced Insertion of Materials (a DARPA program)
AMPAC:	Advanced Materials Processing and Analysis Center (a unit of the University of Central Florida)
APB:	Anti phase boundary (can be formed in ordered phases)
ASM:	American Society for Metals
d:	d spacing (the spacing between planes of atoms)
DARPA:	Defense Advanced Research Projects Agency (a division of the United States Department of Defense)
FWHM:	Full Width at Half Maximum (a parameter that describes the shape of an intensity peak used for XRD deconvolution)
GFQ:	Gas furnace quench (used for solution heat treatment, Helium gas was injected into a vacuum furnace for rapid cooling)
hkl:	Generic term used to indicate the miller indices of a plane
HT:	Used to designate the high temperature age (871°C/32 hr./AC), also a generic abbreviation for “heat treatment”
HT1, HT2, etc.:	Solution heat treatment designations. All heat treatments are defined in Table 3-4
IGT:	Industrial gas turbine (usually used in the power generation industry)
LT:	Used to designate the low temperature age (704°C/24 hr./AC)
LVDT:	Linear Variable Differential Transducer
MAIC:	Major Analytical Instrumentation Center (a unit of the University of Florida)
STD HT:	Designates the commercial heat treatment for the alloy in question (Table 3-4)
$\theta/2\theta$ :	Type of X-ray diffractometer
$2\theta$ :	The angle that a diffractometer measures during a scan
CMSX:	Denotes a single crystal superalloy developed by Canon Muskegon

CMSX-2:	First generation single crystal superalloy developed by Canon Muskegon, Table 2-1
CMSX-4:	Second generation single crystal superalloy developed by Canon Muskegon, Table 2-1
PWA:	Denotes an alloy developed by Pratt & Whitney
PWA 1480:	First generation single crystal, nickel base superalloy made by Pratt & Whitney. The composition is shown in Table 2-1
PWA 1480+Re:	An experimental single crystal, nickel base superalloy created by adding 3wt.% rhenium to PWA 1480. The composition is shown in Table 2-1
PWA 1480+:	Same as PWA 1480+Re
PWA 1484:	Second generation single crystal, nickel base superalloy made by Pratt & Whitney. The composition is shown in Table 2-1
DTA:	Differential Thermal Analysis
EDS:	Energy dispersive spectroscopy
FIB:	Focused ion beam
LEAP:	Local electrode atom probe
SEM:	Scanning electron microscope (or microscopy)
TEM:	Transmission electron microscope (or microscopy)
XRD:	X-ray diffraction
EDM:	Electrical discharge machining
HCl:	Hydrochloric acid
HNO <sub>3</sub> :	Nitric acid
MoO <sub>3</sub> :	Molybdenum oxide
Al:	Aluminum
C:	Carbon
Co:	Cobalt
Cr:	Chromium

Hf:	Hafnium
Mo:	Molybdenum
Ni:	Nickel
Nb:	Niobium (also called Columbium, Cb)
Re:	Rhenium
Ta:	Tantalum
Ti:	Titanium
W:	Tungsten
$\gamma$ :	Gamma phase (fcc Nickel solid solution, matrix)
$\gamma'$ :	Gamma prime phase (L1 <sub>2</sub> ordered Ni <sub>3</sub> Al, precipitates)
$\gamma/\gamma'$ :	Used for discussion of both phases as a system (eg. the $\gamma/\gamma'$ interface)
fcc:	Face centered cubic
L1 <sub>2</sub> :	An ordered fcc-like structure
MC:	Type of carbide (M represents the metal atom, C represents the carbon atom)
M <sub>6</sub> C:	Type of carbide (M represents the metal atom, C represents the carbon atom)
M <sub>23</sub> C <sub>6</sub> :	Type of carbide (M represents the metal atom, C represents the carbon atom)
TCP:	Topologically Close Packed (deleterious phases that precipitate in some alloys: $\mu$ , $\sigma$ , P, and Laves phases)
a:	Lattice parameter
$a^\gamma$ :	Lattice parameter of the $\gamma$ phase
$a^{\gamma'}$ :	Lattice parameter of the $\gamma'$ phase
$\alpha$ angle:	The error (in degrees) of a bar from the [001] orientation
at. %:	Atomic percent
$\delta$ :	Lattice mismatch

$\epsilon_f$ :	Failure strain
FS:	Failure strength
$k_{\alpha 1}$ :	The wavelength of the X-ray radiation caused by $k_{\alpha 1}$ electrons
$k_{\alpha 2}$ :	The wavelength of the X-ray radiation caused by $k_{\alpha 2}$ electrons
$\sigma_f$ :	Failure strength
$\sigma_y$ :	Yield strength
RIA:	Reduction in area
T:	Temperature
$T_m$ :	Temperature of melting (absolute temperature units only)
UTS:	Ultimate tensile strength
wt. %:	Weight percent
YS:	Yield strength
Å:	Angstrom ( $10^{-10}$ m)
cm:	Centimeter ( $10^{-3}$ m)
GPa:	Gigapascal ( $10^9$ kg·m <sup>-1</sup> ·s <sup>-2</sup> )
hr:	Hour
in:	Inch
ksi:	1000 pounds per square inch (1000 psi)
L:	Liter
lb.:	Pound
m:	Meter
µm:	Micrometer ( $10^{-6}$ m)
min:	Minute
mL:	Milliliter ( $10^{-3}$ L)
MPa:	Megapascal ( $10^6$ kg·m <sup>-1</sup> ·s <sup>-2</sup> )

nm: Nanometer ( $10^{-9}$  m)

s: Second

V: Volt ( $\text{m}^2 \text{kg s}^{-3} \text{A}^{-1}$ )

Abstract of Dissertation Presented to the Graduate School  
of the University of Florida in Partial Fulfillment of the  
Requirements for the Degree of Doctor of Philosophy

THE PRIMARY CREEP BEHAVIOR OF SINGLE CRYSTAL, NICKEL BASE  
SUPERALLOYS PWA 1480 AND PWA 1484

By

Brandon Charles Wilson

May 2008

Chair: Gerhard Fuchs

Major: Materials Science and Engineering

Primary creep occurring at intermediate temperatures (650°C to 850°C) and loads greater than 500 MPa has been shown to result in severe creep strain, often exceeding 5-10%, during the first few hours of creep testing. This investigation examines how the addition of rhenium and changes in aging heat treatment affect the primary creep behavior of PWA 1480 and PWA 1484. To aid in the understanding of rhenium's role in primary creep, 3wt% Re was added to PWA 1480 to create a second generation version of PWA 1480. The age heat treatments used for creep testing were either 704°C/24 hr. or 871°C/32hr. All three alloys exhibited the presence of secondary  $\gamma'$  confirmed by scanning electron microscopy and local electrode atom probe techniques. These aging heat treatments resulted in the reduction of the primary creep strain produced in PWA 1484 from 24% to 16% at 704°C/862 MPa and produced a slight dependence of the tensile properties of PWA 1480 on aging heat treatment temperature.

For all test temperatures, the high temperature age resulted in a significant decrease in primary creep behavior of PWA 1484 and a longer lifetime for all but the lowest test temperature. The primary creep behavior of PWA 1480 and PWA 1480+Re did not display any significant dependence on age heat treatment. The creep rupture life of PWA 1480 is greater

than PWA 1484 at 704°C, but significantly shorter at 760°C and 815°C. PWA 1480+Re, however, displayed the longest lifetime of all three alloys at both 704°C and 815°C (PWA 1480+Re was not tested at 760°C). Qualitative TEM analysis revealed that PWA 1484 deformed by large dislocation “ribbons” spanning large regions of material. PWA 1480, however, deformed primarily due to matrix dislocations and the creation of interfacial dislocation networks between the  $\gamma$  and  $\gamma'$  phases. PWA 1480+ contained stacking faults as well, though they acted on multiple slip systems generating work hardening and forcing the onset of secondary creep. X-ray diffraction and JMatPro calculations were also used to gain insight into the cause of the differences in behaviors.

## CHAPTER 1 INTRODUCTION

Conventional wisdom regarding the first and second generation superalloys states that they are well known systems with little left to learn about their behavior. Blanket statements are often used to generalize about these older alloy systems while current research and development continues to refine third, fourth, and fifth generation alloys. Recently, however, renewed interest has been given to this class of alloys due to a curious phenomenon during intermediate temperature creep. Within the temperature range of about 650°C to 850°C and under high stress, some second generation superalloys, bearing 1 atomic percent or about 3 weight percent rhenium, experience excessive primary creep. In these cases primary creep can be as high as 28-30% in as little as 12 hours of creep testing.

These stress and temperature conditions are important as they are present near the root, or attachment point, of turbine blades as well as within the internal support structure directing internal air cooling paths between the airfoil surfaces. If these regions deform at an excessive rate, internal stresses can result and failure can occur. It is also important to note that a turbine blade may fail through multiple methods. The most obvious is failure due to fracture. Another method is by exceeding dimensional tolerances. Gas turbine engines are designed with very tight tolerances. With turbine blades, the allowed expansion due to creep and other processes is often only a few percent. These tolerances, therefore, become threatened if some regions within a turbine blade can creep several percent in the first few hours of operation.

There have been numerous attempts at identifying the causes and controlling factors of primary creep in these alloys. Two suspected causes are rhenium content and the presence of secondary  $\gamma'$  precipitates in the  $\gamma$  matrix channels. Secondary  $\gamma'$  precipitates are produced following the last aging heat treatment. These precipitates are usually about 10-20 nm in size

and populate the  $\gamma$  matrix channels that are about 100-200 nm in diameter. It is widely documented that dislocations in superalloys are found predominately in the  $\gamma$  matrix. If this same region is populated by very fine, densely spaced  $\gamma'$  then dislocation slip in these channels may be greatly impeded. It has been reported that the presence of these secondary particles raises the difficulty of shear in the  $\gamma$  phase to such a level that shearing of the primary  $\gamma'$  precipitates becomes the preferred method of dislocation motion. Once a dislocation pair enters the  $\gamma'$  phase there is little barrier to glide until the opposite  $\gamma/\gamma'$  interface is reached. These long glide paths, then, are possible causes of large primary creep strains.

Another source of  $\gamma$  matrix strengthening takes the form of solid solution strengthening brought about by additions of Re. Rhenium has been used for solid solution strengthening of the  $\gamma$  phase beginning in the 1980's. How Re achieves its strengthening effect has long been a topic for debate in the superalloy community. Recent research has focused on changes in mechanical behavior and the elemental segregation of Re relative to the  $\gamma/\gamma'$  interface. The strengthening effect brought by the addition of Re was so significant that the addition of Re alone was enough to define the second and third generations of superalloys. The most striking difference in behavior can be seen by comparing first and second generation alloys, or alloys with no Re to alloys with 3wt.% (1at.%) Re. The second generation alloys demonstrated greater than 25°C improvements in creep and tensile strength capabilities.<sup>1-4</sup> After over 20 years of research, the so called "Rhenium Effect" is still not fully understood.

Adding impetus to the need to understand the Rhenium Effect, is the sudden climb of the cost of rhenium. Additions of rhenium are found in most of the alloys used for critical applications in aerospace gas turbines as well as some industrial gas turbines (IGT). Over the last 18 months, the price of rhenium has climbed from \$600/pound to \$2500/pound. This drastic

increase in cost has many companies investigating alternative methods to strengthen their alloys. One possible route includes replacing rhenium with another refractory element like tungsten, W. Also, if investigators could determine the effect rhenium has on dislocation behavior, perhaps new strategies for strengthening could be developed.

Interestingly, excessive primary creep and the Rhenium Effect may be related. The alloys most commonly associated with excessive primary creep are rhenium bearing superalloys (i.e. 2<sup>nd</sup>, 3<sup>rd</sup>, 4<sup>th</sup>, and next generation alloys). Typical creep behavior for these alloys will display large primary creep strains in the first few hours of testing under high loads and low temperatures. Following primary creep is a sharp transition to secondary, or steady-state, creep. During secondary creep in these alloys the creep rate is rather low and unchanging. First generation alloys, however, tend to not display much primary creep and the secondary creep rate is higher and slowly increases for the duration of the creep test. Therefore, while rupture times for second generation alloys may be a full order of magnitude longer, time to 1% creep may be significantly shorter than their first generation counterparts. This behavior relates directly to the issue of dimensional tolerance in modern aerospace engines: while second generation alloys will rupture at longer times, they may, in fact, fail dimensional controls significantly earlier than their rupture lives might suggest. Alternatively, this behavior might require unique design considerations during turbine run-in to account for excessive deformation.

The current investigation focuses on commonly used first and second generation alloys: PWA 1480 and PWA 1484, respectively. A third, experimental alloy was also produced to isolate the effect of rhenium during intermediate temperature creep by adding 3 weight percent Re to PWA 1480. The approach used to test the three alloys begins with a solution and homogenizing heat treatment for all three alloys to reduce the effects of segregation during

solidification. Two different aging heat treatments were then used with the intention of creating specimens with and without secondary  $\gamma'$  in the  $\gamma$  matrix channels in order to observe changes in primary creep effected by these precipitates. Full length creep testing and interrupted creep testing was conducted to correlate microstructure with mechanical properties. Additionally, X-ray diffraction studies, JMatPro thermodynamic predictions, and TEM techniques were used to investigate the primary creep behavior of the three alloys. Finally, the problem of secondary  $\gamma'$  and the Rhenium Effect with regard to excessive primary creep is discussed.

## CHAPTER 2 BACKGROUND

### Overview

Modern superalloy technology has a long history of developments in processing, alloy chemistry, and fundamental metallurgical knowledge. The advent of directionally solidified, followed by single crystal, blades and vanes led to major improvements in the high temperature tensile, creep, and fatigue properties of superalloys. Alloy refinement through advanced remelting processes and alloy chemistry has led to consistency between master heats and improvements in mechanical properties and environmental resistance.<sup>2,5</sup> These developments occurred over several decades; however, the pace of research has occasionally exceeded the rate of application of these new alloys. For instance, a typical development cycle from inception to service for a new alloy can take 7-10 years. By the time that alloy is put into service, newer alloys with improved properties are already in development. Adding to this, the United States Department of Defense has instituted the Accelerated Insertion of Materials (AIM) program, a Defense Advanced Research Projects Agency (DARPA) initiative. The goal of this program is to decrease the time to active service of new alloys used for aerospace turbine engine applications.<sup>6</sup> Similarly, the United States Department of Energy instituted a similar program in the early 1990's to improve performance of industrial gas turbines. The Advanced Turbine Systems (ATS) program also created a push for new materials with higher temperature capabilities.<sup>7</sup> These government programs coupled with the already strong drive to increase performance has led to rapid development cycles for new materials.

While the high pace of development in the superalloy industry is beneficial for engine manufacturers, customers, and national defense alike, new alloys are often developed before a firm understanding of previous performance gains could be achieved. A prime example is the

addition of rhenium to second and third generation superalloys. Since the first implementation of Re to these alloys in the early to mid 1980's, the superalloys community has seen the development of 2nd generation (3 wt% Re), 3rd generation (6 wt% Re), 4th generation (with platinum group additions), and now early development of the next generation of superalloys. As the momentum of research continues to advance alloy performance, the method by which Re improves the strength of superalloys is still debated. Early studies examined microstructural effects, changes in  $\gamma'$  stacking fault energy, changes in  $\gamma/\gamma'$  lattice mismatch, and Re segregation to the  $\gamma$  phase during precipitation and coarsening of  $\gamma'$  precipitates.<sup>8-11</sup> Entering the 1990's, interest in exploring this effect was replaced by the need to boost engine performance. Thus the third generation of superalloys was created through even greater rhenium additions, though the exact strengthening mechanism was still not entirely clear.

### **The Rhenium Effect**

Twenty years later, there has been an increase in the interest in the so called "Rhenium Effect". Part of this rekindled interest is due simply to the lag in development between military aircraft engines to commercial engines to industrial gas turbines, IGTs. Alloys that are new to commercial aircraft applications were first used in military aircraft engines 10 years earlier. The same gap exists between commercial engines and industrial gas turbines. These technological divides are due partly to market pressure and partly to processing challenges. New, high performance alloys are often very difficult to cast into a properly oriented single crystal. As the engine increases in size, its turbine blades must increase in size as well. Turbine blades on military aircraft may be 8 to 15 cm in length while commercial engines require 10 to 20 cm and IGTs require blades significantly greater than 30 cm in length. The consequence of these size differences is an increased rejection rate using conventional processing technologies. Thus,

improvements in casting processes were often necessary before an established alloy could be applied or scaled up to new markets.

Now that second generation single crystal alloys have made their way into commercial aircraft and IGT applications, interest is growing to understand their behavior primarily due to cost pressures and increasing loads at intermediate temperatures. These new applications require larger components and, consequently, larger volumes of Re bearing superalloys. The recent rapid rise in the cost of Re has the superalloy community investigating alternative strengthening additions. Additionally, some second generation alloys during intermediate temperature creep (650°C to 850°C) at high loads (greater than 500 MPa) will exhibit severe creep anisotropy that has been linked to stacking fault shear of the  $\gamma'$  precipitates.<sup>12-15</sup> Creep anisotropy has also been linked to large primary creep strains during testing under these same conditions.

By convention, creep behavior is separated into three stages as shown in Figure 2-1. The primary creep stage of interest to the current investigation occurs first. Primary creep is typically marked by a relatively large initial creep rate due to the initially undeformed nature of the microstructure. As deformation occurs, and hardening takes place, the creep rate is reduced. Eventually, a balance between the active deformation processes (dislocation slip) and recovery processes is reached and the creep rate stabilizes. This regime of creep is called secondary creep. Near the end of the life of a specimen, the total accumulation of deformation within the microstructure increases the rate of deformation such that the active recovery processes can no longer maintain a steady-state balance. As a result, the creep rate begins to increase. Approaching failure, the creep rate is continually increasing and this behavior marks tertiary creep. The idealized behavior shown in Figure 2-1, however, is not always applicable. Often, usually at high temperatures, alloys will exhibit brief primary creep that transitions immediately

into tertiary creep with no steady-state secondary creep stage. Another variation, which is discussed in this investigation, is creep dominated by the primary creep stage. In specimens exhibiting this behavior, the primary creep stage is extended to greater levels of strain before secondary creep can occur. Additionally, with alloys exhibiting large primary creep stages, incubation periods of near zero creep usually preceded the primary creep stage. It is thought that these incubation periods mark the formation of stacking fault ribbons prior to  $\gamma'$  shear.<sup>16,17</sup>

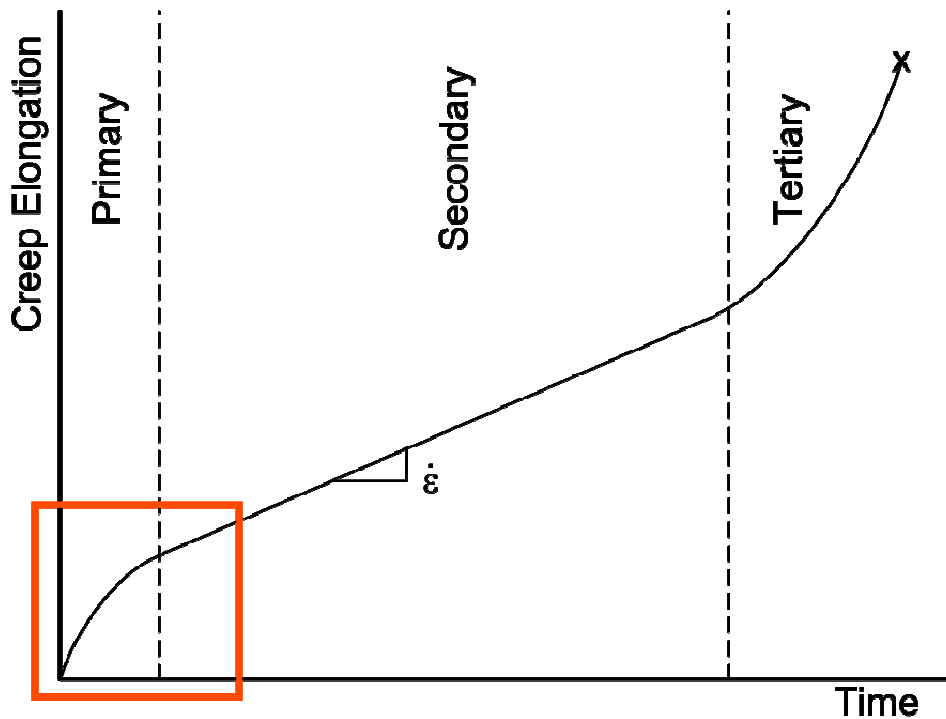


Figure 2-1. Idealized creep curve with the three creep stages labeled. The box marks the region of most interest to the current investigation.

The primary creep regime in some second generation alloys may be so severe that it is the dominant feature of their respective creep curves. As a result, primary creep has become the focus of several recent investigations because intermediate temperature, high stress creep conditions are common in IGT and commercial aerospace applications.<sup>16-20</sup> This phenomenon may have gone unnoticed in the early part of the development cycle because the emphasis was placed on increasing service temperatures beyond 1000°C. Since this behavior is characteristic

of lower temperatures similar to those seen in the attachment and internal support regions of turbine blades, it may also have been deemed less important than high temperature creep strength.

### **Secondary $\gamma'$ Precipitates**

A microstructural feature that may impact the primary creep behavior of single crystal nickel base superalloys is the presence of secondary  $\gamma'$  precipitates. While it has been long known that primary  $\gamma'$  precipitate size has a major impact on mechanical properties,<sup>21,22</sup> research has also shown the importance of controlling the secondary  $\gamma'$ , or cooling  $\gamma'$ , precipitates<sup>20,23</sup>. The final heat treatment step before a turbine blade is released for service is typically a  $\gamma'$  aging heat treatment. This final step significantly impacts the performance of the component. First, the time and temperature for the age heat treatment controls the coarsening behavior of the primary  $\gamma'$  precipitates. Following solution heat treatment, these precipitates are mostly coherent in nature.

Aging serves to increase the size of the precipitates to the optimum 0.3-0.5  $\mu\text{m}$  size range. Additionally, the coherency of the precipitates is reduced adding a misfit strengthening component to the overall strength characteristic of the alloy. Besides time and temperature, the cooling rate following aging has been found to create microstructural differences that can impact mechanical properties. Rapid cooling from the aging heat treatment temperature has been shown to produce a fine dispersion of secondary  $\gamma'$  precipitates of the size range 10-50 nm in diameter. These precipitates reside in the  $\gamma$  matrix channels between primary  $\gamma'$  precipitates. Because dislocations tend to initiate in the  $\gamma$  matrix, it is expected that interactions between dislocations and these precipitates would be common. Furnace cooling, however, from the aging temperature is capable of creating a  $\gamma$  matrix that is devoid of secondary  $\gamma'$  precipitates.<sup>20</sup>

While it is expected that a significant interaction exists between the secondary  $\gamma'$  and the active deformation mechanism, exactly how the secondary  $\gamma'$  effects the deformation process is not fully understood. These precipitates have even been linked to large primary creep strains as they may prohibit deformation in the  $\gamma$  matrix channels, forcing shear of primary  $\gamma'$  precipitates resulting in creep anisotropy. Alternatively, it is thought that these precipitates may stabilize the stacking fault ribbons within the  $\gamma$  matrix, leading to enhanced  $\gamma'$  shear and large primary creep strains.<sup>16, 17, 20, 24</sup>

### **Lattice Mismatch**

Another microstructural feature that is thought to impact primary creep is lattice mismatch (misfit). While it is known that lattice mismatch can alter behavior for high temperature creep, specifically in the case of  $\gamma'$  rafting,<sup>25, 26</sup> lattice misfit also bears a significant impact on dislocation motion in the  $\gamma$  matrix and at the  $\gamma/\gamma'$  interfaces.<sup>27</sup> Lattice mismatch between the matrix and precipitates in superalloys results in coherency strains along these interfaces. If the coherency strain is large enough, misfit dislocations will nucleate and/or congregate at these interfaces to relieve the strain. Alloys with large lattice misfit values have shown a propensity to form dense networks of interfacial dislocations during creep testing. Conversely, alloys with reduced  $\gamma/\gamma'$  misfit, exhibiting creep anisotropy, are characterized by relatively few interfacial dislocations and large regions of stacking faults in the precipitates. This difference is possibly the result of compositional changes (which will cause lattice mismatch modification). In the case of CMSX-2 and CMSX-4, for instance, the most notable changes were the additions of rhenium and hafnium, an increase in cobalt, and a decrease in tungsten and chromium. Between the alloys PWA 1480 and PWA 1484 similar changes were made except for an increase in tungsten, a significant decrease in tantalum, and the removal altogether of titanium. Since lattice

mismatch has been shown to be significantly impacted by composition, and mechanical properties as a result, these changes from the first to second generation alloys can also impact the underlying deformation processes that occur during creep.<sup>22</sup> Therefore, any significant change in composition increases the risk of changes in mechanical properties such as the increased primary creep strains discussed in the current investigation.

Each of the aforementioned examples of alloy developments from the last 20 years results in changes in the intermediate temperature mechanical properties of these alloys. Besides the individual changes brought about by increasing rhenium content, secondary  $\gamma'$  precipitation, and lattice mismatch variation, these three variations may all be interrelated. As is often the case in alloy development, changes in behavior are the results of multiple factors. While significant gains in performance may be made without a complete understanding of these behaviors, future gains may rely on applying lessons learned from investigations into the Rhenium Effect, lattice misfit, and aging heat treatment (among many other aspects of alloy design).

### **Modern Superalloys**

Superalloys are known to combine a mix of high temperature tensile and creep strength and environmental resistance. Their microstructure consists of two phases with a face-centered cubic (fcc) matrix known as  $\gamma$ , and a fcc-like  $L1_2$  cuboidal precipitate known as  $\gamma'$ . They are strengthened through the use of solid solution and precipitation hardening techniques resulting in high strength over a wide temperature range. Typically they are also directionally solidified to produce a single grain through the Bridgman process, thus the application of the phrase “single crystal” to describe these alloys when processed in this manner. Following solidification, these alloys require long, high temperature heat treatments for proper homogenization and aging. Several common alloy compositions representing the first three generations of superalloy

Table 2-1. Compositions in weight percent of several common Nickel-based superalloys<sup>3</sup>.

Alloy	Generation	Co	Cr	Mo	W	Ta	Re	Al	Ti	Nb	Hf	Ni
Pratt & Whitney												
PWA 1480	1st	5	10	-	4	12	-	5	1.5	-	-	Bal.
PWA 1484	2nd	10	5	2	6	9	3	5.6	-	-	0.1	Bal.
General Electric												
Rene N4	1st	8	9	6	6	4	-	3.7	4.2	0.5	-	Bal.
Rene N5	2nd	8	7	2	5	7	3	6.2	-	-	0.2	Bal.
Rene N6	3rd	12.5	4.2	1.4	6	7.2	5.4	5.8	-	-	0.2	Bal.
Cannon-Muskegon												
CMSX-2	1st	5	8	0.6	8	6	-	5.6	1	-	-	Bal.
CMSX-4	2nd	9	6.5	0.6	6	6.5	3	5.6	1	-	0.1	Bal.
CMSX-10	3rd	3	2	0.4	5	8	6	5.7	0.2	0.1	0	Bal.

development are given in Table 2-1. Due to the extreme demand of service conditions, the compositions of modern superalloys are quite complex, requiring 10 or more elemental additions. Additionally, a wide variety of elements not shown in Table 2-1 are commonly added to superalloys. These include, but are not limited to, carbon, boron, nitrogen, ruthenium, and some rare earth elements.

The elemental addition that produced the greatest impact in properties during the early stages of superalloy development was rhenium. Beginning with the second generation of alloys, Re became an important factor for high temperature creep strength and microstructural stability. The second and third generations of superalloys contain 3wt.% and 6wt.% Re, respectively. The first generation of superalloys contain no Re. They do, however, contain the  $\gamma'$  strengtheners Al, Ti, and Ta and the refractory elements W and Mo for solid solution strength and microstructural stability. As development continued, the need to restrict  $\gamma'$  coarsening due to thermal exposure became apparent. This led to the addition of Re to superalloys for its low diffusivity that

restricts the growth of primary  $\gamma'$  precipitates. The diffusivity of rhenium in Nickel is so low that it significantly retards the diffusion controlled coarsening of the  $\gamma'$  precipitates. Additionally, Re was found to be a very potent solid solution strengthener, thus the second generation of superalloys was created.<sup>8, 10, 11</sup>

Continued development saw the addition of greater Re additions resulting in greatly improved temperature capabilities and strength. The third generation contains 6wt.% and marks a significant improvement in properties relative to the generations that preceded it. This increase in Re concentration, however, came with a cost. Castability, as measured by incidence of casting defects, was greatly decreased and the propensity for the formation of deleterious topologically close packed (TCP) phases was greatly increased.<sup>1, 2, 8</sup> Current research in fourth generation alloys and beyond is focused on continuing to improve strength while minimizing the harmful side effects of large Re additions through additions of platinum group metals, such as ruthenium.<sup>28</sup> New research was also initiated to find ways to maintain strength while reducing Re concentrations due to the drastic increase in the cost of Re over the last 2 years.<sup>29</sup>

The state of the art of modern superalloys relies on a variety of alloy strengthening and processing techniques developed over the last 30 years. As the high performance and low cost demands continue to grow, the technology will need to grow. The next discussion will review the challenges of these goals from the alloy and processing viewpoints.

### **The Challenge of High Temperature Service**

The service environment experienced by turbine blades in modern gas turbine engines demands high strength and environmental resistance at high temperatures. Normal alloy systems are not capable of withstanding this type of environment. Structural alloys are typically strengthened by a mix of solid solution strengthening, precipitation hardening, and strain

hardening. At temperatures above half the melting point ( $T > 0.5T_m$ ) strain hardening is less effective due to recovery and recrystallization processes.<sup>30</sup> Additionally, normal alloy systems that are precipitation hardened lose strength at the temperatures experienced in gas turbine engines because the precipitate solvus is exceeded, yielding a single phase material. As a result, most normal alloy systems are insufficient for these applications.

In addition to tensile strength are several other properties to consider: creep strength, high cycle and low cycle fatigue, ductility/toughness, thermo-mechanical fatigue, oxidation resistance, and corrosion resistance. Each of these properties will impact the usefulness of an alloy during high temperature service. Because these alloys are subjected to high temperatures and high stresses for long durations during service, creep has been the subject of numerous investigations over the past 40 years. At low temperatures, deformation processes are controlled by dislocation motion (whole and partial dislocations). The movement of dislocations along glide planes is governed by a variety of material properties like elastic modulus, dislocation friction sources (Peierls stresses), the presence of solute atmospheres (Cottrell atmospheres), cross-slip difficulty, stacking fault energy, and anti-phase boundary energy. Add to these the presence of secondary reinforcing phases and interfacial dislocation networks and the intermediate temperature deformation processes of single crystal nickel base superalloys become quite complex.<sup>31</sup>

### **Tensile Behavior**

Low temperature deformation of superalloys is dominated by dislocation motion and stacking fault propagation. At low temperatures, there is insufficient energy for diffusion controlled processes and cross-slip is also more difficult, though not impossible. At high temperatures, however, diffusion controlled processes become active. These include recovery,

vacancy motion, solute motion (solute drag), and phase instabilities ( $\gamma'$  coarsening, TCP precipitation, and carbide transitions).<sup>32-35</sup>

Despite all of the advances in superalloy technology, the basic microstructure employed for single crystal turbine blades is quite simple. Generally, superalloys consist of an fcc matrix with coherent, stress-free ordered  $L1_2$  precipitates. Most first and second generation alloys contain about 60-70%  $\gamma'$ : the optimum value for excellent creep and tensile properties. Maintaining low misfit through alloying has also been shown to effect change in the morphology of the  $\gamma'$  precipitates. Even alloys with “high” lattice misfits ( $|\delta| > 0.5\%$ ) will exhibit less than one percent misfit between the  $\gamma$  and  $\gamma'$  phases. Changing misfit values can produce  $\gamma'$  precipitate shapes varying from spherical to cuboidal to dendritic. The so-called cuboidal morphology is typically desired for high temperature creep resistance with the ideal precipitate edge length between  $0.35\mu\text{m}$  and  $0.45\mu\text{m}$ .<sup>36</sup> The cuboidal structure consists of uniform cubes of  $\gamma'$  with rounded edges and corners. The resulting interstices between  $\gamma'$  particles consists of the  $\gamma$  matrix. These  $\gamma$  “channels” are relatively large in length and width, but narrow in thickness (typically  $< 50\text{nm}$ ).

Strengthening of superalloys can be achieved through alloying and heat treatment. The most common goals involved in strengthening superalloys through alloying can be broken down into several categories:

- Solid solution strengthening of  $\gamma$  matrix
- Modifying misfit to produce cuboidal  $\gamma'$  precipitates
- Increasing  $\gamma'$  volume fraction to the ideal limit
- Solid solution strengthening of  $\gamma'$  precipitates
- Modifying the anti-phase boundary, APB, energy of the  $\gamma'$  phase
- Stabilizing the microstructure with low diffusivity elements (W, Mo, and Re for example)

The addition of carbide phases may also help with fracture strength, but is not likely to affect yield strength due to their large spacing compared to the dislocation spacing.<sup>37</sup> Another consideration is the prevention of TCP phases. Alloys with large refractory element concentrations are at risk of developing TCP phases during long exposure to high temperatures. While the prevention of TCP phases does not necessarily lead to improved strength, the formation of TCP phases is suspected to result in premature failure of superalloys and should be avoided.<sup>35</sup>

Solid solution strengthening of the matrix is typically accomplished by increasing additions of Cr, W, Mo, and/or Re. While these are suitable for solid solution strengthening, secondary concerns may dictate their use. Increasing the W, Mo, and Re content of an alloy may result in decreased TCP resistance and an increase in the  $\gamma/\gamma'$  misfit as these elements are mostly rejected from the  $\gamma'$  phase.<sup>8, 35</sup> Increasing the volume fraction and strength of the  $\gamma'$  precipitates is typically achieved by additions of Al, Ti, and Ta. Controlling the  $\gamma/\gamma'$  misfit and APB energy is a difficult and not fully understood process; however. They are usually maintained through slight adjustment to the entire set of elemental additions until the desired value is achieved as virtually every element can affect misfit and/or APB energy. Finally, one of the benefits of adding slow-diffusing elements like W and Re for solid solution strengthening is that they also serve to stabilize the  $\gamma/\gamma'$  microstructure. With a diffusivity for self-diffusion within nickel that is much lower than any other elements,  $\gamma'$  coarsening kinetics are reduced allowing for precipitate coherency to be maintained longer.<sup>8</sup>

Tensile strain of superalloys usually begins in the  $\gamma$  matrix phase. Dislocations are created on  $\{111\}\langle 110\rangle$  slip planes which are then able to propagate through the material. As in other fcc materials, these dislocations will often dissociate into Shockley partial dislocations of the

$a/6\{111\}\langle 112\rangle$  type with a stacking fault formed in between. As the strain increases, these dislocations will squeeze through the  $\gamma$  matrix channels as described by the Orowan bowing model. As this process progresses, dislocations begin to lie along the surfaces of the cuboidal  $\gamma'$  precipitates eventually forming interfacial networks of dislocations. Continued strain gradually reduces the distance between dislocations in the interfacial networks. As the distance gets smaller, the strength increases due to work-hardening.<sup>24, 27, 33, 37</sup> The tensile behavior of single crystal, nickel base superalloys may also display a yield-point on an engineering stress vs. engineering strain graph. This phenomenon is not unexpected as it is commonly linked to interstitial or substitutional impurities and these alloys contain both in the form of alloying additions.<sup>31</sup>

### **Creep Behavior**

When superalloys are subjected to tensile loads at temperatures greater than 500°C, creep can occur. Creep is a time-dependent plastic deformation process that occurs at loads below the yield stress of the material in question. Creep occurs because the thermal energy that is available at high temperatures allows for thermally activated processes that do not occur at low temperatures to become viable deformation mechanisms. In the case of single crystal superalloys, vacancy and solute diffusion, dislocation climb, cross-slip, and activation of secondary slip systems are all processes that are either difficult or non-existent at low temperatures. Additionally, microstructural evolution may occur resulting in changes to the creep behavior over time. Superalloys are prone to the following microstructural changes in particular:  $\gamma'$  coarsening and loss of coherency, topological inversion (rafting) of the  $\gamma'$  phase, precipitation of additional phases (especially topologically close packed, TCP, phases), and carbide transition/precipitation (MC,  $M_6C$ , and  $M_{23}C_6$ ).<sup>35, 38-41</sup> It is the activation of these

processes that allow for metals to deform over time at loads significantly lower than their yield stress.<sup>25, 31, 33, 42, 43</sup>

Mechanically, creep tests can be conducted in one of two ways. To obtain a true measure of creep requires that the specimen be subjected to a constant stress throughout the duration of the test. Consequently, as the specimen deforms and the cross-sectional area decreases, the load would be reduced accordingly. Unfortunately, though, creep tests must be run at high temperatures within a furnace so accurate measurements of the specimen dimensions are not feasible during testing. Because of this problem, another test procedure has been adopted for use in most cases. This is the constant load creep test (contrasting with the constant stress test discussed above). A constant load creep test is performed by applying the correct amount of weight to the specimen to produce the desired *initial* stress. As the specimen deforms and the cross-section is reduced, no changes are made to the load. The consequence of this design is that the stress level increases throughout the creep test. This investigation uses constant load creep tests because of the simplicity of data acquisition and commercial relevance, so the following discussion refers to data collected with this type of creep test.<sup>31</sup>

For single crystal, nickel base superalloys, there are primarily two temperature regimes of interest that involve creep. At high temperatures, greater than 850°C, creep tests are run with relatively low stresses and are used to simulate the behavior of the thin, exposed parts of a turbine blade. This environment allows for thermally activated processes to occur at a rapid pace. At temperatures below 850°C, the loads are significantly greater. The performance of alloys under intermediate temperatures and high loads depends largely on the tensile strengths of the alloys being investigated. Because of the link between high loads and intermediate

temperatures to large primary creep strains, this set of conditions is the focus of this investigation.

### **Summary**

In order to conduct an investigation into the primary creep behavior of the superalloys PWA 1480 and PWA 1484, specimens will be creep tested at temperatures between 700°C and 815°C and loads greater than 621 MPa. Tensile testing, metallographic examination, X-ray diffraction (XRD), and transmission electron microscopy (TEM) have been conducted to gain an understanding of the underlying factors involved in creating large primary creep strains. Three alloys have been investigated including the first generation PWA 1480, the second generation PWA 1484, and the experimental second generation PWA 1480+Re. These three alloys helped to shed light on several aspects of primary creep behavior and the effect of age heat treatment. Finally, the current investigation may lead to an improved understanding of the effect of rhenium on single crystal nickel base superalloys.

CHAPTER 3  
EXPERIMENTAL PROCEDURES

**Materials**

All three alloys used in this investigation were provided by Pratt & Whitney Aircraft Engines in East Hartford, CT. Test bars were prepared by Pratt & Whitney in investment casting cluster molds of 12 bars measuring approximately 20 cm (8 in.) long with a 1.6 cm (0.625 in.) diameter. Single crystals were prepared using Bridgman style directional solidification furnaces and single crystal selectors to produce an orientation in the [001] direction. Following solidification, the bars were examined through the use of Laue X-Ray Diffraction to verify that all the bars were near the desired [001] orientation. Laue orientation data and original heat treatments for all the material is presented in Tables 3-1, 3-2, and 3-3. Test material was

Table 3-1. Laue orientation data and original heat treatments for PWA 1480.\*

Master Heat	Bar Number	$\alpha$ angle	Solution Heat Treatment	Coating Heat Treatment
P9976	0401	4.2	1288°C / 2hr.	1080°C / 4hr.
P9976	0402	5.2	1288°C / 2hr.	1080°C / 4hr.
P9976	0403	6.2	1288°C / 2hr.	1080°C / 4hr.
P9976	0404	7.3	1288°C / 2hr.	1080°C / 4hr.
P9976	0405	8.8	1288°C / 2hr.	1080°C / 4hr.
P9976	0406	9.5	1288°C / 2hr.	1080°C / 4hr.
P1083	0901	2.5	As-Cast	As-Cast
P1083	0902	2.1	As-Cast	As-Cast
P1083	0903	19.3	As-Cast	As-Cast
P1083	0904	4.0	As-Cast	As-Cast
P1083	0905	3.0	As-Cast	As-Cast
P1083	0906	0.9	As-Cast	As-Cast
P1083	0907	4.8	As-Cast	As-Cast
P1083	0908	4.5	As-Cast	As-Cast
P1083	0909	3.1	As-Cast	As-Cast
P1083	0910	3.9	As-Cast	As-Cast
P1083	0911	2.3	As-Cast	As-Cast
P1083	0912	4.5	As-Cast	As-Cast

\*Bar number 0903 was rejected due to an excessive  $\alpha$  value.

Table 3-2. Laue orientation data and original heat treatments for PWA 1484.

Master Heat	Bar Number	$\alpha$ angle	Solution Heat Treatment	Coating Heat Treatment
P1096	0407	0.5	1310°C / 0.5hr.	1080°C / 4hr.
P1096	0408	3.8	1310°C / 0.5hr.	1080°C / 4hr.
P1096	0409	5.7	1310°C / 0.5hr.	1080°C / 4hr.
P1096	0410	7.2	1310°C / 0.5hr.	1080°C / 4hr.
P1096	0411	9.4	1310°C / 0.5hr.	1080°C / 4hr.
P1096	0412	10.1	1310°C / 0.5hr.	1080°C / 4hr.
P1086	0913	4.0	As-Cast	As-Cast
P1086	0914	7.0	As-Cast	As-Cast
P1086	0915	5.7	As-Cast	As-Cast
P1086	0916	7.5	As-Cast	As-Cast
P1086	0917	8.5	As-Cast	As-Cast
P1086	0918	7.0	As-Cast	As-Cast
P1086	0919	5.6	As-Cast	As-Cast
P1086	0920	8.1	As-Cast	As-Cast
P1086	0921	5.9	As-Cast	As-Cast
P1086	0922	3.1	As-Cast	As-Cast
P1086	0923	6.5	As-Cast	As-Cast
P1086	0924	5.9	As-Cast	As-Cast

Table 3-3. Laue orientation data and original heat treatments for PWA 1480+.

Master Heat	Bar Number	$\alpha$ angle	Solution Heat Treatment	Coating Heat Treatment
P1106	1201	12.6	As-Cast	As-Cast
P1106	1202	15.5	As-Cast	As-Cast
P1106	1203	5.7	As-Cast	As-Cast
P1106	1204	1.6	As-Cast	As-Cast
P1106	1205	9.3	As-Cast	As-Cast
P1106	1206	10.2	As-Cast	As-Cast
P1106	1207	9.0	As-Cast	As-Cast
P1106	1208	0.3	As-Cast	As-Cast
P1106	1209	9.1	As-Cast	As-Cast
P1106	1210	12.6	As-Cast	As-Cast
P1106	1211	4.2	As-Cast	As-Cast
P1106	1212	3.1	As-Cast	As-Cast

provided in two stages. First, a supply of 6 bars of PWA 1480 and 6 bars of PWA 1484 was delivered having been subjected to the standard commercial solution heat treatments (alloy

specific) used by Pratt & Whitney as well as a coating heat treatment cycle. The bars were not, however, subjected to an aging heat treatment. The second delivery of material expanded the testing possibilities significantly. First, another 11 bars of PWA 1480 and 12 bars of PWA 1484 were provided in the as-cast condition. Then, 12 bars of PWA 1480 with 3 wt% Re added were produced and delivered in the as-cast condition. Altogether, 47 single crystal test bars, allowing for the production of up to 94 creep/tensile specimens, were available for experimentation.

### **Heat Treatment**

The first step in the preparation of test specimens was to heat treat all the bars to an appropriate condition. As stated above, the first batch of PWA 1480 and PWA 1484 had already been given solution heat treatments (HT1), Table 3-4. Additionally, this first batch had already received a coating simulation cycle as these alloys are commonly used in the first and second turbine stages of gas turbine engines where coatings are necessary for thermal and environmental protection. Because one aim of this study is to determine the cause of changes in creep behavior due to age temperature, two different aging heat treatments were given to each alloy. Half of the PWA 1480 bars were given a low temperature age (LT, 704°C/24 hr.) and half were given a high temperature age (HT, 871°C/32 hr.) as shown in Table 3-4. The same aging heat treatments were also given to the PWA 1484 bars. Following aging, this first batch of material was ready for sample machining and subsequent testing.

### **Heat Treatment Development**

The remaining test bars, as-cast PWA 1480, as-cast PWA 1484, and as-cast PWA1480+, still required a complete heat treatment cycle. Following early results and metallography of the first batch with the standard solution heat treatments, it was determined that a longer time, higher temperature solution heat treatment might be helpful to reduce the effects of chemical

Table 3-4. Heat treatments used in this study. Solution heat treatment designations (HT#) are given.\*

First Batch					
Alloy	Solution Heat Treatment		Coating Heat Treatment	LT Age	HT Age
PWA 1480	HT1	1290°C/2hr./GFQ	1080°C/4hr./GFQ	704°C/24hr./AC	871°C/32hr./AC
PWA 1484	HT1	1310°C/0.5hr./GFQ	1080°C/4hr./GFQ	704°C/24hr./AC	871°C/32hr./AC
Second Batch					
Alloy	Solution Heat Treatment		Coating Heat Treatment	LT Age	HT Age
PWA 1480	HT0	None	1080°C/4hr./GFQ	704°C/24hr./AC	871°C/32hr./AC
	HT1	1290°C/4hr./GFQ (STD HT)			
	HT2	1290°C/8hr./GFQ			
	HT3	1295°C/1hr.→1299°C/1hr. →1302°C/10hr./GFQ			
PWA 1484	HT0	None	1080°C/4hr./GFQ	704°C/24hr./AC	871°C/32hr./AC
	HT1	1315°C/4hr./GFQ (STD HT)			
	HT2	1315°C/8hr./GFQ			
	HT3	1325°C/1hr.→1332°C/1hr. →1338°C/10hr./GFQ			
PWA 1480 +	HT0	None	1080°C/4hr./GFQ	704°C/24hr./AC	871°C/32hr./AC
	HT1A	1290°C/4hr./GFQ			
	HT1B	1315°C/4hr./GFQ			
	HT2	1280°C/1hr.→1290°C/7hr./GFQ			
	HT3	1293°C/1hr.→1296°C/1hr. →1299°C/2hr.→1302°C/1hr. →1308°C/4hr./GFQ			

\*All samples were heated from room temperature to 1200°C for 0.5hr. at a rate of 20°C/minute, then samples were heated to the first soak temperature at a rate of 10°C/minute. All ramping following the first soak temperature is at a rate of 1°C/minute. GFQ is Gas Furnace Quench (ultra high purity He) and AC is Air Cool. Solution and Coating heat treatments were performed under vacuum and Age heat treatments were performed in air environments.

segregation and the formation of eutectic regions during solidification. Previous research has also shown that incomplete  $\gamma'$  solutioning and dendrite homogenization can lead to substantial reductions in creep life.<sup>36, 44</sup> To counter this effect, a series of heat treatment trials beginning with the standard Pratt & Whitney developed heat treatments was performed.

The first step taken to design a new solution heat treatment was to increase the amount of time of the original heat treatment. Increasing the maximum temperature hold time from 2 hours to 8 hours for PWA 1480 and 0.5 hours to 8 hours for PWA 1484 did not significantly improve the homogeneity of the samples; however, it proved a useful heat treatment for Differential Thermal Analysis (DTA). With samples in the as-cast condition DTA is only moderately useful as the solidus and solvus temperatures tend to be suppressed and transition temperature peaks tend to be broad due to high segregation. Following even a brief heat treatment, however, meaningful data can be obtained as described below.<sup>45</sup>

### **Differential Thermal Analysis**

Differential Thermal Analysis was performed on all three alloys following the extended version (HT2) of the standard solution heat treatment (HT1). DTA was performed by Dirats Laboratories in Westfield, MA using a DuPont 9000 Thermal Analyzer. Data was collected at a rate of 20°C/minute on heating only to eliminate the effects of undercooling. Samples were cut from the single crystal bars to produce a disk approximately 0.5 cm (0.188 in.) thick by 1.6 cm (0.625 in.) in diameter. The HT2 treatment was applied to all three alloy groups for DTA. All samples were run with pure nickel standards. Additional discussion of DTA practices is provided in Appendix A along with the complete DTA scan profiles generated for each sample. The resulting data allowed for determination of the solidus, liquidus, and  $\gamma'$  solvus temperatures for the three alloys and are given in Table 3-5. Clearly, the increased homogeneity of the

Table 3-5. DTA results for all three alloys as-received (HT1/HT0) and heat treated (HT2).\*

Alloy	PWA 1480		PWA 1484		PWA 1480+	
	HT1	HT2	HT1	HT2	HT0	HT2
$\gamma'$ Solvus (°C)	1288	1298	1291	1300	N/F	1298
Solidus (°C)	1304	1307	1338	1346	1291	1311
Liquidus (°C)	1333	1344	1378	1392	1339	1352

\*The  $\gamma'$  solvus was not found for PWA 1480+, HT0.

samples following the HT2 heat treatment resulted in an increase in all of the transformation temperatures. Using these temperatures as a guide, a new heat treatment (HT3) scheme was developed to improve the degree of solutioning and homogenization.

The third heat treatment included brief hold steps at a few temperatures prior to the final soak temperature. Lower temperature steps were used in the early stages of the heat treatment to prevent incipient melting in the interdendritic regions of the alloy where the solidus temperature is suppressed. The final soak was designed to be as close to the solidus of each of the alloys as possible in order to give the best possible degree of homogenization within the alloy. The final heat treatment (HT3) significantly reduced the presence of  $\gamma/\gamma'$  eutectics and increased the degree of homogenization within the alloys.

## Furnaces

Solution and coating simulation heat treatments were given to all three alloys using an Elatec high temperature vacuum furnace. The furnace is capable of temperatures up to 1400 °C under a vacuum greater than  $10^{-4}$  Torr. The heating elements, hearth plate, and jail are fabricated from graphite. Alumina trays were used to separate the test bars from the graphite hearth plate. Temperature control is provided by three type C (W + 5% Re / W + 26% Re) thermocouples all sheathed in individual molybdenum jackets. Two thermocouples were lowered very near the surface of the test bars in the center of the hearth plate. These were used for controlling the

furnace temperature to within approximately  $\pm 1.5$  °C of the setpoint. The third thermocouple is a survey thermocouple used for monitoring the temperature near the front of the hot-zone.

Following all heat treatments in the vacuum furnace, samples and test bars were cooled by injection of ultra high purity helium and the circulation of the helium through a water cooled copper heat exchanger within the furnace by a fan. This rapid quenching technique allows for high cooling rates greater than 250 °C/minute down to approximately 500 °C. This rapid cooling rate minimizes the precipitation and growth of  $\gamma'$  during cooling. Below 500 °C, cooling slows to between 100-200 °C/minute, however, diffusion in the samples at this point has slowed sufficiently to prevent significant  $\gamma'$  coarsening. Furnace control is managed by a Honeywell controller that manages temperature, vacuum, gas quenching, and all valves.

Aging heat treatments (both LTA and HTA) were performed in Carbolite box furnaces with maximum operating temperatures of 1300 °C. The atmosphere is not controlled for these heat treatments as the temperature is typically low enough and the time is short enough that oxidation is not problematic. Temperature control was maintained through the use of two Type K thermocouples placed in direct contact with the bars inside the furnace. Temperatures in the box furnaces were maintained within  $\pm 3$  °C of the setpoint as verified by handheld digital thermometers. Following aging heat treatments, samples and test bars were removed and allowed to air cool on alumina racks. Cooling rates exceeded 100 °C per minute to prevent undesirable  $\gamma'$  coarsening.

### **Characterization**

Throughout this investigation, sample characterization was crucial to understanding what changes had taken place in the alloys. A variety of characterization methods were used to examine samples including the already mentioned Differential Thermal Analysis. Other methods

include metallographic techniques involving optical and electron microscopes, fractography following creep and tensile testing, and transmission electron microscopy (TEM) on interrupted creep specimens to examine deformation structures.

### **Preparing Samples for Metallography**

Samples were taken from test bars and creep/tensile specimens for metallographic examination. The same basic process can be applied to a variety of sample shapes and geometries. Metallographic preparation was conducted according to the ASM Metals Handbook recommendations. Samples were first sectioned from the bulk by the use of either a Leco abrasive cut-off saw or an Allied slow-cut diamond sectioning saw. Both saws are liquid cooled to keep cutting temperatures low. Once sectioned, the specimens were ground flat and polished.

Specimens were first leveled using silicon carbide grinding papers on an 8 inch Leco metallography wheel, then polished using alumina powder and water suspensions. All metallography specimens were polished to 0.3  $\mu\text{m}$  alumina polishing media. Following polishing, the specimens were etched with a  $\gamma'$  etchant developed by Pratt & Whitney (100 mL HCl, 100 mL HNO<sub>3</sub>, 10g MoO<sub>3</sub>, 100 mL H<sub>2</sub>O). The etchant was applied with cotton tipped applicators and was swabbed evenly about the surface until the surface of the specimen appeared hazy. Specimens were then rinsed with water, then methanol, and were finally dried under a jet of compressed air.

Additionally, a second etchant was used to etch away the  $\gamma$  matrix phase. This etchant was an electrolytic etch utilizing a 20% oxalic acid solution at 20 V. The specimens were mounted on a metal stub to maintain the necessary electrical conductivity from the specimen to the power supply and were connected as the anode. The counter electrode (cathode) was a 500 mL stainless steel beaker. The electrolyte was placed in the beaker and the steel beaker was placed

in an ice water bath to keep the electrolyte from heating. The voltage was applied and the specimens were dipped for no longer than 5 seconds. The specimens were immediately rinsed and dried and were ready for metallographic inspection.

All Specimens were then observed on a Leco optical metallograph, a JEOL 6400 tungsten filament scanning electron microscope, or a JEOL 6335F field emission scanning electron microscope. Both electron microscopes were equipped with Energy Dispersive Spectroscopy (EDS) detectors as well. Images taken on these microscopes were used for examination of microstructures during the heat treatment development cycle. Additionally, post test microstructures and fracture surfaces were observed to aid in the understanding of microstructural changes during high temperature testing.

### **Preparing Samples for TEM**

Making specimens for transmission electron microscopy (TEM) involves the same metallographic techniques described above. Interrupted and full-length creep tests were sectioned using the Allied slow-cut diamond saw in the transverse and longitudinal directions. These samples were mounted on aluminum stubs with mounting wax and polished to 0.3  $\mu\text{m}$  alumina powder suspension. The samples were then transferred to special mounts for use with the Focused Ion Beam (FIB) or were thinned for use with the twin jet electropolisher.

The FIB is a scanning electron microscope with an attached Gallium ion beam for milling the sample. Using the FIB, TEM liftout specimens were cut perpendicular, parallel, and at 45° to the stress axis. On PWA 1484 samples, it was possible to obtain TEM specimens near [001], [011], and [111] zone axes from a single sample due to the orientation based distortion of PWA 1484 during creep testing described in later chapters. Lift-outs were placed on 200 mesh Carbon coated Copper grids using micromanipulators.

Alternatively, specimens were also prepared using a twin jet electropolisher. After samples were sectioned from the interrupted creep specimens, as described above, they were thinned by hand to between 100 and 200  $\mu\text{m}$ . Disks of 3 mm diameter were then removed from the thinned material with a TEM punch. The samples were further thinned using a die polisher with a micrometer to between 30 and 70  $\mu\text{m}$  thick. Electropolishing was performed on the 3 mm disks with a solution of 90% methanol and 10% perchloric acid and a voltage of 20V. Liquid nitrogen was added to maintain the temperature of  $-25^{\circ}\text{C}$ . Transmission electron microscopy was conducted using JEOL 200 CX. The TEM was used to for qualitative observation of microstructural changes, dislocation and stacking fault behavior, and variations in  $\gamma/\gamma'$  misfit.

### **Preparing Samples for LEAP**

Local Electrode Atom Probe (LEAP) specimens were prepared from a single bar of PWA 1484 that had already received a solution heat treatment (HT3) and a coating simulation heat treatment. The bar was first cut in four equal pieces on a water cooled Leco abrasive cut-off wheel. Then, two sections (out of four) were subjected to either the LTA or HTA aging heat treatments. One piece from both groups was then separated and subjected to a brief heat treatment above the  $\gamma'$  solvus (30 minutes at  $1310^{\circ}\text{C}$ ) in order to redissolve the  $\gamma'$  and quickly cool before the slow diffusing rhenium atoms have enough time to redistribute, Figure 3-1. This heat treatment was performed in an attempt to form a better understanding of rhenium segregation behavior at the  $\gamma/\gamma'$  interfaces. Once the samples were heat treated, they were sent to AMT, Clifton Park, NY to be sectioned into specimens by electrical discharge machining (EDM). Specimens were 5 cm long cylinders with a diameter of 1.8 mm. Ten specimens were obtained from each of the four samples mentioned above.

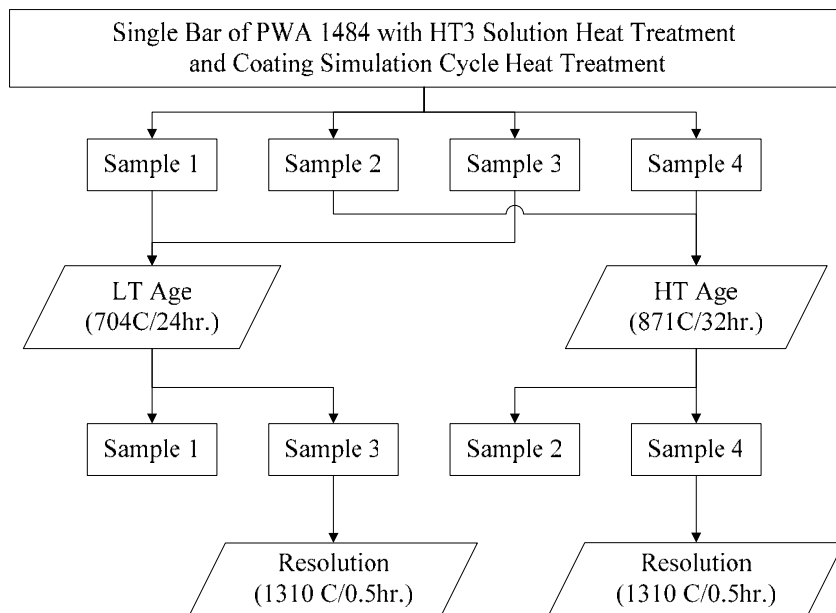


Figure 3-1. Flow-chart of heat treatments for LEAP samples.

The LEAP specimens were then electropolished to reduce the diameter of the cylinder and form a point on one end. The electropolishing unit consisted of a TekPower HY 3005D-3 power supply with 2 variable outputs each capable of 30 V and 5 A. If linked in series or parallel it was capable of 60 V at 5 A or 30 V at 10 A, respectively. The cathode was a 500 mL stainless steel beaker in an ice bath to control the electrolyte temperature. The electrolyte was 90% ethanol and 10% perchloric acid. The specimen was connected to the power supply as the anode and was held in the beaker by a brace such that the cylinder was centered along its length to reduce the effect of varying anode to cathode distance. The applied voltage was varied between 5 V and 20 V until stable polishing took place (typically between 10 V and 15 V). Polishing was stopped once the specimens reached a diameter around 500  $\mu\text{m}$  to 700  $\mu\text{m}$ , which correlates to a tip diameter of approximately 100  $\mu\text{m}$ .

The specimens were then shipped to the Materials Science and Engineering Department at the University of North Texas (Denton, TX). Anantha Puthucode, Ph.D., and Michael Kaufman, Ph.D., of the University of North Texas provided final sample preparations using an Imago

Electropointer. The electropointer used a 3 mm Platinum loop as a cathode to refine the tip radius to less than 75 nm, Figure 3-2. Additional sharpening was occasionally performed using FIB based techniques as well. Once the tip was formed, specimens were run on the Imago LEAP 3000X. Data was then analyzed and manipulated using the Imago IVAS analysis software package. Specimens were run multiple times by reforming the tip following the experiment. Data from these experiments were returned in the form of 3-dimensional and 2-dimensional composition maps with a lateral resolution of 0.1 nm. Additionally, 1-dimensional line scans were also simulated using the same data sets.

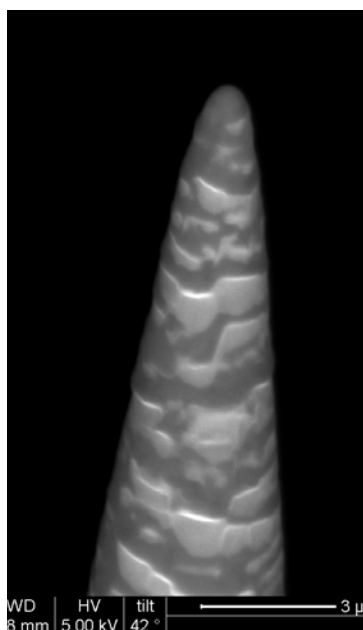


Figure 3-2. SEM micrograph of the tip of a LEAP specimen.

### Preparing Samples for X-Ray Diffraction

Specimens were also prepared for X-Ray Diffraction (XRD) to study the  $\gamma/\gamma'$  misfit in all three alloys. Following the coating heat treatment cycle, bars from each alloy were sectioned to create 4 disks of each alloy 16 mm in diameter by 10 mm thick. These disks were then separated into 4 groups. The first group was tested with no further heat treatment resulting in a total heat treatment time at 1080°C of 4 hours. The other three groups were heat treated an additional 6,

96, or 996 hours to produce samples with total heat treatment times at 1080°C of 10, 100, and 1000 hours. Specimens were cut from the disks at a thickness of 2 mm. The specimens were then thinned and polished on both sides to create a final thickness between 0.3 and 0.7 mm. The polished surfaces were both made parallel to the (001) plane.

All samples were run on Rigaku  $\theta/2\theta$  powder diffractometers at the University of Central Florida's Advanced Materials Processing and Analysis Center (AMPAC). Routine scans were made from 10° to 130° at a scan step of 0.02° and a 1 second dwell time. Local scans of the (002) peak, centered around  $2\theta = 51^\circ$ , and the (004) peak, centered around  $2\theta = 118^\circ$ , were taken with a smaller scan step of 0.01° and a longer dwell time ranging from 3 to 5 seconds. Some specimens were also run at 0.01° steps and 30 second dwell times in an attempt to improve signal clarity. The resulting intensity data were then indexed.

The local scans of the (002) and (004) peaks were used for lattice mismatch calculation. Due to the structure factors and lattice parameters of the fcc  $\gamma$  phase and the  $L1_2 \gamma'$  phase, the peaks produced from both phases overlap at the (002) and (004) positions. In order to separate the contributions, peak deconvolution was performed utilizing the MDI Jade (ver. 7) software package and in agreement with published work.<sup>46</sup> Deconvolution practices included fitting skewed and unskewed Gaussian profiles to account for both phases as well as for the  $\text{Cu } k_{\alpha 1}$  and  $\text{Cu } k_{\alpha 2}$  wavelengths. A complete discussion of the deconvolution procedure and results are given in Appendix B. Once the centers of the  $k_{\alpha 1}$  peaks for both phases are determined, lattice parameters and mismatch were determined. Lattice mismatch values in this investigation were calculated using Equation 3-1. Where  $\delta$  is lattice misfit (multiply by 100 to convert to percent),  $a^\gamma$  is the lattice parameter of the  $\gamma$  phase, and  $a^{\gamma'}$  is the lattice parameter of the  $\gamma'$  phase.

Equation 3-1

$$\delta = \frac{2(a^{\gamma'} - a^{\gamma})}{(a^{\gamma'} + a^{\gamma})}$$

### **JMatPro Thermodynamic Prediction**

The thermodynamic modeling and prediction software package, JMatPro (United Kingdom), was used to predict phase compositions, lattice misfit, and volume fractions of phases as a function of temperature. While these predictions are useful and fast, they are not guaranteed to be accurate for all alloy compositions. To enhance usability and accuracy, the models used for JMatPro have been calibrated through the use of several common benchmark alloys. PWA 1480 is one such benchmark alloy. PWA 1484 and PWA 1480+ predictions, as a consequence of not being used to calibrate the software results, will require some degree of extrapolation to make thermodynamic predictions such as cooling curves, expected compositions, and lattice misfit. Once an alloy composition has been selected, thermodynamic data can be viewed as a function of temperature or calculated at specific temperatures. Data from these predictions were used as a helpful guide and as potential indicators of interesting behaviors. Conclusions based on software results alone, however, should be verified through experimental testing and, for this reason, characterization was conducted to verify several aspects of the JMatPro predictions.

### **Mechanical Behavior**

Following the final aging heat treatment, the test bars were sent to Joliet Metallurgical Labs in Joliet, IL for final machining. Each bar was machined into two creep/tensile specimens according to the drawing in Figure 3-3. The same specimen geometry is suitable for either high temperature tensile testing or creep testing. The specimen gauge length was 2.60 cm and the gauge diameter was 4.5 mm. Specimens were machined from the test bars using low stress grinding techniques to prevent strain hardening along machined surfaces. Following machining,

all specimens were measured to verify all dimensions of interest, most notably gauge length and gauge diameter.

### Tensile Testing

High temperature tensile testing was conducted at 704°C and 815°C to compare the strengths of the three alloys with both age heat treatments. The tensile test matrix can be seen in Table 3-6. Fixtures were lubricated with boron nitride high temperature lubricant and the specimens were threaded into the grips. An Instron servo-hydraulic load frame with a 20,000 lb. load cell was used in coordination with the Merlin control and data acquisition software package.

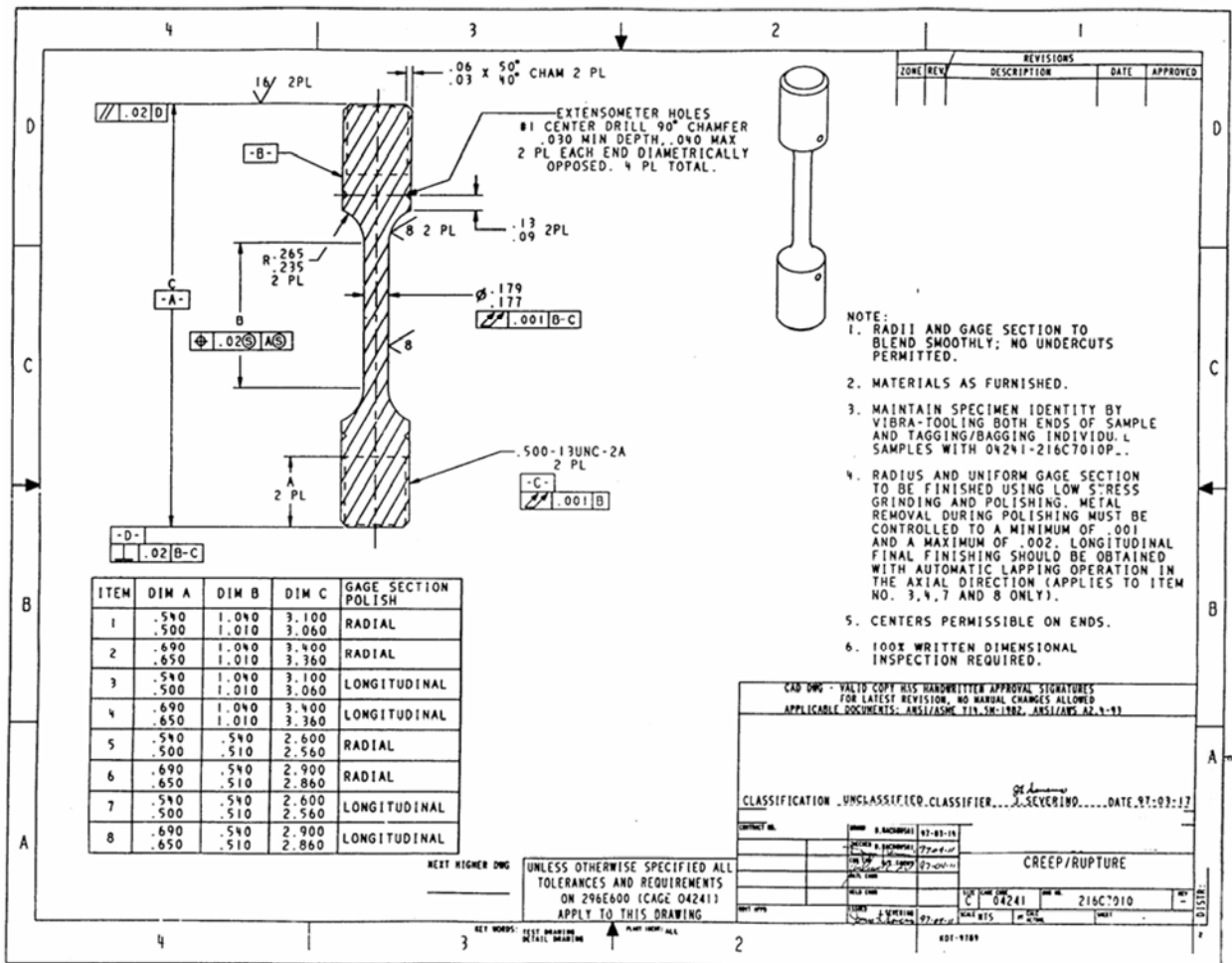


Figure 3-3. Creep and tensile specimen geometry and dimensions.

Table 3-6. Tensile test matrix with sample identification.

Age HT	LT	LT	HT	HT
Test Temp. (°C)	704	815	704	815
PWA 1480	0402-2	0403-2	0405-2	0406-2
	0905-1	0901-2	0906-1	0906-2
PWA 1484	0408-1	0409-2	0411-2	0411-1
	0915-1	0915-2	0919-1	0919-2
PWA 1480+	1205-1	1203-2	1207-1	1209-2

A clam-shell style furnace capable of temperatures up to 1000°C was used to control the temperature to within  $\pm 1.7^\circ\text{C}$  of the setpoint throughout the test. Temperatures were maintained by two Type K thermocouples with Nextel high temperature ceramic insulation for thermal protection. Both thermocouples were tied to the gauge section of the specimen with 24 gauge 80Ni-20Cr wire. Prior to starting the test, all specimens were subjected to a 15 minute soak period to ensure uniform temperature of the sample and fixtures. All tensile tests were performed in air.

During tensile testing, a constant cross-head speed of 0.25 cm/min. was used for all tests. This cross-head speed corresponds with an initial strain rate of 0.25 cm/cm/min (0.1 in./in./min.). Data acquisition was made possible by the use of a high temperature extensometer frame that attached to the specimen through the use of knife edges. This extensometer frame then extended down out of the furnace to an easily accessible area where a digital extensometer connected to the computer could be attached. The Merlin software package (by Instron) was used to record pre-test sample dimensions, control the servo-hydraulic system, and record load, position, and extensometry data during the test. Data recorded during a test were subsequently analyzed to determine yield strength, ultimate tensile strength, percent elongation, and failure strength.

## Creep Testing

Creep tests were conducted on Satec M-3 style creep frames. The tests conducted for this study were constant load creep tests. Each frame has a weight pan for applying the load and a 16 to 1 lever arm ratio to load the specimen. As in the tensile tests, all threaded connections were lubricated with boron nitride high temperature lubricant. Specimens were also affixed into high temperature extensometers as in tensile testing through the use of either knife edges on the gage sections or set screws on the shoulders. The bases of the creep extensometers, though, included fixtures for Linear Variable Differential Transducers (LVDT) for measurement of displacement during the test. Again, clam-shell furnaces capable of 1200°C or 1300°C (depending on which frame was used) heated the specimens to the desired temperature for the duration of the creep test. Temperature control is maintained by the use of 3 Type K thermocouples attached to the gauge section of the specimens by 24 gauge 80Ni-20Cr wire as shown in Figure 3-4.

Temperatures were maintained to within  $\pm 1.7^\circ\text{C}$ . Following heating to the test temperature, all specimens enter a soak period for 1 hour prior to loading and the commencement of the creep test. Hot loading was performed in multiple steps and displacement measurements were taken allowing for calculation of the elastic modulus.

The NuVision Mentor Creep Controller software (Satec) allowed for control of the creep frames, furnaces, and data collection. Creep data was collected at a rate of 5 times per minute for the first hour, then 1 time per minute for the remainder of the test. Additionally, times to 0.1%, 0.2%, 0.5%, 1%, 5%, and 10% creep were recorded automatically. Test specifications were written to conduct creep tests at four conditions: 704°C / 862 MPa, 704°C / 758 MPa, 760°C / 690 MPa, and 815°C / 621 MPa. These conditions were chosen because of their similarity to real-world service conditions and to generate the large primary creep strains as



Figure 3-4. Three Type K thermocouples are attached to the gauge length of creep specimens with 80Ni-20Cr wire.

reported in the literature.<sup>16, 20, 47</sup> The creep test matrix used for this study can be seen in Table 3-

7. Full length and Interrupted creep tests were conducted to obtain a variety of useful data. Full length tests are those that were allowed to run to failure. Interrupted tests are those that were stopped prior to failure in one of two conditions: after 0.5% secondary creep and tests running longer than 1200 hours with no sign of imminent failure.

Table 3-7. Creep test matrix with sample identification. Creep tests were run to failure or terminated following 0.5% secondary creep.

	Temp (°C)	LT Age			HT Age		
		704	760	815	704	760	815
Tests run to failure	PWA 1480	0401-1	0401-2	0403-1	0404-1	0405-1	0406-1
		0402-1		0403-2	0907-1		0907-2
		0902-1		0902-2			
	PWA 1484	0407-1	0408-2	0409-1	0410-2	0410-1	0412-1
		0913-1		0913-2	0412-2		0917-2
					0917-1		
				0920-1			
PWA 1480+	1203-1		1205-2	1209-1		1207-2	
Tests stopped after 0.5% secondary creep	PWA 1480	0903-1		0903-2	0908-1		0908-2
	PWA 1484	0914-1		0914-2	0918-1		0918-2
	PWA 1480+	1204-1		1204-2	1210-1		1210-2

## CHAPTER 4 RESULTS: ALLOY MICROSTRUCTURES

The three alloys used in this study represent first and second generation superalloys. Typically, nickel based superalloys may contain two or more phases including:  $\gamma$  (fcc Ni solid solution, matrix),  $\gamma'$  ( $L1_2$  Ni<sub>3</sub>Al), Carbides (MC, M<sub>6</sub>C, or M<sub>23</sub>C<sub>6</sub>), and/or Topologically Close Packed (Sigma, Mu, Laves, and/or P phases). The occurrence of several of these phases in the three alloys investigated here is discussed as a result of heat treatment and mechanical testing. All three alloys contain primary  $\gamma$  phase as a matrix with a high volume percent of  $\gamma'$  precipitates following solution heat treatment and aging. The presence of a low amount of Carbon results in the formation of both script and blocky carbide phases for all three alloys. PWA 1480 and PWA 1480+ contain the greatest amount of carbide phases possibly as a result of a lower solubility for Carbon in the alloys. This effect is particularly prominent in PWA 1480+ with the Re addition resulting in an increase in carbide amounts when compared to PWA 1480 without Re. Additionally, the alloy PWA 1480+ displayed poor resistance to the formation of TCP phases. The following discussion will focus on the properties of the phases themselves and their incidence as a result of casting and subsequent heat treatment as well as any changes during mechanical testing. Due to the large number of tensile graphs, creep graphs, micrographs, and other figures presented in the current and following results chapters, all figures have been placed at the end of the respective chapters (Chapters 4-7) to aid reading speed and comprehension.

### **Phase Descriptions**

#### **The $\gamma$ Phase**

The matrix of single crystal nickel base superalloys consists of the fcc solid solution  $\gamma$  phase. Due to the large volume fraction of  $\gamma'$  used for high strength and creep resistance in these alloys, the  $\gamma$  phases only constitutes around 25-35% of the alloy by volume. Topographically,

the  $\gamma$  phase forms in the long narrow regions between the cuboidal (cubes with rounded edges)  $\gamma'$  precipitates. These “channels” are typically 50-150 nm thick by 0.3-0.5  $\mu\text{m}$  in length and width. The length and width dimensions, obviously, are controlled by the local  $\gamma'$  size and distribution. The  $\gamma$  phase from all three alloys can be seen in Figures 4-1 through 4-3 as the light gray regions between the darker squares ( $\gamma'$  precipitates).

Compositionally, there are significant differences between the  $\gamma$  and  $\gamma'$  phases. For as long as superalloys have been in development there have been research investigations into the compositions of the two phases. In general terms, the refractory elements added for solid solution strengthening partition to the  $\gamma$  matrix and the so called “ $\gamma'$  strengtheners” partition to the  $\gamma'$  phase. Specifically, Re has been shown to partition especially strong to the  $\gamma$  phase, however the addition of W can result in up to 20% of the added Re partitioning to the  $\gamma'$  phase, effectively reducing the Re content of the  $\gamma$  matrix.<sup>35</sup>

The concentration of the  $\gamma$  phase can be predicted utilizing the JMatPro thermodynamic prediction software. The calculated equilibrium concentration of the  $\gamma$  phase as a function of temperature is given in Figures 4-4 through 4-6. The nickel concentration for the three alloys varies from about 50% to 65% depending on the temperature. The enrichment of the gamma phase by Cr is most prominent in PWA 1480, followed by PWA 1480+ and PWA 1484, respectively. Within the temperature range of interest to the present investigation (700°C to 815°C), the refractory content of the  $\gamma$  phase (with the exception of W) of PWA 1480 and PWA 1480+ is low. The prediction indicates that the  $\gamma$  phase would contain 2% or less of Re and Ta. The W content is around 5% for the PWA 1480 based alloys. The Cr content of PWA 1480 and PWA 1480+ is much larger than that of PWA 1484, while the Co content of PWA 1484 is nearly

double that of PWA 1480 and PWA 1480+. The  $\gamma$  phase of PWA 1484 is also predicted to contain a greater amount of rhenium.

### **The $\gamma'$ Phase**

Because nickel base superalloys are precipitation hardened alloys, the nature of the reinforcing phase is critical to the performance of the alloy. Very early during superalloy development it became clear that  $\gamma'$  ( $\text{Ni}_3\text{Al}$ ) would be a good candidate for the strengthening phase.<sup>37, 48</sup> Single phase  $\gamma'$  has been shown to exhibit a large increase in strength as the temperature is increased to 800°C. Traditional (non-superalloy) alloys exhibit a slow decrease in strength with increasing temperature. When an alloy containing both phases is tested, the Critical Resolved Shear Stress (CRSS) is much larger than the CRSS of either alloy individually and is stable with increasing temperature.<sup>37</sup> The predicted compositions of the  $\gamma'$  phase in all three alloys is presented in Figures 4-7 to 4-9.

Examples of the  $\gamma'$  morphologies present in the three alloys tested here can be seen in Figures 4-10 to 4-13. PWA 1480 exhibits a large variability in  $\gamma'$  size and shape based on the location within the sample. For instance, dendrite core regions contain fine, cuboidal  $\gamma'$  and the interdendritic regions near eutectics contain large, irregular  $\gamma'$  precipitates (Figures 4-10 and 4-11). Both PWA 1480 and PWA 1480+ contain retained eutectics due to the very small heat treatment window (9°C for PWA 1480 and 13°C for PWA 1480+, see Table 3-5). A retained eutectic is shown for PWA 1480+ in Figure 4-12. Additionally, segregation remains after the solution heat treatment and this leads to differences in  $\gamma'$  characteristics by location. To counter these effects, as much as was practical, the solution heat treatments for PWA 1480 and PWA 1480+ ended with final hold temperatures only 5°C and 3°C below the solidus for each alloy, respectively. PWA 1484 has a much larger heat treatment window (defined as the difference in

°C of the  $\gamma'$  solvus and solidus temperatures). As a result, PWA 1484 exhibits very little retained eutectic following casting, Figure 4-13. Solution heat treatment was able to eliminate eutectic regions entirely for this alloy.

### **Primary $\gamma'$**

The cuboidal primary  $\gamma'$  precipitates for all three alloys are between 0.3  $\mu\text{m}$  and 0.5  $\mu\text{m}$  in edge length. In the case of the single crystal nickel superalloys PWA 1480 and PWA 1484, a high volume fraction of primary  $\gamma'$  is precipitated partially from cooling following solution heat treatment and partially during the aging heat treatments. As the temperature is increased, the equilibrium volume fraction of  $\gamma'$  decreases as shown in Figure 4-14. Comparing the three alloys in question it becomes clear that PWA 1480 and PWA 1480+ have a significantly greater volume fraction of  $\gamma'$  as predicted by JMatPro. A larger  $\gamma'$  volume fraction can lead to differences in mechanical behavior.<sup>49</sup>

The nature of the interaction between the  $\gamma'$  phase and Re has been the subject of several investigations spanning the past 30 years. It is generally accepted that Re is rejected from the  $\gamma'$  phase during precipitation and so partitions to the  $\gamma$  matrix. As a result, Re additions are often implicated as the probable cause of large negative lattice misfit values in the vicinity of the  $\gamma/\gamma'$  interface.<sup>8</sup> The local enrichment of the matrix side of the  $\gamma/\gamma'$  interface occurs over a relatively short distance due to the low diffusivity of rhenium. Two theories regarding the nature of the enriched layer have been argued for the last 20 years. One states that the rejected solute atoms form a hardened “shell” around the precipitates. A contrasting study published in 1988 suggests that the rejected Re forms hard clusters roughly 10 Å in size.<sup>10, 11</sup> Similarly, clustering has been shown to occur with Cr forming enriched regions less than 4 nm in size. These Cr clusters are thought to be due to the creation of the ordered structure  $\text{Ni}_3\text{Cr}$  ( $\text{DO}_{22}$ ).<sup>50</sup>

The  $\gamma'$  phase is of particular interest for the present investigation due to the correlation of large primary creep strains with  $\gamma'$  shearing mechanisms. The nature of the  $\gamma'$  phase and the  $\gamma/\gamma'$  interface may be related to the primary behavior described herein. Additionally, while most investigations that pursue an understanding of the  $\gamma'$  phase focus on the primary  $\gamma'$  precipitates, the secondary  $\gamma'$  precipitates are also of significant value due to their location in the  $\gamma$  matrix channels. As discussed in Chapter 6, TEM analysis revealed that dislocations in PWA 1480 are limited to the  $\gamma$  matrix where they are likely to frequently interact with the secondary  $\gamma'$ . PWA 1484, however, is not so constrained and so an understanding of both the primary and secondary  $\gamma'$  precipitates will aid in understanding the active deformation mechanisms.

### **Secondary $\gamma'$**

**Metallography.** Secondary  $\gamma'$  precipitates, Figures 4-15 to 4-17, are much smaller (less than 50 nm in diameter) and spherical. These secondary precipitates lie in the narrow  $\gamma$  channels and in the larger primary  $\gamma'$  free regions near eutectics and minor phases. Figures 4-15 and 4-16 are from PWA 1480 following an interrupted creep test (LTA, 704°C/862 MPa). Figure 4-17 shows the secondary  $\gamma'$  in PWA 1480+ also following an interrupted creep test (LTA, 704°C/862 MPa). Not much is really understood about these ultra-fine precipitates. One key study, (Takehi, 1999), demonstrated the ability to eliminate secondary  $\gamma'$  precipitates by utilizing a slow furnace cool following the final age temperature.<sup>20</sup> It is generally agreed that secondary  $\gamma'$  form during the rapid cooling commonly employed in standard heat treatment practices.<sup>20, 47, 51</sup> The small size of the secondary precipitates coupled with the complex environment in which they occur makes it difficult study the structure and composition of these precipitates. Viewing the secondary  $\gamma'$  precipitates via SEM techniques was unsuccessful with PWA 1484; however.

**Local electrode atom probe (LEAP).** The LEAP system is a new characterization technique developed for high resolution compositional analysis coupled with high spatial resolution. This new system was employed in the present investigation to study the rejection of Re from  $\gamma'$  during aging and solution heat treatments and it allowed for examination of secondary  $\gamma'$  in PWA 1484 where metallographic techniques failed due to the much better solution and homogenization that was achieved in the alloy. In order to interpret LEAP results, a brief discussion of its use is necessary (see Chapter 7 for a complete discussion). Because the LEAP utilizes compositional data, two and three dimensional map representations can be created by assigning colors to individual atoms. To make the images useful, maps are created by applying thresholds to limit the number of atoms appearing in the image. For example, a limit of 18% aluminum would eliminate almost all Al dots in the  $\gamma$  phase while allowing Al dots to appear in the  $\gamma'$  phase. In this way, the limits of the  $\gamma$  and  $\gamma'$  phases can be mapped.<sup>52</sup> To examine the  $\gamma'$  phase, these limits were applied to the Al dots such that the  $\gamma$  phase is transparent and the  $\gamma'$  phase appears in stark contrast. An example of this type of image for PWA 1484 can be seen in Figure 4-18.

The micrographs, coupled with the LEAP data, revealed the presence of secondary  $\gamma'$  in both age conditions of all three alloys. This result is consistent with those reported by Kakehi due to the use of rapid cooling from all heat treatments in the current investigation.<sup>20</sup> Despite the similarities in secondary  $\gamma'$  morphology between alloys, though, significant differences in primary creep occurred during mechanical testing. This behavior will be discussed in further detail in Chapter 8, however, it is clear that primary creep is controlled by many mechanisms and not primarily by the presence of secondary  $\gamma'$  precipitates.

## The $\gamma/\gamma'$ Eutectic

All three alloys formed  $\gamma/\gamma'$  eutectics during solidification. Examples can be seen in Figures 4-19 through 4-20. These two-phase features form during solidification due to the complex nature of the alloys. During dendritic growth of superalloys, the first material to solidify is enriched in the high melting point refractory elements. These first-to-solidify regions eventually comprise the dendrite cores and have the highest solidus temperature compared to other regions in a sample (excluding, of course, minor phases such as high melting point carbides/TCP phases).<sup>44, 53</sup> As solidification progresses the liquid becomes depleted in these refractory elements and, consequently, enriched in lower melting point elements. The solidification temperature of the remaining liquid continues to decline until the eutectic temperature is reached. At this lowest temperature, a two-phase eutectic region is formed with the remaining liquid. This range of solidification temperatures ahead of an advancing solidification front leads to the creation of the so-called “mushy zone” in directional solidification.

Because the eutectic regions solidified at the lowest temperature, these regions limit the thermal capability of the alloy. To improve the thermal capability and reduce the effect of eutectics, solution heat treatments have been developed to provide enough thermal energy for significant diffusion to take place to allow the enriched regions of the dendrite cores and eutectics to approach the original alloy composition. In order for this to occur, solution heat treatments must exceed the  $\gamma'$  solvus but remain below the solidus temperature. One danger, however, is the risk of incipient melting. Increasing the temperature of the material too quickly to a temperature above the  $\gamma'$  solvus may cause inadvertent melting because the solidus may be depressed to the same level as the  $\gamma'$  solvus itself. For this reason, solution heat treatments of

these alloys often takes the form of a multi-step heat treatment that approaches the  $\gamma'$  solvus and the solidus slowly (the HT3 heat treatments, for example, follow this idea, Table 3-4).<sup>2,3</sup>

The  $\gamma/\gamma'$  eutectics that formed during solidification were retained in PWA 1480 and PWA 1480+ following solution heat treatment. The already mentioned narrow solution heat treatment windows for these two alloys prevented the eutectics from being eliminated entirely. Following the HT3 solution heat treatment, however, they were significantly reduced due to the longer time and higher temperature than the HT1 heat treatments. Figures 4-19 and 4-20 contain examples of eutectics in PWA 1480 and PWA 1480+. As seen in Figure 4-20, eutectic regions often occur in close proximity to carbides. Figures 4-21 and 4-22 are close-up views of eutectics in which both eutectic phases ( $\gamma$  and  $\gamma'$ ) can be seen. Figure 4-21 shows an as-cast example and Figure 4-22 shows a eutectic following an interrupted creep test. PWA 1484, however, exhibited no appreciable eutectics following heat treatment due to the much larger solution heat treatment window (46°C in the HT2 condition, Table 3-5).

### **The Carbides**

The presence of a small amount of carbon leads to the formation of carbide phases in most single crystal nickel superalloys. The three alloys discussed herein contain between 0.02 and 0.04 wt.% C. This small addition is enough to produce a low volume fraction of carbide phases. The carbide phases most commonly encountered in superalloys are the primary MC type and the transition, or secondary,  $M_6C$  and  $M_{23}C_6$ . Many other carbides are possible as well in addition to the formation of boride, nitride, and carbo-nitride phases (in the presence of carbon, nitrogen, and/or boron).<sup>38, 50</sup> There has been a recent increase in interest in the many perceived benefits and/or detriments of adding carbon to single crystal superalloys; however, they are beyond the scope of this investigation. Originally added as a grain boundary strengthener, carbon was

removed from early single crystal superalloys. Recently, though, carbon has been added back into single crystal superalloys in low amounts to lower casting defects, to capture tramp elements, and to improve defect tolerance.

The carbides found in PWA 1480 and PWA 1484 are found in interdendritic regions and take on script like morphologies, Figures 4-23 to 4-25. Some blockier shapes are possible as well depending on the local conditions. Larger amounts of carbon are required to produce dendritic carbides and so the carbides appear to be localized and not networked as shown in the longitudinal section in Figure 4-24. Both PWA 1480 and PWA 1480+ exhibit local networks of script like carbides throughout. PWA 1484, however, exhibits isolated clusters of small blocky carbides as shown in Figure 4-26. This difference is likely primarily due to the lower Carbon concentration of PWA 1484 (roughly half of the Carbon concentration of PWA 1480 and PWA 1480+). Additionally, some carbides in the heat treated PWA 1480 and PWA 1480+ samples appear to be in the processes of dissolving as solutioning and homogenizing processes are occurring, Figure 4-27. The carbide phases, while subject of many investigations, are not considered to be cause for concern during primary creep. Because primary creep occurs well before failure, the issue of premature crack initiation is not critical and so these phases are not likely to play much of a role in primary creep.

### **The Topologically Close Packed (TCP) Phases**

Topologically close packed phases are deleterious phases that form during high temperature exposure of many nickel base superalloys. Topologically close packed structures differ from geometrically close packed (GCP) structures (like fcc  $\gamma$  and  $L1_2 \gamma'$ ) by having planes of close packed atoms separated by relatively large planar spacings, while GCP phases are close packed in all directions. The large interplaner distances are caused by large diameter solute

atoms such as the refractory elements Re, W, and Mo. Several related phases fall under the category of “Topologically Close Packed” including  $\sigma$ ,  $\mu$ , P, and Laves. Due to their brittle nature, their often needle and plate-like morphology, and their ability to rob the surrounding material of solid solution strengtheners, TCP phases have been the focus of great concern within the superalloy community. The drive to eliminate TCP phases from commercial alloys has led to the development of computer modeling and prediction methodologies like PHACOMP (PHase COMPutation) utilizing the number of unpaired electrons,  $N_v$ , for each element in an alloy. There have been several attempts to modify this model with varying levels of success (including atomic size factors,  $M_d$ ); however, the basic theory remains the same.

By assigning specific  $N_v$  numbers to each alloy and building assumptions about the typical concentration of phases in an alloy, an average  $N_v$  value can be determined. It has been shown that for many alloys, an  $N_v$  value that exceeds a critical value of 2.45-2.5 will lead to the formation of  $\sigma$  phase. Using the traditional  $N_v$  method of PHACOMP, PWA 1480 has an average  $N_v$  value of 2.54 while PWA 1484 has an average  $N_v$  value of 2.50 (reported in Durrand-Charre, 1997).<sup>50</sup> These values would indicate that PWA 1480 is likely to produce TCP phases during long-term, high temperature exposure, while PWA 1484 is potentially safe from TCP formation. Adding 3 wt.% Re, however significantly increases the already high  $N_v$  of PWA 1480, leading to early and rapid precipitation of TCP phases during high temperature exposure. This prediction has been proven during creep testing as shown in Figures 4-28 and 4-29. The TCP phases shown were produced during primary creep of PWA 1480+ and were prevalent in specimens tested at 704°C and 815°C and with either age heat treatment. While TCP phases are linked to premature failure of superalloys, it should be noted that PWA 1480+ exhibited the longest creep lifetime and the lowest creep rate and primary creep strain as discussed in Chapter

6. These results indicate that TCP formation is not necessarily guaranteed to cause a detriment to mechanical strength properties, however, fracture toughness and ductility may be reduced.

### **Changes Following Primary Creep**

The most significant changes to the microstructures of the three alloys was exhibited by PWA 1484. Interrupted creep tests of PWA 1484 were stopped following as much as 28% creep in 15 hours or less of testing. As will be shown in Chapter 6, PWA 1484 deformed by massive stacking fault shear of the  $\gamma'$  phase. When these specimens were observed after testing, all the PWA 1484 specimens exhibited elliptical cross-sections rather than the original circular cross-sections. This behavior was consistent with work published on both PWA 1484 and another second generation superalloy, CMSX-4.<sup>16, 17, 47</sup> Metallographically, these specimens also exhibited elongation of the  $\gamma$  phase in the [110] direction (observed with a  $\gamma'$  etch), Figures 4-30 and 4-31. Following the use of the electrolytic etch, the primary  $\gamma'$  precipitates appeared to be cut along planes consistent with (111) planes, Figures 4-32 and 4-33. These figures indicate that the  $\gamma'$  shear processes active in PWA 1484 must be severe due to the significant changes to the primary  $\gamma'$  precipitates following interrupted creep testing.

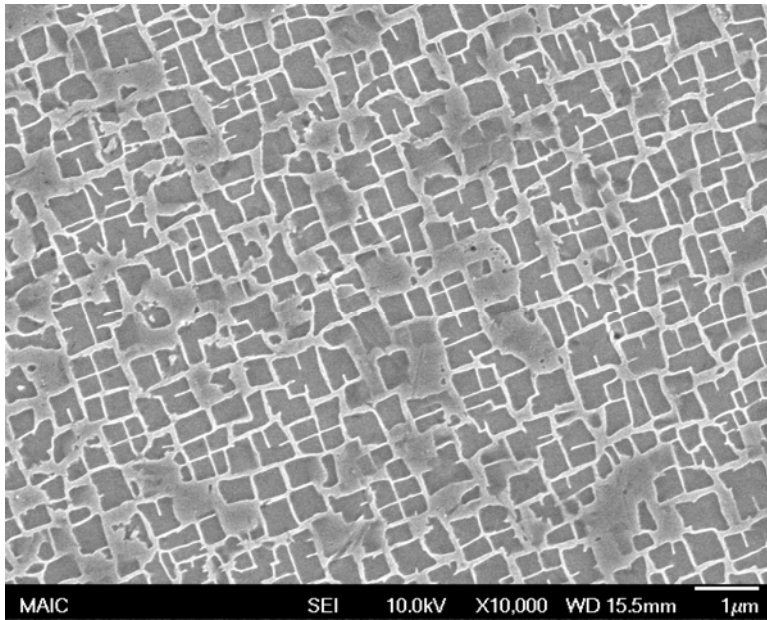


Figure 4-1.  $\gamma/\gamma'$  microstructure of PWA 1480 HT3 ( $\gamma'$  etch). The  $\gamma$  phase is the light gray phase between the cuboidal  $\gamma'$  phase (dark grey).

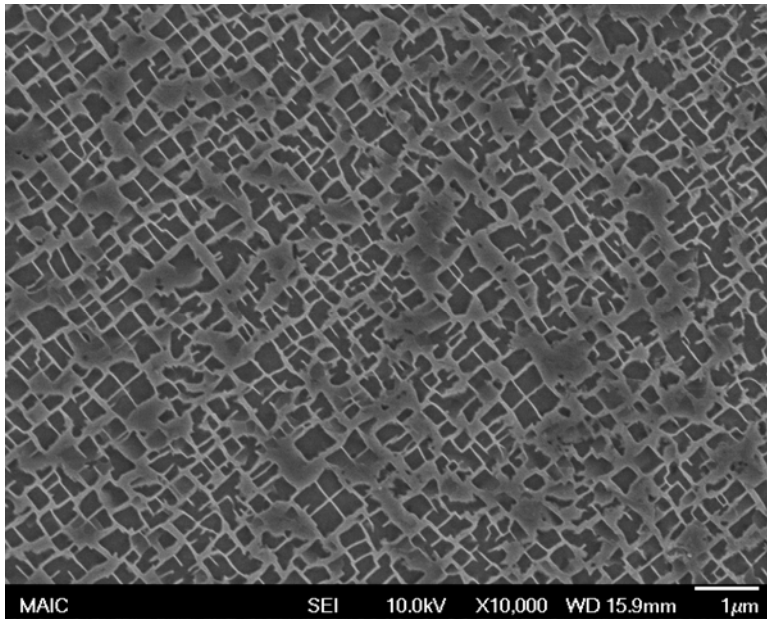


Figure 4-2.  $\gamma/\gamma'$  microstructure of PWA 1480+ HT3 ( $\gamma'$  etch). The  $\gamma$  phase is the light gray phase between the cuboidal  $\gamma'$  phase (dark grey).

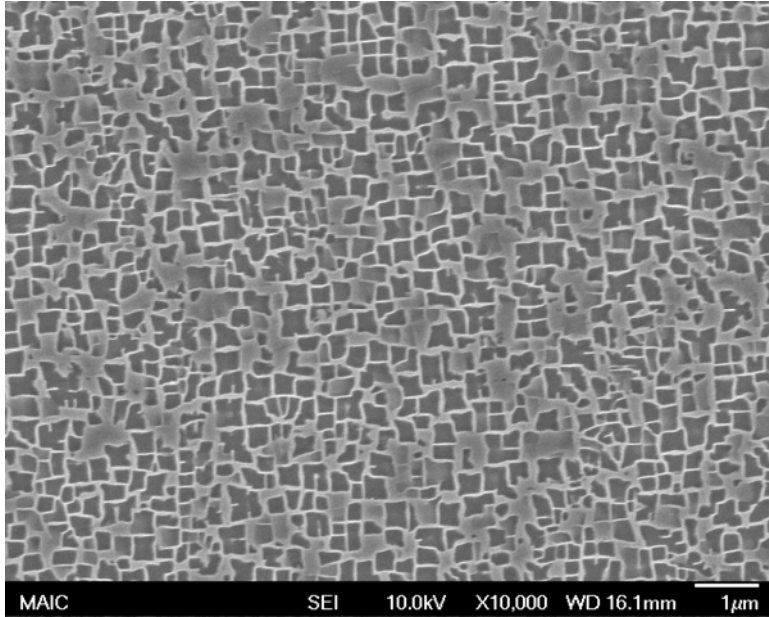


Figure 4-3.  $\gamma/\gamma'$  microstructure of PWA 1484 HT3 ( $\gamma'$  etch). The  $\gamma$  phase is the light gray phase between the cuboidal  $\gamma'$  phase (dark grey).

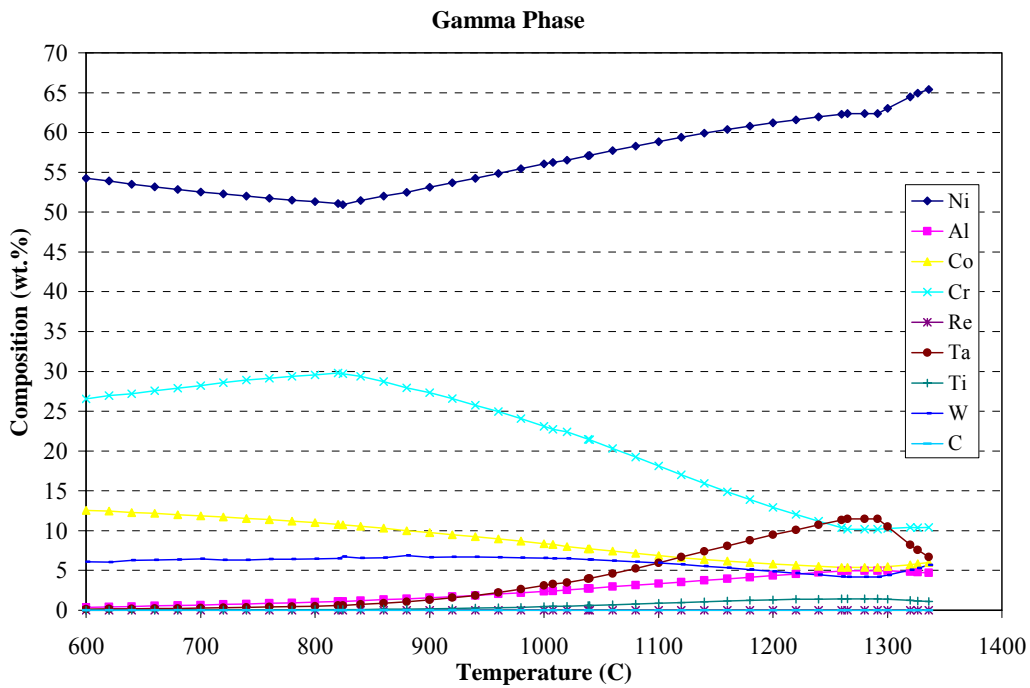


Figure 4-4. Composition of the  $\gamma$  phase of PWA 1480 as a function of temperature as predicted by JMatPro.

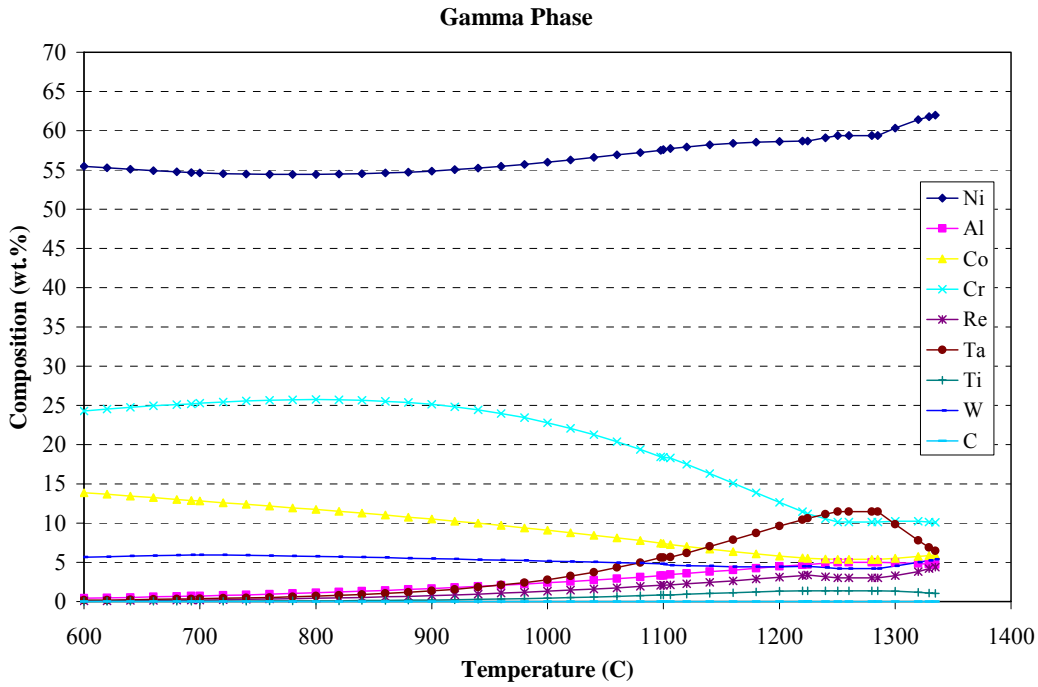


Figure 4-5. Composition of the  $\gamma$  phase of PWA 1480+ as a function of temperature as predicted by JMatPro.

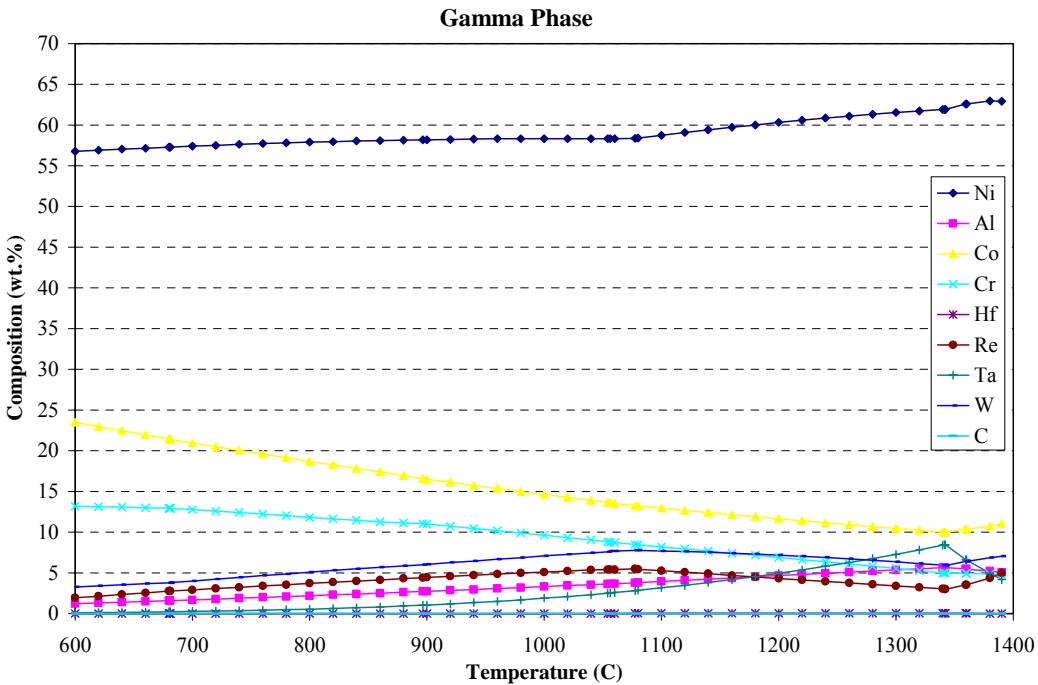


Figure 4-6. Composition of the  $\gamma$  phase of PWA 1484 as a function of temperature as predicted by JMatPro.

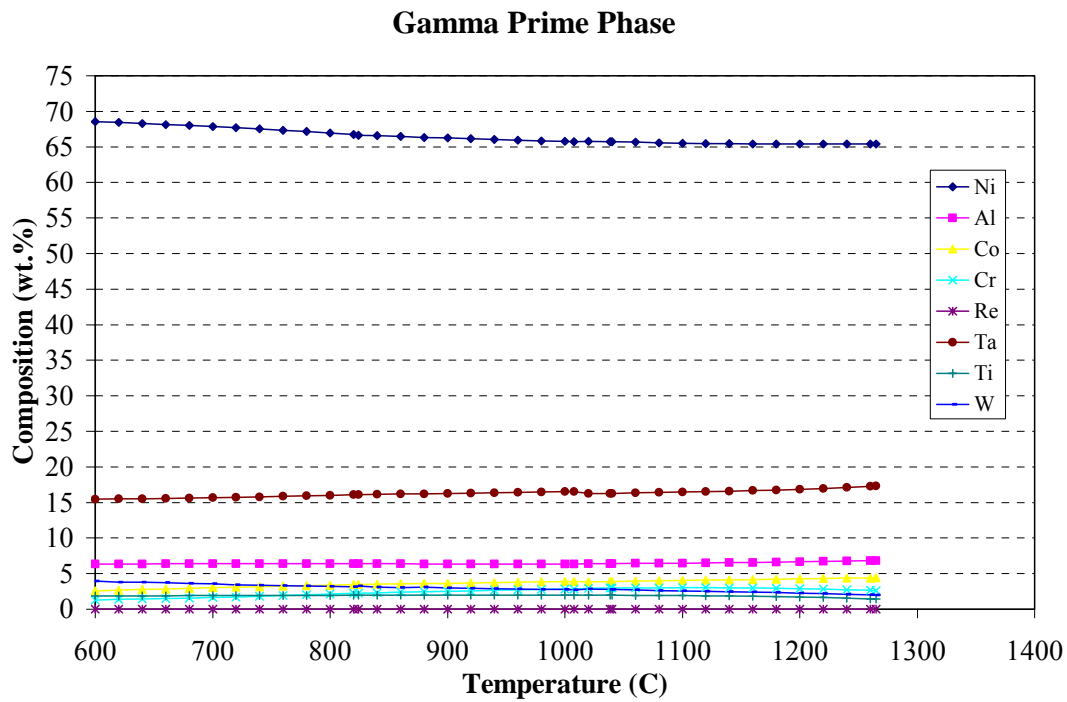


Figure 4-7. Composition of the  $\gamma'$  phase of PWA 1480 as a function of temperature as predicted by JMatPro.

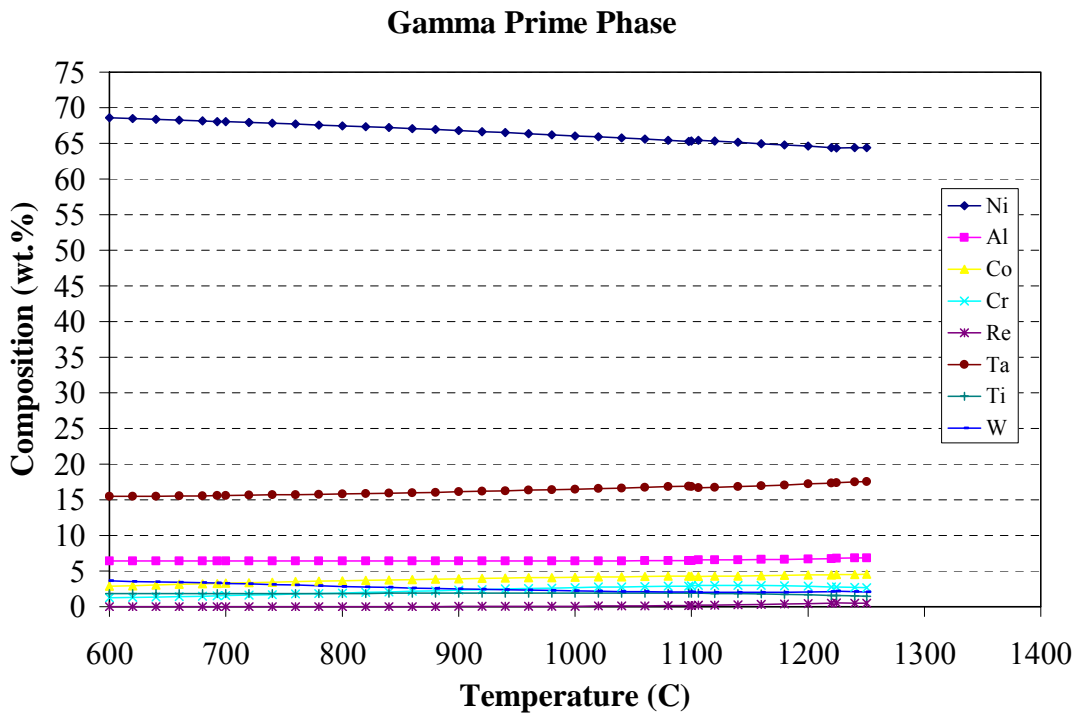


Figure 4-8. Composition of the  $\gamma'$  phase of PWA 1480+ as a function of temperature as predicted by JMatPro.

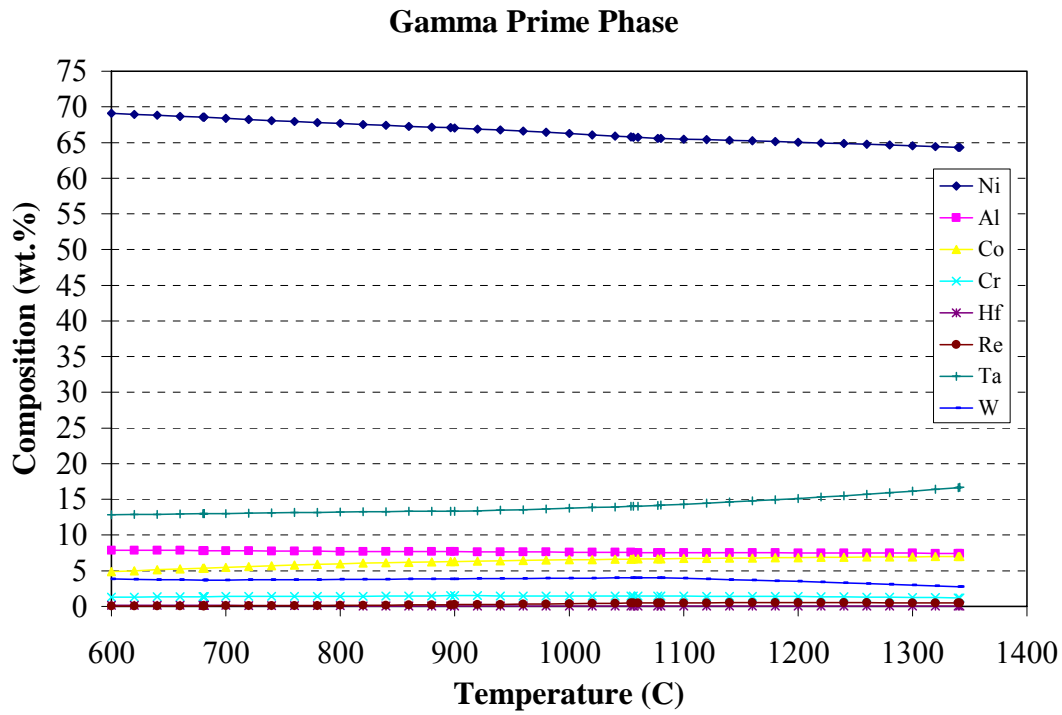


Figure 4-9. Composition of the  $\gamma'$  phase of PWA 1484 as a function of temperature as predicted by JMatPro.

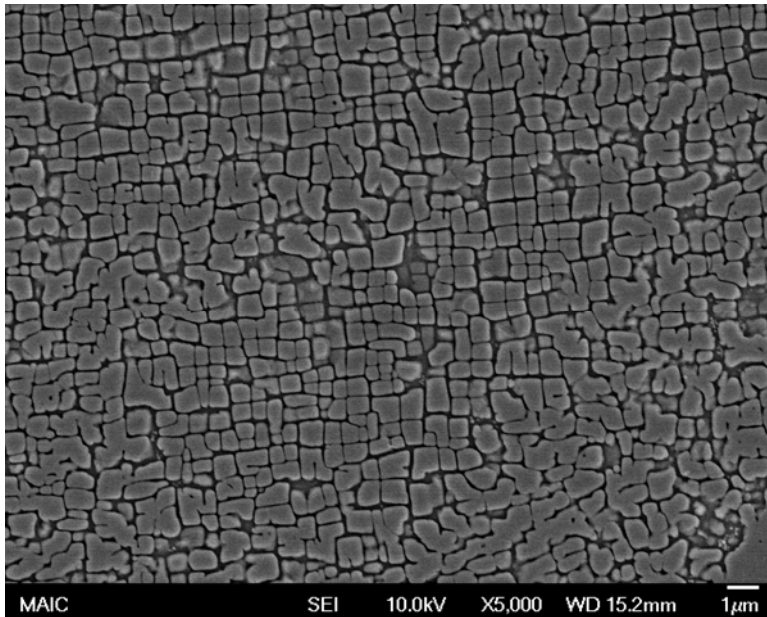


Figure 4-10. The  $\gamma'$  phase in PWA 1480 near a retained eutectic (lower right) as revealed by the electrolytic  $\gamma$  etch.

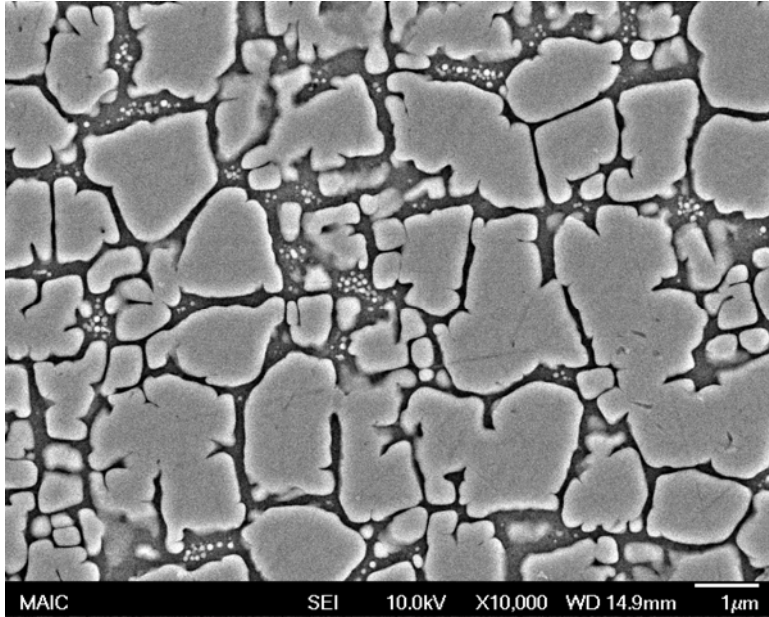


Figure 4-11. Irregular  $\gamma'$  phase in PWA 1480 near a partially solutioned eutectic region ( $\gamma$  etch).

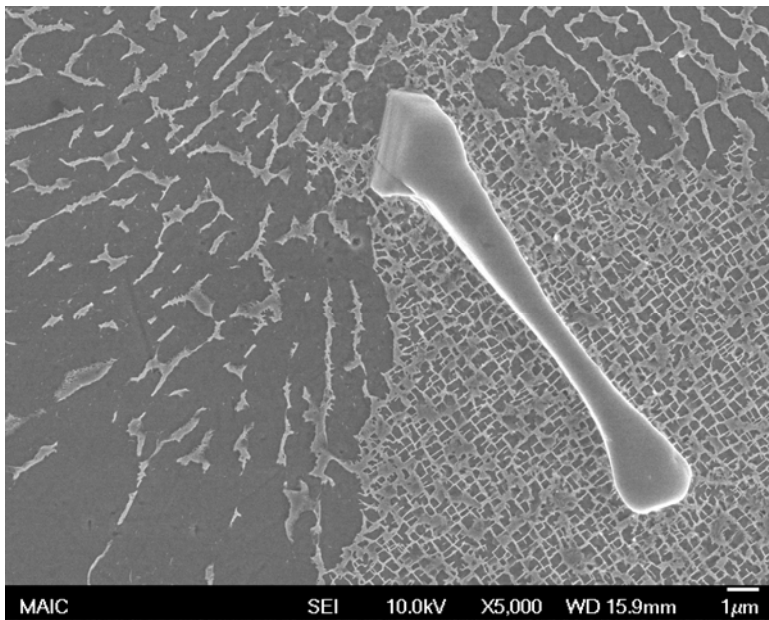


Figure 4-12.  $\gamma/\gamma'$  eutectic region in PWA 1480+ during the early stages of solutioning ( $\gamma'$  etch).  
Fine primary  $\gamma'$  precipitates can be seen in the lower right quadrant of the micrograph.  
The large, hard phase in the middle is a carbide (most likely MC type).

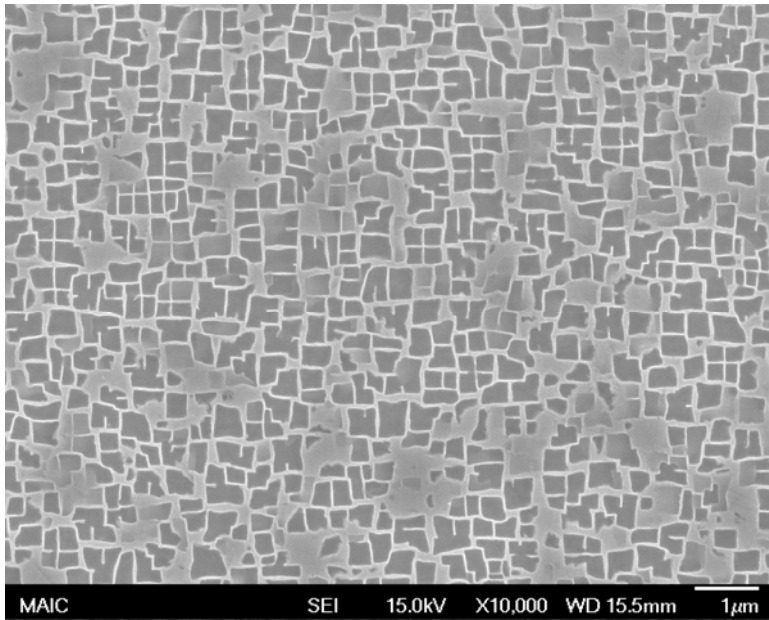


Figure 4-13. The  $\gamma'$  structure of as-cast PWA 1484 ( $\gamma'$  etch).

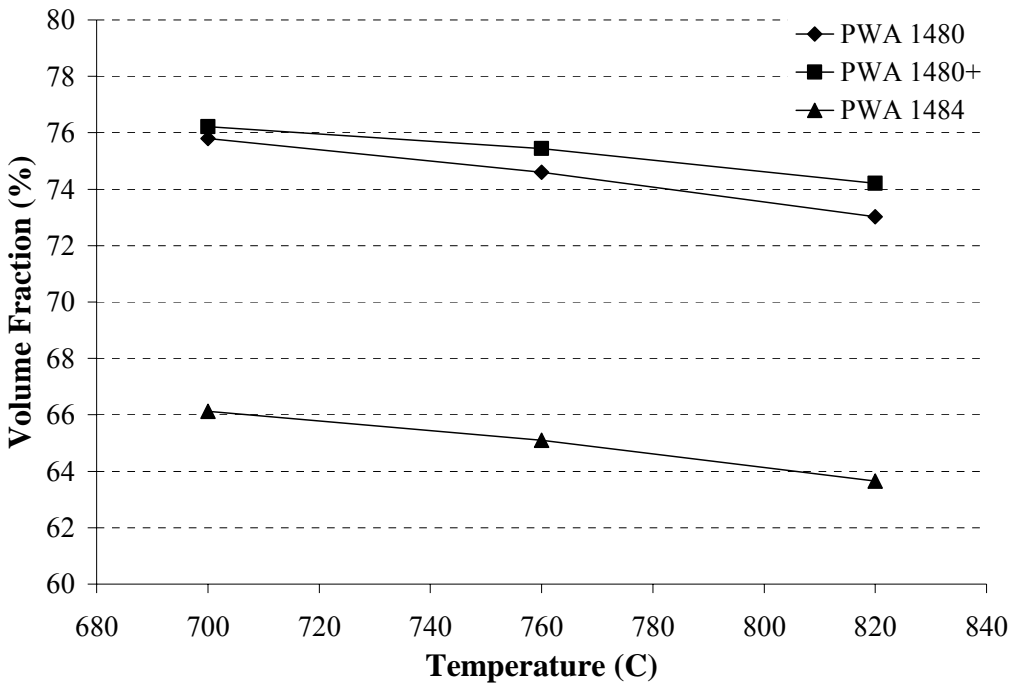


Figure 4-14. The  $\gamma'$  volume fraction vs. temperature for all three alloys.

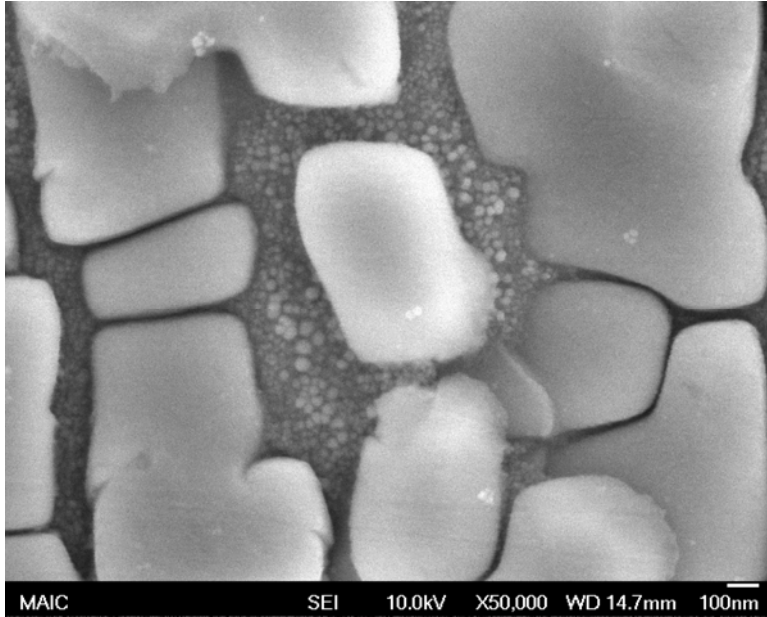


Figure 4-15. Secondary  $\gamma'$  in the  $\gamma$  matrix of PWA 1480 following an interrupted creep test ( $\gamma$  etch).

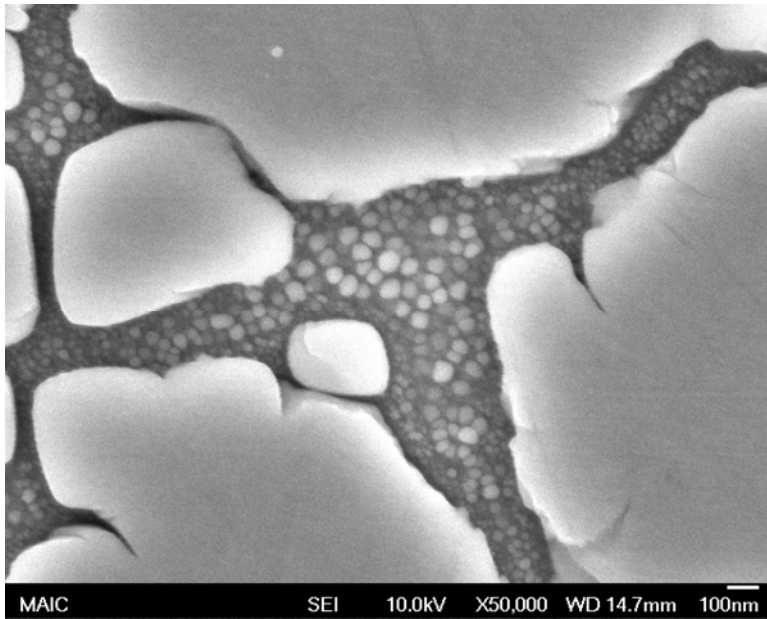


Figure 4-16. Secondary  $\gamma'$  in the  $\gamma$  matrix of PWA 1480 following an interrupted creep test ( $\gamma$  etch).

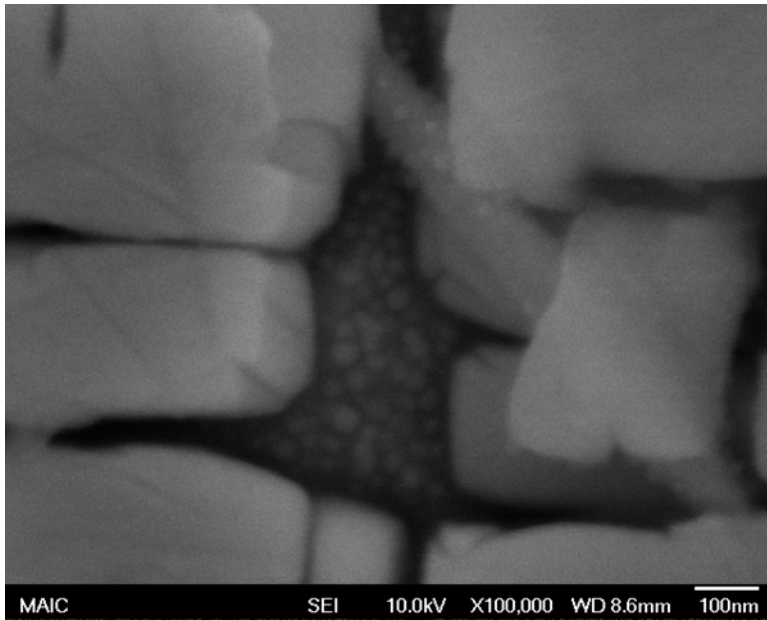


Figure 4-17. Secondary  $\gamma'$  in the matrix of PWA 1480+ following an interrupted creep test ( $\gamma$  etch). A TCP precipitate can be seen positioned diagonally from top to bottom-right.

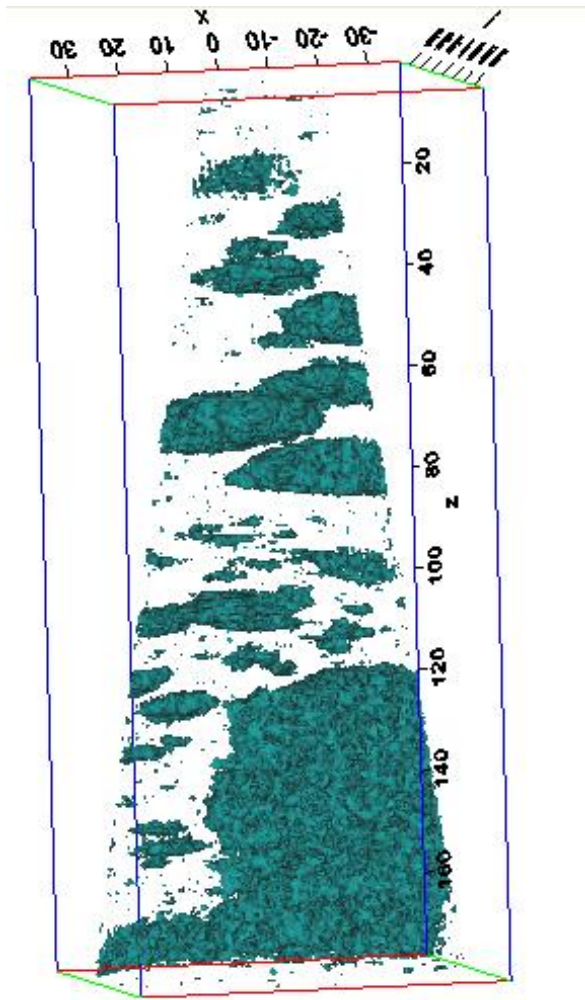


Figure 4-18. Three dimensional LEAP compositional map (18wt.% Al iso-surface) The green surfaces represent areas of Aluminum concentrations averaged at least 18wt.%. These regions are predominately  $\gamma'$  due to the highly ordered of the  $\gamma'$  phase. The  $\gamma$  phase is typically very low in Al concentration. The fine precipitates can be seen in the transparent  $\gamma$  matrix channels (near  $z = 100$  nm). Displacement scales are in units of nanometers (nm).

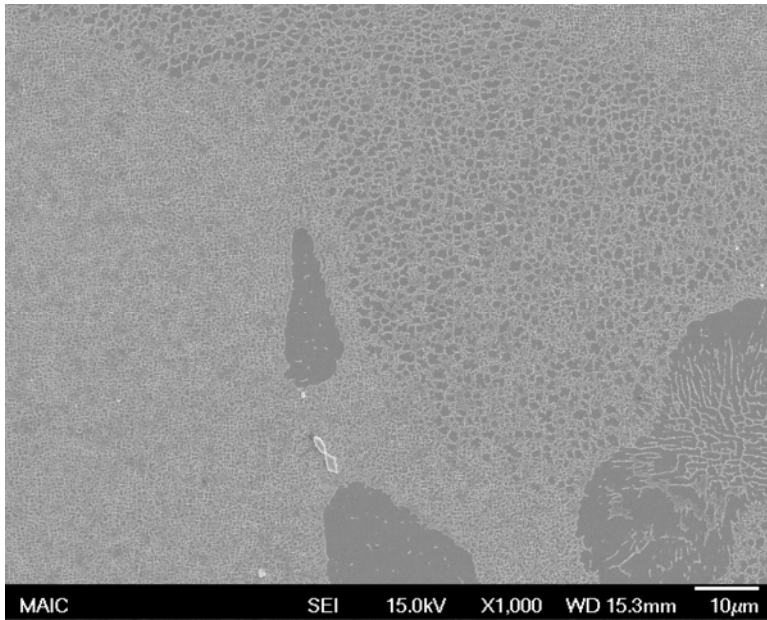


Figure 4-19.  $\gamma/\gamma'$  eutectics in as-cast PWA 1480 ( $\gamma'$  etch).



Figure 4-20.  $\gamma/\gamma'$  eutectics in the vicinity of primary carbides in PWA 1480+ (HT1A solution heat treatment,  $\gamma'$  etch). Solutioning of the eutectics is already underway with the  $\gamma$  phase infiltrating the mostly  $\gamma'$  eutectic (center right).

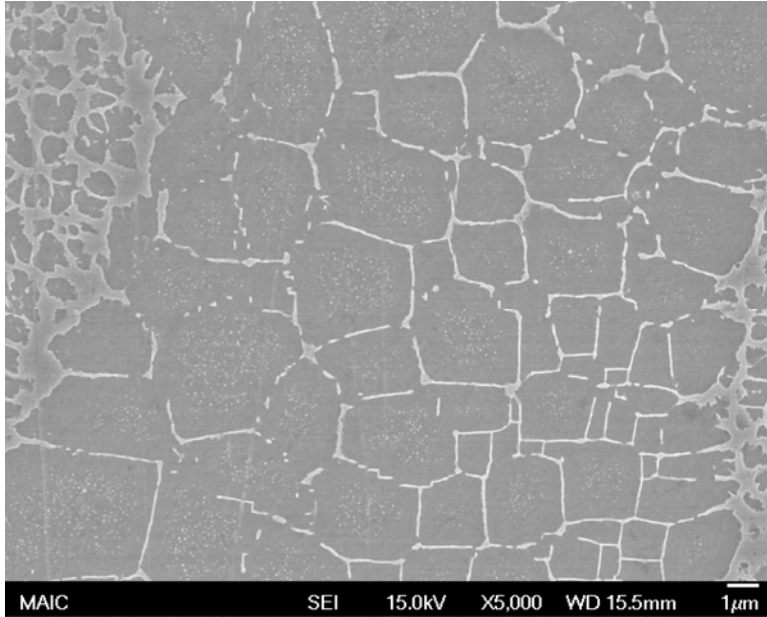


Figure 4-21. Close-up of a eutectic in as-cast PWA 1480+ ( $\gamma'$  etch). Small  $\gamma$  “precipitates” can be seen throughout the eutectic region.

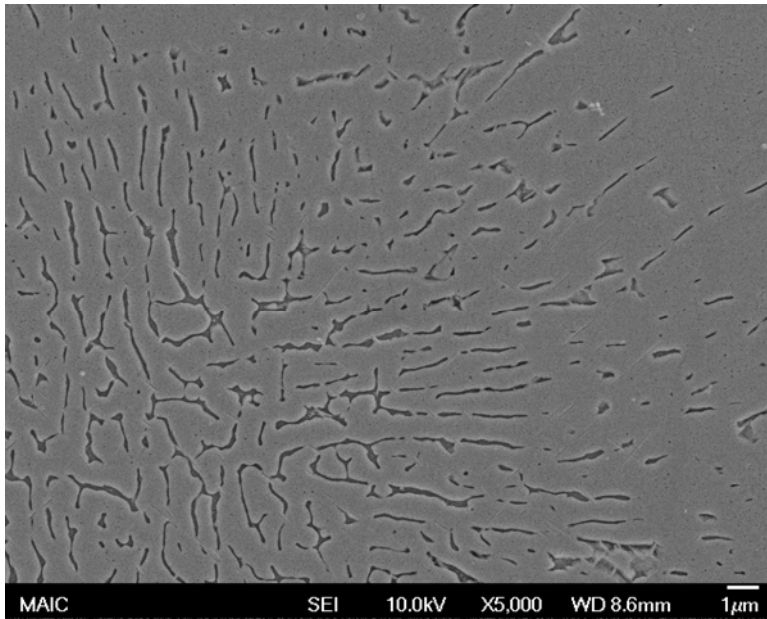


Figure 4-22. Close-up of a retained eutectic in PWA 1480+ following an interrupted creep test (HTA, 704°C/862 MPa,  $\gamma$  etch).

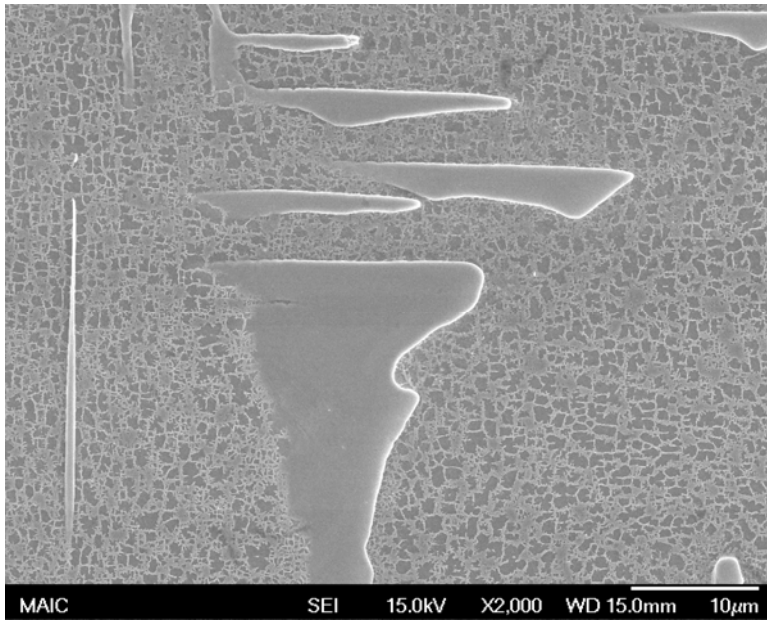


Figure 4-23. Carbide phase in PWA 1480+ (HT1A,  $\gamma'$  etch).

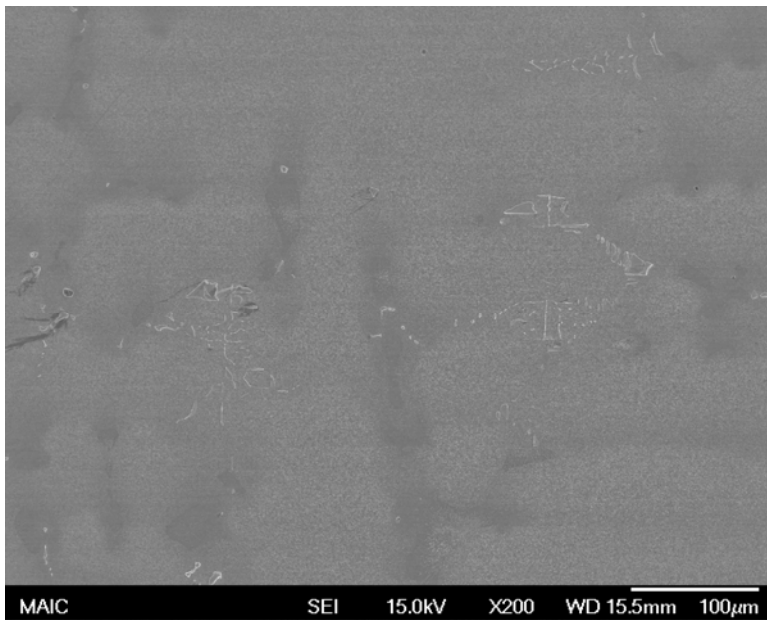


Figure 4-24. Carbide phase in PWA 1480+ (as-cast, longitudinal section,  $\gamma'$  etch). Carbides do not appear to be dendritic in nature, but do wrap around dendrite arms (center-right).



Figure 4-25. Local carbide network in PWA 1480 following an interrupted creep test (HT, 815°C/621 MPa,  $\gamma'$  etch).

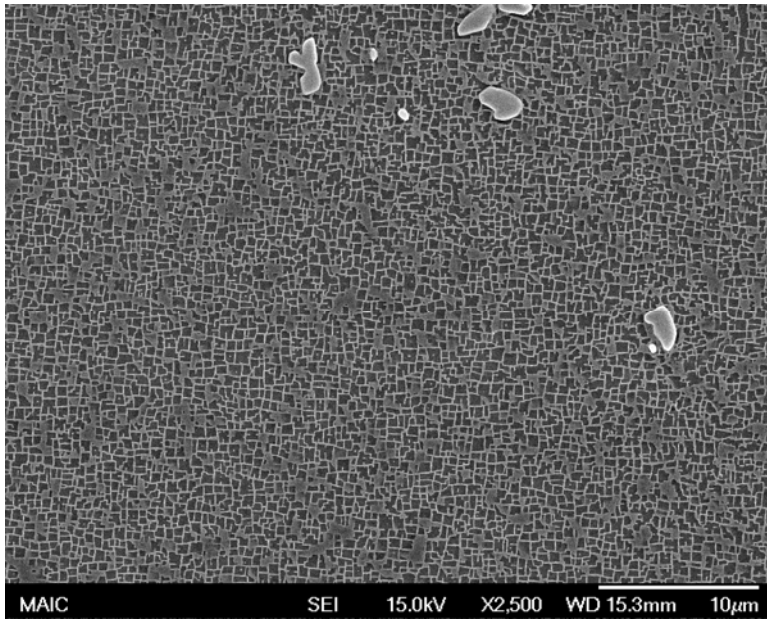


Figure 4-26. Carbide phase in PWA 1484 ( $\gamma'$  etch). Due to the lower wt.% Carbon, PWA 1484 exhibits isolated clusters of small blocky carbides.



Figure 4-27. A possible carbide that dissolved during solution heat treatment leaving behind  $\gamma'$  (PWA 1480 LT, 704°C/862 MPa,  $\gamma'$  etch).

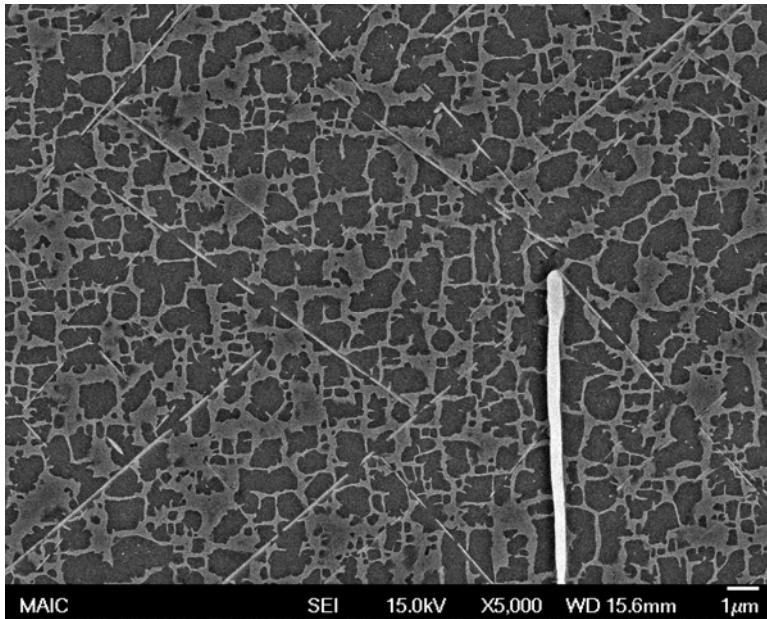


Figure 4-28. TCP phase formation in PWA 1480+ during interrupted creep testing ( $\gamma'$  etch).

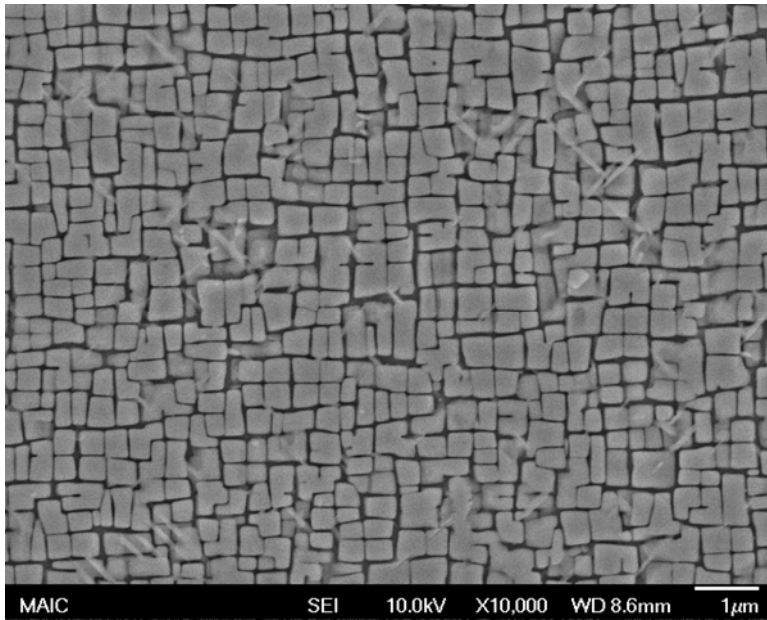


Figure 4-29. TCP phase formation in PWA 1480+ during interrupted creep testing ( $\gamma$  etch).

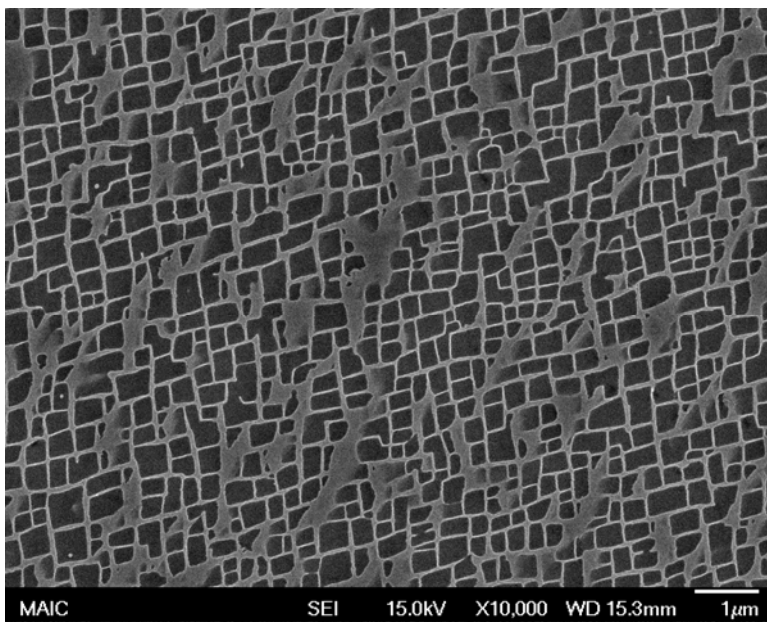


Figure 4-30.  $\gamma$  phase elongation in the [110] direction in PWA 1484 following interrupted creep testing (HT age, 704°C/862 MPa,  $\gamma'$  etch).

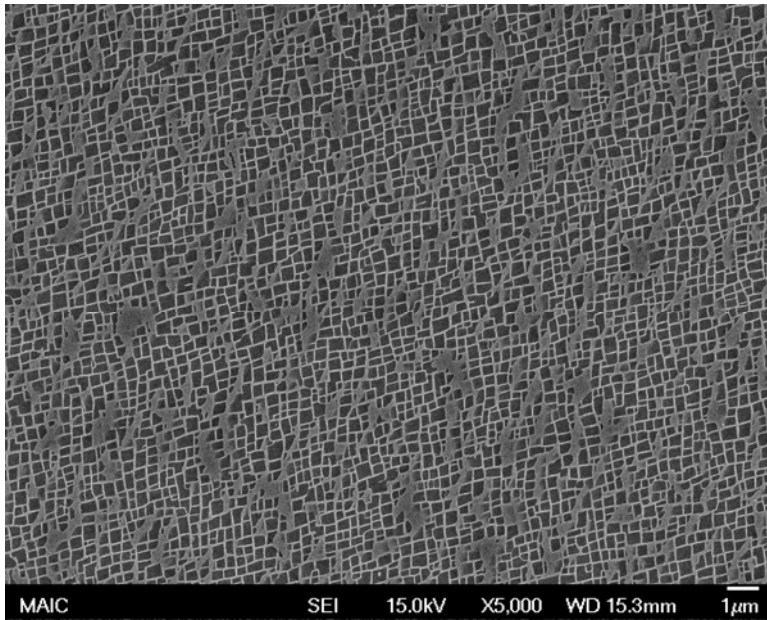


Figure 4-31.  $\gamma'$  phase elongation in the [110] direction in PWA 1484 following interrupted creep testing (HT age, 704°C/862 MPa,  $\gamma'$  etch).

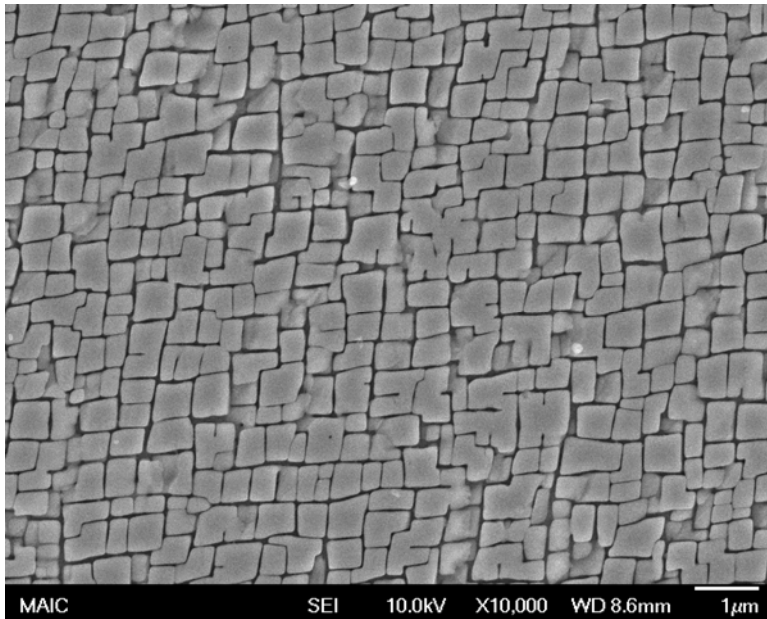


Figure 4-32.  $\gamma'$  phase shear along (111) planes in PWA 1484 following interrupted creep testing (HT age, 704°C/862 MPa,  $\gamma'$  etch).

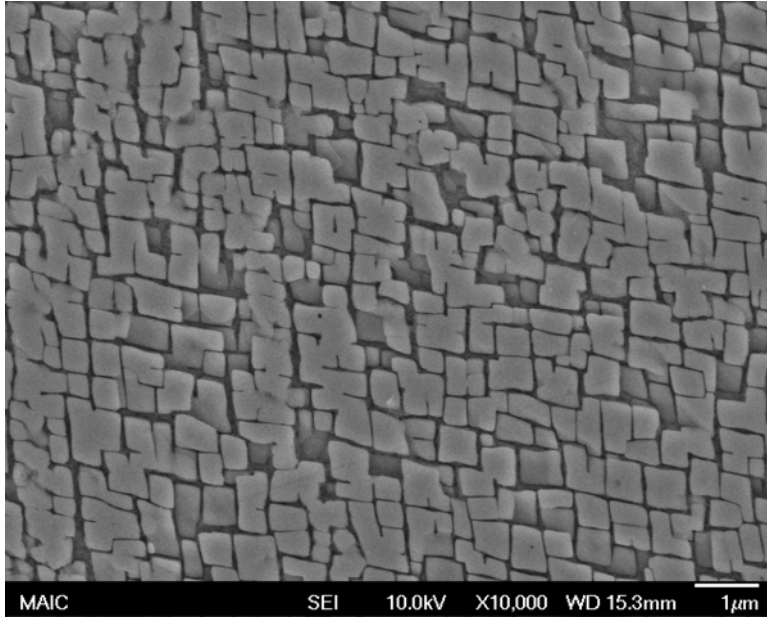


Figure 4-33.  $\gamma'$  phase shear along (111) planes in PWA 1484 following interrupted creep testing (LT age, 704°C/862 MPa,  $\gamma'$  etch)

## CHAPTER 5

### RESULTS: TENSILE BEHAVIOR

Tensile tests of PWA 1480, PWA 1480+, and PWA 1484 were conducted to evaluate the yield and tensile strengths of the three alloys. When designing creep experiments, it is important to understand the relative differences in yield strength between the three alloys. For instance, alloys with different yield strengths subjected to the same creep load may experience different creep behaviors as a result. It is possible that an alloy that is stressed to a greater fraction of its yield stress may experience a shorter creep life because of an increase in deformation (alternatively, a decrease in resistance against creep. Additionally, tensile testing is useful to evaluate work hardening and ductility.

Tensile testing was conducted at two temperatures, 700°C and 815°C, set at the lowest and highest temperatures used for creep testing. The following discussion will focus on the effect of the two different age heat treatments on the tensile strengths of PWA 1480, PWA 1484, and PWA 1480+. As mentioned earlier, the age heat treatment temperatures were 704°C and 871°C and all testing was conducted at or above the LT age temperature, but below the HT age temperature. Additionally, the effect of rhenium on the tensile properties of PWA 1480 was investigated by the creation of a second generation version of PWA 1480 called PWA 1480+.

Because microstructural evolution is not a major concern during the short duration of a tensile test, the relationship between test temperature and age temperature is minor. For instance, if the time required for tensile test was sufficient to change the heat treated condition, then testing at 815°C might be expected to reduce or eliminate entirely any benefit of the low temperature (LT) age heat treatment. In this case (815°C), the thermal exposure during tensile testing following the HT age will act as a secondary age heat treatment much like the multi-step age heat treatments already employed in the processing of some second and third generation

superalloys. Additionally, the HT age would be expected to increase coarsening (size) of the  $\gamma'$  phase and, subsequently, reduce coherency of the precipitates. Rhenium additions have been shown to significantly increase solid solution strengthening of the  $\gamma$  phase. Because Re preferentially segregates to the  $\gamma$  phase, lattice misfit is significantly increased as well.

The tensile behavior of PWA 1480 is very similar for both age heat treatments. At 700°C, both samples exhibit a large yield stress followed by slight work-hardening until failure, as shown in Figure 5-1. The HT aged sample has a yield strength slightly lower than the LT age and the ductility is about half of the ductility of the LT aged samples. At 815°C, both age heat treatments have a yield point that is lower than the yield strength of the samples tested at 700°C. Again, the HT aged samples have slightly lower yield strength, failure strength, and ductility.

The Re modified PWA 1480+ performed similarly to unmodified PWA 1480 with a few notable differences, Figure 5-2. The general shape of the stress-strain curves remained the same, potentially indicating no significant change in deformation mechanisms. The two most notable changes are the resulting increase in yield strength and corresponding reduction in ductility. The LT aged PWA 1480+ sample at 700 °C has a much lower yield strength than the PWA 1480 LT specimen as well as significantly less ductility (11% for PWA 1480 vs. 2% for PWA 1480+). It should be noted, however, that this result may not be valid due to its significant departure from the trend established by the other test results for PWA 1480+. The HT aged PWA 1480+ specimen at 700°C showed a great improvement in yield strength (1333 MPa for PWA 1480 vs. 1376 MPa for PWA 1480+). The ductilities for the HT age specimens of both alloys were similar with a difference of less than 2% elongation.

Both alloys exhibit yield points at 815°C and display very similar strain hardening behavior after yielding. For three of the four conditions, PWA 1480+ has a greater yield stress

than conventional PWA 1480, which is likely due to the solid solution strengthening effect of the Re addition. For both test temperatures, the HT age appears to decrease ductility in PWA 1480 (11.6% to 6.3% and 18.3% to 15.2) while simultaneously reducing the yield stress (1357 MPa to 1333 MPa and 1281 MPa to 1212 MPa, LT and HT respectively). PWA 1480+, though, had increased ductility and yield strength in the HT age when compared to the LT age condition. Additionally, the usually stronger PWA 1480+ does not show as much ductility as PWA 1480 in the LT condition but does in the HT condition. Tensile strength and elongation measurements from all three alloys are presented in Table 5-1.

The tensile behavior of PWA 1484 was somewhat different from PWA 1480 (and PWA 1480+), Figure 5-3. PWA 1484 was characterized by a significantly lower yield point, greater ductility, and greater amount of plastic work hardening. PWA 1484 also has greater strength at the higher temperature test condition while PWA 1480 and PWA 1480+ show a decrease in strength at 815°C. In general, nickel base superalloys have excellent high temperature strength to near 800°C. Continuing to increase the temperature will result in a decrease in strength in nickel base superalloys because of the decreasing strength of the  $\gamma'$  phase at these temperatures.<sup>37, 48</sup> The continuing increase in strength of PWA 1484 at 815°C is noteworthy as the total refractory content (Mo+W+Re+Ta) for PWA 1484 is similar to that of PWA 1480+ (20wt.% vs. 19wt.%, respectively). The total refractory content of PWA 1480, however, is less at 16wt.% with the absence of Re. Despite the similarity in solid solution strengthener content of PWA 1484 and PWA 1480+, PWA 1484 shows an increase in strength at 815°C relative to 700°C while PWA 1480+ does not. At 700°C, the strength of PWA 1484 continues to increase until failure. At 815°C, the strength increases to the ultimate tensile strength, UTS, following 2-4% plastic deformation. All of the PWA 1484 tests produced between 14 and 23% elongation

compared with 5-11% for PWA 1480 and 2-10% for PWA 1480+, Table 5-1. For PWA 1480 and PWA 1484, the LT age condition is slightly stronger than the HT age condition. For PWA 1480+, however, the HT age produces greater yield strength values at both test temperatures.

Direct comparison between the three alloys also reveals the relative differences in performance. Figures 5-4 and 5-5 show direct comparisons of the three alloys tested in the LT age condition at 700°C and 815°C respectively. Figures 5-6 and 5-7 are similar except the HT age is presented (rather than the LT age shown in Figures 5-4 and 5-5). Specimens with the LT age at 700°C exhibited a small amount of work hardening after yielding as shown in Figure 5-4. Of the three alloys, PWA 1484 displayed the greatest potential for work hardening. PWA 1480 had the largest yield strength value and substantial ductility, but little work hardening. PWA 1480+ produced little ductility (less than 2%) but experienced slight hardening after yielding. PWA 1484 had the lowest yield point at this combination of age heat treatment and test temperature.

At 815°C, the LT aged samples all experienced a sharp yield point. In the case of PWA 1480 and PWA 1480+, the yield point was followed by an immediate reduction in tensile stress. PWA 1484, however, maintained the yield stress level briefly before the onset of plastic hardening. The engineering stress is reduced 100 to 150 MPa during this period of the test possibly as a result of the onset of necking. No further strengthening takes place before failure occurs. Contrasting this behavior, PWA 1484 displays a significant increase in strength during the first few percent plastic elongation. The applied engineering stress slowly decreases following the work hardening (the transition occurs around 4-5% elongation). The decrease in stress may be a result of slight necking, though necking was slight. While the yield strength of PWA 1480 is 373 MPa greater than that of PWA 1484, the reduction in measured flow stress of

PWA 1480 and the increase in flow stress of PWA 1484 lead to a larger failure stress for PWA 1484 by 78 MPa. Compared to PWA 1480+, the UTS of PWA 1484 is 152 MPa below that of PWA 1480+; however, the true failure stress of PWA 1484 (corrected by post test measurement) is 57 MPa greater than the failure stress of PWA 1480+. PWA 1484 has the highest failure strength despite a 445 MPa and 374 MPa disadvantage in yield strength to PWA 1480+ and PWA 1480, respectively.

The HT age heat treated specimens share several similarities to the LT age specimens. At 700°C, PWA 1480 and PWA 1480+ exhibited the same high yield strength with a nearly flat plastic hardening region, Figure 5-6. PWA 1480 experienced a significant reduction in ductility with the HT age. PWA 1480+ when tested with the LT age at 700°C had the highest yield strength of the group. The ductility for PWA 1480+ is increased with the HT age from 2.8% to 5.1%. The behavior of PWA 1484 in the HT age condition closely matches its behavior in the LT condition. The yield points and amount of work hardening are very similar as are the ductilities of both alloys. PWA 1480, however, experienced a decrease in yield strength, UTS, and ductility in the HT age condition. Most notable is the decrease in ductility of PWA 1480 from 11.8% to 5.5%.

The HT age when tested at 815°C brought about similar tensile performances to the LT age for all three alloys. Again, PWA 1480+ had the highest yield strength followed by PWA 1480 and PWA 1484. Both PWA 1480 and PWA 1480+ exhibited a sharp yield point followed by a drop in strength of nearly 100 MPa. The measured strength continued to decline until failure. Conversely, PWA 1484 displayed a sharp rise in strength following yielding to a maximum (1141 MPa) at 3.96% elongation. When compared with the results from the 700°C testing, there was little difference in properties for PWA 1480+. PWA 1480 had lower yield strength and less

ductility in the HT age condition and PWA 1484 had similar yield strengths in both conditions but less work hardening in the HT age condition. The total ductility of PWA 1484 was also slightly lower for the HT age condition.

The elastic modulus for all three alloys was calculated during the step loading procedure immediately prior to the beginning of a creep test. These values are used here as the creep loading system is more elastically rigid and the results fit a linear model with much lower error than those generated on the servo-hydraulic tensile test system. The elastic modulus values were obtained at 704°C and 815°C for all three alloys and at 760°C for PWA 1480 and PWA 1484. These values are reported in Table 5-2.

Additionally, the three alloys can be differentiated by their plastic deformation behavior. PWA 1480 displays relatively smooth plastic deformation until failure. The LT condition transitions from elastic to plastic behavior smoothly as shown in Figure 5-8. The HT condition behaves similarly; however, the elastic-plastic transition is marked by a brief spike in stress shown in Figure 5-9. PWA 1484 produced a steady increase in flow stress until an instability point is reached. After this point, the engineering stress is initially reduced and wavy until failure. The UTS may occur at failure or at the point of instability as in the cases of the LT age and the HT age, respectively: Figures 5-10 and 5-11. The point of instability may be caused by necking or a similar behavior; however, only slight necking could be observed on all specimens tested herein. PWA 1480+ exhibited a mix of behaviors from the LT age to the HT age. In the LT aged condition, PWA 1480+ displayed a smooth elastic-plastic transition that was followed by a rapid increase in flow stress to a potential point of instability at which the slope of the plastic deformation region decreased sharply, Figure 5-12. Overall, the LT condition exhibited a smooth plastic response from yielding until failure. The HT age, however, exhibited wavy

behavior with several spikes in flow stress from yielding until failure, Figure 5-13. The spikes produced in the HT condition of PWA 1480 and PWA 1480+ are possibly a result of dynamic strain aging processes such as the formation of solute atmospheres along dislocation cores during the age heat treatment.

Comparing the behaviors of the three alloys between the two test temperatures, it can be seen that two alloys, PWA 1480 and PWA 1480+, exhibit a significant change in behavior over the temperature range in question while PWA 1484 does not. At 700°C, PWA 1480 and PWA 1480+ transition from elastic to plastic deformation with no drop in stress caused by a yield point, Figures 5-14 and 5-16. At 815°C, however, both alloys exhibit a sharp upper yield point followed by a constantly decreasing flow stress, Figures 5-15 and 5-17. This behavior continues until failure for both alloys. The true failure stress of PWA 1480 is only slightly greater than the yield stress and UTS values (both recorded at yielding). The true failure stress of PWA 1480+, however, shows a decrease in strength of 27 MPa following yielding in the LT condition and 2 MPa following yielding in the HT age condition, Table 5-1. PWA 1484, however, does not show a significant change in behavior from 700°C to 815°C. For both age conditions of PWA 1484, the yield point is nearly identical at both temperatures with a difference of 17 MPa at 700°C and 10 MPa at 815°C, Figures 5-18 and 5-19. The primary difference recorded for PWA 1484 is the slope of the plastic deformation region immediately following yielding. For both age conditions, the 815°C sample exhibits a more rapid increase in flow stress due to increased work hardening and a larger value for the ultimate tensile strength. The improvement in tensile properties of PWA 1484 is not unexpected as it is a second generation alloy designed for higher temperature capability than PWA 1480.<sup>54</sup>

Finally, changes with temperature in common tensile properties like yield strength, UTS, and failure strength can also be recognized for each of the three alloys. The yield strength of the three alloys as a function of temperature is given in Figure 5-20. PWA 1480 and PWA 1484 exhibit reductions in yield strength as a result of the increase in temperature from 700°C to 815°C. PWA 1480 showed the largest drop in yield strength (76 MPa for the LT condition and 121 MPa for the HT condition), while PWA 1484 exhibited a reduction of 41 MPa in the LT condition and 34 MPa in the HT condition. PWA 1480+, however, exhibited an increase in yield strength with temperature for both age conditions. The LT condition of PWA 1480+ produced the greatest increase in yield strength with temperature (118 Mpa) while the HT age produced a 3 MPa rise in yield strength at 815°C. Additionally, comparing the measured yield strengths to the applied initial creep loads provides a useful description of the percentage of the yield strength required to support the applied stress, Table 5-.

The ultimate tensile strength of the three alloys as a function of test temperature is given in Figure 5-21. PWA 1480 with both age conditions and PWA 1480+ HT exhibit a substantial reduction in UTS of between 140 and 160 MPa at 815°C when compared with the values produced at 700°C. As the temperature is increased further, it would be expected that the tensile strength of these alloys would continue to decline due to the decreasing strength of the  $\gamma$  matrix and the  $\gamma'$  precipitates.<sup>37, 48</sup> An increase in the measured UTS was exhibited by PWA 1484 with both age conditions and by PWA 1480+ LT. Again, the increase in strength of PWA 1484 at the higher temperature can be attributed to its higher temperature performance capability produced as a result of a greater refractory content than either of the PWA 1480 alloys. The increase in strength for the PWA 1480+ LT sample may be an artifact as a result of the significant departure by the sample as indicated in Figure 5-2.

When true failure stress is graphed for each alloy as a function of temperature, only two specimens exhibited an increase in strength with increasing temperature, Figure 5-22. PWA 1480+ LT and PWA 1484 LT both produced a substantial increase in failure stress at 815°C (90 MPa for PWA 1480+ LT and 83 MPa for PWA 1484 LT). PWA 1480+ HT, PWA 1484 HT, and both conditions of PWA 1480 all exhibited a reduction in failure stress at the higher temperature test with PWA 1480 LT showing the greatest reduction in strength.

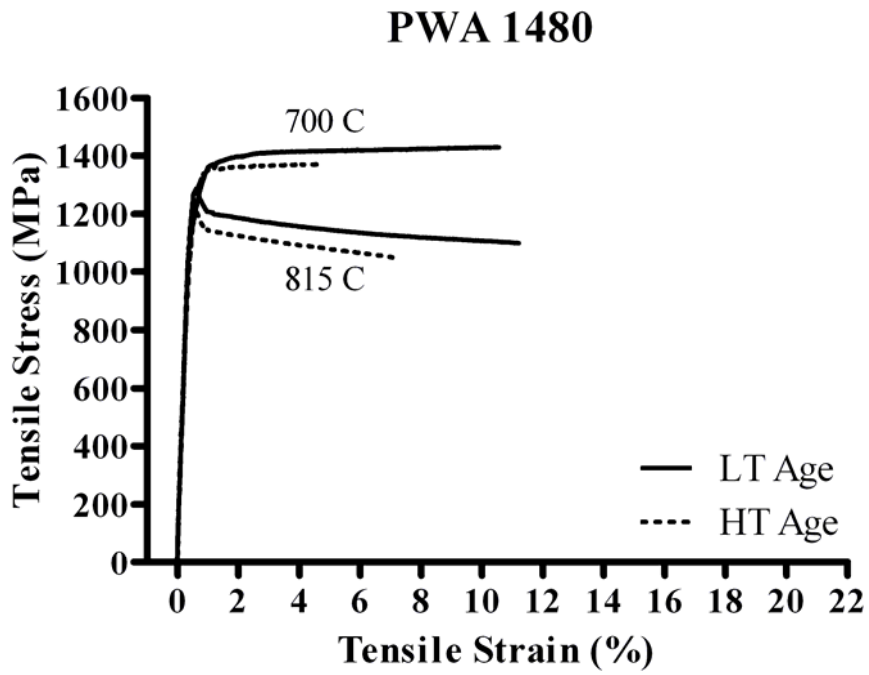


Figure 5-1. Tensile results for PWA 1480 at both age heat treatments and test temperatures.

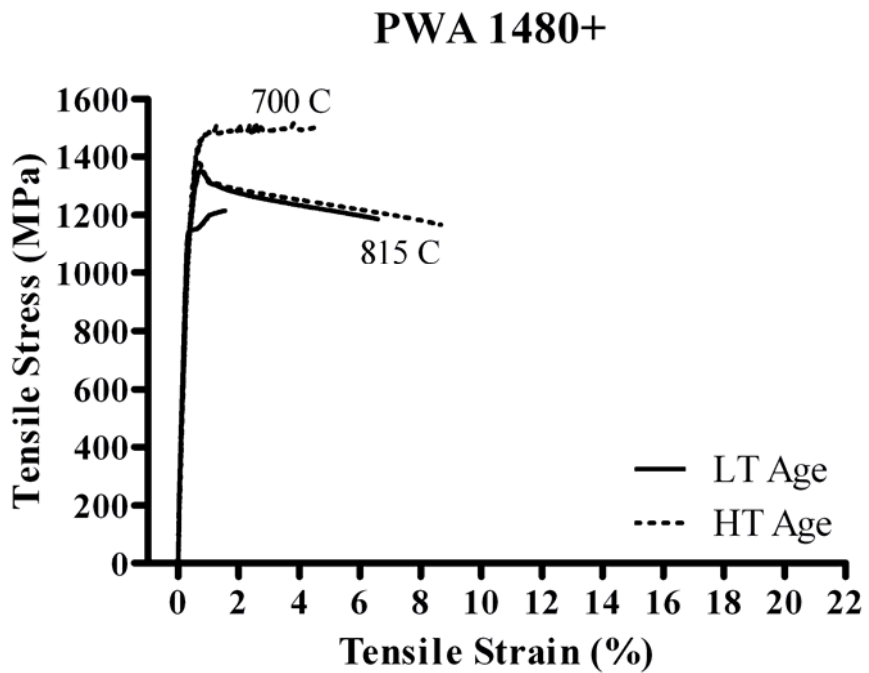


Figure 5-2. Tensile results for PWA 1480+ at both age heat treatments and test temperatures.

Table 5-1. Tensile results at 700°C and 815°C for all three alloys and both age heat treatments.

	Temperature	Age	$\sigma_y$ (MPa)	UTS (MPa) y/p/f*	$\sigma_f$ (MPa)	Elongation at Failure (%)	$\epsilon_f$ (%)	RIA (%)
PWA 1480	700°C	LT	1357.44	1429.33 (f)	1604.29	11.76	11.58	10.93
		HT	1333.45	1371.15 (p)	1459.98	5.49	6.28	6.09
	815°C	LT	1281.39	1287.39 (y)	1321.31	12.36	18.27	16.70
		HT	1212.24	1213.76 (y)	1220.33	7.68	15.18	14.09
PWA 1480+	700°C	LT	1149.77	1215.07 (f)	1250.34	2.58	2.85	2.81
		HT	1375.57	1516.20 (f)	1606.16	5.09	6.86	6.63
	815°C	LT	1267.39	1352.09 (y)	1340.15	7.12	12.17	11.46
		HT	1378.33	1385.63 (y)	1384.00	8.99	17.04	15.67
PWA 1484	700°C	LT	948.72	1112.69 (f)	1314.27	13.46	17.26	15.86
		HT	931.76	1116.55 (p)	1328.08	16.58	18.30	16.72
	815°C	LT	907.90	1199.62 (p)	1397.51	18.22	23.21	20.71
		HT	897.90	1141.44 (p)	1203.85	19.26	13.84	12.92

\*Note: UTS values are designated with a “y” if the UTS occurred at a yield point, a “p” if the UTS occurred during plastic deformation before failure, and an “f” if the UTS occurred at failure.

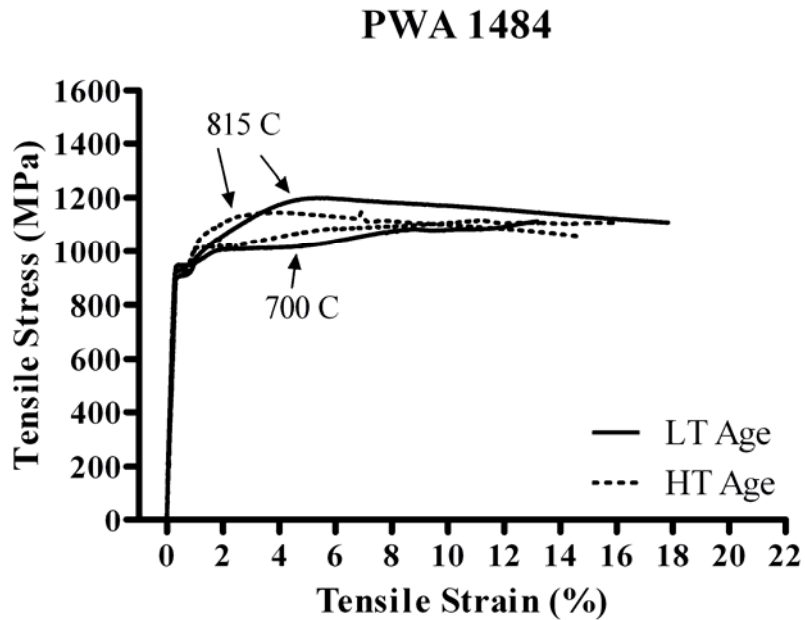


Figure 5-3. Tensile results for PWA 1484 at both age heat treatments and test temperatures.

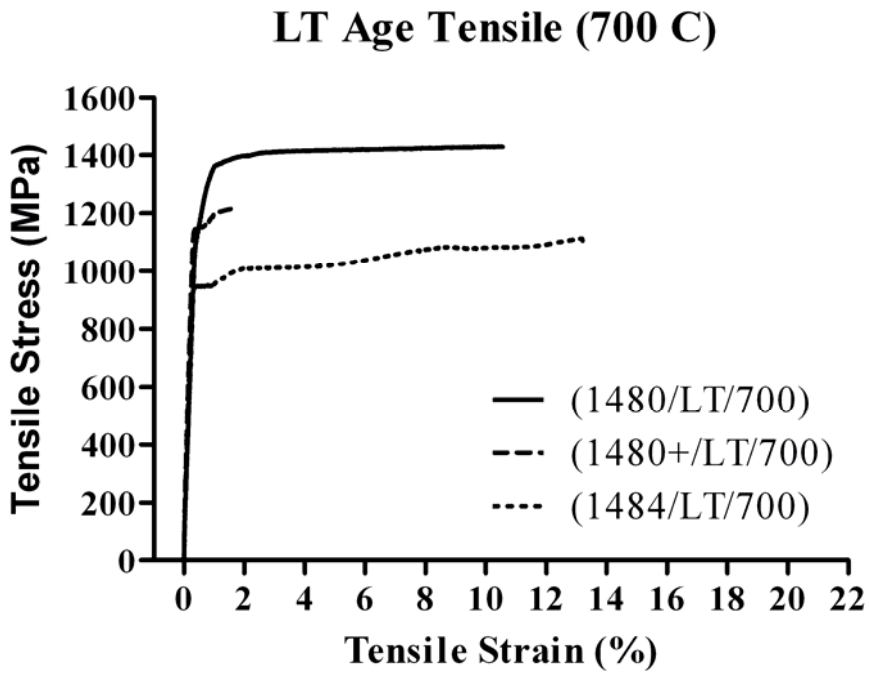


Figure 5-4. Comparison of tensile results for all three alloys with the LT age (704°C/24hr.) tested at 700°C with an air environment.

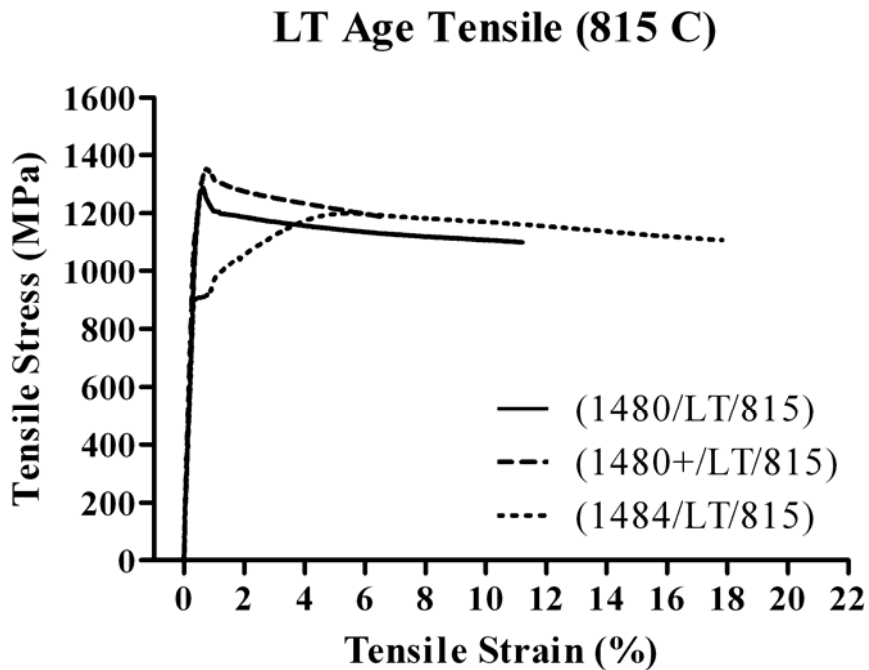


Figure 5-5. Comparison of tensile results for all three alloys with the LT age (704°C/24hr.) tested at 815°C with an air environment.

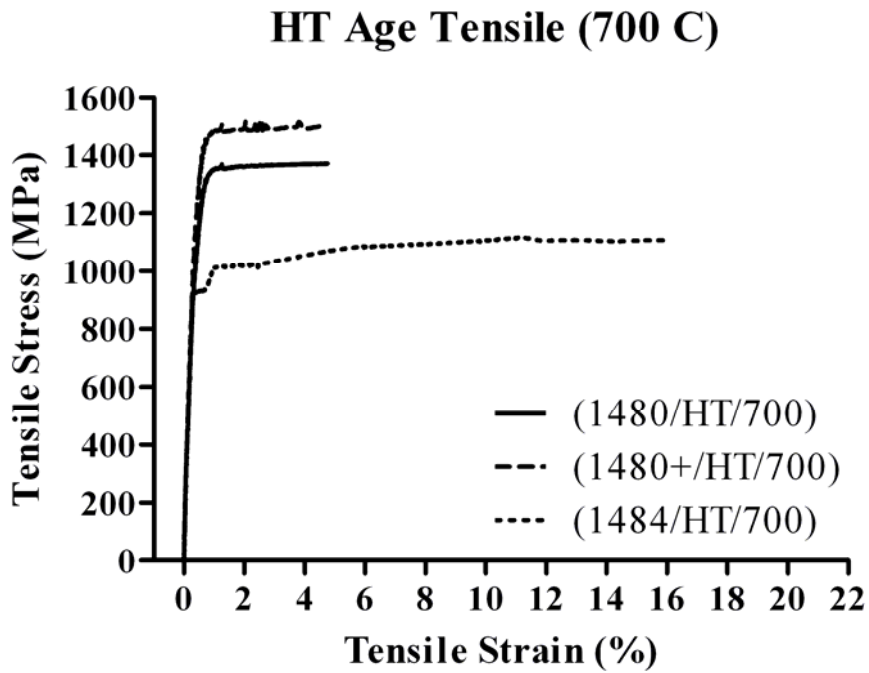


Figure 5-6. Comparison of tensile results for all three alloys with the HT age (871°C/32hr.) tested at 700°C with an air environment.

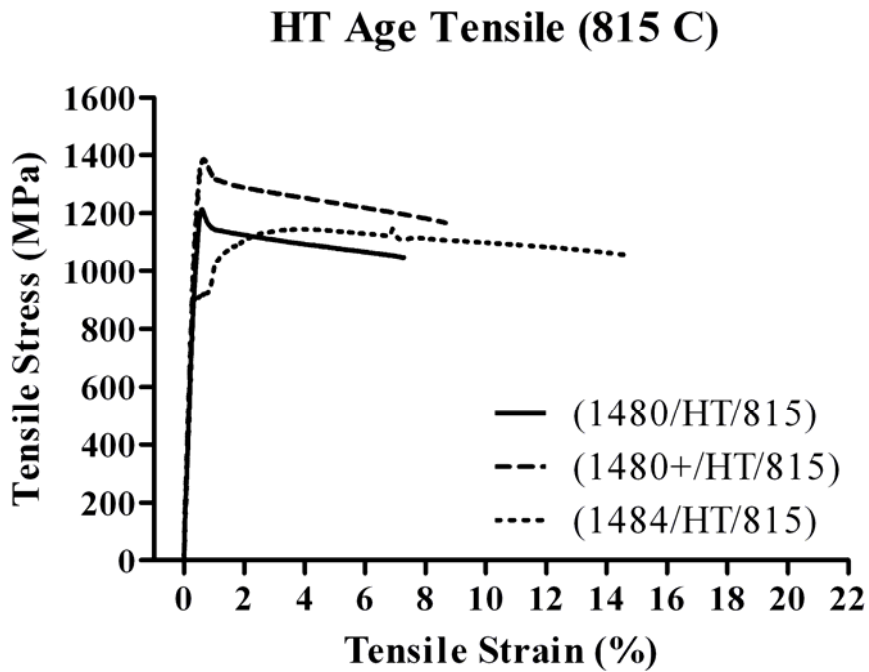


Figure 5-7. Comparison of tensile results for all three alloys with the HT age (871°C/32hr.) tested at 815°C with an air environment.

Table 5-2. Elastic modulus calculations from creep loads.

	Elastic Modulus (GPa)			
	700 C		815 C	
	LT	HT	LT	HT
PWA 1480	81.48	95.75	87.44	64.30
PWA 1480+	95.01	86.63	100.78	79.96
PWA 1484	85.15	86.39	106.44	87.41

PWA 1480/LT/700  
Plastic Deformation

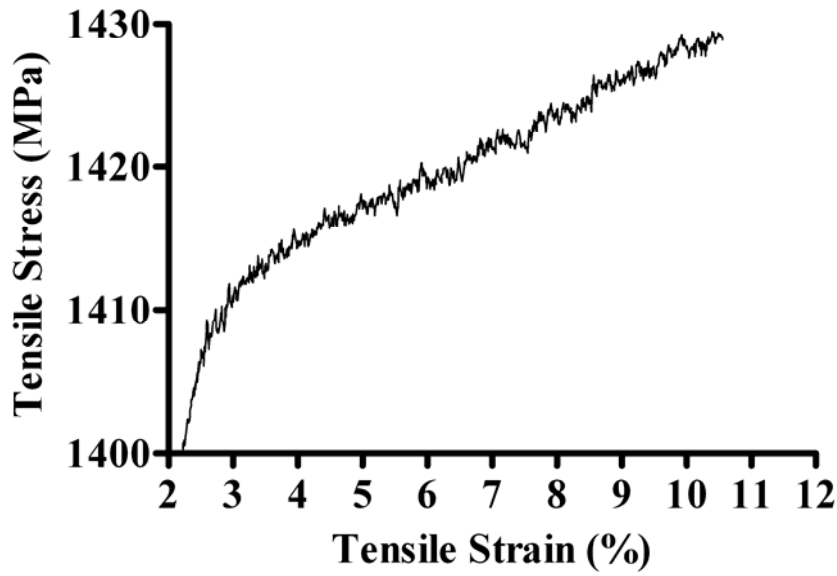


Figure 5-8. Plastic deformation behavior of PWA 1480 LT at 700°C.

PWA 1480/HT/700  
Plastic Deformation

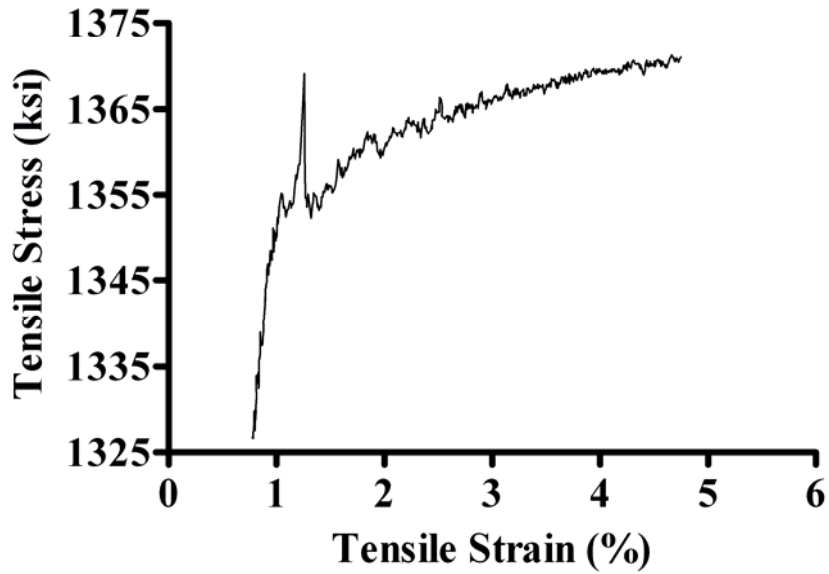


Figure 5-9. Plastic deformation behavior of PWA 1480 HT at 700°C.

PWA 1484/LT/700  
Plastic Deformation

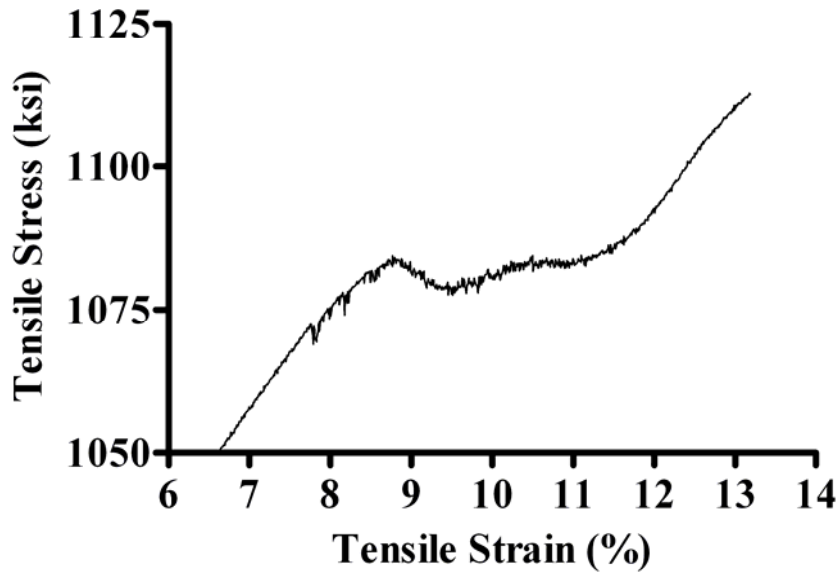


Figure 5-10. Plastic deformation behavior of PWA 1484 LT at 700°C.

PWA 1484/HT/700  
Plastic Deformation

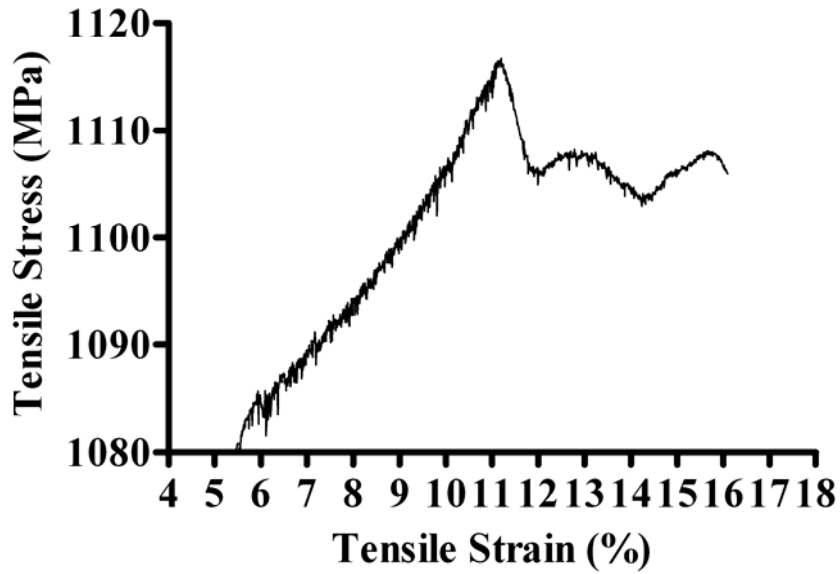


Figure 5-11. Plastic deformation behavior of PWA 1484 HT at 700°C.

PWA 1480+/LT/700  
Plastic Deformation

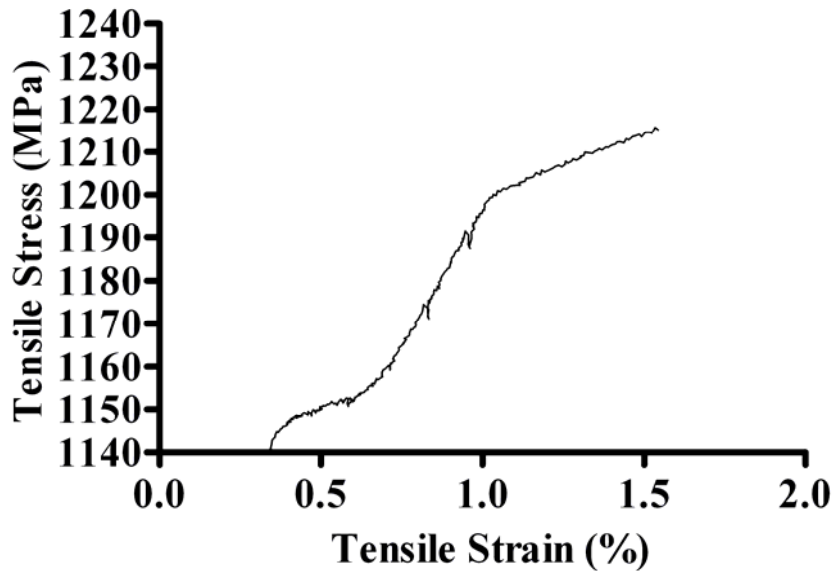


Figure 5-12. Plastic deformation behavior of PWA 1480+ LT at 700°C.

PWA 1480+/HT/700  
Plastic Deformation

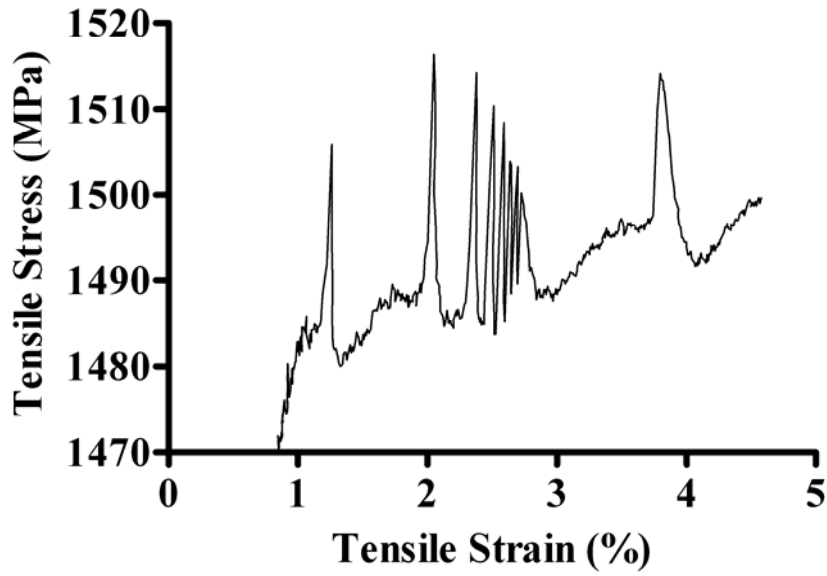


Figure 5-13. Plastic deformation behavior of PWA 1480+ HT at 700°C.

PWA 1480 LT Tensile

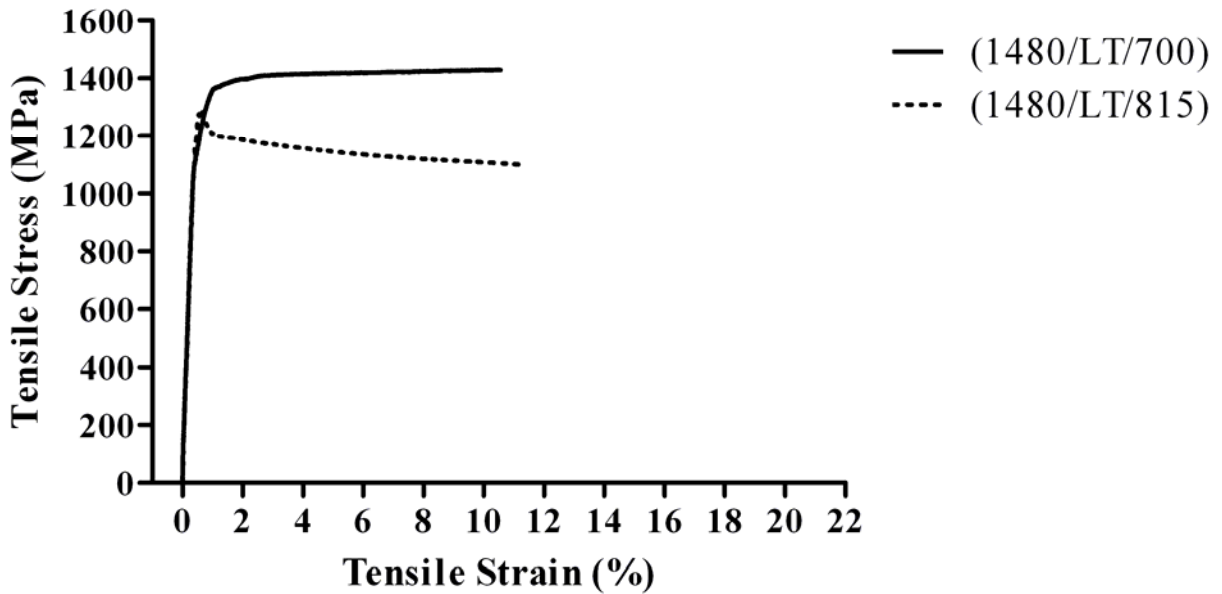


Figure 5-14. Tensile behavior of PWA 1480 LT at both temperatures.

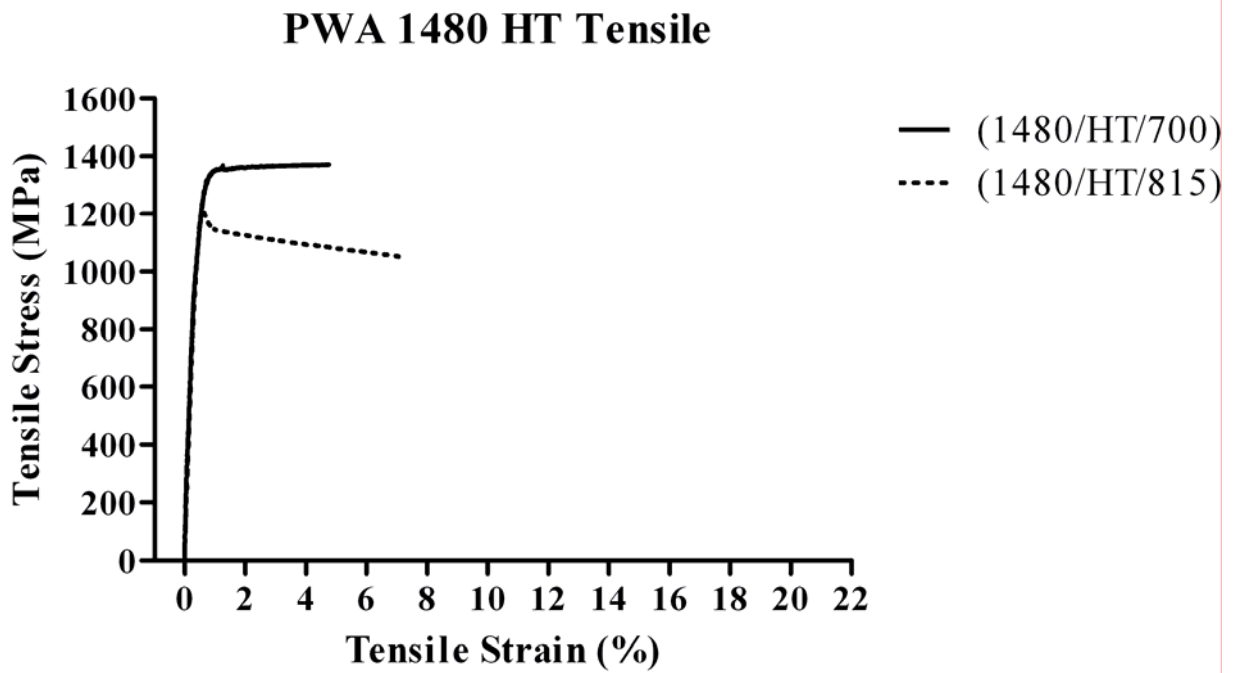


Figure 5-15. Tensile behavior of PWA 1480 HT at both temperatures.

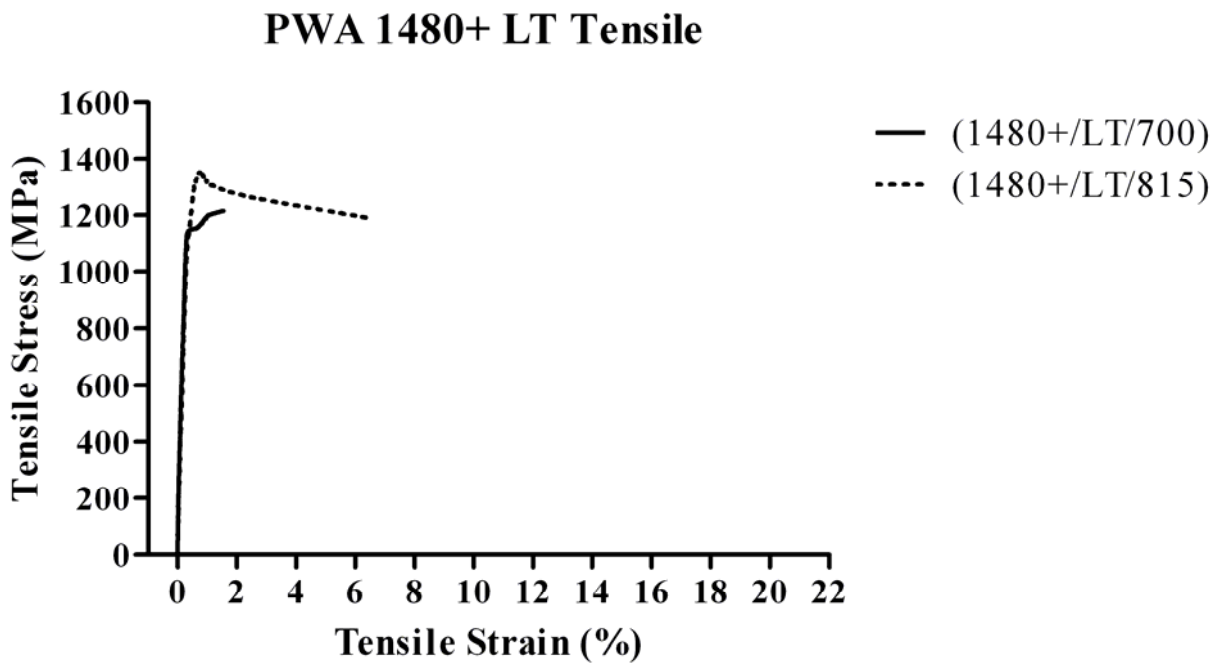


Figure 5-16. Tensile behavior of PWA 1480+ LT at both temperatures.

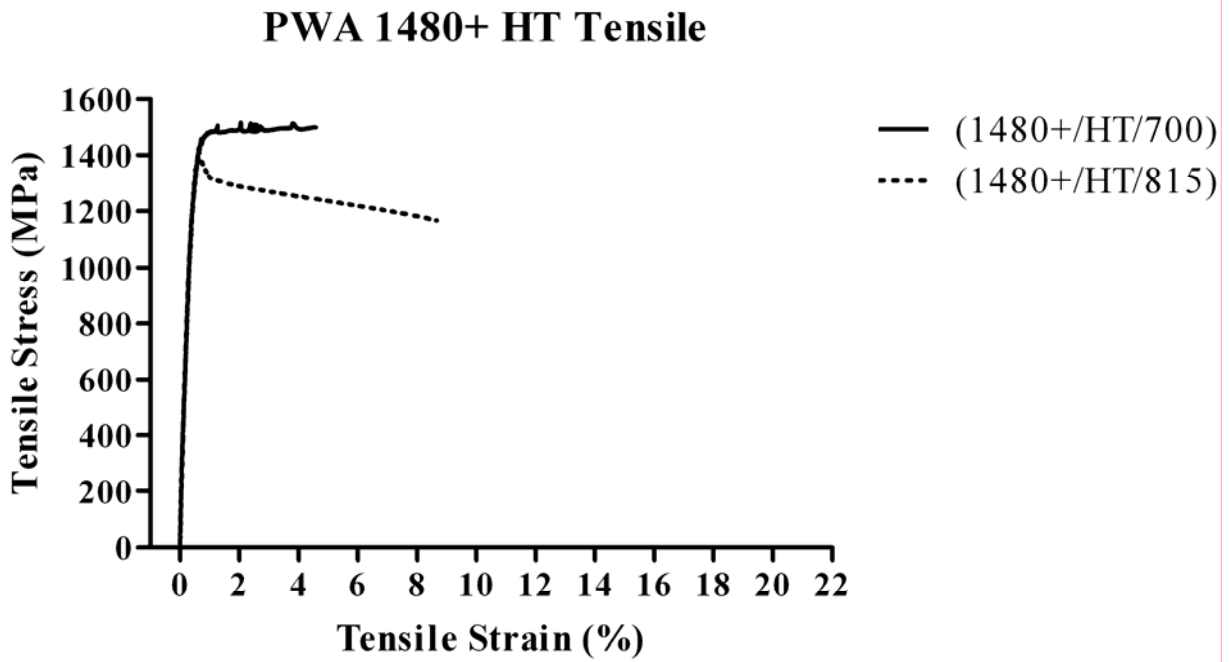


Figure 5-17. Tensile behavior of PWA 1480+ HT at both temperatures.

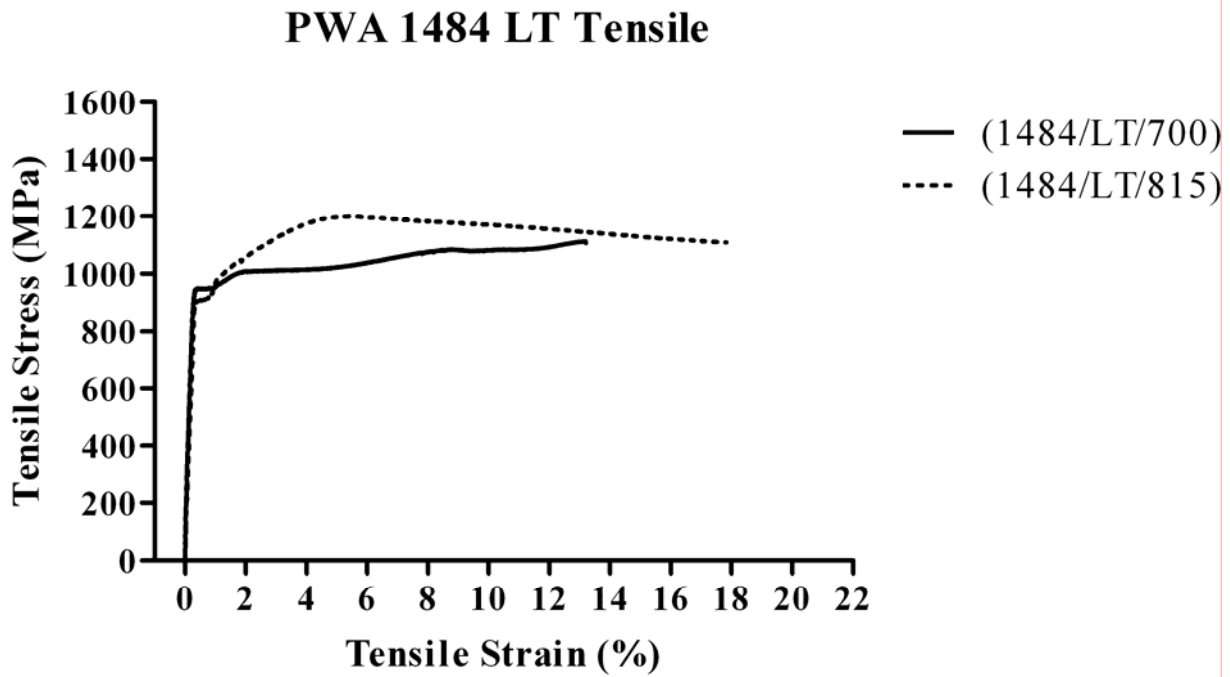


Figure 5-18. Tensile behavior of PWA 1484 LT at both temperatures.

### PWA 1484 HT Tensile

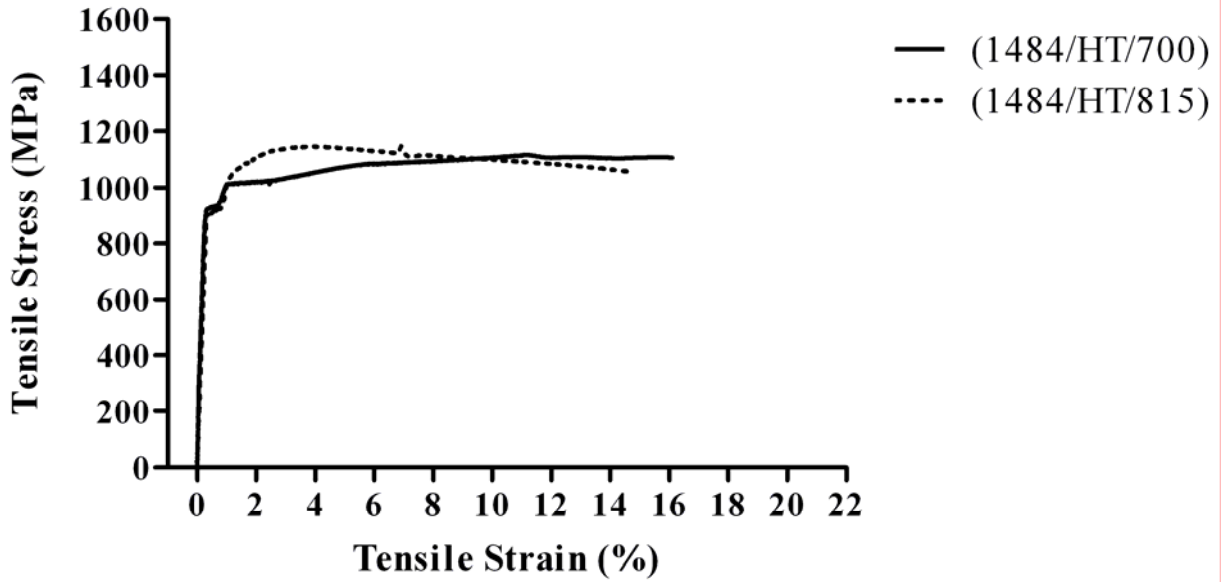


Figure 5-19. Tensile behavior of PWA 1484 HT at both temperatures.

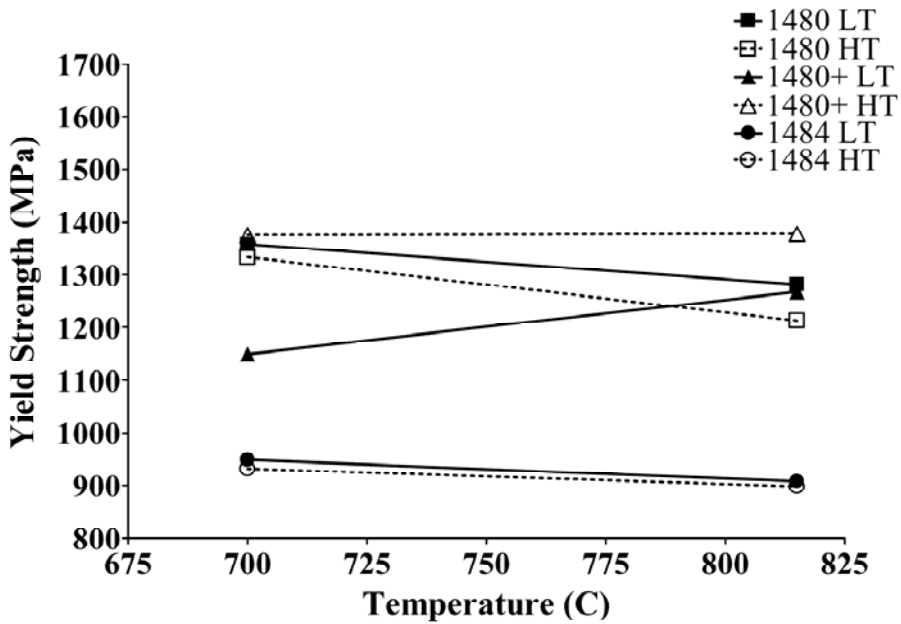


Figure 5-20. Yield strength as a function of temperature for all three alloys.

Table 5-3. Creep loads vs. yield strength for all three alloys.

		Age	$\sigma_y$ (MPa)	Creep Load (MPa)	% $\sigma_y$
700°C	PWA 1480	LT	1357.44	862	63.5
		HT	1333.45	862	64.6
	PWA 1480+	LT	1149.77	862	75.0
		HT	1375.57	862	62.7
	PWA 1484	LT	948.72	862	90.9
		HT	931.76	862	92.5
815°C	PWA 1480	LT	1281.39	621	48.5
		HT	1212.24	621	51.2
	PWA 1480+	LT	1267.39	621	49.0
		HT	1378.33	621	45.1
	PWA 1484	LT	907.90	621	68.4
		HT	897.90	621	69.2

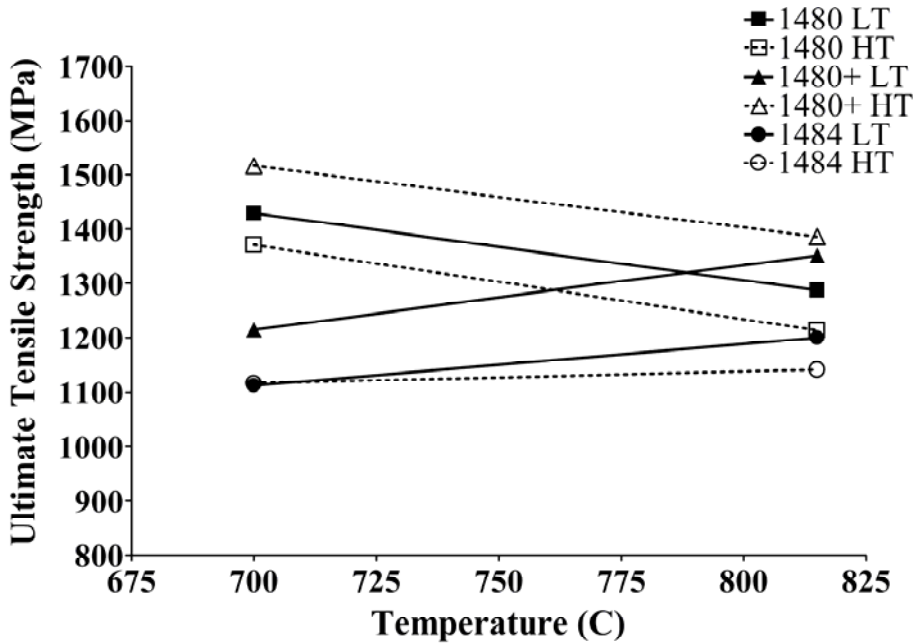


Figure 5-21. Ultimate Tensile Strength as a function of temperature for all three alloys.

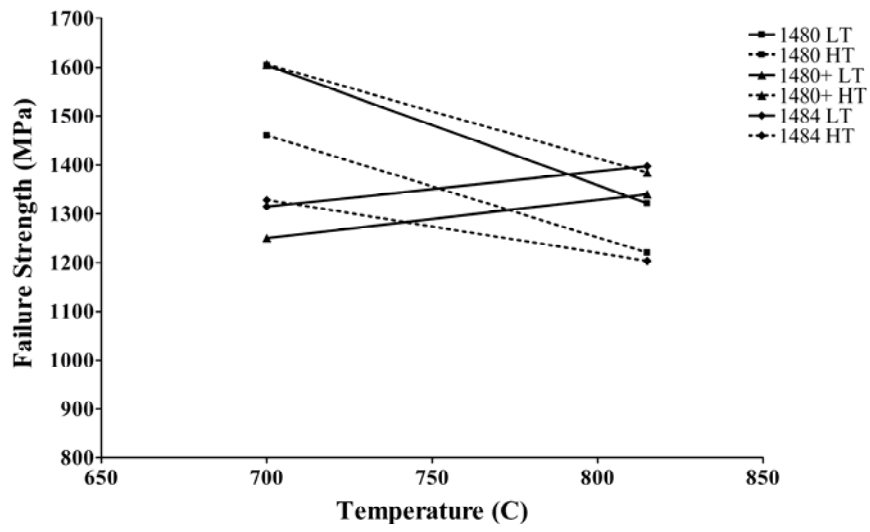


Figure 5-22. True Failure Stress as a function of temperature for all three alloys.

## CHAPTER 6 RESULTS: CREEP BEHAVIOR

Creep testing was initially performed at three combinations of temperature and initial stress as follows: 704°C/758 MPa, 760°C/690 MPa, and 815°C/621 MPa. After running several tests at 704°C/758 MPa the initial applied stress was increased to 862 MPa due to the excessive failure lives of PWA 1484 specimens (greater than 1700 hours). As discussed earlier in Chapter 3, creep testing consisted of two phases of testing. First, full-length testing was performed to establish lifetime and performance expectations. The original goal of this investigation was to study the effect of secondary  $\gamma'$  precipitates and (related) age heat treatments. Following the first complete round of testing, the unique primary creep behavior became obvious and the investigation took up a new focus (on primary creep behavior). The second batch of single crystal bars of PWA 1480 and PWA 1484 was acquired to investigate primary creep further. Additionally, the third alloy (PWA 1480+) was created due to the prevalence of primary creep in rhenium bearing alloys. Full length creep tests continued with the second batch of material.

The second phase of testing was performed after observing the primary creep behavior of PWA 1484. In order to view a similar condition for all three alloys, it was decided to stop samples following 0.5% secondary creep. This level of creep ensured that primary creep mechanisms were still obvious while allowing for useful comparison between alloys. Stopping primary creep specimens at a specific amount of primary creep (e.g. 0.3%) would not have been very useful due the significant difference in primary creep behaviors expressed by the alloys. Additionally, ending the interrupted creep tests during the maximum primary creep rate would only allow useful examination of PWA 1484. PWA 1480 and PWA 1480+ exhibited continuously declining creep rates beginning almost immediately following loading of the specimens. As a result of these concerns, the deformation mechanisms were observed for

specimens just entering the secondary creep stage. Finally, another benefit of interrupting creep early in secondary creep is that data from the entire primary creep regime are preserved for all three alloys as will be presented below (for example, total primary creep strain, maximum primary creep rate, minimum secondary creep rate).

### **Full Length Tests**

#### **PWA 1480**

The first generation PWA 1480 exhibits a brief primary creep stage followed by a continuously increasing creep rate. None of the four creep conditions produced true steady-state secondary creep behavior in PWA 1480. This is especially obvious when viewing the creep rate change with temperature. The minimum creep rate is usually recorded soon after the end of the primary creep stage. The creep rate then slowly increases throughout the remainder of the creep test. As a result, a true secondary creep stage is not observed. The initial creep rates of PWA 1480 reflect the early onset of primary creep and are typically larger than all creep rates to follow until late in the tertiary creep stage. Immediately after primary creep the creep rates are at their minimum values and significantly lower than the maximum primary creep rates earlier in the life of the specimens, Table 6-1.

The complete lifetime of the PWA 1480 specimens at 704°C/862 MPa, 760°C/690 MPa, and 815°C/621 MPa can be seen in Figures 6-1, 6-2, and 6-3. Additionally, creep test results are given in Table 6-2 for all three alloys. A number of points can be made about the creep behavior of PWA 1480. First and as already mentioned, tertiary creep dominates the life of the alloy at all three test conditions. Second, as the temperature is lowered from 815°C to 704°C, and the load increased, the performance of PWA 1480 improves significantly. Third, the amount of primary creep is virtually unchanged for all three test conditions and both age heat treatments. And

finally, the creep behavior of PWA 1480 does not seem to have a strong dependence on age heat treatment temperature.

While tertiary creep behavior is dominant for PWA 1480 at all test conditions, changes in creep rates and lifetimes are clearly evident. For instance, time to 1% creep ( $t_{1\%}$ ) at 704°C/862 MPa and 760°C/690 MPa are similar; however, time to 2% creep ( $t_{2\%}$ ) begins to show some variation in performance with the higher temperature test resulting in a shorter  $t_{2\%}$  time. When the temperature is raised still further to the 815°C test condition the  $t_{1\%}$  and  $t_{2\%}$  values are decreased significantly. The creep rupture life of PWA 1480 declines from the lowest temperature test condition to the highest temperature test condition. As the creep life decreases with increasing temperature, the minimum creep rates increase with increasing temperature. The creep rates at 815°/621 MPa are more than double the creep rates at 704°C/862 MPa. The reduction in lifetime and creep rate performance has not affected the amount of primary creep, however.

The primary creep strains produced by PWA 1480 at all three conditions are unchanged. The amount of primary creep is between 0.3% and 0.5% for all test conditions even though the maximum creep rate during primary creep is significantly increased at higher temperatures, Table 6-1. Changing the age heat treatment temperature does not change these behaviors in a predictable manner. In fact, no obvious dependence on age heat treatment was found. One exception to this was found during interrupted creep testing, Figure 6-4. Here, the LT aged specimens experienced less creep than their HT age counterparts. The amount of primary creep, however, was the same. Overall, the performance of both heat treatments was similar enough to be within the expected range of scatter for creep testing. Additionally, there is no change in the amount of primary creep strains due to age heat treatment.

## **PWA 1480+**

The addition of Re to PWA 1480 that improved the tensile properties discussed in Chapter 5 also significantly improved the creep behavior of the alloy. The already low primary creep of PWA 1480 was reduced in PWA 1480+ and the creep rate under all heat treatment and test conditions was significantly lower than any other alloy/heat treatment combinations in this investigation, Figures 6-1 to 6-3 and Tables 6-1 and 6-2. Also, the rupture lifetimes of PWA 1480+ specimens were much longer than the same of PWA 1480 specimens. The overall lifetime and creep rate performance of the experimental alloy were significantly improved; however, creep ductility was reduced for all conditions. Most PWA 1480+ samples failed with less than 5% creep elongation. This reduction in ductility is likely a direct consequence of the large strengthening effect of the Re addition to PWA 1480. The alloy may have been hardened to such a point that ductility is greatly reduced. Though not tested during this investigation, the fracture toughness of PWA 1480+ is potentially reduced as well.

Similarly to PWA 1480, the age heat treatments did not create any obvious differences in creep performance. The primary creep strains produced with both age heat treatments were similar. While PWA 1480 exhibited similar primary creep strains at all test temperatures, PWA 1480+ exhibited lower primary creep strains at higher temperatures, Table 6-1. The primary creep strains of PWA 1480+ specimens at 704°C/862 MPa are in the same range as those produced in PWA 1480 without Re. At 815°C/621 MPa, PWA 1480+ exhibits less than half the primary creep of the lower temperature specimens.

The creep behavior of PWA 1480+ still maintained some similarities to the behavior of PWA 1480. For instance, the minimum creep rate slowly climbed during the test and the overall creep behavior appeared to be dominated by tertiary creep. The rise in creep rates of PWA

1480+ were much less pronounced than the rise in minimum creep rates of PWA 1480. Additionally, primary creep for both alloys was similar, with the exception of 815°C. This remains true despite a significant increase in  $t_{1\%}$  and  $t_{2\%}$  times, indicating that the amount of primary creep that is attained is not necessarily linked to the amount of time required for the completion of primary creep. For example, the interrupted creep tests of PWA 1480 and PWA 1480+ were terminated around 0.75% creep elongation for TEM analysis. The PWA 1480 tests were terminated between 10 and 25 hours, Figure 6-4. The PWA 1480+ samples, however, finished between 250 and 450 hours for the same elongation, Figure 6-5.

The amount of primary creep produced was the same in this case at both temperatures and for both age heat treatments. If it was only a matter of time to complete primary creep, PWA 1480+ would likely have produced much less primary creep than PWA 1480. In actuality, it appears that the total primary creep strain is the determining factor. Another way of stating this is to say that the onset of secondary creep terminates primary creep. This reasoning may sound redundant; however, the onset of secondary creep is related to work hardening processes in the alloys. Once significant work hardening is produced to slow the primary creep deformation processes, secondary creep begins. The primary contributor to the onset of secondary creep, then, is not time, but strain. The amount of work hardening necessary for an alloy to enter secondary creep will vary based on microstructural characteristics and composition. As will be shown later, substantial work hardening takes place in PWA 1480 and PWA 1480+ during the early stages of primary creep leading to rapid work hardening and only 0.3% to 0.5% primary creep strain. PWA 1484, however, does not exhibit this behavior and instead demonstrates very little dislocation and stacking fault interaction during primary creep leading to reduced work hardening. Finally, because strain is the controlling factor in the onset of secondary creep, it is

not surprising that PWA 1480 and PWA 1480+ can produce the same amount of primary creep with large differences in the time required.

#### **PWA 1484**

The creep behavior of the second generation alloy PWA 1484, however, displays a brief incubation period followed by a large primary creep strain. Primary creep typically ends very soon after it starts by transitioning to secondary creep with a constant, low creep rate. Despite the large primary creep strains, most of the rupture lives of the PWA 1484 specimens occurred during secondary creep. Plotted as creep elongation (%) vs. run time (hr.), the secondary creep stage of these alloys is very nearly linear. As the test nears the eventual failure life of the alloy, the creep rate slowly begins to increase. The rising creep rate continues to increase until failure, and thus comprises the tertiary stage of creep for PWA 1484.

Compared to PWA 1480 for the highest temperature test, PWA 1484 has a rupture life that is roughly 10 times (1000%) the rupture life of PWA 1480, Table 6-2. As the temperature is lowered (and the stress increases), the relative difference decreases. At 760°C, PWA 1484 has a lifetime of about 4 times (400%) the lifetime of PWA 1480. At 704°C, however, PWA 1480 has the greater rupture life. In the LT age condition, for example, the rupture life of PWA 1484 is now only 1/10 (10%) of the life of PWA 1480, Figures 6-1 through 6-3.

The prominence of the primary creep stage of PWA 1484 is evident for all test conditions used in this investigation. Generally, as the temperature is increased and the load decreased, the magnitude of primary creep decreases, Figure 6-6. Alternatively, as the temperature is reduced and the load is increased, the magnitude of primary creep in PWA 1484 increases. By comparison, there does not appear to be a significant difference in primary creep as a result of test condition in PWA 1480 and PWA 1480+, Figures 6-4 and 6-5. PWA 1484 also shows a

fairly strong primary creep dependence on age heat treatment. For all PWA 1484 creep tests, the LT aged specimens produced significantly more primary creep than the HT aged specimens. The effect of test temperature/stress and age heat treatment can be readily seen in Figures 6-1 to 6-3, and 6-6 to 6-7. The HT age reduced the primary creep strain of PWA 1484 by up to 10% of the LT primary creep strain at all temperatures. Alternatively, the primary creep strains of the HT aged specimens have been reduced to as low as 50% of the primary creep strains of the LT aged counterparts.

Post-test measurements revealed that the PWA 1484 specimens deformed non-uniformly during creep testing. Inhomogeneous creep has been shown to occur frequently in second generation superalloys like CMSX-4 and PWA 1484.<sup>13, 47, 55</sup> All of the PWA 1484 specimens were elongated from the original circular cross-section to an elliptical cross-section. The major and minor axes of the ellipse were parallel to  $\langle 110 \rangle$  directions. It has been reported that the elliptical cross-section is formed mostly during primary creep if few slip systems are active. After the initiation of secondary creep, work-hardening should result in greater uniformity of deformation due to the activation of multiple slip systems.

Following this reasoning, the difference in creep rate between the two age heat treatments of PWA 1484 at 815°C/621 MPa, Figure 6-3, may be due to changes in cross-sectional area during primary creep. With a smaller cross-section the LT age sample will deform faster than the HT age, giving the impression of a higher creep rate. Contrasting this reasoning are the data produced at 760°C/690 MPa, Figure 6-2. Here, an even greater difference in primary creep strain yielded nearly identical secondary creep rates between the two age heat treatments. More testing is needed before the cause of the varied secondary creep rate can be stated with confidence.

## Interrupted Tests

Interrupted creep results are presented in Figures 6-4 to 6-6 for all three alloys and both age heat treatments. From these results it is immediately clear that PWA 1484 exhibits unusually large primary creep strains. Additionally, the amount of time that elapses during primary creep changes significantly for each alloy. In order of increasing time to complete primary creep: PWA 1484 (5-15 hours), PWA 1480 (12-22 hours), and PWA 1480+ (230-410 hours). This order also applies to decreasing amounts of primary creep produced during interrupted testing.

Comparing the age heat treatments for the three alloys reveals a few correlations of interest. First, the primary creep behavior of PWA 1480 may have slight age heat treatment dependence; however, as already mentioned the overall behavior of PWA 1480 does not appear to follow a dependence on age heat treatment temperature. Second, the primary creep of PWA 1484 has a strong dependence on age heat treatment temperature, Figure 6-6. At both temperatures, the HT age specimens resulted in the lowest primary creep which is consistent with full length creep testing. By comparison, at 704°C the HT age reduced the primary creep of PWA 1484 by 32% and at 815°C reduced the primary creep by 67%. Finally, PWA 1480+ shows no correlation to age heat treatment, which is also consistent with full length testing.

The test temperature also brought about some behavioral changes. Both PWA 1480 and PWA 1480+ exhibited less time to reach 0.7% creep at 815°C. The minimum and maximum creep rates were slightly higher at 815°C than at 704°C for both alloys, Table 6-1. PWA 1484 exhibited a much more dramatic change in properties with increasing temperature. While PWA 1480 and PWA 1480+ produced approximately the same amount of primary creep at both temperatures, the primary creep of PWA 1484 was greatly reduced at 815°C for both age heat treatments. For the LT age, the primary creep strain of PWA 1484 at 704°C was 24.44% and

3.68% at 815°C. For the HT age, the results were 16.66% at 704°C and 1.20% at 815°C. For the LT age, this represents an 85% reduction in primary creep. For the HT age it is a 93% reduction.

### **Transmission Electron Microscopy (TEM)**

Transmission electron microscopy was performed to produce a qualitative understanding of the active deformation mechanisms because the two reported deformation mechanisms are distinct in appearance. First, the more common deformation mechanism reported in superalloys consists of matrix dislocations bowing to fill the  $\gamma$  matrix channels and creating interfacial dislocation networks.<sup>19, 27, 56, 57</sup> This mechanism applies to most superalloys due to the growing incoherency of the  $\gamma/\gamma'$  interface during a creep test. Deformation usually begins in the  $\gamma'$  matrix and this leads to the formation of interfacial networks to one degree or another in all nickel base superalloys. The second deformation mechanism commonly associated with primary creep occurs by stacking fault shear of the  $\gamma'$  precipitates and has been reported in several alloys.<sup>16, 17, 23, 24, 33, 58</sup> The alloys most commonly linked to this behavior are second generation and later alloys like PWA 1484 and CMSX-4; however, one first generation alloy has been reported to exhibit this method of creep deformation as well.<sup>33</sup> Following the interrupted creep tests it would be expected that all of the specimens would exhibit sufficient formation of  $\gamma/\gamma'$  interfacial dislocation networks to cause the onset of secondary creep, which was found to be true for the specimens examined here.<sup>16, 19</sup>

#### **PWA 1480**

The deformation of PWA 1480 during interrupted creep consisted primarily of matrix dislocations bowing to fill the  $\gamma$  matrix channels, Figures 6-11 and 6-12. Most of the deformation appears to be limited to the matrix phase; however, a low amount of stacking fault

formation was also found within the specimens, Figures 6-13 to 6-15. The stacking faults that were found tended to be limited to a range of one or two  $\gamma'$  precipitates only. It will be shown that the limited nature of stacking fault formation stands in contrast to the prevalent nature of the stacking faults in PWA 1484. The limiting of dislocations to the  $\gamma$  matrix during primary creep is also consistent with low amounts of primary creep as reported by several sources.<sup>16, 17, 19, 20, 27, 33, 56, 57</sup> Additionally, the presence of secondary  $\gamma'$  precipitates was confirmed by TEM, Figure 6-16.

### **PWA 1480+**

The second generation version of PWA 1480, PWA 1480+Re, exhibited a significant change in behavior (relative to PWA 1480). Most notably was an increase in the number of stacking faults within the material, Figure 6-17. Additionally, stacking faults were often seen interacting with stacking faults lying on different slip planes, Figures 6-17 to 6-19. While stacking fault formation is tied to large primary creep strains, they are typically limited to a single slip system in alloys exhibiting large primary creep strains.<sup>16, 17, 33</sup> PWA 1480+, however, was shown to exhibit low amounts of primary creep. Additionally, the fact that the stacking faults appear to be interacting with other stacking faults, indicating slip on more than one slip system, is worth exploring. These interactions are common in superalloys displaying stacking fault shear, but not until the final stages of creep leading to failure.<sup>33</sup> These interactions in PWA 1480+ occurred early in the life of the specimens during primary creep and failure is not imminent. These interactions, coupled with the active matrix dislocations, may be generating relatively large amounts of strain hardening that brings about the onset of secondary creep earlier than alloys, such as PWA 1484, that exhibit stacking fault shear on a single slip system during primary creep. Additionally, stacking faults in PWA 1480+ are limited to regions spanning only

2 to 3  $\gamma'$  precipitates (or fewer). The localized nature of the stacking fault shear may be a result of these stacking fault interactions restricting the propagation of the shear bands as they form. In this way, the ability to produce strain is reduced and the expected primary creep strains would be lower. Despite the formation of larger numbers of stacking faults, deformation is limited and the secondary creep stage occurs early (in terms of total strain, not time).

#### **PWA 1484**

The PWA 1484 specimens, when observed on the TEM, appear to share the same deformation mechanisms widely reported among second generation alloys at low temperatures and high loads as used in this investigation. Wide-spread stacking fault shear that appears to act on a single slip system was apparent over large regions within the specimens, Figures 6-20 to 6-21. This highly planar deformation mechanism, as reported by others<sup>16, 17</sup>, occurs by the passage of two  $a/2\langle 110 \rangle$  matrix dislocations (same slip plane with burger's vectors at  $60^\circ$  to each other) into the  $\gamma'$  precipitates. These dislocations then dissociate into  $a/3\langle 112 \rangle$  and  $a/6\langle 112 \rangle$  partial dislocations with stacking faults in between. The two pairs of partials (with stacking faults in between) are separated by an anti phase boundary (APB) due to the ordered nature of the  $\gamma'$  precipitates. It is this complex system of dislocations, stacking faults, and the associated anti phase boundary that is able to shear large distances with relatively little impedance, generating large primary creep strains.<sup>17</sup> The numerous rows of stacking fault ribbons in PWA 1484 can be seen in Figures 6-20 and 6-21. Additionally, a large density of matrix dislocations has formed in PWA 1484 following primary creep, Figure 6-22. Again, this is consistent with the onset of secondary creep. These shear bands are also conservative in nature and leave no dislocation debris at the  $\gamma/\gamma'$  interfaces (assuming no other dislocations are interacting with the stacking fault “ribbons”). As a result, the ribbons are free to expand and glide until they interact with other

matrix dislocations. These matrix dislocations will eventually form interfacial networks; however, the amount of primary creep that has been produced is already quite large by this point. Therefore, by the time enough work hardening is present to force the onset of secondary creep in PWA 1484, the amount of primary creep that has been conferred can be quite large. The matrix dislocations shown in Figure 6-22 are the likely cause of the beginning of the secondary creep stage.

Table 6-1. Primary creep and creep rates from interrupted creep tests.

Alloy	Age HT	704°C/862 MPa			815°C/621 MPa		
		Primary Creep (%)	Max. Primary Creep Rate (%/hr.)	Minimum Creep Rate (%/hr.)	Primary Creep (%)	Max. Primary Creep Rate (%/hr.)	Minimum Creep Rate (%/hr.)
PWA 1480	LT	0.35	0.1632	0.0116	0.34	0.6001	0.0277
	HT	0.49	0.4015	0.0166	0.32	1.0377	0.0418
PWA 1480+	LT	0.36	0.0073	0.0007	0.22	0.0339	0.0021
	HT	0.34	0.0296	0.0011	0.11	0.0304	0.0022
PWA 1484	LT	24.44	10.704	1.8697	3.68	2.4563	0.0768
	HT	16.66	4.3877	0.7010	1.20	0.6751	0.0454

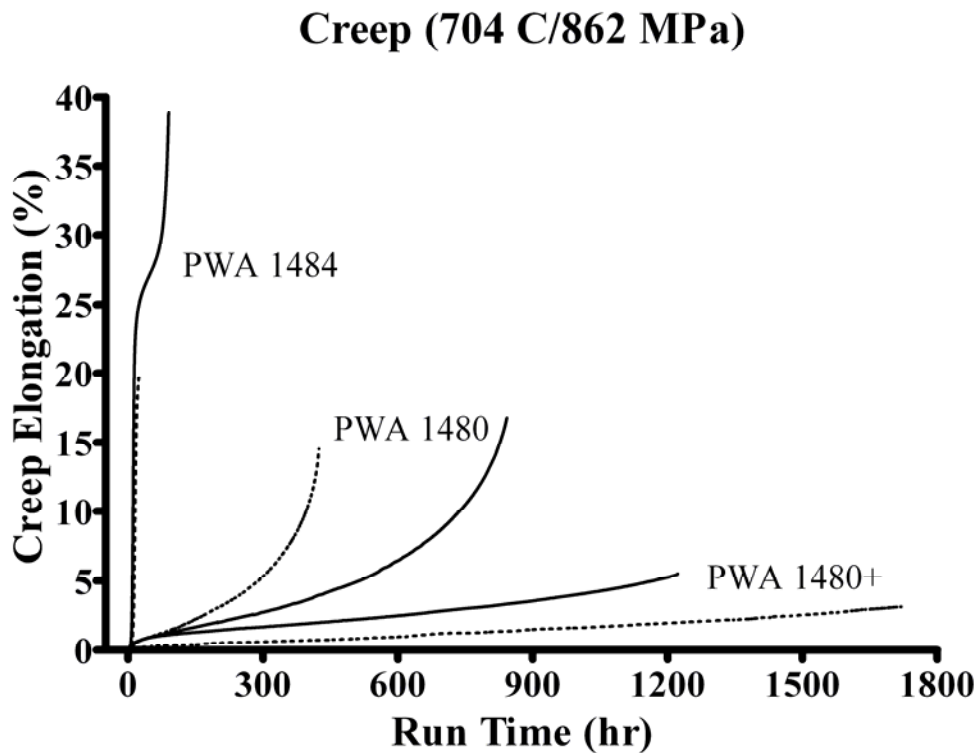


Figure 6-1. Creep at 704°C/862 MPa of all three alloys.

### Creep (760 C/690 MPa)

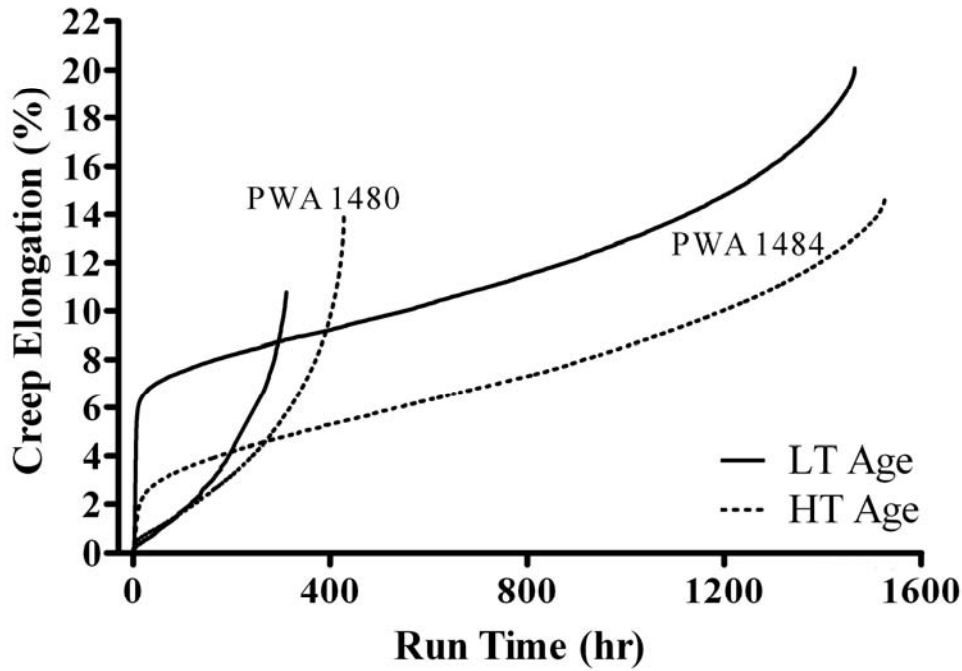


Figure 6-2. Creep at 760°C/690 MPa of all three alloys.

### Creep (815 C/621 MPa)

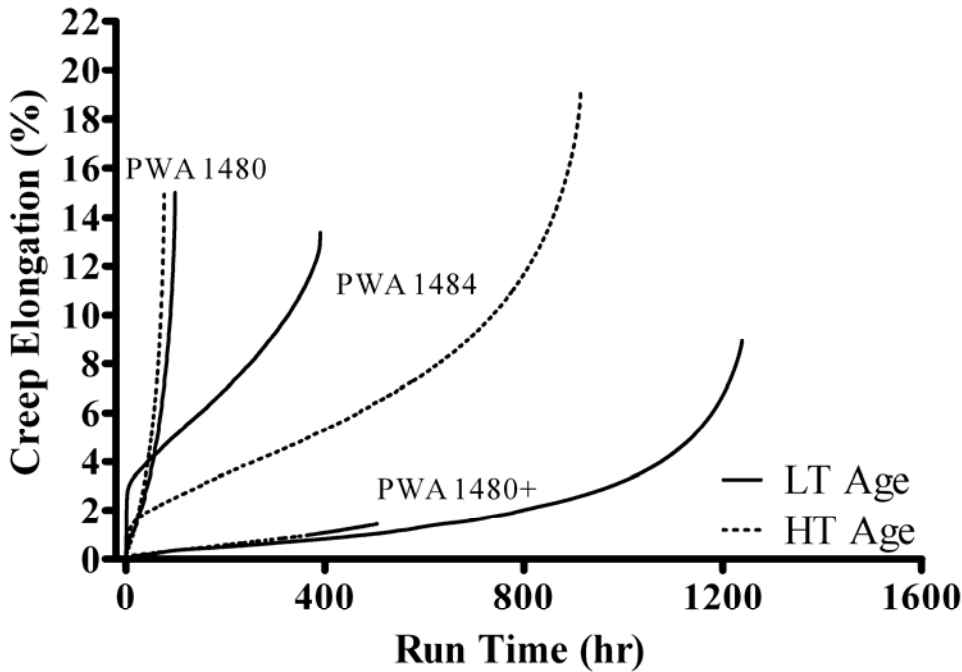


Figure 6-3. Creep at 815°C/621 MPa of all three alloys.

Table 6-2. Rupture lives and total creep elongation from full-length creep tests. Also included is time to 1% and time to 2% creep. Note: The PWA 1480+ HT sample at 815°C/621 MPa failed before 2% creep was achieved.

	Alloy	Age	t <sub>1%</sub> (hr.)	t <sub>2%</sub> (hr.)	t <sub>rupture</sub> (hr.)	Elongation (%)
704°C 862 MPa	1480	LT	55.2	199	842	16.77
		HT	52.0	135	424	14.52
	1480+	LT	63.0	427	1223	5.52
		HT	619	1225	1721	3.32
	1484	LT	7.19	8.33	90.3	38.81
		HT	10.1	11.7	23.7	19.64
760°C 690 MPa	1480	LT	56.6	117	311	10.78
		HT	47.4	124	428	13.90
	1484	LT	3.27	4.10	1465	20.08
		HT	5.96	13.9	1525	14.69
815°C 621 MPa	1480	LT	11.2	28.8	99.3	15.01
		HT	14.4	26.8	77.2	14.93
	1480+	LT	486	797	1239	8.94
		HT	372	N/A	505	1.45
	1484	LT	1.15	1.18	391	13.40
		HT	4.92	49.8	914	19.06

### Interrupted Creep: PWA 1480

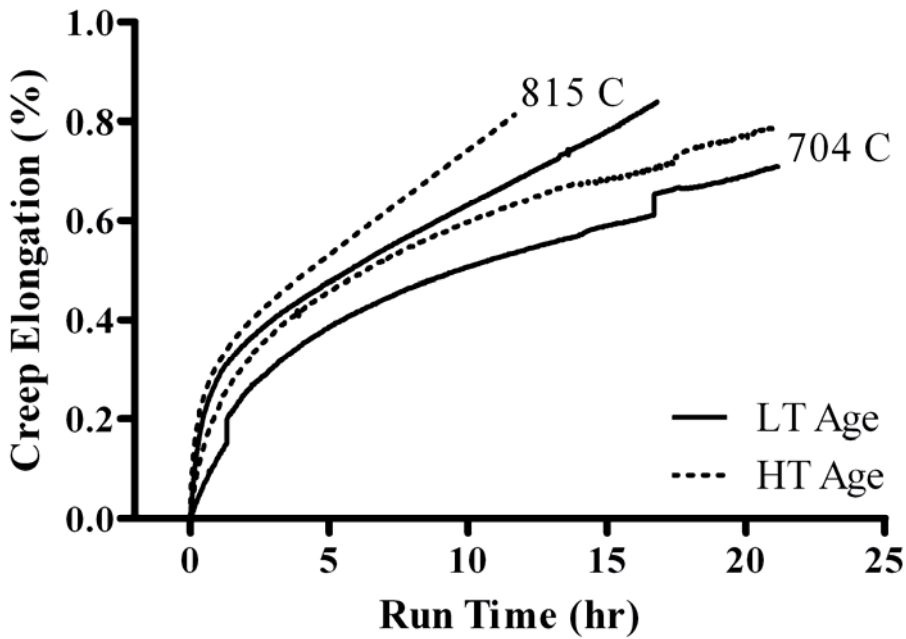


Figure 6-4. Primary creep of PWA 1480.

### Interrupted Creep: PWA 1480+

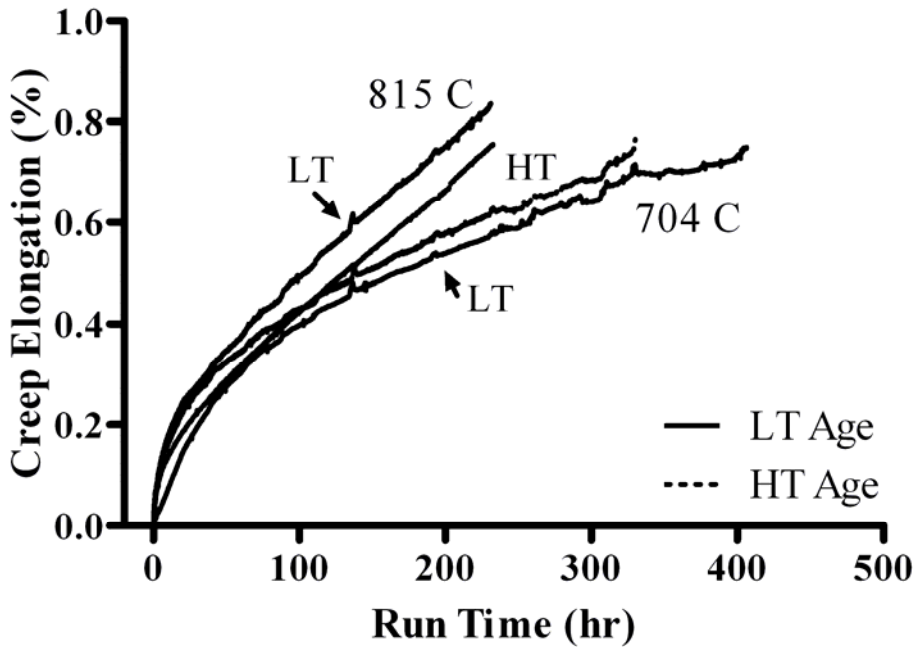


Figure 6-5. Primary creep of PWA 1480+.

## Interrupted Creep: PWA 1484

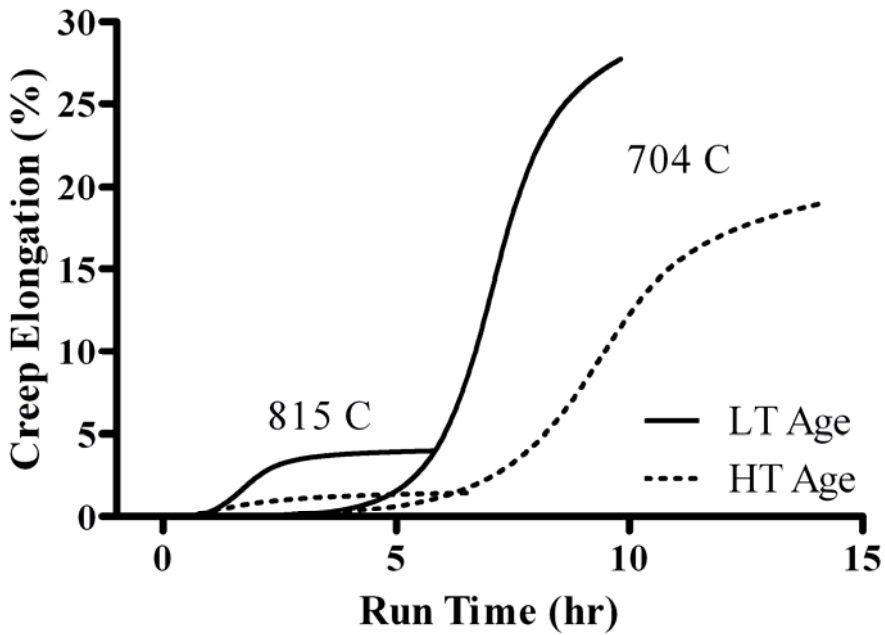


Figure 6-6. Primary creep of PWA 1484.

## Creep (704 C/862 MPa)

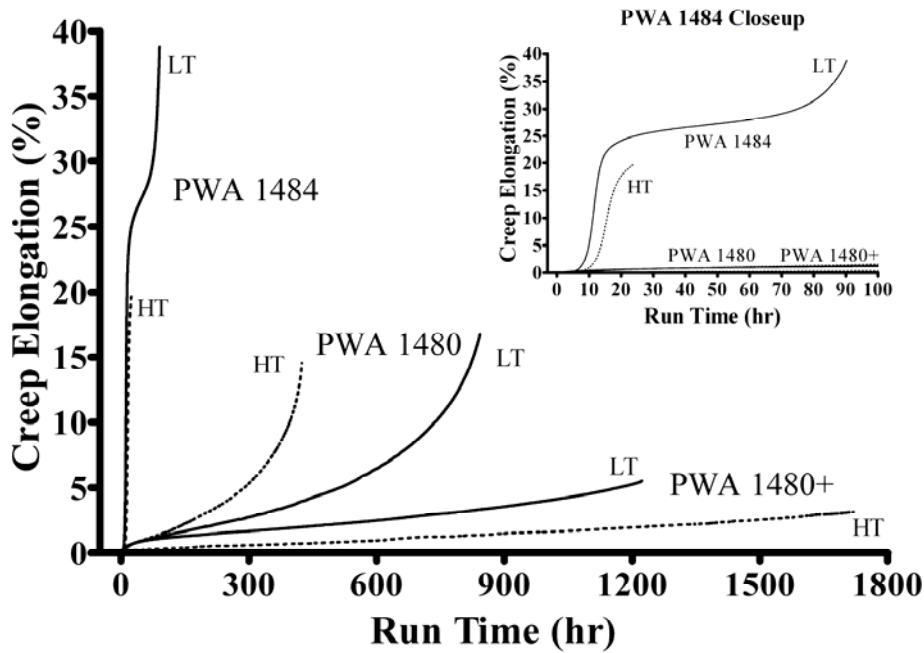


Figure 6-7. Creep at 704°C/862 MPa of PWA 1484 compared to PWA 1480 and PWA 1480+. Inset: magnified view of the creep behavior of PWA 1484.

### Primary Creep (704 C/862 MPa)

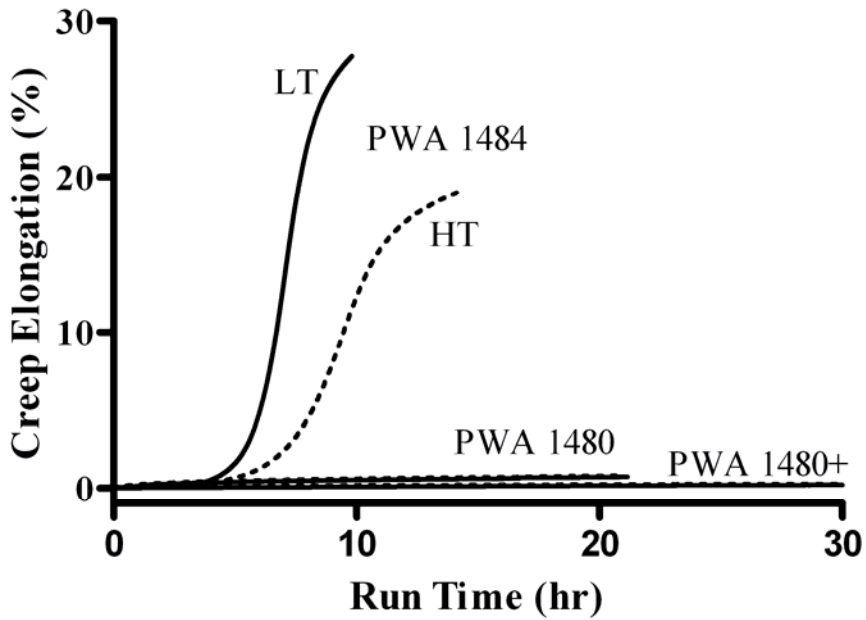


Figure 6-8. Primary creep comparison at 704°C/862 MPa for all three alloys. Note: large strain range was used better viewing of the behavior of PWA 1484.

### Primary Creep (704 C/862 MPa)

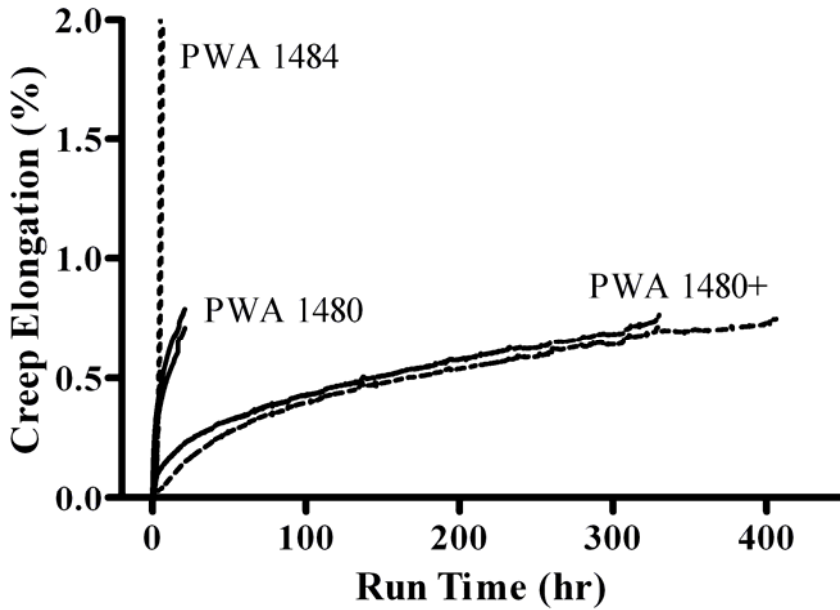


Figure 6-9. Primary creep comparison at 704°C/862 MPa for all three alloys. Note: long time range was used for better viewing of the behavior of PWA 1480 and PWA 1480+.

### Primary Creep (815 C/621 MPa)

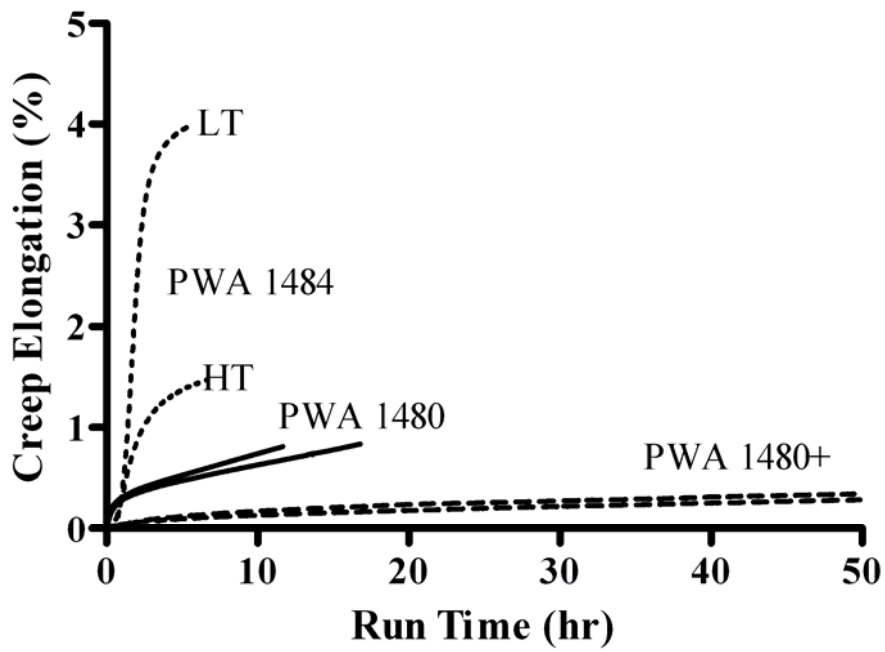


Figure 6-10. Primary creep comparison at 815°C/621 MPa for all three alloys.

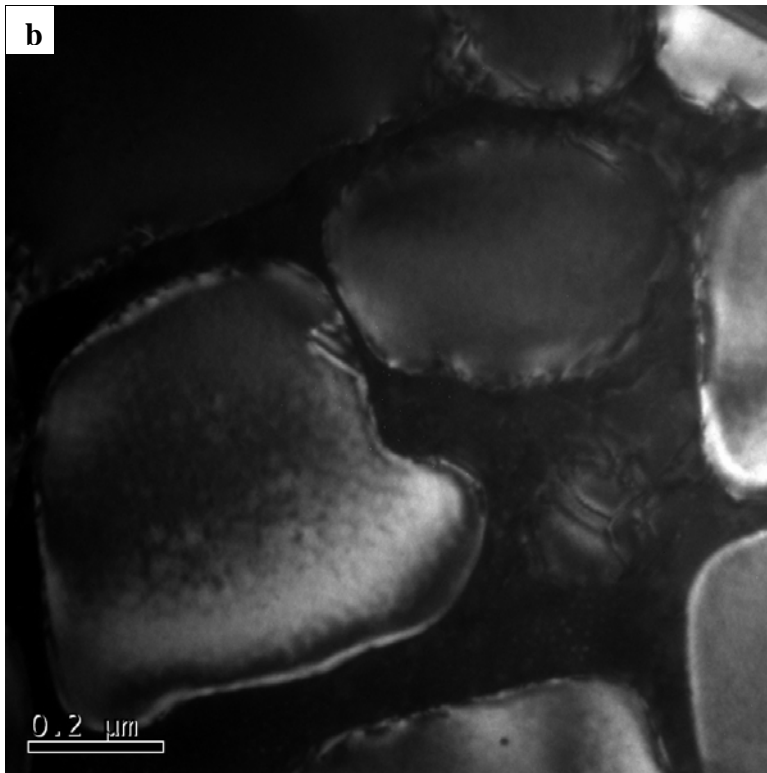
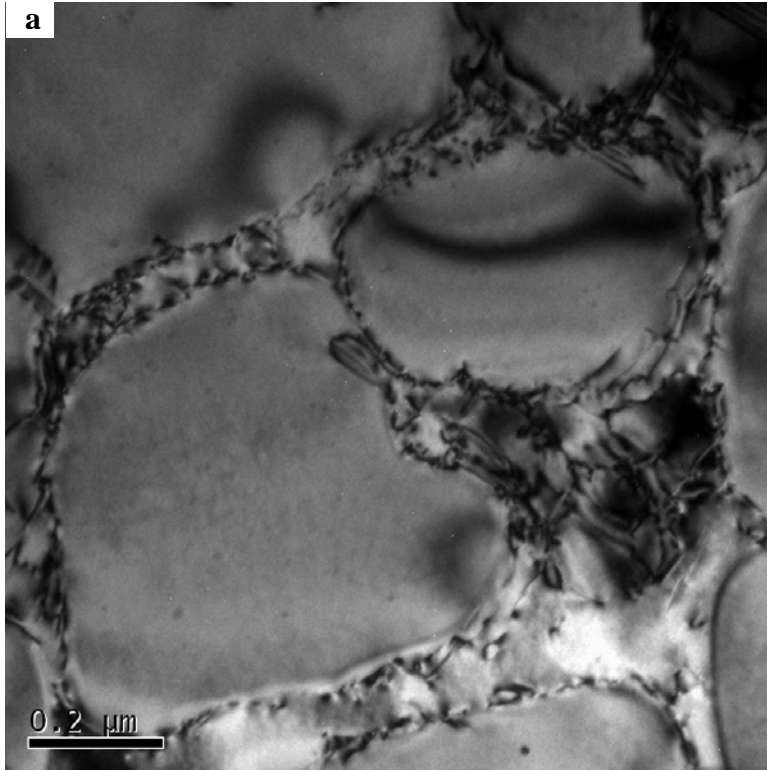


Figure 6-11. Bright field(a)/Dark field(b) pair of deformation in PWA 1480 (HT age, 704°C). Creep deformation is primarily limited to the  $\gamma$  matrix and interfacial dislocation networks have already formed.

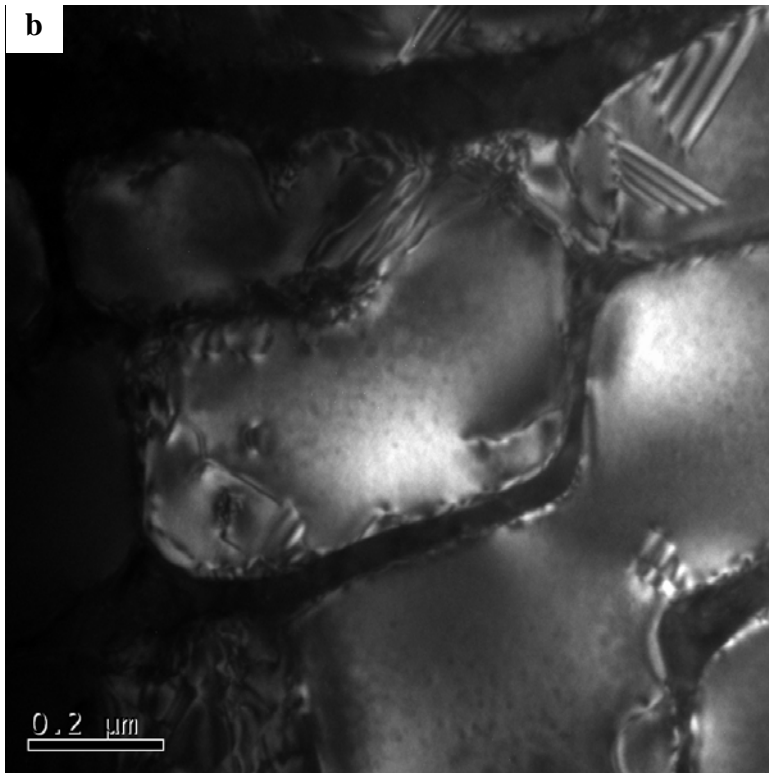
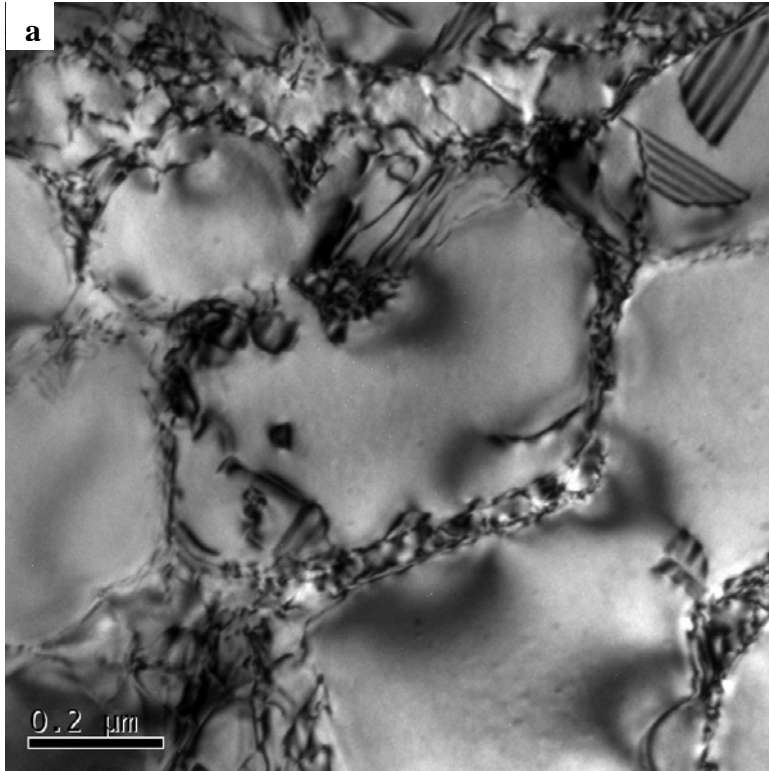


Figure 6-12. Bright field(a)/Dark field(b) pair of deformation in PWA 1480 (HT age, 704°C) revealing the formation of few stacking faults.



Figure 6-13. Bright field TEM image of dislocation networks in PWA 1480 following primary creep.

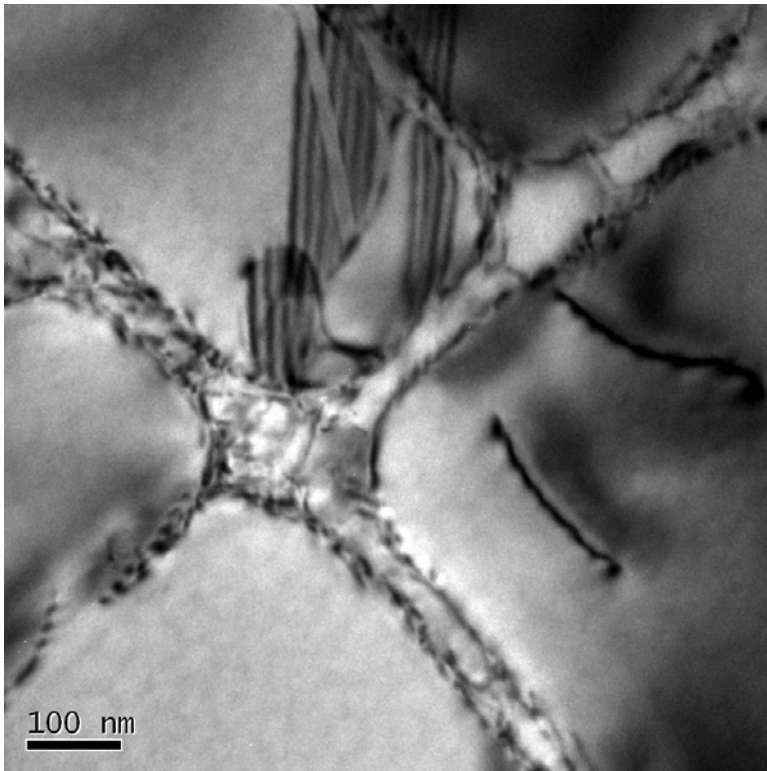


Figure 6-14. Stacking fault and dislocation shear of PWA 1480 is limited to small regions within the specimens (bright field).

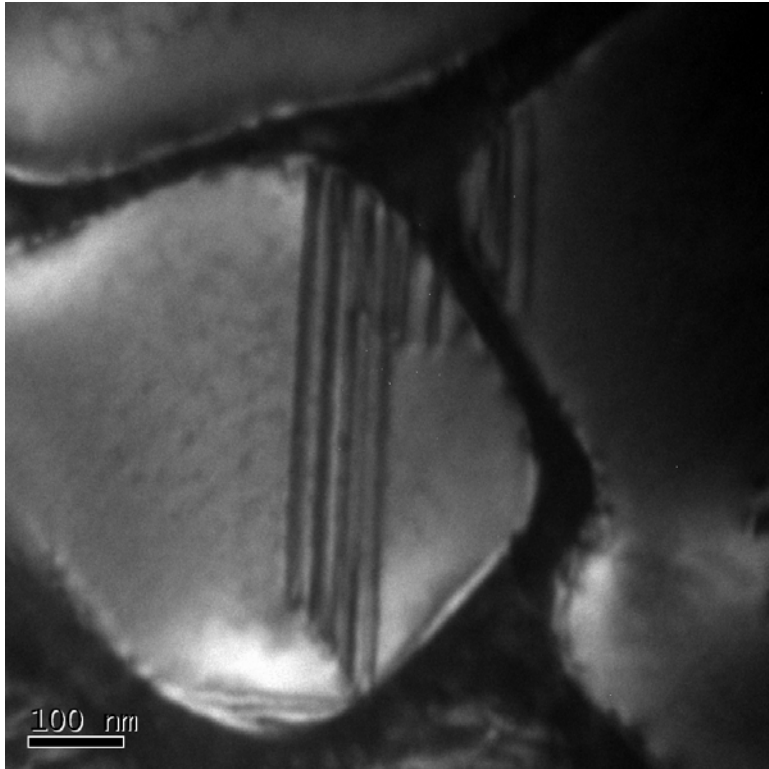


Figure 6-15. A stacking fault in PWA 1480 (dark field).



Figure 6-16. Secondary  $\gamma'$  precipitates (marked by arrows) in PWA 1480 following interrupted creep.

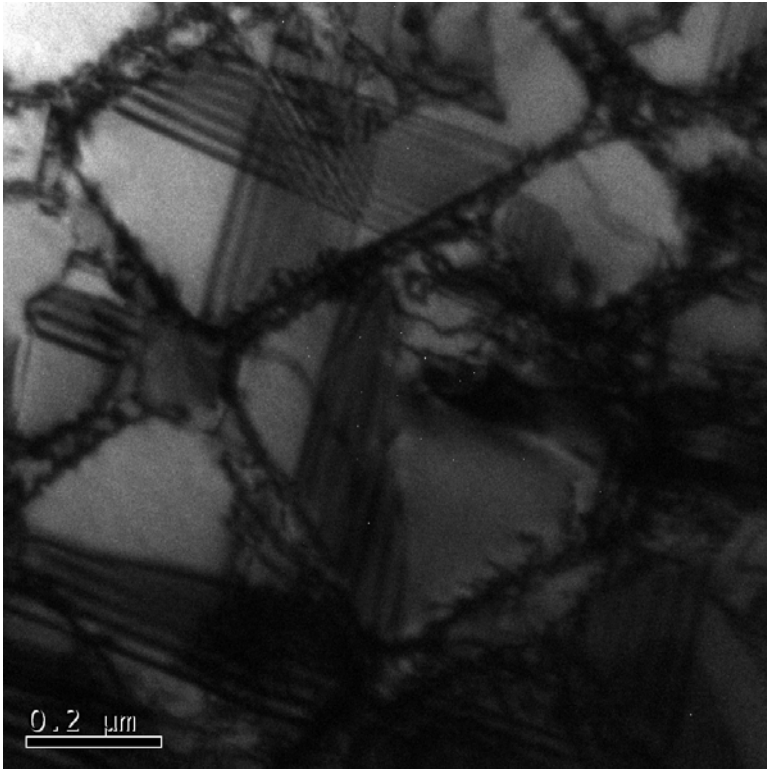


Figure 6-17. Stacking fault interactions following primary creep in PWA 1480+.

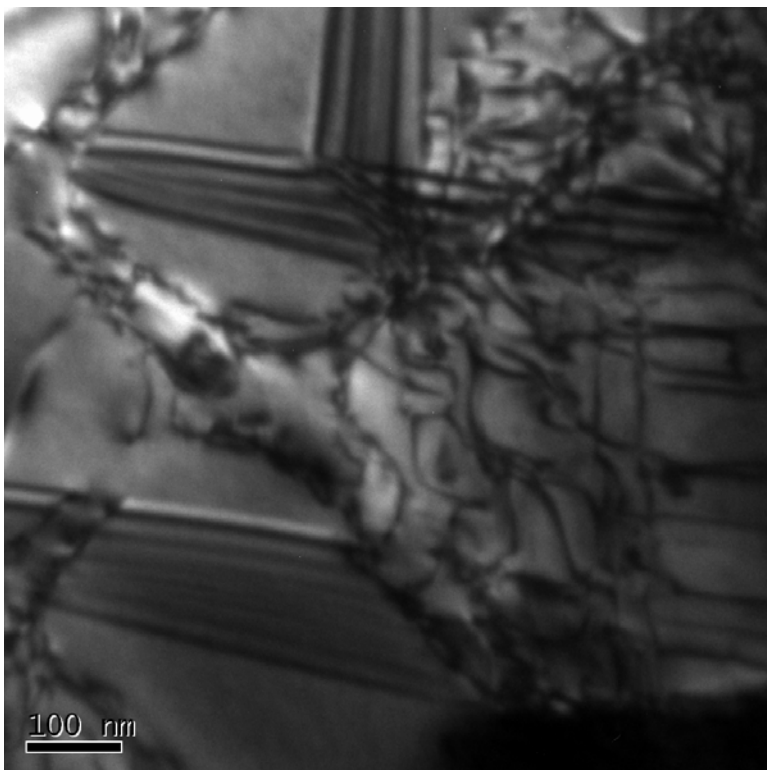


Figure 6-18. Stacking fault interactions and a dislocation network in PWA 1480+.

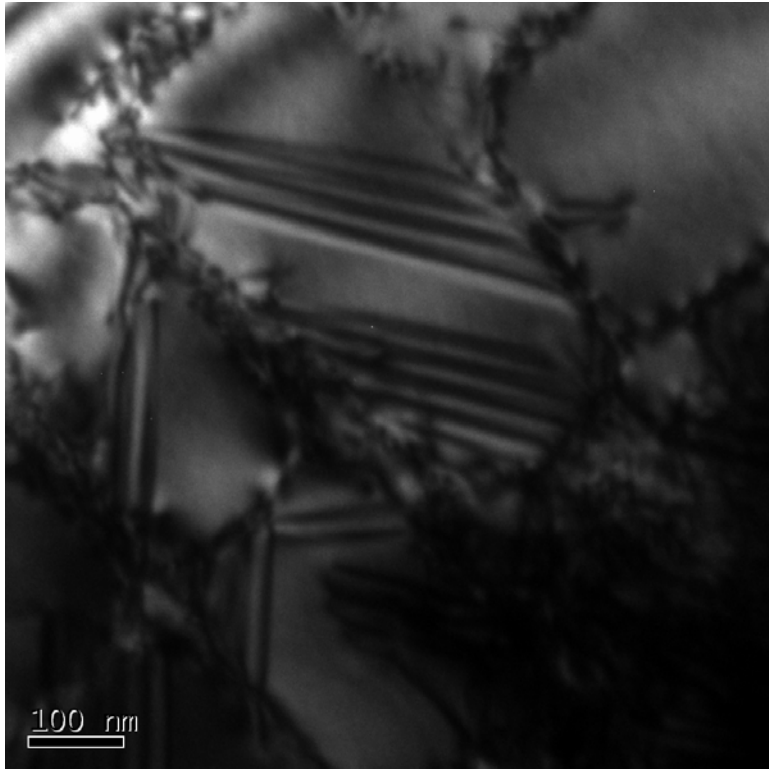


Figure 6-19. Short range stacking fault shear of PWA 1480+.

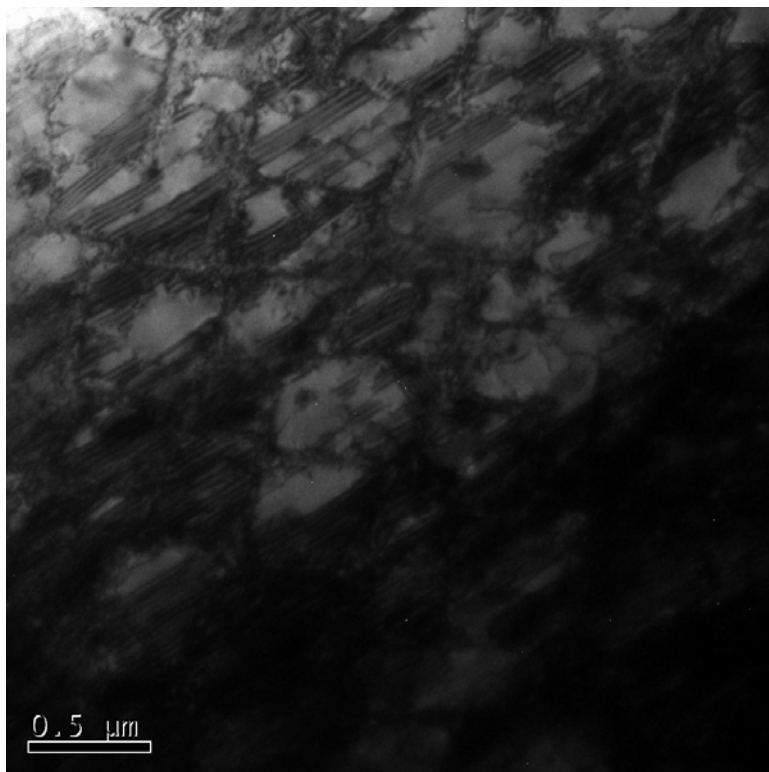


Figure 6-20. Bright field TEM image of PWA 1484 LT (704°C) following interrupted creep. Inhomogeneous deformation by stacking fault shear of the  $\gamma'$  precipitates is apparent.

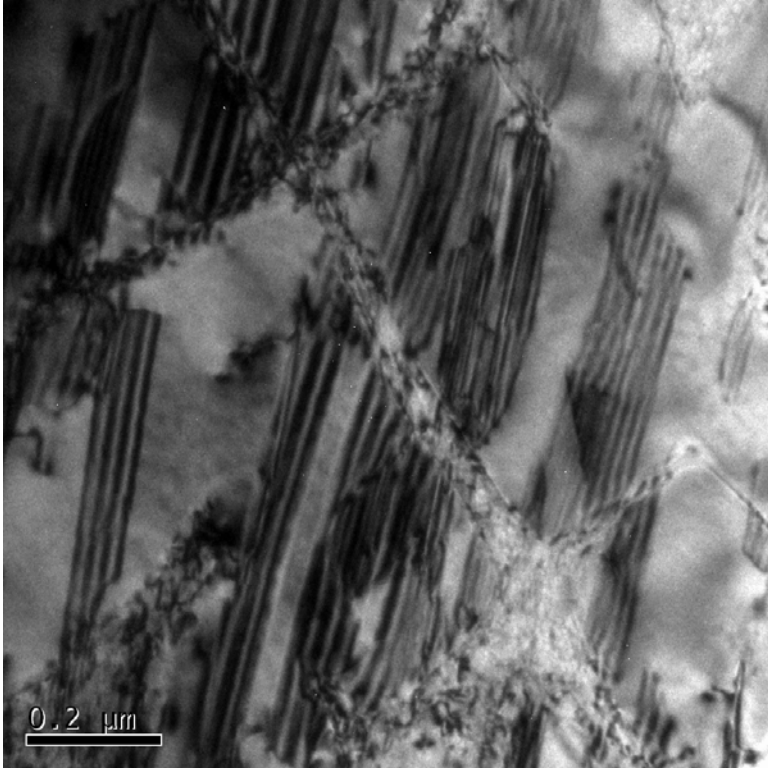


Figure 6-21. Stacking fault shear of  $\gamma'$  precipitates in PWA 1484 (bright field).

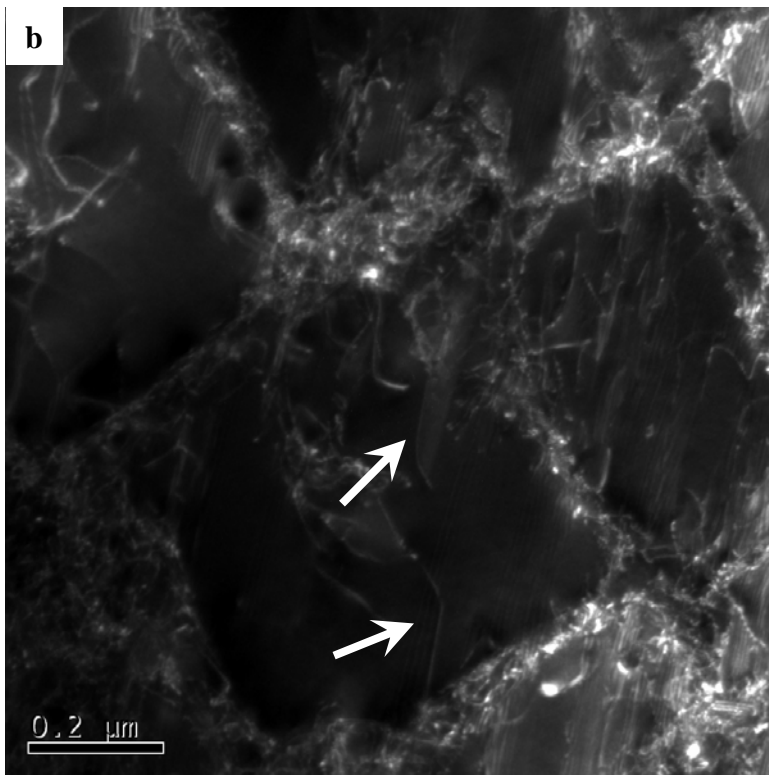
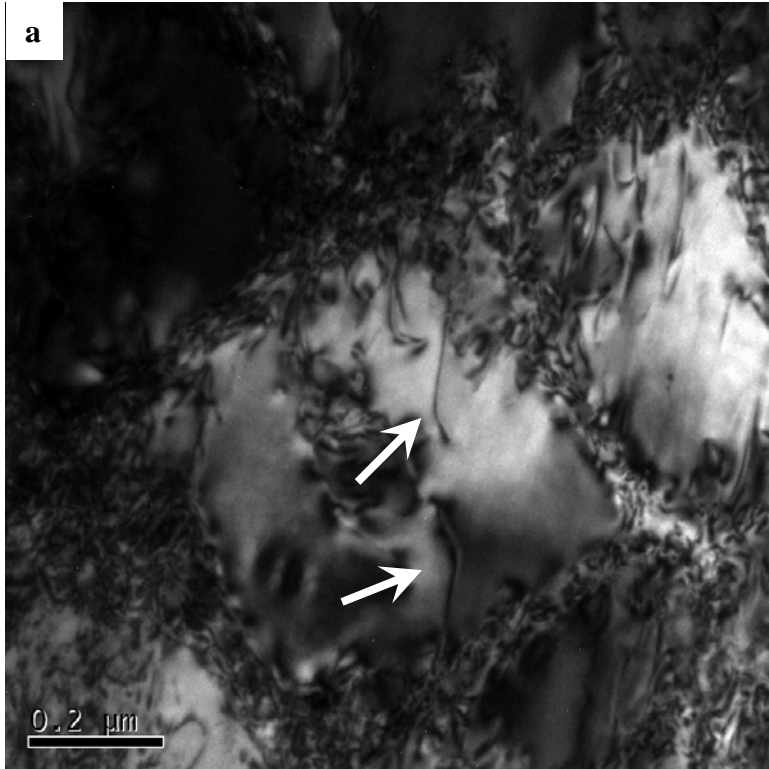


Figure 6-22. Bright field(a)/Dark field(b) pair showing the interfacial dislocation networks present in PWA 1484. Note: stacking fault shear is also present, but out of contrast (marked by arrows).

## CHAPTER 7 RESULTS: ADDITIONAL CHARACTERIZATION

In addition to common metallographic characterization, mechanical testing, and transmission electron microscopy, two additional approaches were used to characterize the three alloys in this investigation. The first is a recently developed method called the Local Electrode Atom Probe (LEAP). This technique improves upon ideas established with the Scanning Atom Probe (SAP) and the 3 Dimensional Atom Probe (3DAP) that were developed in the early 1990's. The LEAP allowed for high resolution compositional characterization in three dimensions and was used to observe the secondary  $\gamma'$  in PWA 1484 as well as the segregation behavior of Re to the  $\gamma$  matrix. The results presented in the LEAP section of this chapter were conducted at the University of North Texas by Anantha Puthicode and Mike Kaufman in conjunction with the University of Florida.

The second characterization method included in this chapter is X-ray diffraction (XRD). X-ray diffraction was used to study the lattice misfit of all three alloys and to observe how misfit changes with heat treatment. Additionally, the data collected by XRD needed to be processed to separate the contributions of the  $\gamma$  and  $\gamma'$  phases that otherwise overlap. This extra step involved deconvolution of the intensity data produced by the (002) and (004) planes within the alloys. Both of these techniques were used in an attempt to gain an understanding of the fundamental differences between the alloys as a result of chemistry and processing.

### **Local Electrode Atom Probe (LEAP)**

The Local Electrode Atom Probe is capable of near atomic resolution in both three dimensional space and mass number. As a result, these instruments are capable of rendering three dimensional representations of the distribution of atoms within a specimen. Due to the relatively recent development of the LEAP, a brief discussion of its operation will be included

below. A full review of the development and capability of the LEAP can be found in (Kelly and Larson, 2000).<sup>52</sup> At its most basic, the LEAP functions by extracting ions (atoms) from a specimen and accelerating the ions towards a detector. With the system highly calibrated, the time of flight of an ion is used to determine the mass and the location of the ion on the detector determines the location in two dimensions of the point of origin for the ion at the tip of the specimen. The third dimension (along the axis of the specimen) is controlled by careful adjustment of the specimen and rate of extraction. A two dimensional side-view schematic of the device is given in Figure 7-1.

As shown in the figure, the specimen is positioned beneath the extraction electrode. The extraction electrode resembles a hollow cone with the tip removed to create an opening at the tip. It is through this opening that the extracted ions are accelerated towards the detector. The secondary electrode is a disk (with a concentric hole in the center) of larger diameter than the base of the extraction electrode. The presence of the secondary electrode is required because the LEAP requires a relatively low extraction potential, thus the ions must be accelerated towards the detector. Additionally, the extraction electrode can be pulsed with a high frequency to control the rate of extraction events.<sup>52</sup>

Specimens for the LEAP take the form of tall narrow cones resembling spikes or needles. These spikes need to be very small in diameter with a tip radius less than 10 to 50 nm. Smaller tip radii aid in focusing the applied field at the tip, improving the ability to extract ions from the specimen. The specimen size utilized for this investigation consisted of a diameter of less than 50 nm and a length (of analyzed volume) of at least 150 nm. The complete method of sample preparation is given in Chapter 3. Creating the specimens, however, involved two stages of electropolishing in order to achieve the dimensions required for the LEAP system, Figure 7-2.

The first step was a “bulk” electrothinning operation that resulted in tip radii between 250 nm and 500 nm. The second step used a small platinum loop to refine the tip to a radius below 50 nm. All LEAP specimens in this investigation are oriented parallel to the [001] direction (also parallel to the applied stress axis). Additionally, the compositions of the individual LEAP specimens may vary slightly based on location. Due to incomplete homogenization, a specimen near a dendrite will be more enriched in Re, Mo, and W and depleted of Al and Ta, while a specimen near the interdendritic region will express the opposite. PWA 1484, however, exhibits relatively little segregation and a large solution heat treatment window so these effects should be small.

Four sets of LEAP specimens were created from a single bar of PWA 1484. The four sections of PWA 1484 received heat treatments to induce changes in the microstructure for observation of secondary  $\gamma'$  and the segregation behavior of rhenium. Two sections received the LT age and two received the HT age. One section from each of the two age heat treated groups was then subjected to another brief solution heat treatment. This extra solution heat treatment was conducted with the goal of quickly dissolving the  $\gamma'$  precipitates but not allowing enough time for the enriched Re layer around the prior  $\gamma'$  interface boundaries time to homogenize. The samples were then quenched rapidly. The goal was to create a condition that would allow the Re shells (or clusters) to be examined by the LEAP method. The results of the LEAP analysis are presented below and separated by heat treatment. It should be noted that a successful analysis of PWA 1484 LT (age heat treatment only) could not be accomplished due to losses during specimen preparation.

## **PWA 1484 LT**

### **Reconstruction (solution HT)**

The first of the LEAP reconstructions is given in Figure 7-3. Figure 7-3a is an 18% aluminum iso-surface and Figure 7-3b is an 18% chromium iso-surface from PWA 1484 LT with the extra solution heat treatment following aging. An iso-surface is a concept used to develop an understanding of the distribution of specific elements within the specimen. In the case of Figure 7-3a, any region with a concentration of at least 18% Al will create a surface that encompasses the region. In this case, the areas that are colored in green are most likely  $\gamma'$  precipitates, while the areas with no color are most likely the  $\gamma$  matrix. The  $\gamma'$  precipitate with its thickness fully contained within the LEAP specimen is potentially a secondary  $\gamma'$  precipitate based on the measured thickness of 75 nm. Primary precipitates, by comparison, in PWA 1484 measure between 300 and 500 nm in thickness. The small, Al-rich regions in Figure 7-3 in the  $\gamma$  matrix between the larger secondary  $\gamma'$  precipitates measure less than 5 nm in diameter. These locations may mark clustering of Al atoms leading to the development of secondary  $\gamma'$  precipitates. Without further characterization, no specific conclusion can be made as to the structure of these regions. Figure 7-3b is an 18% Cr iso-surface. Because Cr partitions more to the  $\gamma$  matrix, the  $\gamma$  phase becomes apparent. It should be noted, however, that the  $\gamma'$  phase still contains a significant Cr concentration and, as a result, blue surfaces appear in the  $\gamma'$  phase as well.

### **Composition profile (solution HT)**

The image in Figure 7-4 is an SEM image of the specimen tip used to create the reconstruction in Figure 7-3. The line along the specimen axis is the direction and length of the analyzed volume for both the reconstruction in Figure 7-3 and for the composition profile in Figure 7-5. The composition profile in Figure 7-5 is very similar in appearance to a composition

line scan that can be produced on an Electron Probe Micro Analysis (EPMA) microscope except with greater accuracy. In actuality, the profile produced by the leap is created from a cylinder of user defined length, diameter, and orientation within the collected data. This cylinder can be oriented parallel to the axis of the specimen or perpendicular to the specimen or at any other angle that is deemed useful. In the case of the profile in Figure 7-5, the cylinder of analyzed volume was oriented within the center of the specimen (concentric) and parallel to the long axis.

From the compositional profile, it can be seen that fine  $\gamma'$  precipitates are present between the distances of 20 and 95 nm and 125 and 170 nm. Studying the profile reveals several distinct partitioning behaviors among the elements added to PWA 1484. First, aluminum and tantalum partition strongly to the  $\gamma'$  phase. As a result, the composition of these elements is much greater in the  $\gamma'$  phase than in the  $\gamma$  matrix. Additionally, it can be seen that Al partitions so strongly to the  $\gamma'$  phase that a significant depletion of Al exists for the  $\gamma$  matrix in the vicinity of the  $\gamma'$  precipitate. The second behavior of interest results from those elements that partition to the  $\gamma$  matrix. These elements are rhenium, molybdenum, chromium, and cobalt. Rhenium and chromium appear to partition the most to the  $\gamma$  phase with a slight enrichment layer on the  $\gamma$  side of the  $\gamma/\gamma'$  interface. Molybdenum only slightly partitions to the  $\gamma$  phase as it expresses significant solubility in both the  $\gamma$  and  $\gamma'$  phases. The third behavior is exhibited by tungsten. Tungsten does not partition particularly strong to either phase and, as a result, maintains relatively uniform composition throughout the analyzed volume. This behavior is interesting as previous research has indicated that W additions enable increased Re solubility in the  $\gamma'$  phase.<sup>35</sup> If W does not partition strongly to the  $\gamma$  phase like the other solid solution strengtheners, then a significant portion of the added W is present in the  $\gamma'$  phase. This allows for the possibility that W additions

increase the average lattice parameter in the  $\gamma'$  resulting in a synergistic effect between W and Re.

## **PWA 1484 HT**

### **Reconstruction (age HT)**

The next reconstruction is presented in Figure 7-6 for a PWA 1484 HT specimen in the age heat treated condition. This reconstruction is an example with all of the recorded ions present. Each ion species is recorded as a different color dot placed within the volume at its place of origin. Figure 7-7 is another iso-surface construction to illustrate the partitioning behavior of Cr (Figure 7-7a) and Al (Figure 7-7b). From these figures it is apparent that the lower phase is most likely  $\gamma'$  due to the high Al concentration. The upper phase is most likely  $\gamma$ . No fine precipitates were observed for this specimen, however, it should be noted that only 30 nm in the length of the specimen were analyzed due to excessive specimen thickness.

### **Composition profile (age HT)**

The composition profile given in Figure 7-8 was produced from the analyzed volume presented in the reconstruction in Figure 7-6. This profile is similar in nature to the one in Figure 7-5 except for a higher scale on the composition axis to allow for the Ni profile. Based on the composition profiles it is apparent that the  $\gamma$  phase is present over the distances 0 to 20 nm and the  $\gamma'$  phase is present over the distances 20 to 30 nm. All of the partitioning behaviors discussed above are present with the addition Ni partitioning to the  $\gamma'$  phase (due to the  $\text{Ni}_3\text{Al}$  formula). Unfortunately, few conclusions can be drawn from this specimen due to the small volume that was analyzed. Additionally, significant enrichment and/or depletion were not observed with this specimen.

### **Reconstruction (solution HT)**

The final reconstruction was produced with a PWA 1484 HT specimen exposed to the extra solution heat treatment following aging. The two images in Figure 7-9 are two different views of the same reconstruction. Figure 7-9 is an 18% Al iso-surface, again coloring regions of  $\gamma'$  green. The  $\gamma'$  precipitates all appear to be secondary  $\gamma'$  with thicknesses of 20 nm or less (except for the relatively large precipitate in the bottom corner). Additionally, as with Figure 7-3, there are many small aluminum rich regions of less than 5 nm in thickness. Again, it is difficult to conclude if these are ultra-fine  $\gamma'$  precipitates or just Al rich clusters that are precursors to  $\gamma'$  precipitate formation. Another representation of the same reconstruction is provided in Figure 7-10. Here only the Al, Ta, Cr, and Mo ions are displayed. Because Al and Ta partition to the  $\gamma'$  phase and Cr and Mo partition to the  $\gamma$  phase, the contrast between the two phases is still evident. From both Figure 7-3 and Figure 7-9, it is apparent that PWA 1484 is capable of producing secondary  $\gamma'$  precipitates. It has already been shown that PWA 1480 and PWA 1480+ are capable as well via SEM techniques, Chapter 4.

### **Composition profile (solution HT)**

Finally, Figure 7-11 is a composition profile generated from the reconstruction in Figure 7-9. Figure 7-12 illustrates the location and orientation of the cylinder of material selected to produce the composition profile. This region spans two secondary  $\gamma'$  precipitates between the distances 8 and 15 nm and 36 and 47 nm. The measured thickness of these two precipitates is then 7 and 11 nm, respectively. Slight local enrichment by Re and depletion of Al in the  $\gamma$  matrix in the vicinity of the 7 nm precipitate can be seen on the profile. Additionally, the partitioning behaviors already discussed were also present for the PWA 1484 HT (solution HT) specimen as expected.

## Secondary $\gamma'$ Concentrations

One benefit of the LEAP system is the ability to determine the concentrations of the secondary  $\gamma'$  precipitates. These concentrations were determined from the “line” scan data generated with cylinders of data selected from the reconstructions. Of the most interest to the current investigation are the differences in secondary  $\gamma'$  concentration as a function of precipitate size (thickness). These precipitate composition data were collected from the composition profiles in Figures 7-5, 7-8, and 7-11. Contained within these profiles are the entire thicknesses of 3  $\gamma'$  precipitates and partial thicknesses of 2  $\gamma'$  precipitates. The compositions, listed in order of thickness, are given in Table 7-1. The aluminum concentration is similar in all five precipitates (roughly 18 wt%). The elements chromium, molybdenum, and tungsten were also maintained at the same composition regardless of precipitate size (approximately 2wt% for Cr, 3wt% for Mo, and 3wt% for W). The elements nickel, cobalt, tantalum, and rhenium, however, all varied with precipitate size. As the  $\gamma'$  precipitates increased in size, the concentrations of Ni and Ta increased while the concentrations of Co and Re decreased. The relative changes in composition for these four elements are given in Table 7-2. Compared to the smallest  $\gamma'$  precipitate, the largest precipitate (in this set of measurements) exhibited an increase in Ni concentration of 10wt%, an increase in Ta concentration of nearly 5wt%, a decrease in Co concentration of 7wt%, and a decrease in Re concentration of nearly 2wt%. These results appear to be consistent with normal precipitate coarsening behavior. As the precipitate grows, the concentration of the  $\gamma'$  formers would be expected to grow (Ni and Ta) while the elements that are rejected from the  $\gamma'$  phase would be expected to decrease in concentration (Co and Re). The elements Cr, Mo, and W, however, do not display this behavior as they maintain uniform composition with precipitate size.

## X-Ray Diffraction (XRD)

The X-ray diffraction study was initiated to determine the lattice misfit of the three alloys in this investigation: PWA 1480, PWA 1480+, and PWA 1484. Sections were taken from the single crystal bars of each alloy and heat treated to 4 hr., 10 hr., 100 hr., and 1000 hr. at 1080°C. This temperature was selected as a continuation of the coating heat treatment cycle that these alloys were subjected to prior to service which is consistent with experimental procedures utilizing over-aging heat treatments between 950°C and 1100°C used in other sources.<sup>27, 59-62</sup> Additionally, this temperature was selected, rather than the LT or HT age temperature, because the higher temperature allows faster coarsening and a better approximation of the equilibrium structure after 1000 hours.

Following the over-aging heat treatments, the specimens were thinned and polished to produce the best results. Upon recording the intensity data, peak deconvolution was employed to differentiate the contributions of the  $\gamma$  and  $\gamma'$  phases in agreement with other sources working with nickel base superalloys.<sup>46, 59</sup> Figure 7-13 illustrates the deconvolution process. Two peaks are assigned to both phases creating a total of 4 peaks. The two peaks for each phase represent the Cu  $k_{\alpha 1}$  and Cu  $k_{\alpha 2}$  wavelengths of X-ray radiation to which the specimens were exposed. Due to the slight difference in wavelength between the two, the diffracted peak produced by each is slightly displaced. This effect necessitates the separation of both wavelengths for each phase accounted for in a given peak. The MDI Jade (ver. 7) software is programmed to account for the difference in Cu  $k_{\alpha 1}$  and Cu  $k_{\alpha 2}$  radiation and is calibrated to the diffractometer. Creating four peaks from the original is a mathematic operation and takes place utilizing an iterative algorithm. Upon completion of a deconvolution routine, a report is generated detailing critical information about the peaks and the fit of the model. These reports have been included in full in Appendix

B. Repeated deconvolution of the same data set does not guarantee the same result every time. Depending on the selected starting conditions and the choices made among seven peak fit options, these results can vary. As a result, it is critical that each report is observed to verify if the model is useful or if it has strayed too far from the expected result. An example of this is Figure B-57 in which the contribution of the  $\gamma$  phase has been almost entirely eliminated due to the ability of the  $\gamma'$  phase to fit the original intensity data without any further contribution by the  $\gamma$  phase. In this case, the deconvolution was repeated producing Figure B-59. Due to these concerns, repeated deconvolution was necessary to generate accurate predictions that could be averaged to produce a valid lattice parameter measurement.

The results of the deconvolution procedures were then processed using a spreadsheet to calculate the lattice parameters and lattice misfit values from each of the alloys. These calculations are also presented in Appendix B. The results presented here are the most reliable data from the deconvolution process. The lattice misfit of the three alloys was found for the 4 hr., 10 hr., and 1000 hr. specimens. The 100 hour specimens produced low peak intensities and were not useful for deconvolution and subsequent misfit calculation. The calculated lattice parameters for the (002) plane are provided in Table 7-3. These results are also plotted in Figure 7-14 along with the limited results from the (004) plane. From observation of Figure 7-14, it is apparent that PWA 1484 has the largest, negative misfit value of the three alloys. This is expected as PWA 1484 contains more solid solution strengtheners that partition strongly to the  $\gamma$  matrix, including Re which is known to partition to the  $\gamma$  phase particularly potently. The lattice misfit of PWA 1480, however, varies on the slightly negative side of zero. The magnitude of the misfit of PWA 1480 is low (less than 0.15%). The addition of Re to PWA 1480 resulted in a

continually decreasing (from positive to negative, but increasing in magnitude) lattice misfit from an initially positive value of +0.034% to a final value of -0.114%.

The results from the (004) plane were more difficult to obtain due to the lower intensity produced through diffraction. As a result, fewer specimens yielded strong enough intensity measurements over the  $2\theta$  range  $117^\circ$  to  $120^\circ$ . For this reason, fewer results are reported for the (004) plane in Figure 7-14. Additionally, the greater spacing achieved at this high angle proved more difficult for the deconvolution process. Increased difficulty in data acquisition coupled with decreased analysis accuracy resulted in fewer reportable results. The results shown in Figure 7-14 consistently indicated more positive values for lattice misfit for all three alloys. PWA 1480, for instance, is calculated to have a positive misfit of roughly the same magnitude that was calculated from the (002) data. PWA 1480+ is also shown to have positive misfit of the same range in magnitude. Finally, the (004) result for PWA 1484 after 1000 hours is over 0.1% more positive representing greater than 50% difference in calculated misfit values from the same specimen. The result of these inconsistencies is an apparent need to continue examining the lattice misfit of these alloys. Alternative methods (TEM based) also likely need to be employed to verify the results from the XRD deconvolution process.

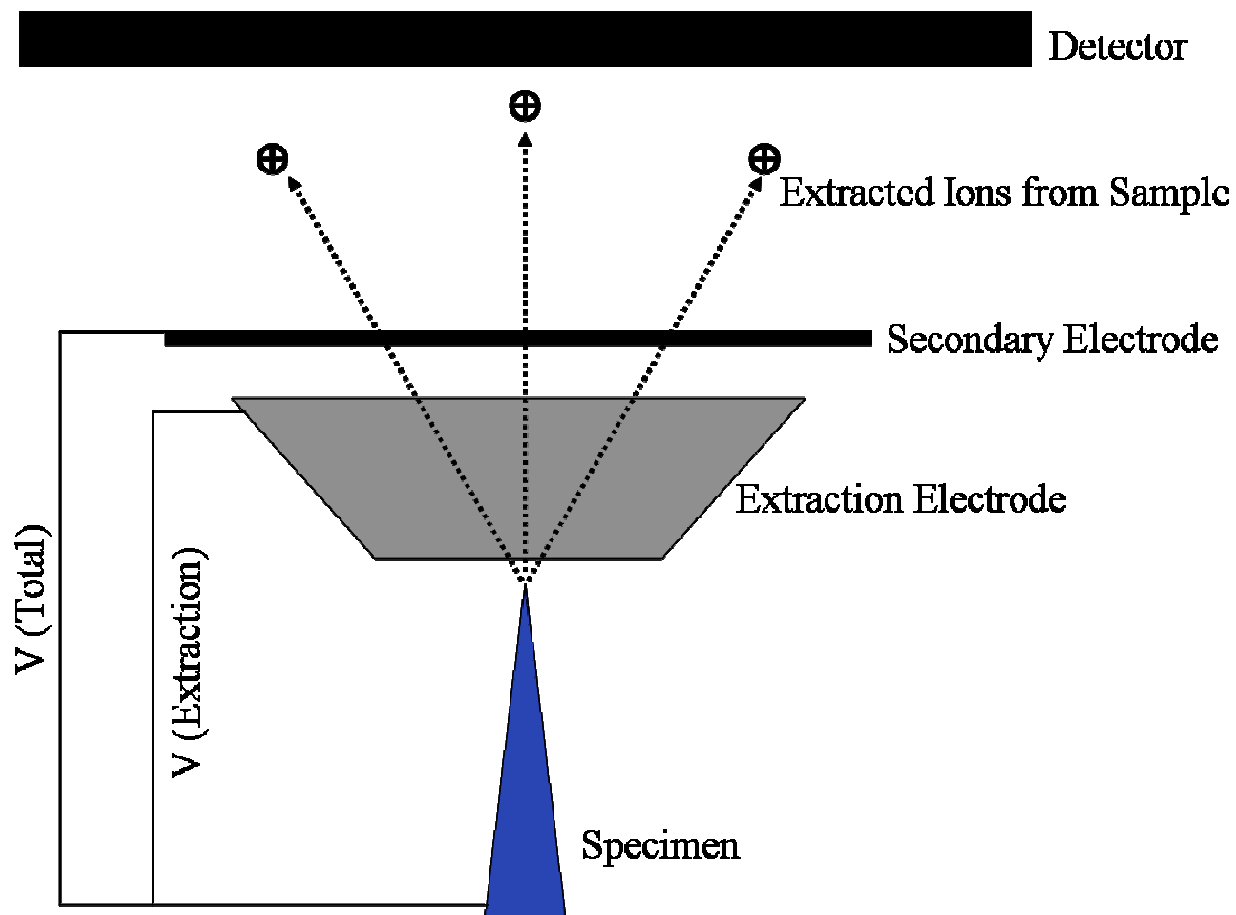


Figure 7-1. Schematic illustrating the basic function of the LEAP system. The specimen is positioned beneath the cone of the extractor anode and ions are extracted using a pulsing voltage. The ions are then accelerated towards the detector by a secondary electrode.<sup>52</sup>

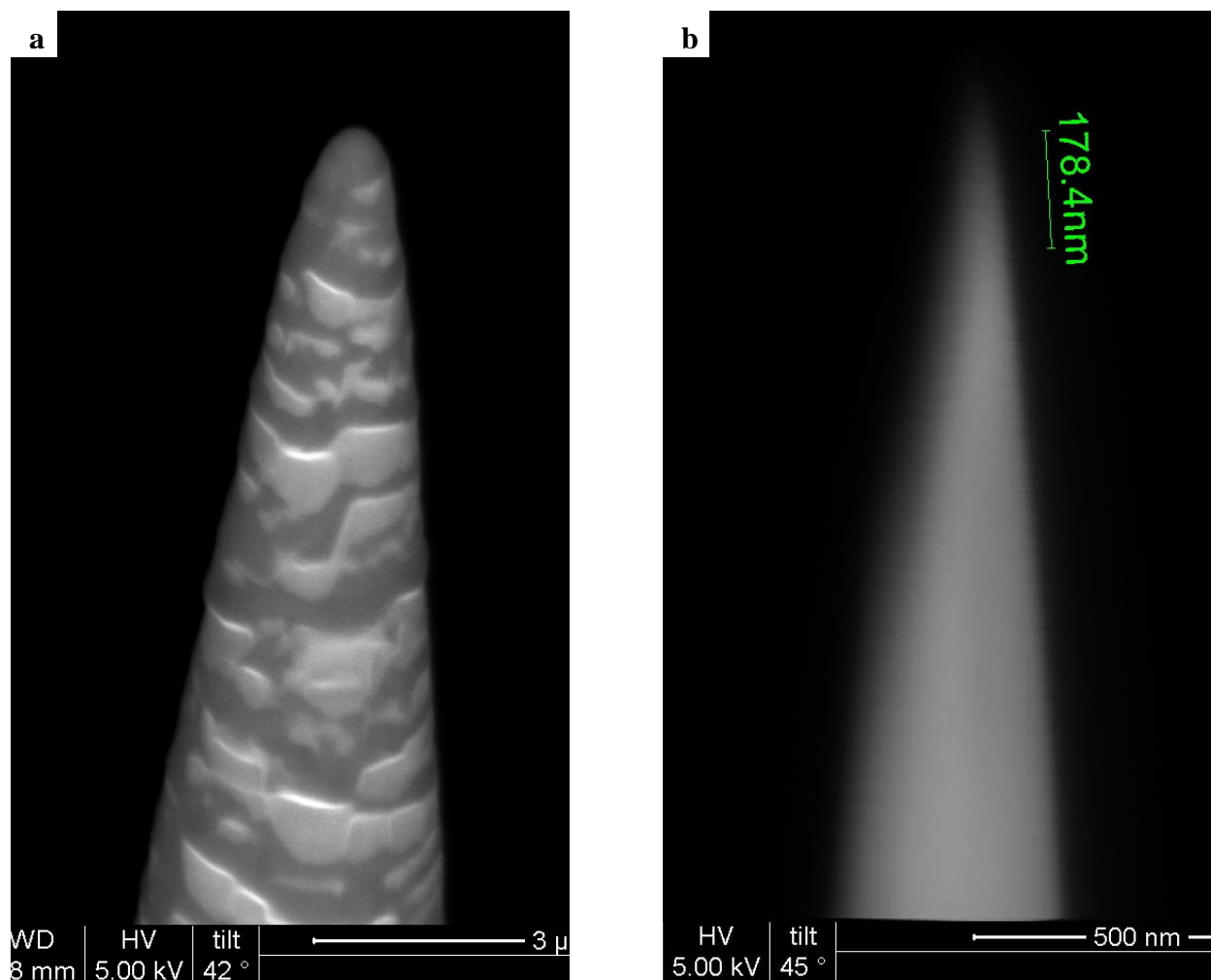


Figure 7-2. LEAP specimens before, (a), and after, (b), the final polishing step with the Imago Electropointer.

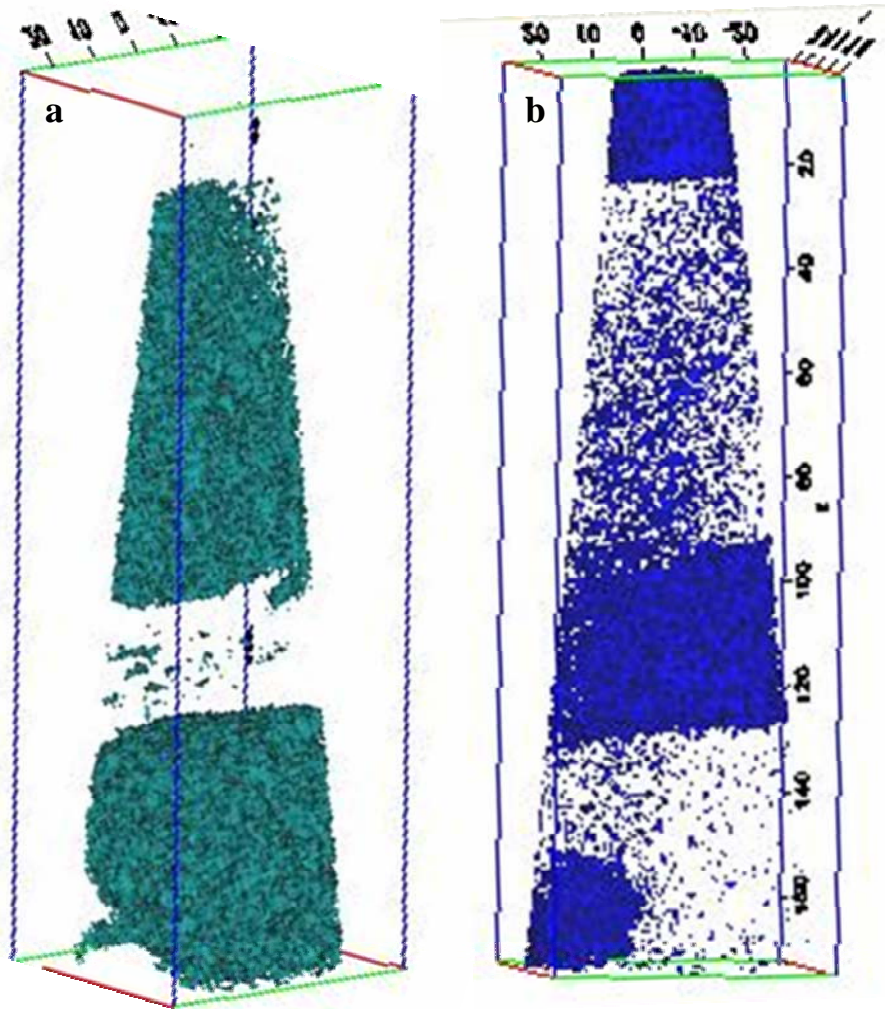


Figure 7-3. Iso surfaces created with the LEAP system (PWA 1484 LT with solution HT). (a) 18% Aluminum surface, (b) 18% Chromium surface.

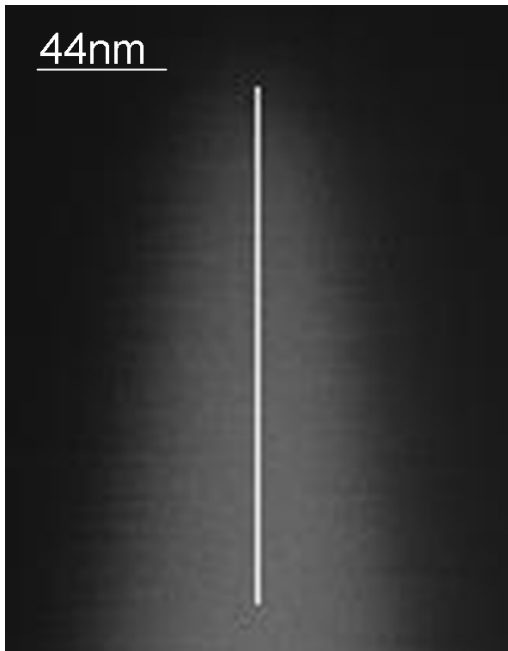


Figure 7-4. Magnified (SEM) view of the tip analyzed in Figure 7-3.

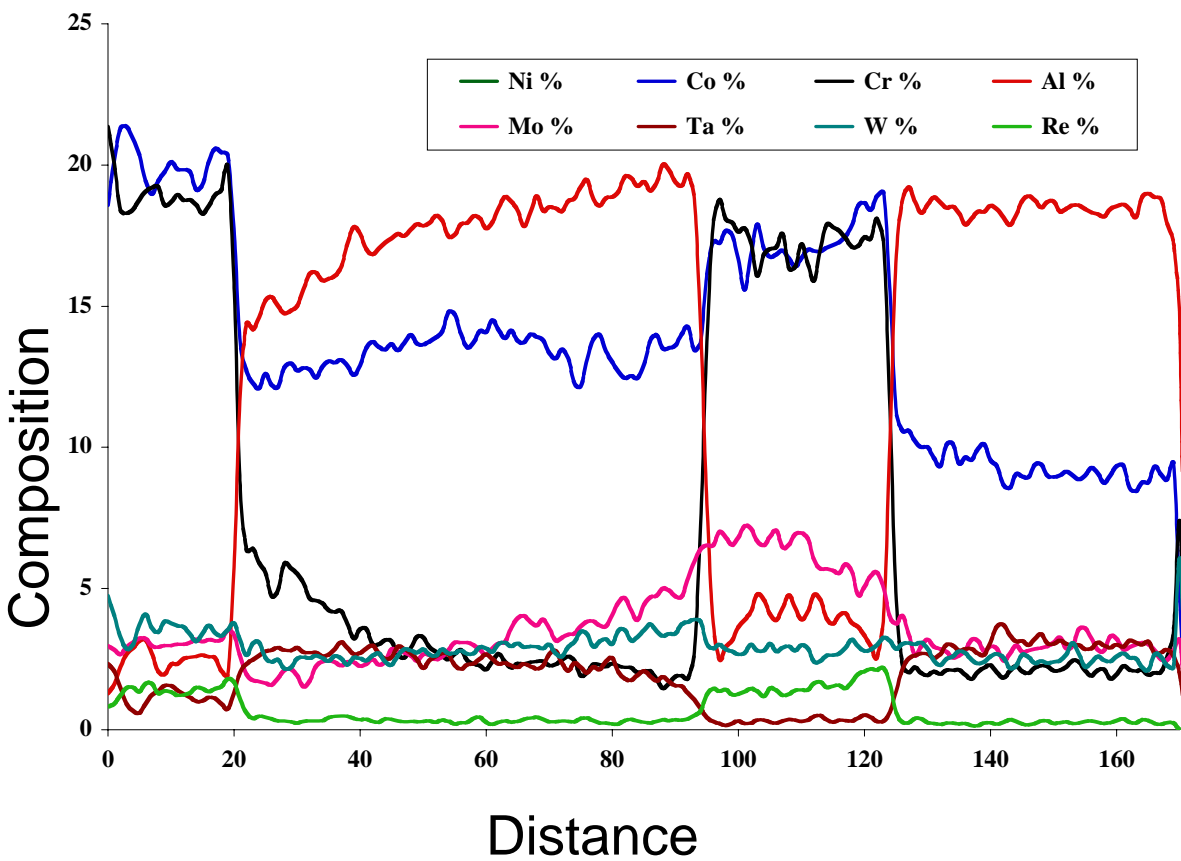


Figure 7-5. Composition profile from the specimen in Figure 7-3 (PWA 1484 LT with solution HT). Fine  $\gamma'$  precipitates are present at distances between 20 and 95 nm and between 125 and 170 nm (Corresponds with Figure 7-3a).

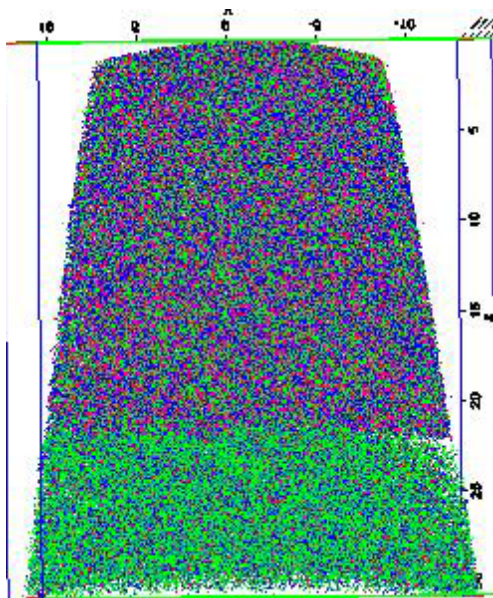


Figure 7-6. The distribution of all recorded ions for PWA 1484 HT with no additional solution heat treatment.

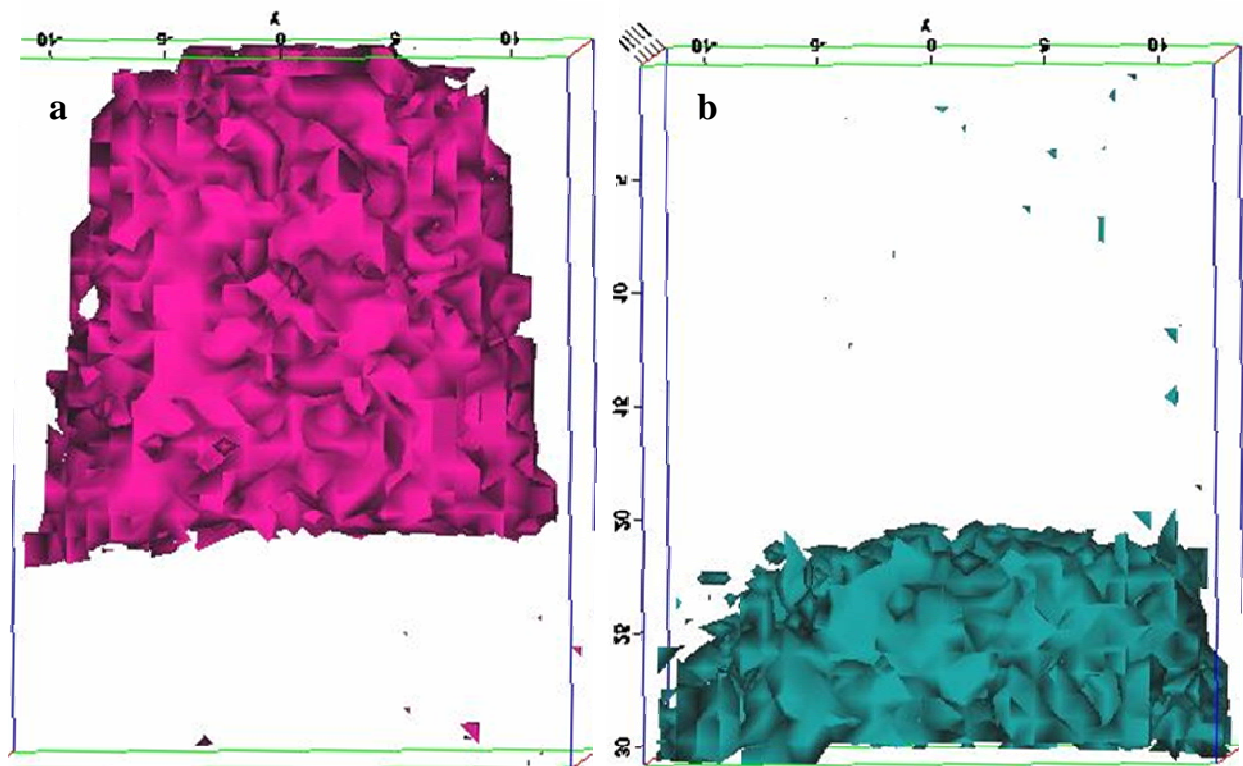


Figure 7-7. Iso surfaces created with the LEAP system (PWA 1484 HT no solution HT). (a) 18% Chromium surface, (b) 18% Aluminum surface. These results are from the same specimen shown in Figure 7-6.

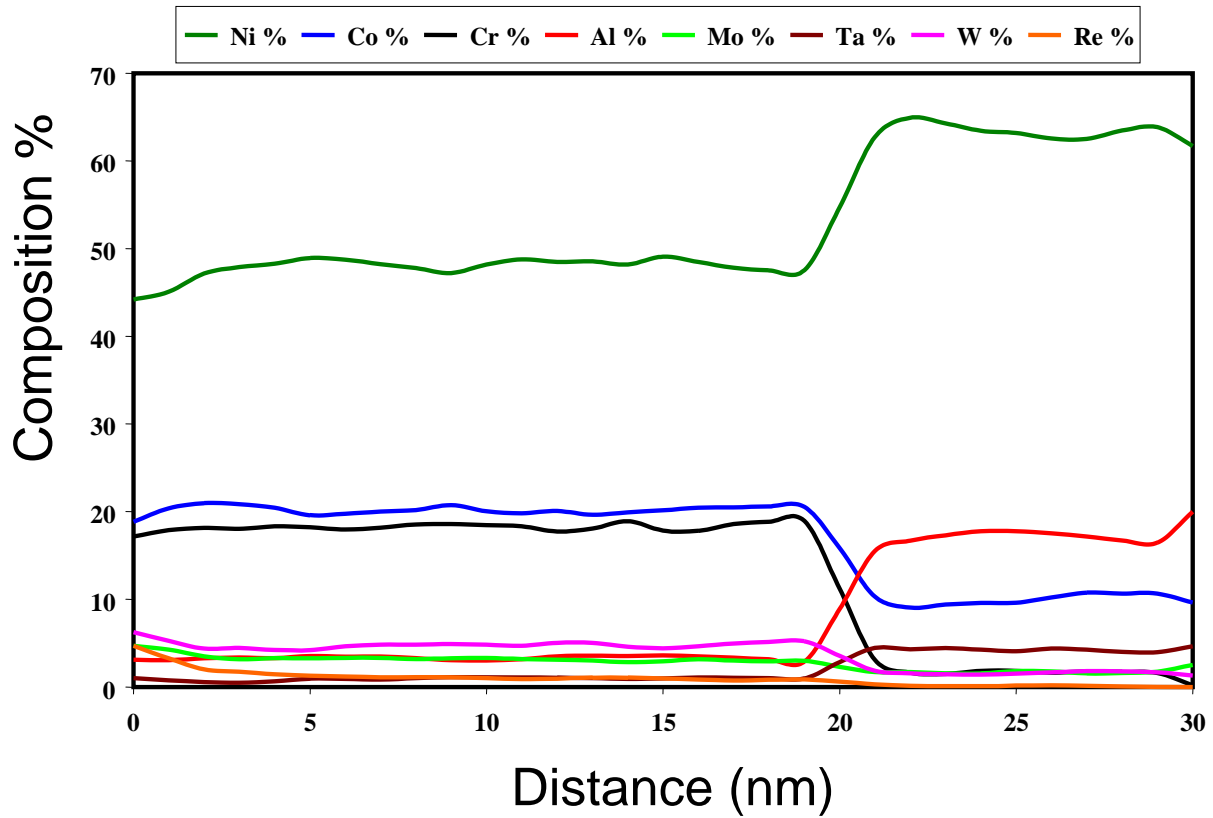


Figure 7-8. Composition profile from the specimen in Figure 7-7 (PWA 1484 HT no solution HT). A primary  $\gamma'$  precipitate is present at distances between 20 nm and 30 nm (corresponds with Figure 7-7a)

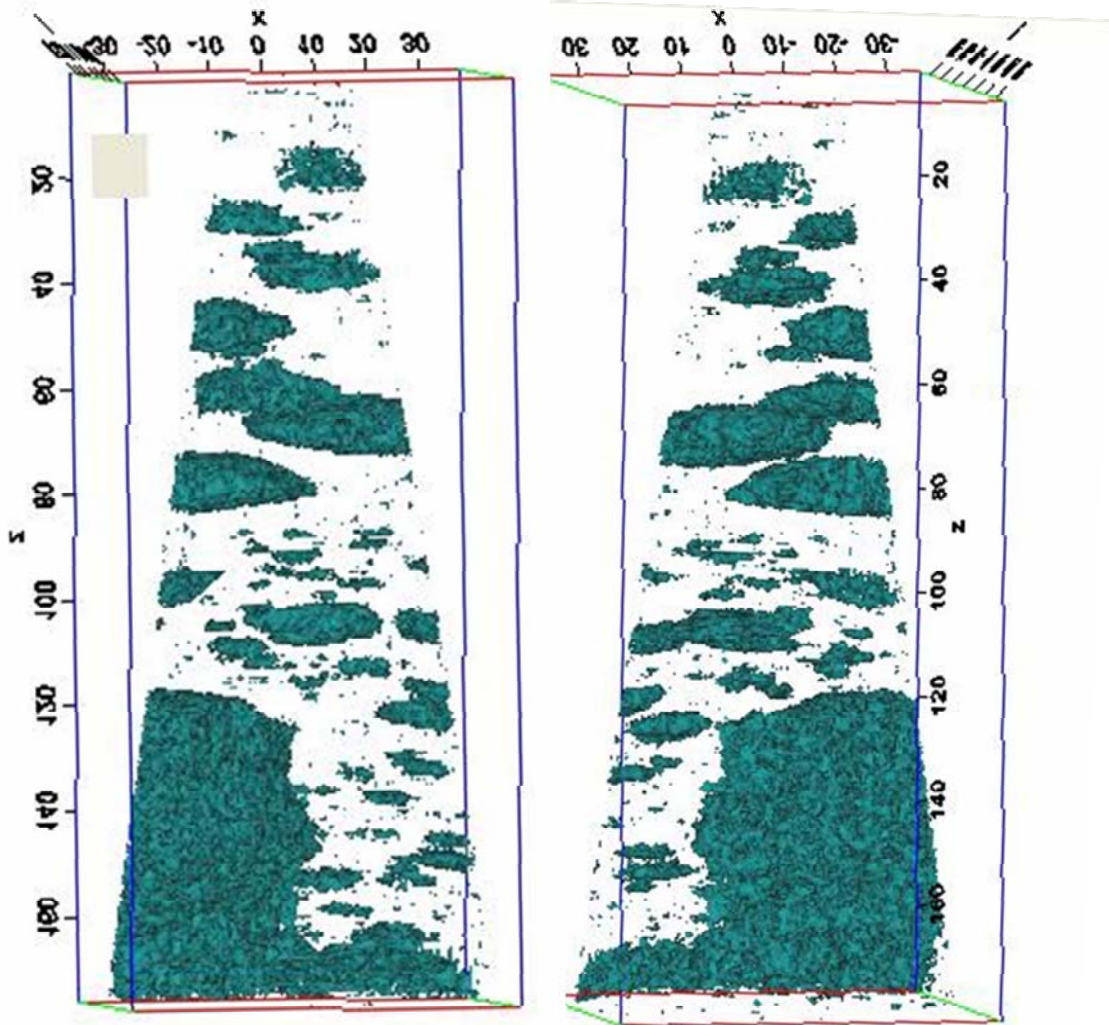


Figure 7-9. Iso surface (18% Aluminum) created with the LEAP system (PWA 1484 HT with solution HT). Secondary  $\gamma'$  precipitates are apparent in the  $\gamma$  matrix.

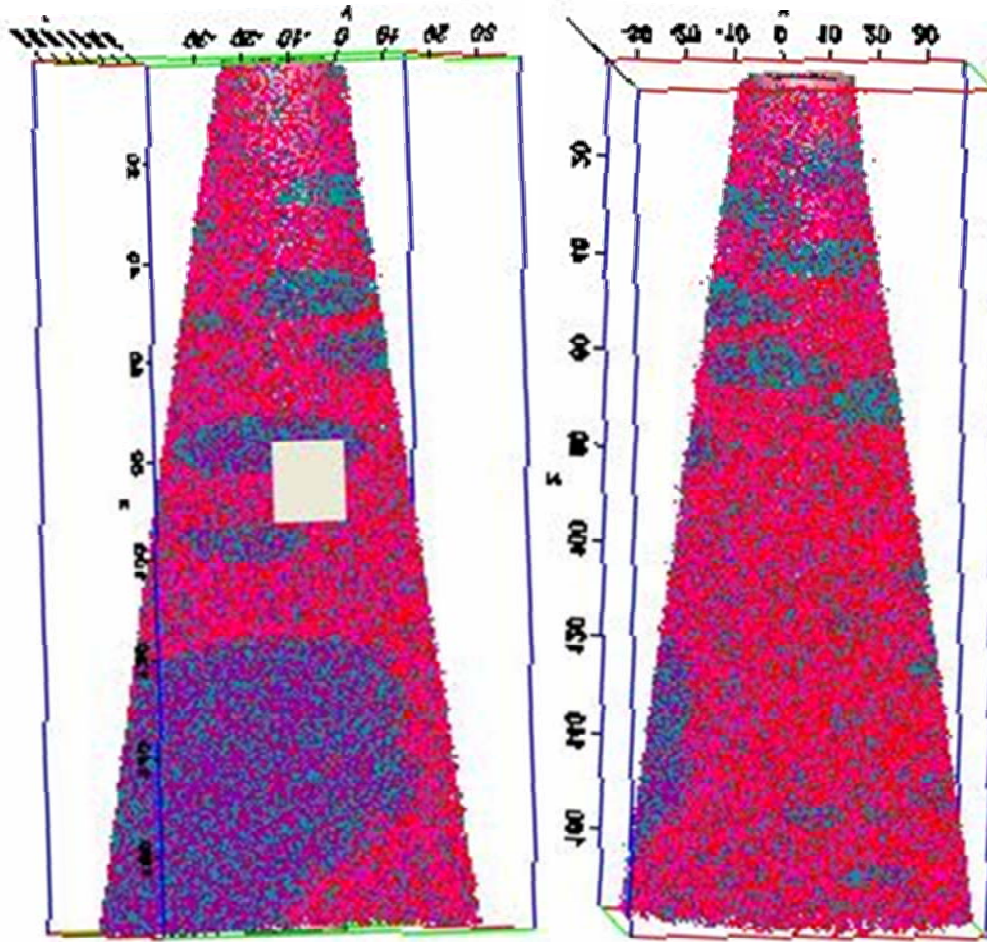


Figure 7-10. LEAP results with only Al, Ta, Cr, and Mo ions represented (PWA 1484 HT with solution HT). The results shown here are from the same specimen reported in Figure 7-9.

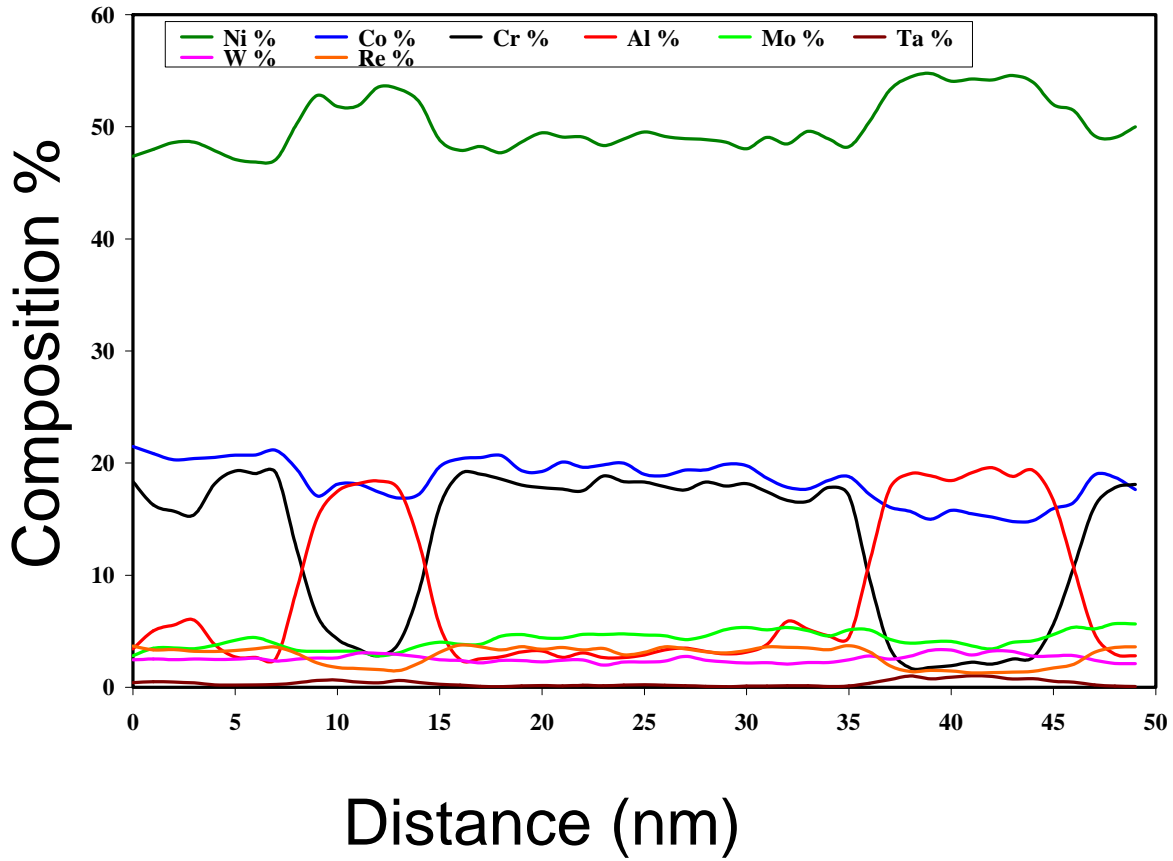


Figure 7-11. Composition profile from the specimen in Figures 7-9 and 7-10 (PWA 1484 HT with solution HT). An illustration of the volume of material used for this composition profile is given in Figure 7-12.

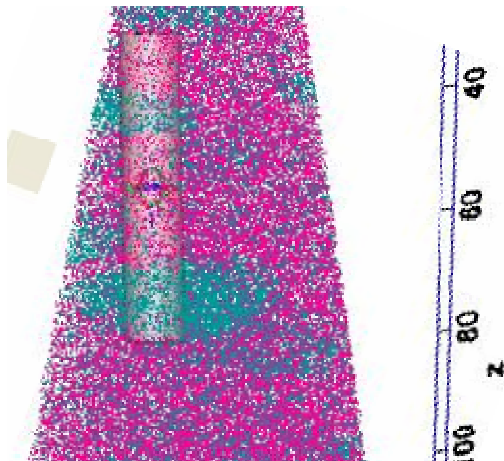


Figure 7-12. Illustration of the data selected for the compositional profile shown in Figure 7-11. The cylinder is user selected and only the data contained within this region is counted in the profile.

Table 7-1. Composition (wt%) of secondary  $\gamma'$  precipitates of varying diameter in PWA 1484.

Diameter: 6nm							
Ni	Co	Cr	Al	Mo	Ta	W	Re
53	17	3	18	3	<1	3	2
Diameter: 11nm							
Ni	Co	Cr	Al	Mo	Ta	W	Re
54	16	2	19	4	1	3	1
Diameter: 74nm							
Ni	Co	Cr	Al	Mo	Ta	W	Re
58	14	2	18	3	2	3	<1
Diameter: 46+nm							
Ni	Co	Cr	Al	Mo	Ta	W	Re
62	9	2	18	3	3	3	<1
Diameter: 10+nm							
Ni	Co	Cr	Al	Mo	Ta	W	Re
63	10	2	18	2	5	2	<1

Table 7-2. Net changes in secondary  $\gamma'$  concentration with increasing precipitate size.

Particle size (nm):		6	11	74	46+	10+	Net Change (wt%)	% change
Composition (wt%)	Nickel	53	54	58	62	63	+10	+19
	Cobalt	17	16	14	9	10	-7	-41
	Tantalum	<1	1	2	3	5	+5	+1000
	Rhenium	2	1	<1	<1	<1	-2	-75

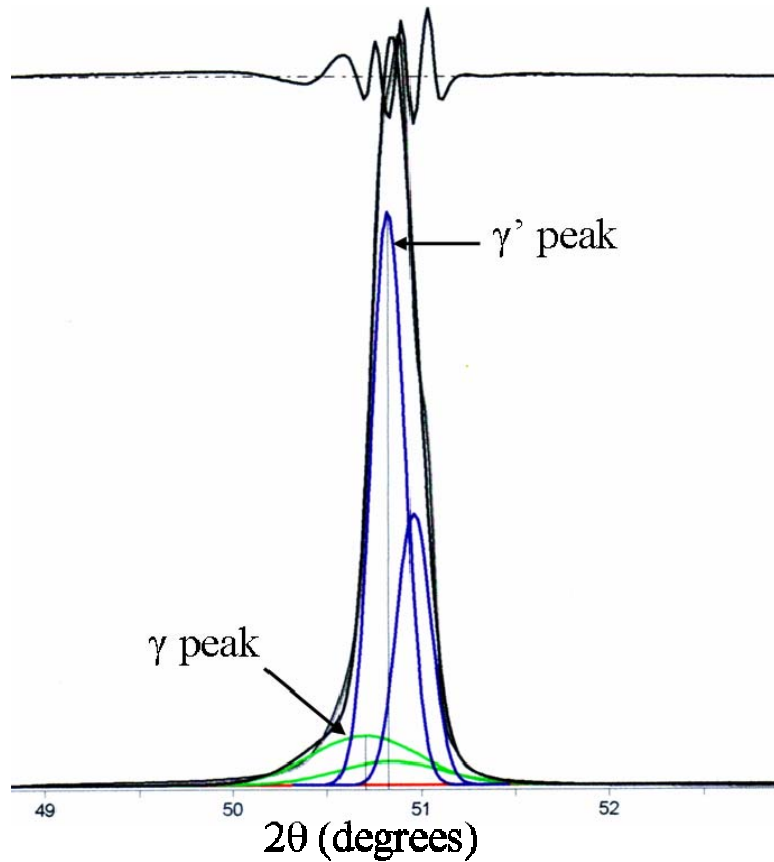


Figure 7-13. An example of the deconvolution process used to separate the contributions of the  $\gamma$  and  $\gamma'$  phases. Notice, both phases have two peaks associated with them from the  $\text{Cu } k_{\alpha 1}$  and  $\text{Cu } k_{\alpha 2}$  wavelengths.

Table 7-3. Lattice misfit (%) for the (002) plane following heat treatments at 1080°C.

	Heat treatment time at 1080 C		
	4 hr.	10 hr.	1000 hr.
PWA 1480	-0.075	+0.002	-0.138
PWA 1480+	+0.034	-0.052	-0.114
PWA 1484	-0.228	-0.251	-0.201

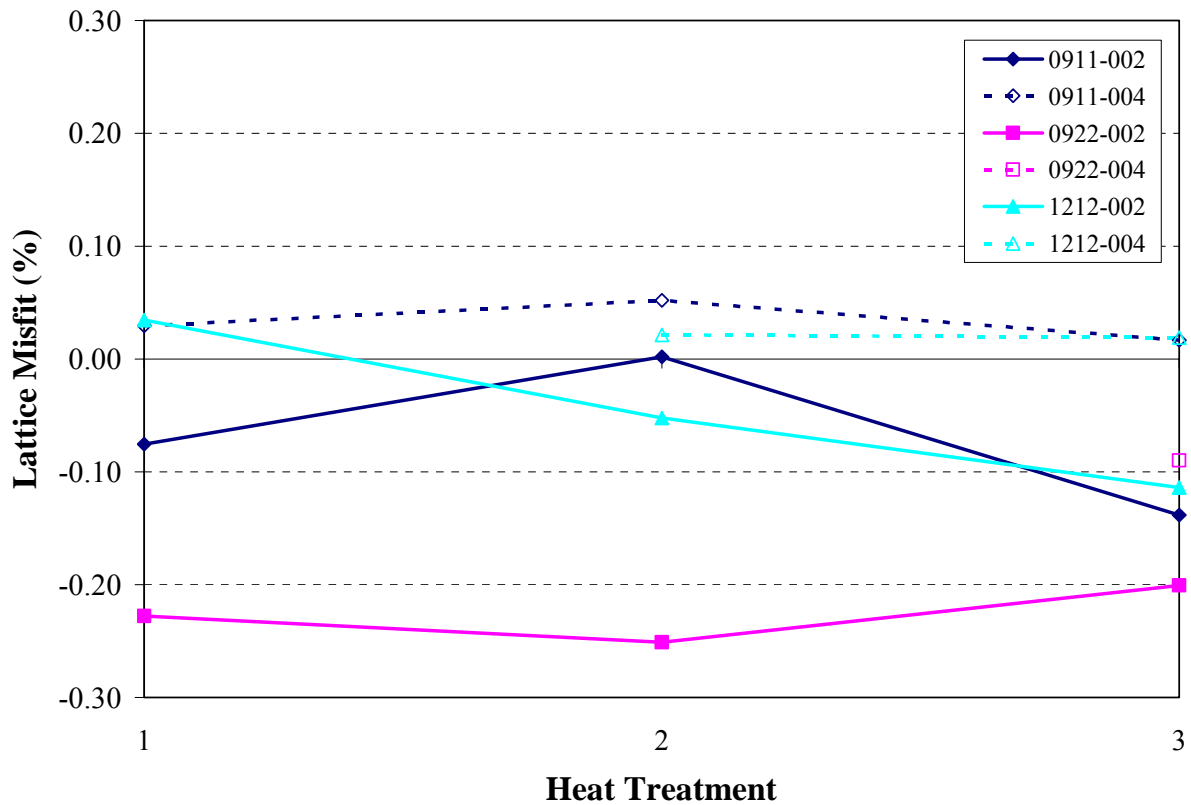


Figure 7-14. Lattice misfit vs. heat treatment from measurements of both the (002) and (004) peaks. Note: The heat treatments for each point are given by numbers (1: 4 hr. at 1080°C, 2: 10 hr. at 1080°C, and 3: 1000 hr. at 1080°C). The 100 hr. at 1080°C heat treatment is not shown due to the unreliable nature of the data produced from samples given the 100 hour heat treatment. Also the sample names are as follows: 0911 is PWA 1480, 0922 is PWA 1484, and 1212 is PWA 1480+.

## CHAPTER 8 DISCUSSION

Through the course of the investigation into the primary creep behavior of PWA 1480 and PWA 1484 several relationships between processing and creep behavior were observed. The composition and processing an alloy has received plays a vital role in determining the nature of the creep behavior that should be expected. Numerous studies have been performed to incorporate the many inherent differences in microstructure into a material based modeling scheme. The following list includes several material conditions that are impacted by chemistry and/or processing often included in creep models:

- Stacking fault energy (both  $\gamma$  and  $\gamma'$  phases)<sup>13, 63, 64</sup>
- Anti-phase boundary energy ( $\gamma'$  phase only)<sup>13, 63, 64</sup>
- $\gamma/\gamma'$  morphology
  - Precipitate dimensions and distributions<sup>21, 23, 63</sup>
  - The absence/presence of secondary  $\gamma'$  precipitates<sup>16, 20</sup>
  - $\gamma'$  volume fraction<sup>63, 65</sup>
  - $\gamma$  channel thickness<sup>66, 67</sup>
  - $\gamma'$  composition (relates to the strength of the  $\gamma'$  phase)<sup>11, 68, 69</sup>
  - $\gamma$  composition (relates to the strength of the  $\gamma$  phase)<sup>10, 11, 68, 69</sup>
  - Microstructural stability ( $\gamma'$  coarsening, rafting)<sup>38, 70-73</sup>
- Chemistry effects
  - Segregation (eg. Re segregation to the  $\gamma$  matrix)<sup>10, 11</sup>
  - Short range order (eg. presence of DO<sub>22</sub> ordered clusters of W and/or Cr)<sup>69</sup>
  - Formation of secondary phases (carbides and TCP phases)<sup>35, 38</sup>
- Active deformation mechanism
  - Dislocation shear of the matrix<sup>21, 74</sup>
  - Stacking fault shear of the  $\gamma'$  phase<sup>12, 13, 16, 17, 23, 64</sup>
  - Mixed-mode deformation<sup>63</sup>

Each of the above points can impact the behavior of a single crystal superalloy during creep. Consequently, it is necessary to investigate any relationships that may exist between these material attributes in order to simplify any models that are derived. The current investigation represents an attempt to understand the effect of secondary  $\gamma'$  precipitates and the element rhenium on the primary creep behavior of first and second generation superalloys PWA 1480 and

PWA 1484, respectively. A third alloy, named PWA 1480+ for this investigation, was also produced by adding 3wt% Re to PWA 1480 to make a second generation version of PWA 1480. The following discussion will focus on the different behaviors among the three alloys produced by two different aging heat treatment schemes and alloy chemistry. Special attention will be given to several of the material attributes listed above and their effect on the creep behavior of all three alloys at low temperatures (700°C-815°C) and high stresses ( $\sigma > 500$  MPa) where primary creep dominates the creep behavior of PWA 1484. Finally, methods of applying the knowledge gained from this investigation towards creep behavior modeling and future alloy development will be discussed.

### **Microstructure**

The three alloys used for this investigation all share several microstructural similarities. First, the typical cuboidal  $\gamma/\gamma'$  microstructure for high  $\gamma'$  volume fraction superalloys extends to all three alloys. Second, all three contain a low volume fraction of carbide phases due to the addition of between 0.02wt% and 0.04wt% C. Additionally, secondary  $\gamma'$  precipitates were found in all three alloys with both age heat treatments. All of these similarities were impacted by alloy chemistry and processing.

### **$\gamma/\gamma'$ Morphology**

The cuboidal microstructure common among modern single crystal nickel base superalloys is produced due to a combination of the high volume fraction of  $\gamma'$  and a negative lattice misfit.<sup>40</sup> In the case of PWA 1480, the lattice misfit is small and only slightly negative at room temperature. The addition of Re to create PWA 1480+ did not significantly reduce the lattice misfit as expected. For both PWA 1480 and PWA 1480+, the measured values of lattice misfit at room temperature would be expected to become more negative as the temperature is raised

due to thermal expansion effects. The low misfit values have led to slightly rounded  $\gamma'$  precipitates and slightly larger  $\gamma$  channels (than PWA 1484). A benefit of low lattice misfit, and rounded  $\gamma'$  precipitates, is increased stability against coarsening and coherency loss. As the misfit is increased, the internal stress near the  $\gamma/\gamma'$  interfaces is increased. Under an applied stress, dislocations will be attracted to the interfaces to alleviate the high stresses. Additionally, diffusion-based processes will occur to reduce the misfit stresses still further. The second generation PWA 1484, however, has a larger misfit resulting in sharper edges and corners on the cuboidal  $\gamma'$  precipitates.

Rhenium additions have also been tied to changes in the  $\gamma/\gamma'$  morphology.<sup>8,75</sup> In particular, the addition of Re has been linked to smaller  $\gamma'$  precipitate size and an increase in rounded edges (to the point of spherical shapes in some lower volume fraction superalloys).<sup>8</sup> Within the present investigation, the effect of Re on the  $\gamma/\gamma'$  microstructure is small. Following the HT3 solution heat treatment, there is little difference between PWA 1480 and PWA 1480+ in size and shape of the  $\gamma'$  phase. The effect of Re, as reported in the literature, is caused due to the low diffusivity of the element in both  $\gamma$  and  $\gamma'$ . During cooling from the solution heat treatment, the supersaturated nature of the  $\gamma$  phase brings about nucleation of fine primary  $\gamma'$  precipitates. The low diffusivity of Re prevents these precipitates from growing significantly during cooling. Upon subsequent aging heat treatments, the growth of the  $\gamma'$  precipitates is slower due, again, to the rejection of the slow diffusing Re from the precipitates into the matrix. Additionally, the rounded corners of  $\gamma'$  precipitates were caused by Re due to reduced growth kinetics. These results were produced in alloys with lower  $\gamma'$  volume fractions than are present in PWA 1480 and PWA 1484.<sup>8,75</sup>

Precipitate coarsening is also driven by the Gibbs-Thompson effect by which the reduction in interfacial energy drives the growth of larger precipitates at the expense of smaller precipitates.<sup>76</sup> The Oswald coarsening of precipitates in a matrix has been shown to be impacted by a number of factors including composition, coherency, precipitate size, radii of curvature near corners (morphology), and applied stresses.<sup>76</sup> In the case of single crystal superalloys, both primary and secondary  $\gamma'$  precipitates are subject to the Gibbs-Thompson effect. This effect can usually be seen in the  $\gamma$  matrix near the  $\gamma/\gamma'$  interface where the population of secondary  $\gamma'$  precipitates is reduced. The growth of the much larger primary  $\gamma'$  precipitate depletes the matrix near the  $\gamma/\gamma'$  of  $\gamma'$  formers and causes the elimination of the ultra-fine secondary  $\gamma'$  precipitates in this region. These growth processes occur during isothermal aging heat treatments in order to obtain optimal mechanical properties shown to be maximized with a primary  $\gamma'$  size between 0.30  $\mu\text{m}$  and 0.45  $\mu\text{m}$  for high volume fraction nickel-base superalloys.<sup>36</sup> Modelling the compositions of precipitates with varied sizes and shapes can be performed based on this effect. Another application of the Gibbs-Thompson effect can be found with the application of an external stress at elevated temperature on the primary  $\gamma'$  precipitates. The Gibbs-Thompson equation can be modified to account for applied stress on coherent, or partially coherent, precipitates in a matrix. The application of stress can create directional growth of normally spherical or cuboidal precipitates do to the superposition of interfacial stresses that vary by location around the precipitates. As these stresses are relaxed, the microstructure can become directionally oriented. This has been shown experimentally as well as theoretically and has been called  $\gamma'$  rafting or topological inversion.<sup>70, 71, 76</sup>

For the alloys in this investigation, these effects are limited by the high equilibrium volume fraction of  $\gamma'$ . The predicted equilibrium volume fractions for PWA 1480, PWA 1480+, and

PWA 1484 are shown in Figure 4-14. The super-saturated  $\gamma$  phase, upon cooling, nucleated a fine dispersion of coherent  $\gamma'$  precipitates. Because the equilibrium volume fraction of  $\gamma'$  was so high, it is expected that the this thermodynamic driving force caused growth of the precipitates, possibly with slightly rounded corners, until the narrow  $\gamma$  channels became depleted with  $\gamma'$  former elements. As two  $\gamma'$  precipitates grew with parallel  $\{001\}$  faces approaching each other, the depletion of the  $\gamma$  channel adjacent to the centers of the  $\gamma'$  precipitate surfaces in  $\gamma'$  formers slowed the local growth of  $\gamma'$  precipitates. The  $\gamma$  channel regions near what would become the corners of the  $\gamma'$  precipitates would have contained a greater amount of  $\gamma'$  formers and precipitate growth would have continued until these regions also became depleted. The result would be cuboidal  $\gamma'$  precipitates with fairly well defined corners and edges even if Re additions would dictate slightly rounded corners in lower volume fraction alloys. Comparing the  $\gamma/\gamma'$  microstructure of PWA 1480 and PWA 1480+ revealed nearly identical  $\gamma'$  shapes and sizes despite the addition of Re. The  $\gamma$  channel widths also shared the same size and shape within both alloys.

PWA 1484, however, exhibited sharper  $\gamma'$  corners and slightly narrower  $\gamma$  channels. This effect can be described by comparing the alloy chemistry with that of PWA 1480. Aside from the addition of Re which would be expected to increase misfit and create rounded  $\gamma'$  cubes, an increase in Co and reduction in Ta were made in the newer alloy.<sup>77</sup> The presence of both of these elements has been shown to reduce the lattice misfit which would lead to further rounding of the  $\gamma'$  precipitate edges.<sup>8, 32, 75</sup> Countering these effects, though, is the increased diffusion coefficient produced by increasing Co and reducing Ta. Reported results have shown that increased cobalt concentrations can reduce or even eliminate any adverse effects caused by the addition of Re.<sup>75</sup> The increase in diffusion caused by these alloy modifications are possibly

responsible for the slight improvement in  $\gamma'$  shape and the reduction in  $\gamma$  channel thickness in PWA 1484 when compared to PWA 1480.

### **Carbides**

Carbides were found to be present for all three alloys. PWA 1480 and PWA 1480+ both contained about 0.04wt% C and PWA 1484 contained about 0.02wt% C. These small C additions were sufficient to bring about precipitation of carbide phases in the form of localized carbide networks. The level of carbon in the three alloys was insufficient to cause dendritic carbide formations.<sup>78, 79</sup> All three alloys contained script carbide networks with a few small blocky carbides associated with the local networks. Carbon additions have been shown to reduce casting defect formation and reduce  $\gamma/\gamma'$  eutectic formation.<sup>79</sup> Because the carbide content for all three alloys was low, the carbides did not impact the primary creep process significantly. Research has shown that carbide interfaces are often the site of void and crack formation leading to failure.<sup>39</sup> It was not found that the carbides present in PWA 1480, PWA 1480+, and PWA 1484 played a significant role during primary creep.

### **Topologically Close Packed Phases**

The addition of rhenium to PWA 1480+, while improving creep properties, brought about precipitation of plate-like TCP phases produced during high temperature exposure consistent with the formation of  $\sigma$  phase.<sup>35, 38</sup> The TCP phases present in PWA 1480+ grew throughout the heat treated microstructure with the length parallel to  $\langle 110 \rangle$  directions. The presence of these phases during primary creep indicates that the alloy is very unstable with regard to TCP phase formation. A direct consequence of this is that PWA 1480+ is not a suitable alloy for commercial use. These phases are expected to be the cause of the reduced ductility exhibited during creep and tensile testing. It is also expected that the fatigue life of PWA 1480+ would be

reduced as a result of the formation of the TCP precipitates. As a consequence, the applicability of PWA 1480+ is primarily limited to experimental testing and investigation of the rhenium effect. The formation of TCP phases during primary creep occurred over a much longer time period than the time for completion of primary creep in PWA 1480 and PWA 1484 due to the reduction of creep rate caused by the addition of rhenium. Increased rhenium content has been tied to increased TCP phase content as a result of the increase in overall refractory element content.<sup>35, 38, 50</sup> While TCP phases have received a great amount of attention due to the acicular morphology that is often associated with their presence, PWA 1480+ demonstrated the greatest creep lifetime at every test condition. The PWA 1480+ specimens failed with low ductility which might be tied to the formation of cracks and voids associated with TCP precipitates. Interesting future work could pursue the link between TCP precipitation and the early failure of PWA 1480+. Additionally, slight modifications in alloy chemistry might be made that preserve the excellent creep behavior of PWA 1480+ while reducing the TCP content to increase lifetime and/or ductility. While all three alloys share several similarities in microstructure, differences in performance are apparent as a result of the impact the microstructures of the three alloys in this investigation had on the active deformation mechanisms during tensile and creep testing.

### **Tensile Behavior**

The tensile strength properties of the three alloys of interest are necessary for a complete understanding of their respective creep behavior. The strain controlled nature of a tensile test reveals a different material response than a load controlled creep test. For example, superalloys most often exhibit  $\langle 110 \rangle$  type deformation in the  $\gamma$  phase.<sup>80, 81</sup> Depending on a variety of factors, including lattice misfit, dislocations will either shear or bypass the  $\gamma'$  precipitates during tensile testing. Shear of the  $\gamma'$  phase often occurs with pairs of  $a/2\langle 110 \rangle$  dislocations. Similarly

to creep testing, the  $a/2\langle 110 \rangle$  super-dislocation pair can further dissociate into partial dislocations separated by a complex fault.<sup>80</sup> Deformation during creep, however, has been shown to occur through a variety of methods: dislocation shear of the  $\gamma$  matrix by  $\langle 110 \rangle$  and  $\langle 112 \rangle$  dislocations,  $\gamma'$  shear by  $\langle 112 \rangle$  super-dislocation pairs and stacking fault pairs, and  $\langle 010 \rangle$  cube slip.<sup>12, 13, 16, 17, 24, 56, 63, 74, 82, 83</sup> Both test methods bring about complex deformation mechanisms. Tensile testing, therefore, is complementary to creep testing and can aid in generating a more complete understanding of the uniaxial properties of these alloys.

As with creep deformation, tensile deformation primarily begins within the  $\gamma$  matrix through the generation of  $a/2\langle 110 \rangle\{111\}$  dislocations. Initially, the microstructure is relatively free of dislocations. Upon yielding, these dislocations begin moving through the microstructure as more dislocations are created by the available sources. During the early stages of plastic deformation, dislocations begin bowing between  $\gamma'$  precipitates, lining the  $\gamma/\gamma'$  interfaces and filling the channels rather than entering and shearing the relatively hard  $\gamma'$  precipitates. It would be expected that this process will be affected by the presence (or absence) of secondary  $\gamma'$  precipitates within the narrow  $\gamma$  channels. The ultra-fine secondary  $\gamma'$  may play a role in tensile deformation by a number of possible methods.

### **Secondary $\gamma'$**

First, because secondary  $\gamma'$  precipitates are very small in size (spherical and 10-50 nm in diameter), they would be highly coherent, increasing the probability of  $\gamma'$  shear. In this case, the  $\langle 112 \rangle$  dislocations would be likely to shear the  $\gamma'$  without dissociating into partials due to the small size of the precipitates. Anti phase boundaries would be created and so additional dislocations would be drawn into these precipitates to relieve this energy. While shear of the secondary  $\gamma'$  precipitate would be more difficult for the first dislocation, the second dislocation

would experience softening while eliminating APB.<sup>20</sup> The second potential interaction between secondary  $\gamma'$  precipitates and matrix dislocations is due to the possibility of dislocation bypass mechanisms. At high temperatures, dislocation climb would be expected to play a vital role in bypass operations. Within the lower temperature range of 700°C to 815°C, however, climb is kinetically slow. As a result, cross-slip is more likely to account for precipitate bypass by dislocations. Both mechanisms would require added stress to accomplish.

The composition of the secondary  $\gamma'$  precipitates is also useful while considering either method of secondary  $\gamma'$ -dislocation interaction. The composition of the secondary  $\gamma'$  precipitates (determined by LEAP analysis, Tables 7-1 and 7-2) revealed that the precipitates contained lowered levels of Ta than is present in the base alloy (1-5 wt% vs. 9 wt% nominal composition). Additionally, in the smaller secondary  $\gamma'$  the Mo content was nearly double the nominal alloy composition (3-4 wt% vs. 2 wt%), the Co content was higher (14-17 wt% vs. 10 wt%), the W content was reduced to half (3 wt% vs. 6 wt%), and the Cr content was lower (2 wt% vs. 5 wt%). With reduced  $\gamma'$  strengthener content, namely Ta, and lower solid solution strengthener content these precipitates may be lower in strength than the larger primary  $\gamma'$  precipitates. As a result, the strength benefit due to the presence of secondary  $\gamma'$  would be expected to be relatively small and interactions would be frequent due to the dense, fine dispersion within the  $\gamma$  matrix.

The serrations that appeared in the plastic deformation regime during tensile testing of PWA 1480, PWA 1480+, PWA 1484 are likely due to the presence of secondary  $\gamma'$ . Of the possible interactions described above,  $\gamma'$  shear is the most likely due to the coherent nature (and potentially lower strength) of the secondary  $\gamma'$ . Similar interactions would be expected during creep with some exceptions. The differences that are observed during creep are due to

differences in deformation mechanism and will be discussed further in the Creep Mechanism discussion.

### **$\gamma$ Channel Thickness**

Another microstructural feature that impacts tensile properties is the thickness of the  $\gamma$  channels. This feature is primarily important for the early stages of tensile deformation because as precipitate shear becomes more common in the later stages, the channel widths become less important as dislocation bowing becomes less preferred. The importance of the  $\gamma$  channel width can be seen in Equation 8-1 that describes the stress increment to cause bowing of a straight dislocation between two precipitates:

Equation 8-1: 
$$\Delta\sigma \propto \frac{Gb}{(\lambda - 2r)}$$

Where the stress increment due to bowing is  $\Delta\sigma$ ,  $G$  is the elastic modulus,  $b$  is the burgers vector for the dislocation,  $\lambda$  is the center-to-center particle spacing, and  $r$  is the particle radius (assuming the particles are the same size). In this case, it can be seen that the strengthening effect is increased if the inter-particle distance is reduced.<sup>84</sup> Strengthening due to dislocation bowing is likely to play a role in the tensile deformation of PWA 1480, PWA 1480+ and PWA1484; however, there are several interactions that occur that complicate the problem. For example, the already mentioned secondary  $\gamma'$  would serve to drastically reduce the inter-particle spacing (if no shear was assumed and bypass was not active).

It is likely that a combination of these effects takes place during tensile deformation. For example, when a dislocation is stretched across a  $\gamma$  channel (“pinned” by the primary  $\gamma'$  precipitates), the first strength increment to be accounted for should be the bowing stress from the primary precipitates. As the stress is increased, the dislocation will come against many fine secondary  $\gamma'$  precipitates. The effective inter-particle spacing becomes significantly reduced and

the bowing strength effect is increased. As the applied stress continues to increase, either the stress to shear the secondary  $\gamma'$  or the stress to cross-slip and bypass the secondary  $\gamma'$  is reached and the dislocation begins to glide. These interactions continue until the stress to shear the primary  $\gamma'$  precipitates is reached and large scale shear becomes dominant leading to eventual failure.

### **Lattice Misfit**

Additional considerations are related to the effect of alloy composition and, more specifically, the equilibrium concentration of the  $\gamma'$  phase. Three aspects related to composition and heat treatment are lattice misfit, stacking fault energy, and anti-phase boundary energy. The magnitude of the lattice misfit can impact the resolved shear stresses within the  $\gamma$  channels. High misfit alloys experience large misfit stresses that can create compressive stresses in the  $\gamma$  channels parallel to the applied stress direction. These misfit stresses can be quite large. During high temperature, low stress creep testing, for instance, these compressive stresses can exceed the applied external stress creating a very large driving force for microstructural change and, subsequently, drives rafting. During tensile testing, these compressive stresses can relieve the applied stress from a dislocation and reduce the actual shear stress felt by the dislocation creating a strengthening effect. In order to relieve misfit stresses, dislocations can be attracted to the  $\gamma/\gamma'$  interfaces to create dislocation networks. The formation of these networks increases the stress in the  $\gamma$  matrix leading to  $\gamma'$  shear.<sup>65, 80</sup>

### **Stacking Fault Energy**

Shear of the  $\gamma'$  phase usually involves the formation of stacking faults as matrix dislocations enter the  $\gamma'$ . Stacking faults are regions of atoms shifted from normal lattice sites by the passage of a partial dislocation. Stacking faults are contained between two partial

dislocations that can be combined, with enough stress, to form a perfect dislocation. The stacking fault energy, SFE, is composition dependent and is related to the energy required to create the fault. The larger the SFE the smaller the spacing between partial dislocations. With large SFE alloys recombination and cross-slip is easier, but with low SFE alloys, the partial dislocations can spread out further and recombination becomes more difficult and interactions with other stacking faults and/or dislocations becomes more likely. The SFE of the  $\gamma'$  phase can also impede deformation of the  $\gamma'$  phase. If the SFE of the primary  $\gamma'$  precipitates is high, more resolved shear stress will be needed to force a dislocation to enter the precipitate. Shear of the  $\gamma'$  precipitates is slightly easier with lower stacking fault energy alloys.<sup>65, 80</sup>

### **Anti-Phase Boundary Energy**

Related to SFE is the anti-phase boundary energy. While stacking faults displace atoms a partial atomic spacing, anti-phase boundaries are created by displacing atoms in an ordered precipitate by a whole atomic spacing. The result is a change in nearest neighbor species type. For the highly ordered  $\gamma'$  phase, an APB will position Al atoms next to Al atoms and Ni atoms next to Ni atoms across the boundary. The result is increased energy and resistance to deformation. To relieve the energy produced by the creation of an APB, a second dislocation must shear along the same plane to shift the atoms into “proper” atomic positions. Like the SFE discussed above, the magnitude of the APB relates to the energy required to create it. Alloys with large APB energies will have short dislocation spacing and vice-versa for low APB energy alloys. There is a strength increment required to produce an anti-phase boundary that prevents dislocations from entering the  $\gamma'$  phase. Once a single dislocation has entered (either in whole form or dissociated into partials with a stacking fault), though, a second dislocation will be attracted into the  $\gamma'$  phase to relieve the APB. The consequence of this behavior is the

observation of stacking fault pairs that shear the  $\gamma'$  phase. As a result of each of these strengthening effects, the tensile deformation of single crystal superalloys can become complex.<sup>65, 80</sup>

## **Tensile Results**

The results of the tensile testing conducted on PWA 1480, PWA 1480+, and PWA 1484 revealed several differences between the alloys. The first generation superalloy PWA 1480 provides a basis of comparison for both the Re modified PWA 1480+ and the second generation PWA 1484. Both second generation alloys are descendant from the original PWA 1480 alloy. As discussed earlier, the transition from PWA 1480 to PWA 1484 during the development cycle was brought about by several key changes in composition including Cr, Co, Ta, Ti, and Re. The creation of PWA 1480+ was performed by adding 3 wt% Re (the same amount added to PWA 1484) to PWA 1480 to create a second generation version of the alloy.

The second generation superalloy, PWA 1484, has demonstrated significant improvements in high temperature creep capability compared to PWA 1480.<sup>77</sup> A consequence of the changes in composition that led to improved creep strength was a decrease in tensile strength for PWA 1484 relative to the original PWA 1480. The yield strength of PWA 1484 is over 400 MPa lower at 700°C and over 300 MPa lower at 815°C. PWA 1480 exhibited high yield strength, UTS, and failure strength values for both aging heat treatments and test temperatures used in this study, Table 5-1. PWA 1484 exhibited significantly lower yield strength, as mentioned earlier, but demonstrated a greater ability to work harden following yielding. In fact, at 815°C the failure strength of PWA 1484 LT exceeds the failure strength of PWA 1480 LT. Additionally, the strength of the HT version of both alloys at 815°C is only separated by 16 MPa at failure despite

a 214 MPa disadvantage in yield strength. Clearly the alloy design approach taken for PWA 1484 significantly changed the mechanical behavior of the alloy relative to PWA 1480.

While the behavior of PWA 1484 is very different from the original PWA 1480 alloy, the performance of PWA 1480+ was quite similar to PWA 1480. The modified alloy is marked by a greater yield strength (in the HT condition) and less ductility. This response is not unexpected due to the addition of rhenium. Rhenium has long been known to be a “potent” solid solution strengthener as well as a retardant of  $\gamma'$  coarsening.<sup>77</sup> Simply adding Re raised the yield strength of PWA 1480+ HT by 42 MPa at 700°C and 162 MPa at 815°C. The LT condition, however, exhibited lower yield strength than HT condition at both test temperatures.

Another effect of the age heat treatments that were given to the three alloys can be seen in PWA 1480 with which the LT age produced greater than 10% ductility during tensile testing. The HT age, however, significantly reduced the ductility, yield strength, and UTS values. The HT age does not, however, produce this same effect in PWA 1484. The HT aged specimens of PWA 1484 exhibited a more rapid increase in flow stress during work hardening, but the ductility and UTS values were similar to the LT aged specimens. Additionally, it is noteworthy that while the *tensile* behavior of PWA 1480 was significantly altered by age heat treatment and PWA 1484 was not, creep testing, as discussed below, produced *creep* behavior of PWA 1484 that was significantly altered by age heat treatment while PWA 1480 was not.

### **Creep Behavior**

Primary creep at low temperatures and high stresses has become an important topic as models of creep behavior are being developed for modern superalloys. The early superalloys required relatively simple to design creep models. These first generation superalloys, such as PWA 1480, exhibit tertiary creep behavior across a broad range of temperatures and stresses.

Modern superalloys, beginning with the second generation superalloys, however, exhibit a range of creep behaviors depending on the stress and temperature regime to which they are subjected. For CMSX-4, for example, the three creep regimes that are displayed are primary creep ( $T < 850^\circ\text{C}$ ,  $\sigma > 500$  MPa), tertiary creep ( $700^\circ\text{C} < T < 1050^\circ\text{C}$ ,  $200$  MPa  $< \sigma < 500$  MPa), and rafting ( $T > 950^\circ\text{C}$ ,  $\sigma < 200$  MPa).<sup>63</sup> Each of these creep regimes are related to the microstructure and, consequently, the processing that the alloy was subjected to prior to service. Additionally the behaviors at these three temperature/stress regimes have been shown to be highly dependent on the chemistry of the alloy.

### **Tertiary Creep**

The most common creep regime that is encountered in testing of single crystal nickel-base superalloys is tertiary creep. For example, the alloy PWA 1480, a first generation superalloy, exhibits increasing creep rate as creep strain accumulates (tertiary creep), over a wide range of temperatures and stresses including those used for this investigation. Tertiary creep behavior has been linked to a continuously increasing dislocation density implying a creep softening process.<sup>63</sup> Often, the tertiary creep rate can be modeled with the relatively simple equation given below:

Equation 8-2: 
$$\dot{\varepsilon} = \dot{\varepsilon}_0(1 + C\varepsilon)$$

Where  $\dot{\varepsilon}$  is the creep strain rate,  $\dot{\varepsilon}_0$  is the initial creep rate, C is a fitting constant and  $\varepsilon$  is creep strain.<sup>43</sup> The dislocations responsible for tertiary creep are primarily  $a/2\langle 110 \rangle \{111\}$  type dislocations that are mostly contained within the  $\gamma$  matrix. These dislocations, under the applied stress, are forced to bend between the primary  $\gamma'$  precipitates and stretch such that they line both sides of the  $\gamma$  “channels”. As dislocations from different sources begin to meet along the  $\gamma/\gamma'$

interfaces, nodal networks are formed. As the dislocation density continues to rise, the spacing between dislocations at the interfacial networks is reduced.

For alloys that display tertiary creep in the absence of rafting, the  $\gamma/\gamma'$  microstructure is relatively stable for the duration of the creep test. This is largely due to the fact that shearing of primary  $\gamma'$  precipitates is low and migration of vertical  $\gamma$  channels to horizontal  $\gamma$  channels is slow. Failure during creep of single crystal superalloys typically involves the condensation and coalescing of vacancies to create voids. Often, cracks and voids are nucleated in conjunction with casting porosity. In alloys containing hard, brittle carbides and/or TCP phases, voids typically form at the interface between the hard particle and the more ductile matrix. For cases where these hard interfaces are not present (or present in low amounts), it is thought that void formation may also occur through the development of dense dislocation cells near  $\gamma/\gamma'$  interfaces where dislocation annihilation can lead to a local increase in vacancy concentration.<sup>63</sup> Changing the temperature and/or stress such that another creep regime becomes active reduces the accuracy of the basic creep rate model shown above. As rafting or primary creep become dominant, more complex models are required.

### **Rafting**

Rafting in single crystal nickel base superalloys has become commonplace at low stresses and high temperatures. Rafting, also known as topological inversion, is a process by which the original cuboidal  $\gamma'$  precipitate morphology evolves into long plate-like “rafts”. The final orientation of the rafts depends on the lattice misfit between the  $\gamma$  and  $\gamma'$  phases. Most often this misfit value is negative, leading to  $\gamma'$  rafts oriented perpendicular to the applied stress. The rafting response occurs through diffusion of matter from thinner rafts through the  $\gamma$  channels to the thicker rafts. The result is a widening of the perpendicular  $\gamma$  channels. This morphological

shape change results in the elimination of  $\gamma$  channels parallel to the applied stress direction. The  $\langle 110 \rangle \{111\}$  matrix dislocations begin gathering along the  $\gamma/\gamma'$  interfaces creating dense dislocation networks.

Because matter is primarily diffusing across the  $\gamma$  channels during rafting, the  $\gamma$  channel widening can be described by a parabolic rate law:

Equation 8-3: 
$$\Delta w = C_1 \sqrt{t}$$

Where  $\Delta w$  is the change in thickness,  $C_1$  is a material and temperature dependent constant (for isothermal creep), and  $t$  is time. Notice, equation 8-2 describes widening of the  $\gamma$  channels using a  $t^{1/2}$  time dependence. Coarsening of the  $\gamma'$  precipitates, or Ostwald ripening, typically follows a  $t^{1/3}$  time dependence.<sup>32</sup> As matter diffuses from the  $\gamma$  channels that are parallel to the applied stress into  $\gamma$  channels perpendicular to the applied stress, matter from the cube surfaces of the  $\gamma'$  precipitates parallel to the applied stress is simultaneously diffusing into the parallel  $\gamma$  channels, effectively closing the  $\gamma$  channels oriented parallel to the applied stress. The change in  $\gamma$  channel width due to this morphology change effect has been described by the following:

Equation 8-4: 
$$\Delta w_{MC} = 2 \frac{(2w_o s_o^2 + w_o^2 s_o)}{2(w_o + s_o)^2}$$

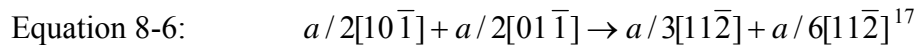
Where  $w_o$  is the initial  $\gamma$  channel thickness and  $s_o$  is the initial  $\gamma'$  edge length. The morphology effect is used to calculate the amount of change in channel width as a result, simply, of the formation of  $\gamma'$  rafts (ie. the change in shape necessary to create rafts). Finally, the parabolic rate constant from equation 8-3 can be found by:

Equation 8-5: 
$$\Delta w = w(t) - w_o - \Delta w_{MC}$$

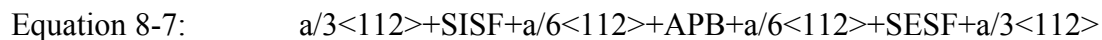
Plotting  $\Delta w$  versus  $\sqrt{t}$  allows for determination of the rate constant (slope of the line). Modeling the  $\gamma$  channel widening kinetics of superalloys experiencing rafting is necessary for the development of constitutive equations to predict the creep behavior at these conditions.<sup>66,67</sup>

### Primary Creep

While numerous studies have focused on developing accurate descriptions of tertiary creep behavior and  $\gamma/\gamma'$  rafting, the origin of primary creep has relatively little attention until recently. Large primary creep strains produced at low temperatures and high loads are typically found in second generation and later single crystal superalloys. While creep deformation in the tertiary creep regime is governed primarily by  $\langle 110 \rangle \{111\}$  dislocation shear in the  $\gamma$  matrix, deformation during primary creep under these conditions is produced by pairs of stacking faults that cooperatively shear both the  $\gamma$  and  $\gamma'$  phases. Specifically, stacking faults in the  $\gamma'$  are formed by reactions of dislocations of the type  $a/2\langle 110 \rangle$  to form  $a/3\langle 112 \rangle$  and  $a/6\langle 113 \rangle$  dislocations. An example reaction is given below:



Between the  $a/3\langle 112 \rangle$  and  $s/6\langle 112 \rangle$  dislocations lies a stacking fault that exist in both the  $\gamma$  and  $\gamma'$  phases. As the pair of dislocations (with the stacking fault between) enter an ordered  $\gamma'$  precipitate an anti-phase boundary is created in the  $\gamma'$  phase, but not in the  $\gamma$  phase. To reduce the energy required to create the APB, a second pair of  $\langle 112 \rangle$  dislocations enters the  $\gamma'$  in the opposite configuration. As they progress, the APB is eliminated. An example of this configuration is given below:



Where SISF and SESF are intrinsic and extrinsic stacking faults, respectively, and APB is anti-phase boundary. It is this configuration that is referred to as a dislocation or stacking fault “ribbon.”<sup>14</sup>

These dislocation ribbons, two stacking faults separated by an APB cooperatively shearing both phases, are capable of traveling relatively long distances within the material without leaving dislocation segments behind at the  $\gamma/\gamma'$  interfaces. It should also be noted that while the first pair of dislocations is impeded by the formation of the APB, the second pair is aided by the elimination of the APB. Large creep strains can be produced by this mechanism in the absence of forest dislocations at the  $\gamma/\gamma'$  interfaces. As common  $a/2\langle 110 \rangle$  matrix dislocations expand to fill the  $\gamma$  channels and create interfacial networks, the difficulty of cooperative shear increases. Eventually, the networks that are formed are sufficient to reduce the rate of shear of the  $\gamma/\gamma'$  microstructure and a steady-state condition is reached where the dislocation density would remain constant under constant stress creep conditions.<sup>16, 17, 63</sup>

Adding primary creep behavior to existing creep behavior models is a challenge due to the complexity of the behavior. For example, as shown in Figure 8-5, the dislocation pairs required to form the stacking fault pairs form from  $a/2\langle 110 \rangle$  type dislocations. This implies that before cooperative shear can take place, a population of  $a/2\langle 110 \rangle$  dislocations must already be present in the microstructure.<sup>16</sup> For this reason, it is believed that this population is produced during the incubation period that often precedes primary creep. In this way, alloys that deform by  $\gamma'$  shear exhibit the same deformation mechanisms prior to the start of primary creep that are found in alloys that display tertiary creep behavior only. Developing a model that can predict when the transition to  $\gamma/\gamma'$  shear will take place has proven difficult.<sup>63</sup>

Additionally, primary creep of superalloys does not always occur by  $\gamma'$  shear due to stacking fault ribbons. Alloys exhibiting tertiary creep do experience primary creep in the form of a higher initial creep rate that is reduced during the first stages of exposure to creep conditions. For conditions governed by tertiary creep, primary creep typically occurs by  $\langle 110 \rangle$  dislocations bowing to fill the  $\gamma$  channels. This process is similar to the deformation process exhibited during the later stages of tertiary creep; however, prior to the start of a creep test the native dislocation density is low. Due to this low initial density, the creep rate is more rapid than in later stages when dislocation-dislocation interactions are common. Primary creep under these conditions occurs as the small dislocation population is increased until the dislocation interactions bring about the transition to tertiary creep (ie. the creep rate is reduced to the minimum creep rate immediately following primary creep).<sup>74</sup>

## **Creep Results**

The primary creep behavior of single crystal nickel-base superalloys has proven to be controlled by multiple factors. Previous research has shown a dependence of primary creep on orientation, magnitude of the load applied, secondary  $\gamma'$  precipitates, lattice misfit, and possibly rhenium and/or ruthenium content, all of which may lead to non-uniform deformation (only 1 or 2 slip systems) and stacking fault shear (of the  $\gamma'$  phase).<sup>16, 17, 19, 20, 23, 24, 27, 33, 47, 56-58</sup> Comparing yield strength to the applied initial creep stress, Table 5-3, it is apparent that the large primary creep strains of PWA 1484 at 704°C were produced at greater than 90% of the yield strength. This high load condition produced primary creep strains of 17% for the LT age and 24% for the HT age. Such a high stress level, however, was not necessary to produce large primary creep strains in PWA 1484. Also at 704°C and a reduced load of 758 MPa, primary creep strains of 5% for the LT age and 10-14% for the HT age were observed. This clearly indicates that the

magnitude of the applied initial stress contributes to the amount of primary creep that results, as reported by (Rae and Reed, 2006) and (Shah et al., 2004).<sup>16, 47</sup> Under creep testing at conditions that yield large primary creep strains, raising the initial stress results in larger primary creep strains and shorter times to complete primary creep.

This lower stress ratio for PWA 1484 at 815°C is similar to the stress ratios for creep testing of PWA 1480 and PWA 1480+ at 704°C. Even still, the primary creep of PWA 1484 is significantly larger than the other two alloys. Additionally, a PWA1480 HT specimen was tested at 704°C/1200 MPa which represents a creep stress to yield stress ratio of 0.9 (90%). The PWA 1480 HT specimen failed in 0.9 hours with no discernable primary creep stage because the creep rate exhibited continuous acceleration beginning with the earliest measurements. These results demonstrate two related points. First, the ratio of creep stress to yield stress does not cause primary creep nor do high ratios increase the primary creep seen in PWA 1480. The second point is that the magnitude of the applied stress, while increasing the primary creep strain produced in alloys prone to large primary creep strains, does not cause large primary creep strains in alloys resistant to primary creep.

Related to the previous discussion are reports that there may be a stress threshold that, above which, stacking faults in the  $\gamma'$  phase may form due to the entry of pairs of dislocations that dissociate into pairs of stacking faults, separated by an APB, that then shear the  $\gamma'$  phase. It is thought that at stresses below this threshold matrix dislocations do not shear precipitates but, instead, exhibit cross-slip or climb to bypass barriers such as the fine secondary  $\gamma'$  in the  $\gamma$  channels. During this process work hardening is more likely due to the distribution of slip on multiple planes. If the stress exceeds this threshold, however, climb and cross-slip do not occur and deformation is able to proceed without generating significant work hardening and secondary

creep is delayed.<sup>16, 17, 20</sup> Incorporating the findings of the current investigation, these results are likely to only apply to alloys prone to primary creep. The distinguishing factors that differentiate alloys exhibiting primary creep are not low yield strengths or the magnitudes of the applied loads, but microstructural differences as a result of alloy chemistry and processing that resist primary creep strain production.

When dislocations are confined to the  $\gamma$  matrix, primary creep is low due to the interaction of dislocations within the narrow spaces of the  $\gamma$  channels. During  $\gamma'$  shear, dislocations can move longer distances without interacting with an obstacle in the  $\gamma'$  precipitates resulting in large creep strains and few dislocation interactions.<sup>16</sup> Creep behavior following the HT age heat treatments supports these findings. The longer time and higher temperature of the HT age allows the  $\gamma'$  to coarsen, decreasing coherency. The greater degree of incoherency of the  $\gamma'$  precipitates after the HT age may be responsible for the decrease in primary creep at all test conditions for PWA 1484 while no significant change in primary creep can be found in PWA 1480 and PWA 1480+. Increasing incoherency in PWA 1484 following heat treatment may reduce the ability of dislocations to enter the  $\gamma'$  phase to form stacking faults. PWA 1480 shows little effect with heat treatment because the formation of stacking faults is already difficult, Figures 6-11 to 6-15. PWA 1480+, while able to produce stacking faults, deforms by multiple deformation systems so that work hardening is rapid and secondary creep starts soon after the initiation of primary creep. Because both PWA 1480 and PWA 1480+ are prone to wide-spread dislocation and stacking fault interactions, leading to hardening, they show little change in primary creep strain with age heat treatment.

Research into primary creep mechanisms has yielded interesting findings into the efficiency of these two shear mechanisms. Calculating dislocation densities and predicting the

expected amount of strain produced for each mechanism, differences in the ability of the different processes to confer shear can be seen. For alloys that deform primarily by the movement of matrix dislocations, the matrix channels become filled with dislocations and dislocation interactions become common following 0.3% to 0.5% creep deformation. The large amount of dislocation interactions at this point is related to the onset of secondary creep, where a balance exists between deformation processes (slip) and recovery processes. As a result, it is predicted that deformation provided primarily the movement of matrix dislocations will only yield about 0.5% primary creep at the maximum. If the ability to form stacking faults is included, the dislocation density in the  $\gamma$  matrix increases more slowly. The result is a deformation process that can operate much longer before work hardening in the matrix causes secondary creep. For this scenario, primary creep strains greater than 5% can be expected.<sup>16, 17</sup> These results are consistent with the current investigation and those of other researchers.<sup>19, 20, 57</sup>

In the narrow sense of comparing overall rupture lives only, PWA 1484 out-performed PWA 1480 at all but highest load at the lowest temperature (704°C/862 MPa). Simply adding Re to PWA 1480, however, remarkably improved the rupture life of PWA 1480. Creep ductility and toughness were reduced, but the minimum creep rate was decreased by over an order of magnitude and the same low primary creep behavior was maintained. The time to 1% creep, however, shows the difference in primary creep behaviors very clearly, Table 6-2. While the lifetime of PWA 1484 is the longest at several conditions, the time to 1% creep is the shortest, indicating rapid deformation early in the life of the specimens. Continuing the discussion to time from 1% to 2% creep strain, it can be seen that PWA 1480 and PWA 1480+ experience a much longer time from 1 to 2% than from 0 to 1%. For several PWA 1484 samples, however, the time

from 1% to 2% creep was achieved faster than the first 1% of creep strain because the creep rate was still increasing through the first several percent primary creep.

If the usual benchmarks of rupture life, time to 1% creep, and minimum creep rate are utilized in turbine engine design then an alloy might be selected that could exhibit rapid creep during the early stages of its service life. Thus it is necessary to incorporate an understanding of the nature of the active primary creep behavior into the usual design schemes. Within the context of current investigation, a simple change in the aging heat treatment temperature of a turbine component may be enough to manage the primary creep that will be produced. Another method of avoiding large primary creep strains is to pre-creep the alloy prior to service. Some reports indicate that specimens that usually yield large primary creep strains were crept to small strains (<0.1%) at 950°C before being subjected to low temperature, high stress creep testing. The primary creep produced during the second test was reduced to low values similar to those produced by PWA 1480 and PWA 1480+. It is thought that this reduction in the expected primary creep strain is related to the formation of matrix dislocations that then interfere with the passage of stacking faults and bring about the onset of secondary creep earlier than in specimens that were not pre-crept. These changes in processing are both examples of simple techniques that can dramatically improve the usefulness of alloys that are prone to excessive primary creep by stacking fault shear.

### **Modeling Primary Creep**

There have been several models developed to describe the creep process for single crystal nickel-base superalloys since the introduction of PWA 1480 in the early 1980's. Most of these were made to describe the tertiary creep regime that is most common among superalloys. PWA 1480, for example, exhibits tertiary creep across a very wide range of stress and temperature

including loads as high as 90% of the yield strength of PWA 1480 at 704°C. The second generation superalloy PWA 1484, however, exhibits a more complex combination of creep behaviors. During high temperature, low stress creep PWA 1484 displays tertiary creep behavior. At low temperatures and low stresses, tertiary creep still persists. If the stress is raised above a critical threshold, however, PWA 1484 (and other second generation superalloys) produces large primary creep strains followed by steady-state creep.<sup>16</sup> It is this transition that has proven difficult to predict with conventional models often leading to large inconsistencies between models and experimental data.<sup>63</sup>

The alloy that has received the most attention for primary creep modeling is CMSX-4.<sup>16, 17,</sup>  
<sup>63</sup> CMSX-4 and PWA 1484 share fairly similar compositions, Table 2-1, and the reported creep behavior and deformation substructures are similar in nature to those found for PWA 1484 in the current investigation so modeling approaches for both alloys are expected to be similar.<sup>3, 16, 47</sup> Deformation modeling of creep of superalloys usually begins by separating the deformation gradient into constituents representing the  $\gamma$  matrix and the  $\gamma'$  precipitates using an equation similar to the one given below:

Equation 8-8: 
$$\mathbf{L}_p = f_y \left( \sum_{\alpha=1}^{12} \dot{\gamma}_\alpha \tilde{\mathbf{d}}_\alpha \otimes \tilde{\mathbf{n}}_\alpha \right)_\gamma + f_{\gamma'} \left( \sum_{\alpha=1}^{12} \dot{\gamma}_\alpha \tilde{\mathbf{d}}_\alpha \otimes \tilde{\mathbf{n}}_\alpha \right)_{\gamma'}$$

where  $\dot{\gamma}$  is the shear strain rate,  $\tilde{\mathbf{d}}$  is the unit vector representing the slip direction,  $\tilde{\mathbf{n}}$  is the slip plane normal unit vector,  $\alpha$  designates a slip system (12 systems included in this calculation), and  $f$  is volume fraction of each phase denoted by  $\gamma$  and  $\gamma'$  subscripts. Because the model ignores any contribution by TCP phases or carbides, the sum of the volume fractions of  $\gamma$  and  $\gamma'$  are set equal to one.

The next step is to define the shear strain rate ( $\dot{\gamma}$ ). This step typically begins with the Orowan equation:

$$\text{Equation 8-9: } \dot{\gamma}_{\alpha} = \rho_{\alpha} \cdot b \cdot v_{\alpha}$$

where  $\rho$  is the mobile dislocation density,  $b$  is the burgers vector, and  $v$  is the velocity of mobile dislocations. Note that Equation 8-8 is specific to a given slip system. Also, shear strain rate calculations are performed for each phase independently. Substituting an expression for the mobile dislocation velocity gives:

$$\text{Equation 8-10: } \dot{\gamma}_{FCC} = \rho_{FCC} \cdot b \cdot \lambda_{FCC}^{\alpha} \cdot F_{attack} \exp \left\{ -\frac{Q_{slip}^{110}}{k_b T} + \frac{|\tau + \tau_{mis}| - \tau_{pass} - \tau_{oro}}{k_b T} V_c \right\}$$

$$\text{Equation 8-11: } \dot{\gamma}_{L1_2} = \rho_{L1_2} \cdot b \cdot \lambda_{L1_2}^{\alpha} \cdot F_{attack} \exp \left\{ -\frac{Q_{slip}^{112}}{k_b T} + \frac{|\tau| - \tau_{pass}}{k_b T} V_c \right\}$$

Where the subscripts FCC and L1<sub>2</sub> denote the  $\gamma$  and  $\gamma'$  phase, respectively. Also,  $\lambda$  denotes dislocation jump distance,  $F$  denotes dislocation jump frequency,  $k_b$  is Boltzmann's constant,  $\tau$  is the resolve shear stress. Also note, the misfit stress,  $\tau_{mis}$ , passing stress,  $\tau_{pass}$ , and Orowan stress,  $\tau_{oro}$ , are all accounted for in the  $\gamma$  phase, but just the passing stress is involved in the calculation for the  $\gamma'$  phase. The Orowan stress as defined in the model is based on the  $\gamma$  channel width and does not account for secondary  $\gamma'$  within the channels. The strengthening contribution from secondary  $\gamma'$  was not included as a separate contribution within any description of the creep behavior so its contribution was most likely accounted for in the more general terms like passing stress. Each of these terms are described in detail as is the rest of the model in the work by A. Ma et al.<sup>63</sup> As the model was developed, additional terms were added to account for additional behaviors to be described.

The above described model goes on to account for  $\langle 110 \rangle$  dislocation shear within the  $\gamma$  matrix as well as the generation of  $\langle 112 \rangle$  stacking fault ribbons. To account for tertiary creep, the model ignores dislocation ribbons and  $\gamma'$  shear because tertiary creep occurs almost exclusively by deformation contained within the  $\gamma$  matrix. The distribution of slip between  $\gamma$  channels was found to be critical to the success of the model. The simplest microstructural constituents are a cube shaped  $\gamma'$  phase, and three rectangular  $\gamma$  channels (two sides equal to the edge length of the  $\gamma$  precipitate and one side equal to the specified  $\gamma$  channel thickness) oriented in three directions with the normal to the “plate” parallel to the cube directions [100], [010], and [001].<sup>63</sup> With the applied stress axis parallel to the [001] direction, one  $\gamma$  channel is perpendicular to the stress [001], and two are parallel [100] and [010]. Misfit stresses were found to interact quite strongly with the active deformation mechanisms. Initially, deformation takes place almost exclusively in the perpendicular, [001], channels due to the superposition of the misfit stress and applied stress. As long as the  $\gamma/\gamma'$  interfaces remain coherent, the [001] channels are preferred. As the misfit stresses are relieved, however, the preference is reduced and deformation increases within the [100] and [010] channels.<sup>63</sup>

### **Lattice Misfit**

Lattice misfit plays a significant role during both tertiary creep and primary creep. Alloys with lower values for lattice misfit are reportedly more prone to the formation of the dislocation ribbons responsible for  $\gamma'$  shear and, therefore, large primary creep strains.<sup>59-61, 71, 85</sup> Large, negative lattice misfit values have been shown to produce better creep resistance at high temperatures and are thought to be beneficial to the prevention of large primary creep strains. Alloys with large lattice misfit have been shown to form dislocation networks along the  $\gamma/\gamma'$  interfaces more quickly due the large misfit stresses that result. Dislocations then build up at the

$\gamma/\gamma'$  interfaces to relieve the misfit. As the interface becomes lined with dislocations forming the interfacial network, shear of the  $\gamma'$  phase becomes more difficult, the creep rate is reduced, and secondary creep begins. Alloys with low misfit are more coherent and it has been suggested that low misfit alloys are prone to shear of the  $\gamma'$  phase. In addition, the dislocation ribbons that form glide relatively easily and leave little, if any, dislocation segments at  $\gamma/\gamma'$  interfaces. These two factors combine to delay the formation of the interfacial networks that herald the start of the secondary creep stage. As a result, the primary creep stage ( $\gamma'$  shear) occurs over a longer time allowing for the production of greater primary creep strains.<sup>16</sup>

In the current investigation, PWA 1484 was shown to have the largest, negative lattice misfit (-0.20% to -0.25%) of the three alloys tested in this investigation. This finding would tend to contradict conventional wisdom regarding the effect of lattice misfit due to the large degree of stacking fault shear in PWA 1484 during primary creep. PWA 1480 exhibited low lattice misfit values ranging from 0.00% to -0.14% and the Re addition to PWA 1480 increased the lattice misfit values to a slightly more positive range (-0.05% to +0.034%) for PWA 1480+. These results suggest that the emphasis placed on lattice misfit in creep modeling may need to be reevaluated. While it is clear, that lattice misfit plays a large role in tensile and creep deformation of superalloys, the more recent second and third generation superalloys have larger magnitudes for lattice misfit than the older first generation alloys. The first generation alloys, however, do not deform by large-scale  $\gamma'$  shear unlike the second generation alloys PWA 1484 and CMSX-4. Additional work is clearly necessary to clarify the effect of lattice misfit while modeling primary creep behavior these alloys.

## Secondary $\gamma'$

In addition to accounting for the nature of the  $\gamma/\gamma'$  interface during creep deformation, the  $\gamma$  channels play a vital role in creep (both primary and tertiary). The  $\gamma$  channels are the location where  $\langle 110 \rangle$  dislocations nucleate and propagate leading to the nucleation of dislocation ribbons in the  $\gamma'$  phase or  $\gamma/\gamma'$  interfacial networks. In addition to  $\gamma$  channel thickness, discussed earlier, the secondary  $\gamma'$  that forms within the matrix interact with dislocations as they expand to fill the matrix. Despite these interactions, the secondary  $\gamma'$  precipitates are omitted from most models even though  $\gamma$  channel thickness is nearly unanimously utilized for creep and tensile modeling.

There is some disagreement as to which stage of heat treatment is responsible for precipitating secondary  $\gamma'$ . The presence of secondary  $\gamma'$  has been shown to occur following solution heat treatment with coarsening occurring during the ensuing aging heat treatment<sup>69</sup> and secondary  $\gamma'$  has been reported to appear during rapid cooling from the final aging heat treatment.<sup>20</sup> In either case, the secondary  $\gamma'$  are likely to always be present in the  $\gamma$  channels prior to service for most high volume fraction superalloys. For PWA 1480, PWA 1480+, and PWA 1484, secondary  $\gamma'$  was shown to be present in all three alloys following both age heat treatments. These precipitates are expected to be highly coherent with the matrix due to their small size resulting in an increased probability of shear by matrix dislocations bowing within the  $\gamma$  channels.

Using the LEAP technique, compositions for a small sample of secondary  $\gamma'$  precipitates in PWA 1484 were determined. While no statements can be made with high statistical certainty, four composition variation trends could be seen with increasing size. The larger secondary  $\gamma'$  precipitates contained higher levels of Ni and Ta and lower levels of Co and Re. This indicates that as these precipitates, or potentially clusters, grow in size, strengthening is likely to occur due

to the increased  $\gamma'$  former content. The larger secondary  $\gamma'$  precipitates reside towards the centers of the  $\gamma$  channels with smaller secondary precipitates near the relatively large primary precipitates. As a result, the interaction between secondary  $\gamma'$  and matrix dislocations is complex. Despite the differences in strength and size distribution across the  $\gamma$  channel, it is likely that matrix dislocations shear these ultra-fine precipitates during tensile testing. Creep testing, however, allows for thermally activated processes to occur that might alter the paths of dislocations when they meet these precipitates. For alloys that exhibit tertiary creep, such as PWA 1480 and PWA 1480+, matrix dislocations remain in the  $\langle 110 \rangle$  form and likely shear through or cross-slip past the secondary  $\gamma'$ . Alloys that produce large primary creep strains, such as PWA 1484, deform largely by  $\langle 112 \rangle$  dislocations separated by stacking faults. While these dislocations and stacking faults typically nucleate  $\gamma/\gamma'$  interfaces prior to shearing the  $\gamma'$  phase, this configuration is relatively stable in the  $\gamma$  matrix as well. As a result, these dislocation ribbons likely shear the secondary  $\gamma'$  in a similar manner to shear of the primary  $\gamma'$ . It has even been suggested that the secondary  $\gamma'$  may act to stabilize the dislocation ribbons through the  $\gamma$  channels between primary precipitates. Additionally, it should be noted that there is no APB formed in the  $\gamma$  matrix so the dislocation pairs (and associated stacking faults) tend to separate further apart in the  $\gamma$  channels.<sup>16, 17, 63</sup> Clearly the secondary  $\gamma'$  present in the  $\gamma$  channels plays a role in creep deformation during both primary and tertiary creep. The ability of PWA 1484 to produce large primary creep strains while PWA 1480 does not, though, must be linked to another material attribute as the uniform presence of secondary  $\gamma'$  in all three alloys did not yield similar behaviors.

## Composition

Alloy composition clearly controls several aspects of mechanical behavior. From controlling the strengths of phases to the lattice misfit, composition plays a direct role in deformation. Several key compositional changes were made from PWA 1480 to PWA 1484. While the effect of composition has already been discussed, a few points will be readdressed. Rhenium additions to superalloys have been praised for their potency in solid solution strengthening of the  $\gamma$  phase. This effect was so significant that the first three generations of superalloys are defined by their Re content (0 wt%, 3 wt%, and 6 wt%, respectively). Despite the clear benefit in strength, the addition of Re has been identified as potential contributor to large primary creep strains due to the large number of second and third generation alloys that show this behavior. While it is possible that Re has some sort of contributory effect on primary creep in second generation and later alloys, this investigation showed an improvement in creep properties and a slight decrease in primary creep when Re was added to PWA 1480. It was found, however, that PWA 1480+ appeared to produce more stacking faults than PWA 1480 indicating a possible decrease in the stacking fault energy of the  $\gamma'$  phase. A lower stacking fault energy would allow dislocations shearing the  $\gamma'$  phase to spread further leading to an increased potential of dislocation-dislocation interactions. In fact, the stacking faults observed in PWA 1480+ exhibited many interactions similar to the deformation found in specimens of other alloys interrupted near failure. As a result of this and other investigations, the effect of Re on the microstructure and properties of single crystal nickel base superalloys has been regarded as positive. Specifically, Re additions increase lattice misfit, improve creep life, improve tensile strength, reduce the  $\gamma'$  size, and reduce the rate of  $\gamma'$  coarsening.<sup>2-4, 8, 9, 77</sup> One disadvantage with

the use of large Re additions, though, is decreased stability against TCP phase formation as shown by the precipitation of TCP phases during primary creep of PWA 1480+.

There is also agreement within the superalloys community that Re segregates to the  $\gamma$  matrix during nucleation and growth of  $\gamma'$  precipitates. This effect is expected to cause an increase in lattice misfit near the  $\gamma/\gamma'$  interface as Re is rejected from the  $\gamma'$  precipitates result in an enriched region in the  $\gamma$  matrix. Research has also shown, however, that in the presence of W, up to 20% of the Re that has been added will segregate to the  $\gamma'$  precipitates.<sup>35</sup> As rhenium additions modify the compositions of the  $\gamma$  and  $\gamma'$  phases, changes in deformation mechanisms might be expected as a consequence of the potent strengthening effect.

Aside from the well known solid solution strengthening effect are reports of the formation of Re-rich clusters in the  $\gamma$  phase near the  $\gamma/\gamma'$  interface. Understanding the nature of the distribution (in the  $\gamma$  matrix) of the Re that has been rejected from the  $\gamma'$  phase could lead to improved model accuracy and potentially aid in the search for a Re replacement. Reported research is still contradictory in this area. The two leading theories, currently, indicate that Re may either form clusters around 10 nm in diameter or may form hardened shells in the  $\gamma$  matrix around the  $\gamma'$  precipitates. Recent studies, including the present one, have attempted to utilize the Local Electrode Atom Probe (LEAP) to examine the local concentration distribution of Re in the  $\gamma$  matrix with limited results. While publications have yet to be produced, a recently presented collaboration between Cambridge University (Cambridge, UK) and Oak Ridge National Lab (Oak Ridge, TN) pointed to possible evidence of the formation of Re clusters. The formation of clusters by solid solution strengtheners is not a new phenomenon and has been shown to occur with Cr and W as well.<sup>8, 35, 50</sup> Chromium clusters have been found to have the DO<sub>22</sub> crystal structure and are also formed due to rejection from the  $\gamma'$  phase. It is expected that

these clusters would make dislocation shear of the  $\gamma$  phase in the vicinity of the  $\gamma/\gamma'$  interface more difficult. Dislocations that encounter these regions are likely to be disrupted by changes in crystal structure and strength leading to greater buildup of dislocations at the  $\gamma/\gamma'$  interface.

How Re clusters or shells interact with dislocations and stacking faults during primary creep is certain to be the subject of many future investigations as, clearly, additional work is necessary. It still remains unclear what the interactions are between the rejected Re in the  $\gamma$  phase and the matrix dislocations. Additionally, the high price of Re has forced both industry and academia to begin researching viable alternative strengtheners to replace or reduce Re in future superalloys. Continued research into the rhenium effect as it relates to these interactions is likely to grow in the coming years.

The difference between PWA 1480 and PWA 1484, however, is more than just the addition of rhenium. PWA 1484 has increased solid solution strengthener/refractory content and decreased  $\gamma'$  hardening. Based on the present investigation, Re alone does not appear to cause increased primary creep. In fact, the opposite effect was realized in PWA 1480 when Re was added. With the many changes in alloy composition between the first generation PWA 1480 and the second generation PWA 1484, it is likely that the stacking fault energy and anti-phase boundary energy were also modified. These two properties very strongly influence shear of the  $\gamma'$  phase during creep leading to the possibility of reduced resistance to large primary creep strains caused by  $\gamma'$  shear.

### **Concluding Remarks**

The large primary creep strains exhibited by PWA 1484 were shown to occur through deformation processes consistent with  $\gamma'$  shear reported among some second generation superalloys. The first generation alloy PWA 1480, however, exhibited tertiary creep behavior

that is commonly reported among superalloys. The goal of this investigation was to study the effect of Re and secondary  $\gamma'$  precipitates on the primary creep behavior of PWA 1480 and PWA 1484. In order to see the effect of Re additions on PWA 1480, a third alloy was created by adding 3 wt% Re to PWA 1480 (the new alloy was named PWA 1480+ for this study).

Through this investigation, several aspects of the primary creep behavior of the PWA 1480 and PWA 1484 alloy systems have become clear. First, while all three alloys contained secondary  $\gamma'$  precipitates within the  $\gamma$  channels, only PWA 1484 exhibited large primary creep strains. While secondary  $\gamma'$  has been linked to large primary creep strains in CMSX-4, primary creep was limited for both PWA 1480 and PWA 1480+ despite the presence of secondary  $\gamma'$  in the matrix. It is reasonable to expect that these ultra-fine precipitates are rather coherent in nature due to their small size and, as such, would be susceptible to shear by matrix dislocations during tertiary creep as well as by dislocation ribbons (pairs of stacking faults) during primary creep.

Second, the addition of rhenium did not increase the primary creep strains produced in PWA 1480. This alloy addition (PWA 1480+) was responsible for decreased primary creep, lower creep rates, and longer creep lifetimes. While PWA 1480+ is clearly not suitable for service due to the early formation of TCP phases and reduced ductility, the potency of the solid solution strengthening effect of Re was again proven. Significant increases in yield strength and temperature capability of PWA 1480+ also accompanied the improved creep properties when compared to PWA 1480. The exact nature of the “Rhenium Effect” still eludes researchers to this day; however, it can be seen to offer substantial benefits over the current alternative strengtheners. The LEAP data presented herein affirmed the expected rejection of Re from the  $\gamma'$

precipitates into the  $\gamma$  matrix. An enriched layer was found along the  $\gamma$  side of the  $\gamma/\gamma'$  interface, though evidence proving the formation of clusters or shells was not produced.

Third, the HT age was reasonably effective at reducing the primary creep strains of PWA 1484 without reducing the lifetime or increasing the secondary stage creep rate. This effect has been attributed to a decrease in coherency at the  $\gamma/\gamma'$  interface. Decreased coherency may have increased the difficulty of nucleating dislocation ribbons in order to shear the  $\gamma'$  phase. This effect would result in increased hardening and an earlier termination of primary creep due to the generation of more interfacial dislocations. PWA 1480 showed no response to age heat treatment because the already difficult ability to produce stacking faults within the alloy prevented significant primary creep. As a result, PWA 1480 only exhibited the amount of primary creep that would be expected from an alloy deforming primarily by dislocations confined to the  $\gamma$  matrix. The Re modification of PWA 1480 was observed to increase stacking fault production slightly; however, the stacking fault energy may have been lowered leading to increased dislocation interactions and the formation of “locks” leading to low primary creep strains. More work is necessary to fully understand the nature of the primary creep deformation mechanism of PWA 1480+ due to the appearance of deformation structures more often reported in specimens terminated near failure.

The origin of large primary creep strains is likely not the result of a single cause. Several investigations have attempted to point out the primary cause only to reveal several underlying issues that contribute to the primary creep behavior. The current investigation approached the problem of primary creep by attempting to illustrate the effects of rhenium additions and age heat treatment. Both of these processing changes can impact primary creep. The Re addition reduced primary creep and improved creep performance of PWA 1480. Utilizing a higher age

temperature produced less primary creep in PWA 1484 specimens. Several other factors, however, should be considered when designing alloys to avoid this behavior. Alloy composition, for instance, involves several synergistic effects among alloying additions. Even small changes in composition can impact microstructural properties like lattice misfit, stacking fault energy, APB energy, and the strengths of the  $\gamma$  and  $\gamma'$  phases (among others). The primary creep behavior of PWA 1484 is most likely due to an “ideal” combination of the following: lower volume fraction of  $\gamma'$ , changes in SFE and APB, slightly narrower  $\gamma$  channel widths, stabilization of stacking faults across  $\gamma$  channels by secondary  $\gamma'$ , higher misfit stresses superimposed on the applied stress, and an increased ease of nucleation of  $\langle 112 \rangle$  dislocation ribbons in the  $\gamma'$  phase.

Future development of single crystal alloys for gas turbine engines will continue to pursue higher temperature capability; however, additional emphasis has been placed on lower temperature properties as the applied loads are increasing in the lower temperature regions of turbine blades. While the increased concern regarding large primary creep strains will continue to yield a deeper understanding of this behavior, the effect of rhenium will bear greater scrutiny in the future. Rhenium related research will focus on developing new alternative strengthening approaches in order to reduce Re consumption. As a result, renewed investigation into how Re achieves its strengthening effect, such as this study, will aid future alloy development strategies.

## CHAPTER 9 CONCLUSION

### Conclusions

This investigation into the primary creep behavior of the single crystal nickel base superalloys PWA 1480 and PWA 1484 has led to the following conclusions:

- The ability of PWA 1484 to exhibit large primary creep strains during testing at low temperatures and high stresses appears to be linked to a combination of many factors including secondary  $\gamma'$ , composition,  $\gamma$  channel width, stacking fault energy, anti-phase boundary energy, and  $\gamma'$  volume fraction.
- The first generation superalloy PWA 1480 did not produce large primary creep strains when subjected to a wide range of creep loads (including the application of stress equal to 90% of the yield strength of PWA 1480). From these results, it is concluded that large primary creep strains are the result of a combination of microstructural and compositional attributes (such as listed above for PWA 1484).
- Stated another way, it is unlikely that a single cause is responsible for the production of large primary creep strains. The first generation superalloy, PWA 1480, appears to be incapable of exhibiting large primary creep strains because the deformation during creep is contained within the  $\gamma$  matrix as  $\langle 110 \rangle$  dislocations that shear the secondary  $\gamma'$ , but not the primary  $\gamma'$  precipitates. The second generation superalloy, PWA 1484, allows the matrix dislocations generated during the incubation period to enter the  $\gamma'$  as  $\langle 112 \rangle$  dislocation ribbons that are capable of shearing the  $\gamma'$  phase on a large scale. The specific microstructural attributes responsible for the entry of dislocations into the  $\gamma'$  phase are still not entirely clear and are likely the result of increased sensitivity due to many factors.
- The rhenium addition to PWA 1480+ resulted in lowered primary creep and secondary creep rate as well as increased rupture life (compared with PWA 1480). This effect is most likely due to the already known solid solution strengthening effect and a lowered stacking fault energy. The former effect increased load bearing capability and resistance to dislocation motion, while the latter effect resulted in wider separations of dislocations in the  $\gamma'$  phase that led to dislocation interactions and lock formation. Both effects aided in improving the creep life of PWA 1480+.
- The use of the high temperature aging heat treatment reduced the primary creep strain exhibited by PWA 1484 by nearly half at all conditions. This effect is attributed to reduced coherency at the  $\gamma/\gamma'$  interface that resulted in an increase in interfacial dislocations. These “forest” dislocations added resistance to the  $\gamma'$  shear mechanisms active in PWA 1484 as well as interacted with matrix dislocations to form interfacial networks of dislocations earlier during primary creep. The earlier formation of dislocation networks would lead to the earlier onset of secondary creep and a reduction in the primary creep strain exhibited by the alloy.

## Future Directions

As a result of this work, several future paths of research have been opened. These future directions are listed in brief below:

- Additional work involving alloy modification and the resulting effects on overall and primary creep behavior: Suggested alloy modifications are PWA 1484 without Re and alloys that substitute W for Re at various ratios. Removing Re from PWA 1484 would be useful to determine if the stacking fault formation in the alloy is indeed linked to Re content. Substitutions of W (or another refractory solid solution strengthener) for Re could be used with a slightly different goal. The rising cost of Re warrants investigation in strengthening alternatives that are lower in cost and are more readily available. As with any alloy modification work, these projects would require broad characterization and testing to examine the effects of the modifications.
- Continued X-ray diffraction studies of the change in lattice misfit as a function of heat treatment: Additional XRD studies would be useful to aid in determination of the correlation between lattice misfit and primary creep. Because primary creep appears to be impacted directly by the  $\gamma/\gamma'$  interface, any technique that sheds light on the nature of the interface would be useful in generating a complete understanding the primary creep process.
- Additional creep testing with specimens prepared without secondary  $\gamma'$  could eliminate confusion regarding the effect these precipitates have on the primary creep behavior of these alloys. While a simple furnace cool following aging is the only processing change necessary to create this condition, extra coarsening and decreased coherency of the  $\gamma'$  will result. Care would need to be directed towards proper heat treatment development to ensure that the end product maintains similar values for  $\gamma'$  size and coherency. This is to eliminate the possibility that the decrease in primary creep associated with secondary  $\gamma'$  free matrix channels is actually due to an enhanced ability to work harden due to increased incoherency.
- Renewed work on the Local Electrode Atom Probe could serve to answer the question of Re shell or cluster formation. As Re is rejected from the precipitates into the matrix, exactly how the element is distributed in the  $\gamma$  matrix is in question. If ordered clusters or disordered shells are found, then the use of other strengthening elements that behave similarly might improve the strength of alloys and/or allow for further reductions in Re content.
- Detailed TEM analysis of the deformation mechanism in PWA 1480+ could yield information on how the alloy achieves such a low creep rate and long lifetime. The early appearance of deformation structures commonly tied to failure requires investigation to understand how PWA 1480+ is capable of superior creep properties to PWA 1484 over the temperature range in question (700°C-815°C)

## APPENDIX A DIFFERENTIAL THERMAL ANALYSIS

Differential thermal analysis, or DTA, was performed on six specimens for the purpose of designing new solution heat treatments for all three alloys: PWA 1480, PWA 1484, and PWA 1480+. In the case of single crystal superalloys, the solution heat treatment is necessary to dissolve the  $\gamma/\gamma'$  eutectics that remain after solidification as well as to promote homogenization of the alloy due to the high degree of segregation exhibited between the dendrites and the interdendritic regions of the alloy. Thus a solution heat treatment for these alloys must not simply exceed the  $\gamma'$  solvus temperature long enough to dissolve the remaining eutectics. These heat treatments must also approach the solidus temperature in order to deliver enough thermal energy into the alloy to allow for diffusion of slow diffusing elements like tungsten, tantalum, and rhenium. The final heat treatments selected for this study stop just 5°C, 8°C, and 3°C short of the solidus temperatures for each of the aforementioned alloys, respectively. It should also be noted that the final hold temperature for the PWA 1484 HT3 heat treatment equals the solidus temperature following the HT1 heat treatment. The final temperature for PWA 1480+ exceeds the solidus of the as-cast condition by 19°C. The fact that the HT3 heat treatment can be performed without incipient melting in the alloy is an indication of just how much the solidus of these alloys can be suppressed as a result of segregation. Throughout the course of the heat treatment, the solidus temperature of the interdendritic region climbs as homogenization proceeds. The solidus values after the HT2 heat treatment are likely within a few degrees of the actual values for these alloys<sup>44, 45, 53</sup>.

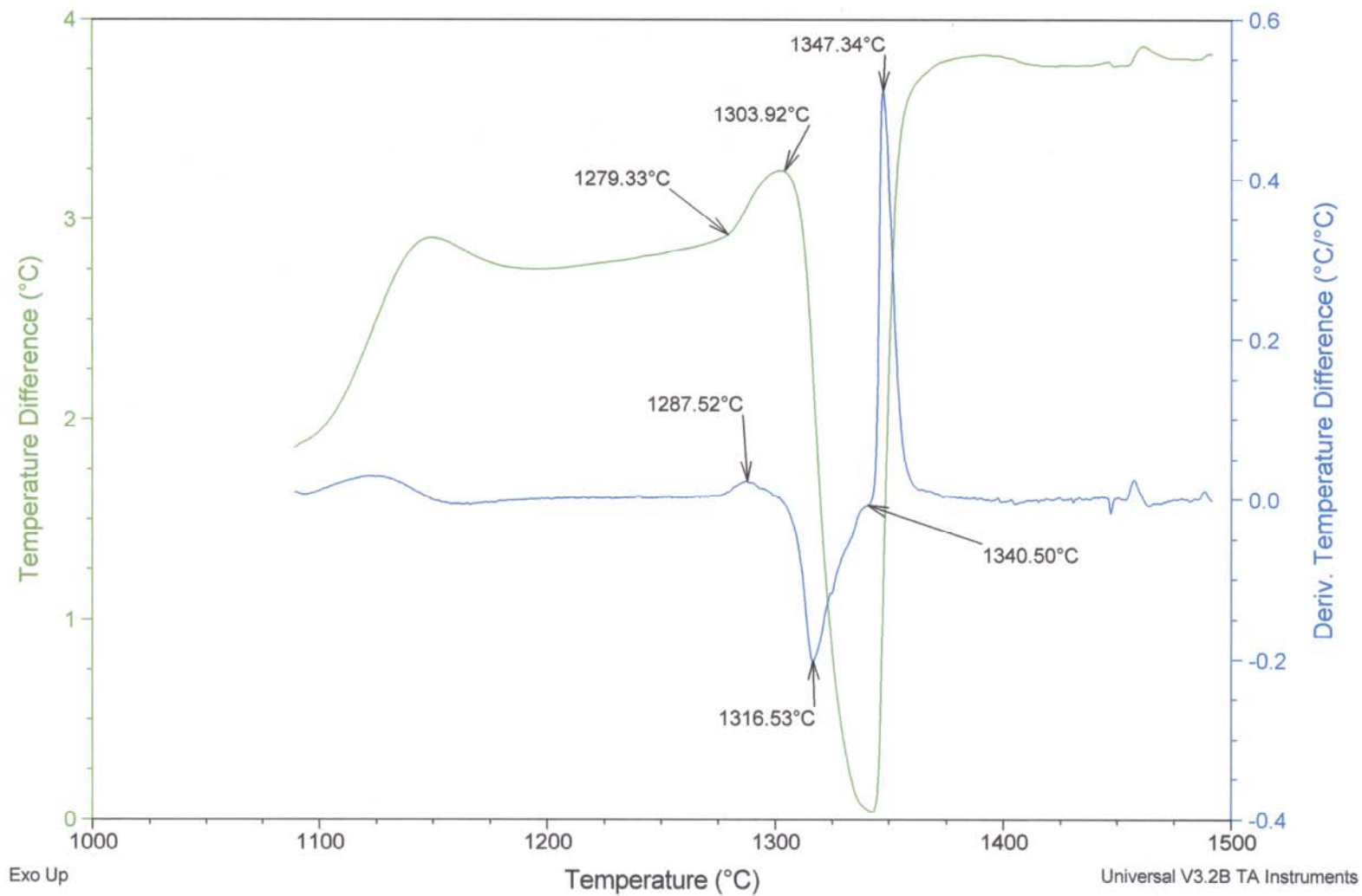


Figure A-1. DTA trace for PWA 1480 in the HT1 condition.

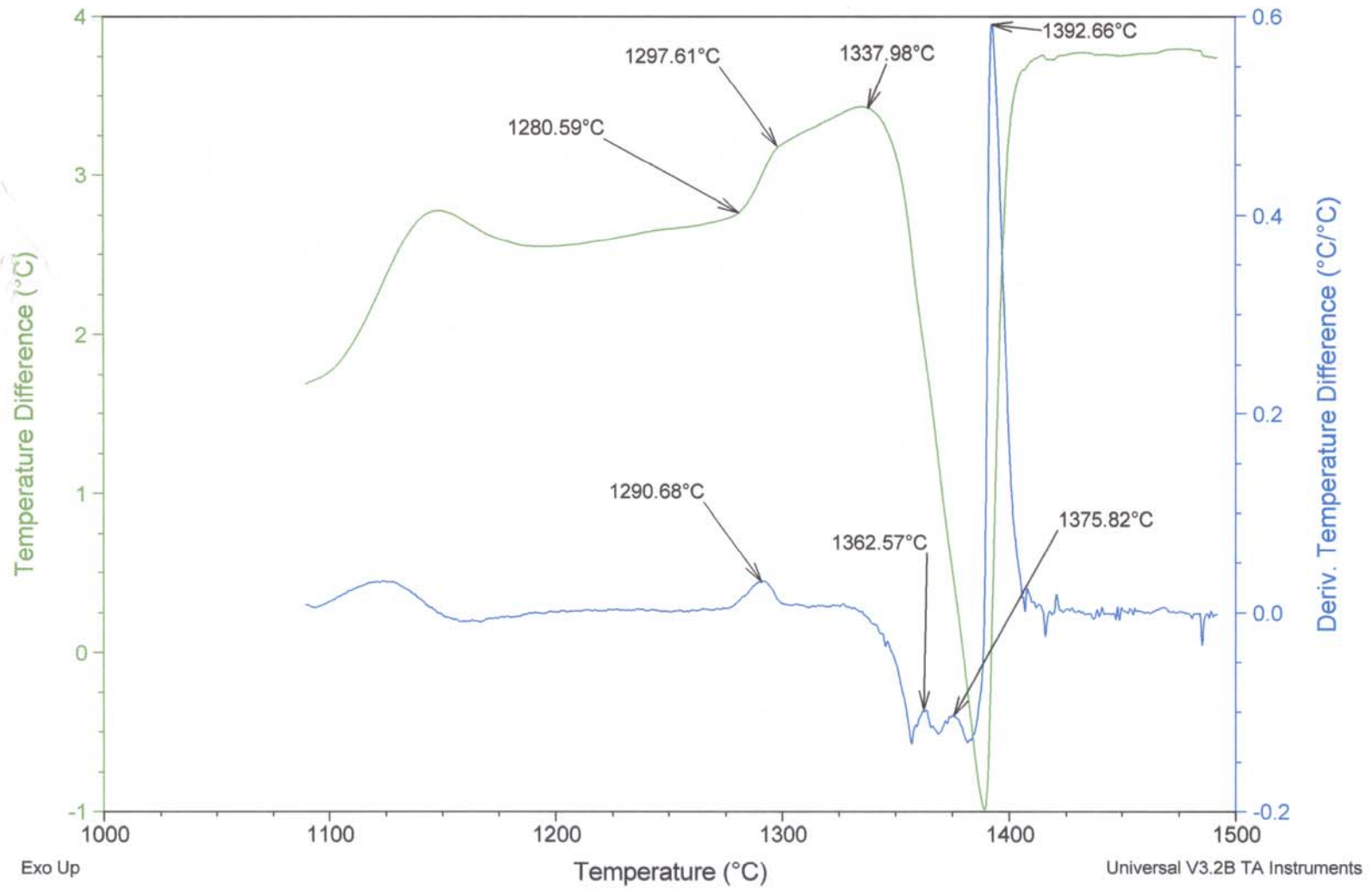


Figure A-2. DTA trace for PWA 1484 in the HT1 condition.

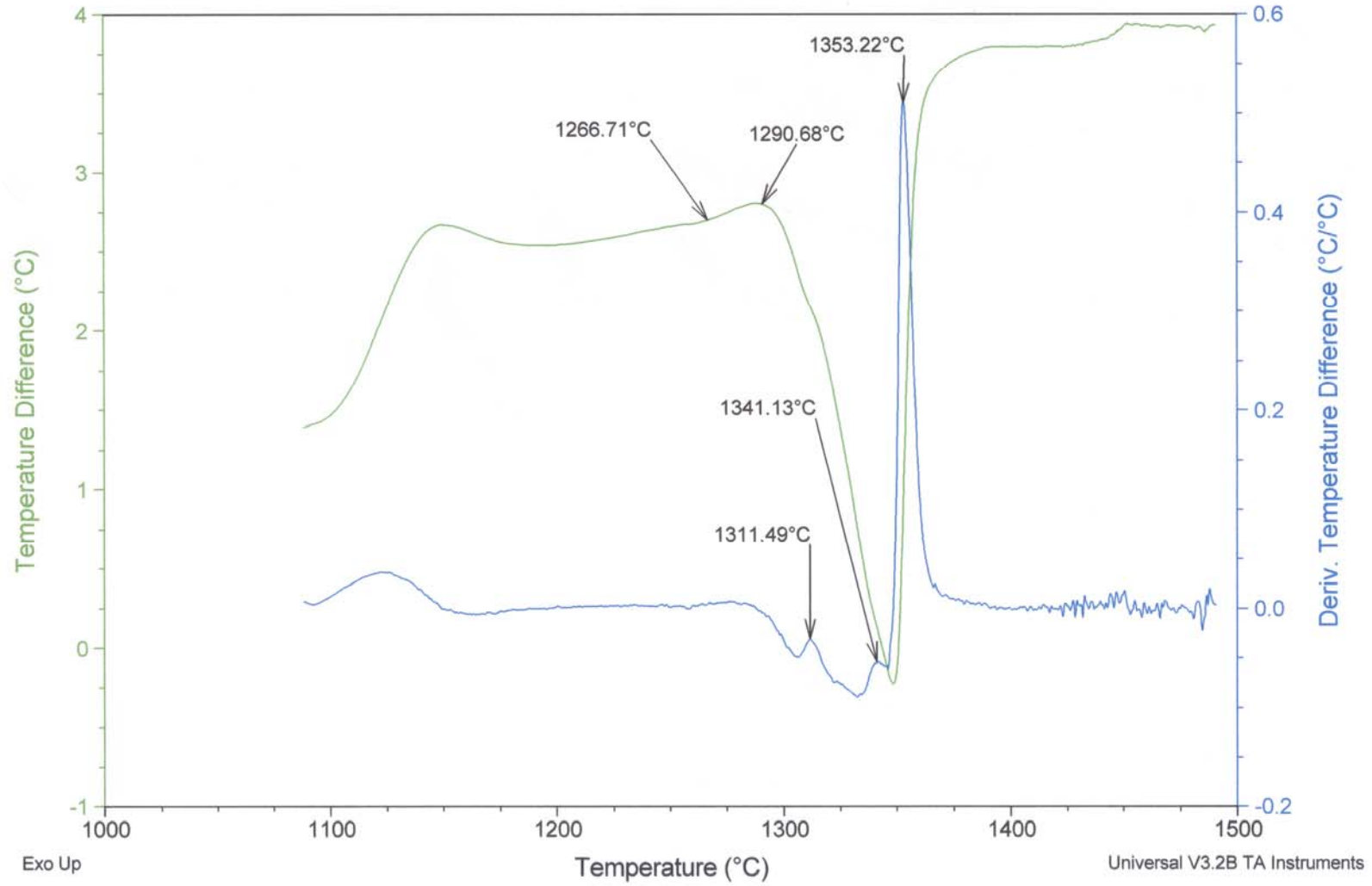


Figure A-3. DTA trace for PWA 1480+ in the HT0 condition.

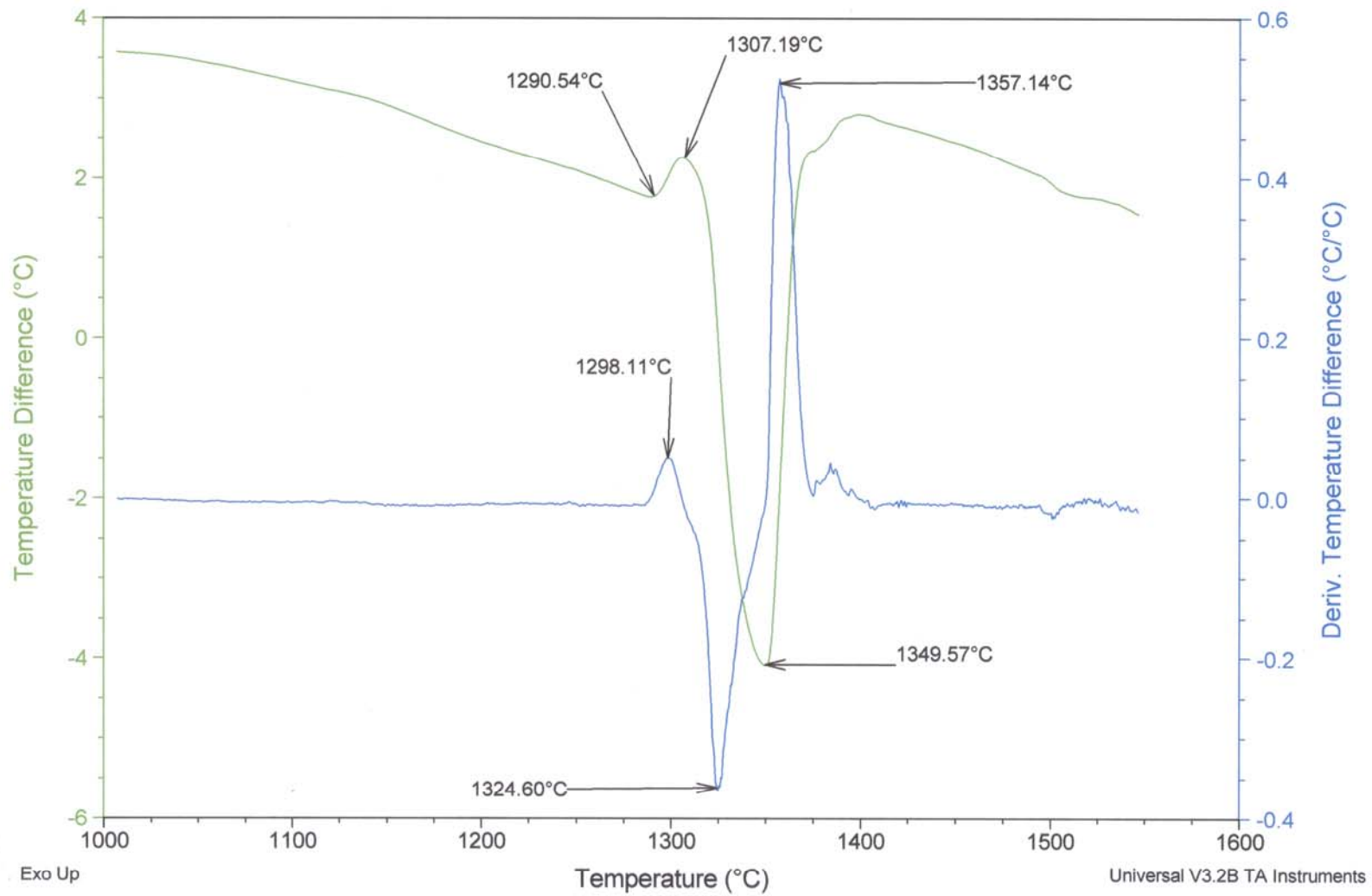


Figure A-4. DTA trace for PWA 1480 in the HT2 condition.

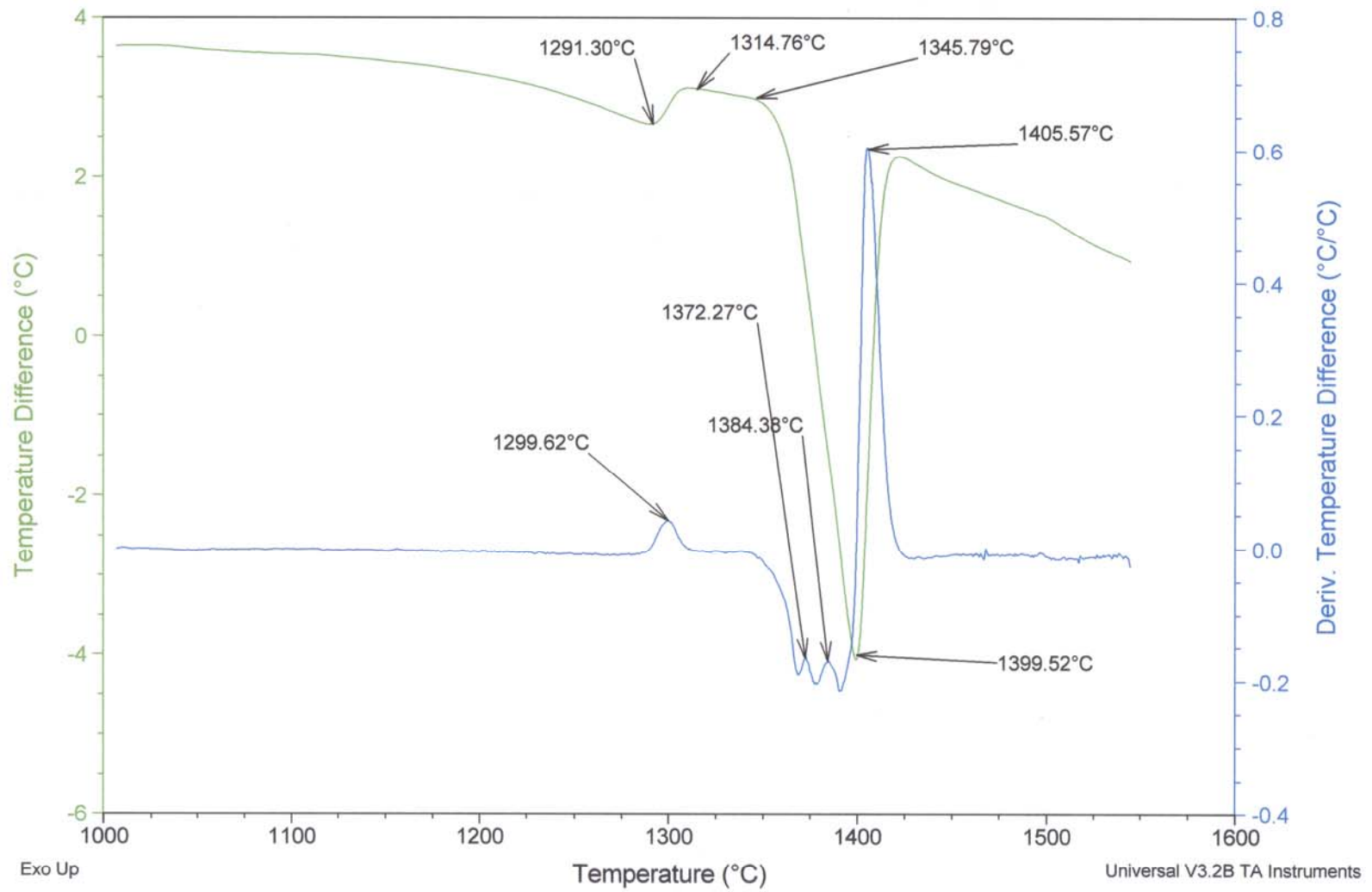


Figure A-5. DTA trace for PWA 1484 in the HT2 condition.

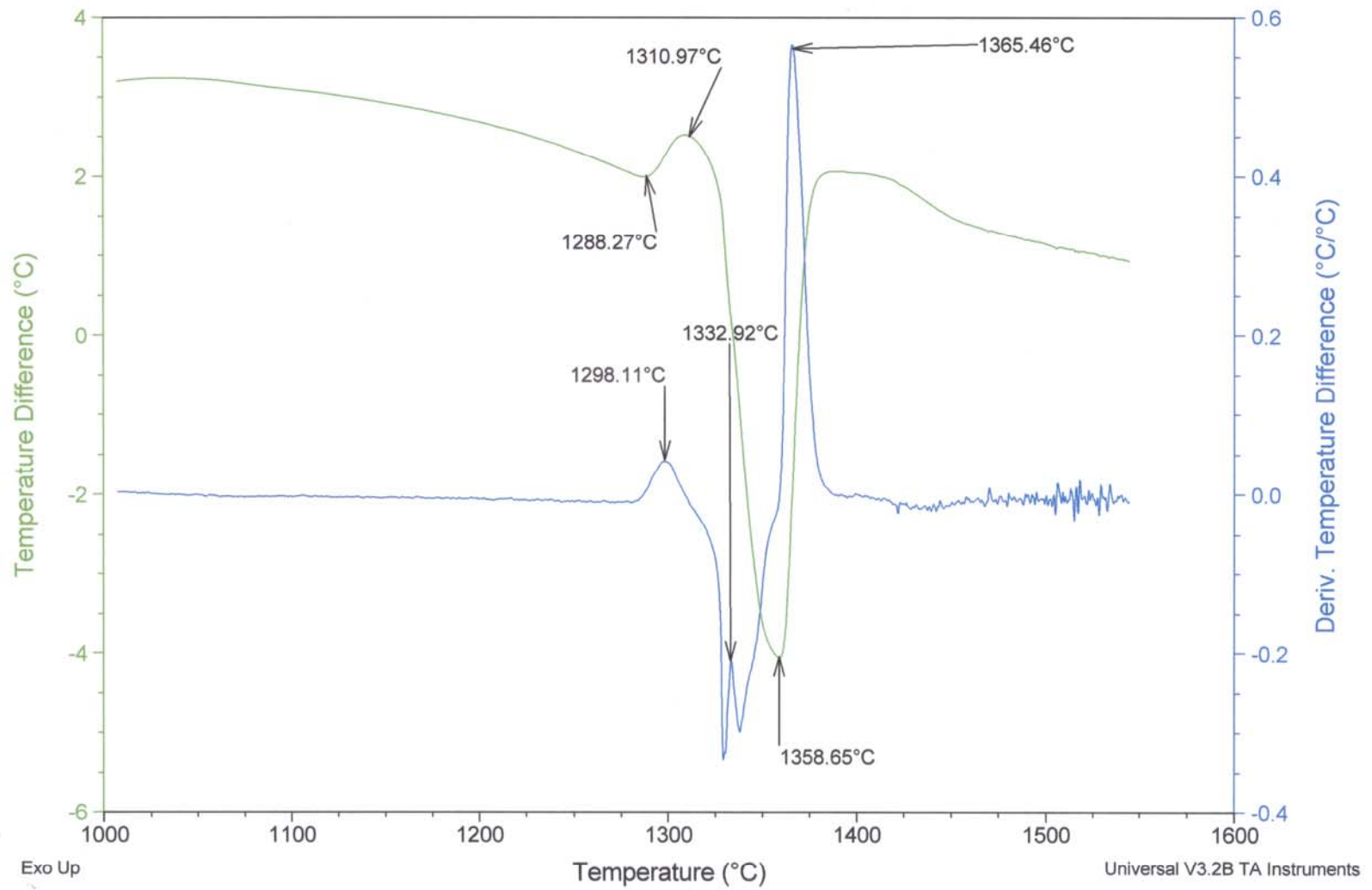


Figure A-6. DTA trace for PWA 1480+ in the HT2 condition.

## APPENDIX B XRD PEAK DECONVOLUTION

The use of X-ray diffraction to determine the lattice parameters for the  $\gamma$  and  $\gamma'$  phases for misfit determination requires the use of peak deconvolution to separate the contribution of both phases from the total intensity of the peak. The ordered  $L1_2$  space group of the  $\gamma'$  precipitates allows for all simple cubic reflections to appear due to the difference in structure factor of the Ni and Al atoms in the unit cell. The fcc space group of the  $\gamma$  matrix, however, only allows for planes in which hkl from the miller index of the plane in question is all even or all odd. For example, the (002), (222), (333) planes show positive intensity while the (001), (011), (321) planes will show no intensity.

In single crystal specimens oriented with a [001] surface normal under Cu  $k_{\alpha}$  radiation as used in this study, the  $\gamma$  phase will only yield the following peaks between the  $2\theta$  angles of  $10^\circ$  and  $140^\circ$  (using the diffractometers described in Chapter 3): (111), (002), (022), (113), (222), and (004). The  $\gamma'$  precipitate phase will yield peaks at the same planes as the  $\gamma$  phase with the addition of mixed index phases like (001) and (011). From the above list of peaks produced by the  $\gamma$  phase, the (002) and (004) peaks show the greatest intensity and as a result are the most useful for quantitative XRD analysis. The (002) peak can be found for all three alloys between a  $2\theta$  angle of  $50.5^\circ$  and  $51.5^\circ$  while the (004) peak can be found between  $117.5^\circ$  and  $119.0^\circ$ . While both peaks can be used for lattice parameter determination (and subsequent misfit calculation), the higher angle peak, (004), will produce the more accurate result because at higher  $2\theta$  angles the contributions from the  $\gamma$  and  $\gamma'$  phase have a greater separation than at lower angles. Additionally, since the radiation used contains both Cu  $k_{\alpha 1}$  and Cu  $k_{\alpha 2}$ , the separate contribution from both wavelengths of radiation is also displaced further.

Peak deconvolution was accomplished using the MDI Jade (ver. 7) software package on a workstation at the University of Central Florida's Advanced Materials Processing and Analysis Center (AMPAC). The software package allows for easy manipulation and indexing of diffraction patterns as well as peak deconvolution. Utilizing 6 constraints including peak height, Full Width at Half Maximum (FWHM), location, skew (symmetry), and type of distribution (Gaussian, Lorentzian, etc.), XRD scans of (002) and (004) peaks could be mathematically separated into as many peaks as necessary. For this investigation, scans were taken of both the (002) and (004) peaks. Each peak was then separated to produce a total of four peaks as follows:  $\gamma$  phase Cu  $k_{\alpha 1}$ ,  $\gamma$  phase Cu  $k_{\alpha 2}$ ,  $\gamma'$  phase Cu  $k_{\alpha 1}$ , and  $\gamma'$  phase Cu  $k_{\alpha 2}$ . All peaks were assumed to have a Gaussian distribution in agreement with published work.<sup>46, 59, 60, 85</sup> Deconvolution was performed by first selecting the approximate peak locations with a special "peak fit cursor" and the peak fit window was opened. After selecting the approximate location of the Cu  $k_{\alpha 1}$  peaks for the two phases (the software automatically accounts for the presence of Cu  $k_{\alpha 2}$ ), the deconvolution algorithm allows for further modifying of the starting conditions. The Gaussian distribution was selected and the skew was set to zero initially. The FWHM was not specified to allow the software to find the best fit. The first deconvolution was then performed.

The result of the deconvolution appears as a table of data describing the fit as well as a plot of the raw data and the model fit. The calculated centers of the Cu  $k_{\alpha 1}$  peaks for both the  $\gamma$  and  $\gamma'$  phases were used for lattice parameter determination. To further reduce the error of fit, deconvolution was run a second time with the option to skew the peaks in use. This allows for a "better" fit (or reduction in residual error of fit), but is not necessarily better for analysis. Each deconvolution should be evaluated to ensure that the algorithm did not skew the peaks too much resulting in unrealistic peak shifts.

The tables presented in Tables B-1 through B-8 are the resulting lattice misfit values calculated from the results of the deconvolution of the XRD data that were collected. The figures that follow are the results of the deconvolution algorithm. They have been included to aid in the understanding of the deconvolution process and to compare the quality of the fit for each peak. Each peak was analyzed with this method at least once, while several were analyzed several times. The degree of peak skew is highlighted at the top of each figure. Blue designates a result with zero skew while orange designates nonzero skew values. Also given are the Full Width at Half Maximum values, which help to define how broad or narrow a peak may be. For the purposes of lattice parameter calculation, the tall, narrow peak is assumed to be the  $\gamma'$  contribution while the shorter, broader peak is assumed to represent the  $\gamma$  contribution. This assumption is made because the  $\gamma'$  phase is highly ordered (therefore narrower) and though it is a precipitate phase it is present in volume fractions greater than 70% (therefore taller, more intense). The solid solution strengthened  $\gamma$  phase would be expected to be significantly broader in width and of less intensity due to a smaller volume fraction and the random nature of the solid solution.<sup>46, 59</sup>

Note: Two methods were employed to codify the data presented in Tables B-1 through B-8. A number code was used to differentiate the overaging heat treatments and a color code was used to differentiate attempts at deconvolution. These two methods are explained below:

- Number code: The last digit in the specimen name indicates which of the four overaging heat treatments to which the specimen was exposed: xxxx3 for 4 hr., xxxx4 for 10 hr., xxxx5 for 100 hr., and xxxx6 for 1000 hr. at 1080°C
- Color code: Tan for the first attempt, Blue for skewed deconvolution, and yellow for unskewed deconvolution

Table B-1. PWA 1480 (002) peak lattice misfit calculations.

	$h^2+k^2+l^2$	tall/short?	$2\theta$	$\theta$	$\lambda^2$	$\sin^2\theta$	$a^2$	$a$	$\delta$
<b>09113</b>	4	t	50.81	25.41	2.373	0.1841	12.8943	3.5909	0.0918
	4	s	50.86	25.43	2.373	0.1844	12.8707	3.5876	
	4	t	50.82	25.41	2.373	0.1841	12.8924	3.5906	0.0790
	4	s	50.86	25.43	2.373	0.1844	12.8721	3.5878	
	4	t	50.79	25.39	2.373	0.1839	12.9057	3.5925	-0.0074
	4	s	50.78	25.39	2.373	0.1839	12.9076	3.5927	
	4	t	50.80	25.40	2.373	0.1840	12.8995	3.5916	-0.1416
	4	s	50.72	25.36	2.373	0.1835	12.9361	3.5967	
	4	t	50.85	25.42	2.373	0.1843	12.8778	3.5886	-0.0092
	4	s	50.84	25.42	2.373	0.1843	12.8801	3.5889	
<b>09114</b>	4	t	50.77	25.38	2.373	0.1838	12.9142	3.5936	0.1103
	4	s	50.83	25.41	2.373	0.1842	12.8858	3.5897	
	4	t	50.79	25.40	2.373	0.1839	12.9038	3.5922	0.1873
	4	s	50.89	25.45	2.373	0.1846	12.8556	3.5855	
	4	t	50.81	25.40	2.373	0.1840	12.8972	3.5913	0.0018
	4	s	50.81	25.40	2.373	0.1840	12.8967	3.5912	
<b>09115</b>	4	t	50.74	25.37	2.373	0.1836	12.9280	3.5956	-0.0202
	4	s	50.73	25.36	2.373	0.1835	12.9333	3.5963	
	4	t	50.74	25.37	2.373	0.1836	12.9276	3.5955	-0.1400
	4	s	50.67	25.33	2.373	0.1831	12.9638	3.6005	
	4	t	50.73	25.37	2.373	0.1835	12.9309	3.5960	-0.3800
	4	s	50.53	25.26	2.373	0.1821	13.0295	3.6096	
<b>09116</b>	4	t	50.72	25.36	2.373	0.1835	12.9371	3.5968	0.1416
	4	s	50.80	25.40	2.373	0.1840	12.9005	3.5917	
	4	t	50.68	25.34	2.373	0.1832	12.9552	3.5993	0.1289
	4	s	50.75	25.38	2.373	0.1837	12.9218	3.5947	
	4	t	50.72	25.36	2.373	0.1835	12.9366	3.5967	0.0699
	4	s	50.76	25.38	2.373	0.1837	12.9185	3.5942	
	4	t	50.72	25.36	2.373	0.1834	12.9380	3.5969	0.0847
	4	s	50.77	25.38	2.373	0.1837	12.9161	3.5939	
	4	t	50.71	25.36	2.373	0.1834	12.9423	3.5975	-0.1364
	4	s	50.64	25.32	2.373	0.1829	12.9777	3.6025	
	4	t	50.71	25.35	2.373	0.1834	12.9433	3.5977	-0.1401
	4	s	50.63	25.32	2.373	0.1829	12.9796	3.6027	

Table B-2. PWA 1480+ (002) peak lattice misfit calculations.

	$h^2+k^2+l^2$	tall/short?	$2\theta$	$\theta$	$\lambda^2$	$\sin^2\theta$	$a^2$	$a$	$\delta$
<b>12123</b>	4	t	50.75	25.38	2.373	0.1836	12.9233	3.5949	0.1324
	4	s	50.82	25.41	2.373	0.1841	12.8891	3.5901	
	4	t	50.72	25.36	2.373	0.1835	12.9356	3.5966	0.0552
	4	s	50.75	25.38	2.373	0.1837	12.9214	3.5946	
	4	t	50.70	25.35	2.373	0.1833	12.9495	3.5985	0.0037
	4	s	50.70	25.35	2.373	0.1833	12.9485	3.5984	
	4	t	50.70	25.35	2.373	0.1833	12.9495	3.5985	-0.0166
	4	s	50.69	25.34	2.373	0.1832	12.9538	3.5991	
	4	t	50.73	25.37	2.373	0.1835	12.9328	3.5962	0.0405
	4	s	50.75	25.38	2.373	0.1837	12.9223	3.5948	
	4	t	50.73	25.37	2.373	0.1835	12.9318	3.5961	0.0239
	4	s	50.75	25.37	2.373	0.1836	12.9257	3.5952	
	4	t	50.69	25.35	2.373	0.1833	12.9504	3.5987	-0.0682
	4	s	50.66	25.33	2.373	0.1830	12.9681	3.6011	
	4	t	50.75	25.37	2.373	0.1836	12.9247	3.5951	0.0460
	4	s	50.77	25.39	2.373	0.1838	12.9128	3.5934	
4	t	50.75	25.37	2.373	0.1836	12.9238	3.5950	0.0276	
4	s	50.76	25.38	2.373	0.1837	12.9166	3.5940		
<b>12124</b>	4	t	50.72	25.36	2.373	0.1834	12.9395	3.5971	-0.0607
	4	s	50.75	25.37	2.373	0.1836	12.9238	3.5950	
	4	t	50.73	25.36	2.373	0.1835	12.9342	3.5964	-0.0516
	4	s	50.70	25.35	2.373	0.1833	12.9476	3.5983	
	4	t	50.73	25.36	2.373	0.1835	12.9342	3.5964	-0.0534
4	s	50.70	25.35	2.373	0.1833	12.9480	3.5983		
<b>12125</b>	4	t	50.67	25.34	2.373	0.1831	12.9600	3.6000	-0.1381
	4	s	50.75	25.37	2.373	0.1836	12.9242	3.5950	
	4	t	50.70	25.35	2.373	0.1833	12.9471	3.5982	-0.1012
	4	s	50.76	25.38	2.373	0.1837	12.9209	3.5946	
	4	t	50.53	25.26	2.373	0.1821	13.0300	3.6097	-0.4095
	4	s	50.75	25.37	2.373	0.1836	12.9238	3.5950	
	4	t	50.52	25.26	2.373	0.1821	13.0324	3.6100	-0.4206
4	s	50.75	25.38	2.373	0.1836	12.9233	3.5949		
<b>12126</b>	4	t	50.77	25.38	2.373	0.1837	12.9161	3.5939	-0.0129
	4	s	50.76	25.38	2.373	0.1837	12.9195	3.5944	
	4	t	50.76	25.38	2.373	0.1837	12.9180	3.5942	-0.0129
	4	s	50.75	25.38	2.373	0.1837	12.9214	3.5946	
	4	t	50.76	25.38	2.373	0.1837	12.9171	3.5940	-0.0405
	4	s	50.74	25.37	2.373	0.1836	12.9276	3.5955	
	4	t	50.76	25.38	2.373	0.1837	12.9190	3.5943	-0.0423
	4	s	50.74	25.37	2.373	0.1836	12.9299	3.5958	
	4	t	50.76	25.38	2.373	0.1837	12.9180	3.5942	-0.1160
	4	s	50.70	25.35	2.373	0.1833	12.9480	3.5983	
	4	t	50.76	25.38	2.373	0.1837	12.9195	3.5944	-0.1123
4	s	50.70	25.35	2.373	0.1833	12.9485	3.5984		

Table B-3. PWA 1484 (002) peak lattice misfit calculations.

	$h^2+k^2+l^2$	tall/short?	$2\theta$	$\theta$	$\lambda^2$	$\sin^2\theta$	$a^2$	a	$\delta$
<b>09223</b>	4	t	50.79	25.39	2.373	0.1839	12.9062	3.5925	0.1836
	4	s	50.89	25.44	2.373	0.1846	12.8589	3.5859	
	4	t	50.86	25.43	2.373	0.1844	12.8702	3.5875	0.0349
	4	s	50.88	25.44	2.373	0.1845	12.8612	3.5863	
	4	t	50.83	25.41	2.373	0.1842	12.8872	3.5899	-0.2281
	4	s	50.70	25.35	2.373	0.1833	12.9461	3.5981	
<b>09224</b>	4	t	50.77	25.39	2.373	0.1838	12.9123	3.5934	-0.0920
	4	s	50.72	25.36	2.373	0.1835	12.9361	3.5967	
	4	t	50.66	25.33	2.373	0.1831	12.9643	3.6006	-0.2049
	4	s	50.55	25.28	2.373	0.1823	13.0175	3.6080	
	4	t	50.66	25.33	2.373	0.1830	12.9671	3.6010	-0.1901
	4	s	50.56	25.28	2.373	0.1823	13.0165	3.6078	
	4	t	50.64	25.32	2.373	0.1829	12.9767	3.6023	-0.2605
	4	s	50.50	25.25	2.373	0.1819	13.0445	3.6117	
	4	t	50.63	25.32	2.373	0.1829	12.9786	3.6026	-0.2420
<b>09225</b>	4	t	50.49	25.24	2.373	0.1819	13.0493	3.6124	0.0740
	4	s	50.53	25.26	2.373	0.1821	13.0300	3.6097	
<b>09226</b>	4	t	50.72	25.36	2.373	0.1834	12.9385	3.5970	0.0865
	4	s	50.77	25.38	2.373	0.1837	12.9161	3.5939	
	4	t	50.82	25.41	2.373	0.1841	12.8896	3.5902	-0.2650
	4	s	50.68	25.34	2.373	0.1832	12.9581	3.5997	
	4	t	50.77	25.39	2.373	0.1838	12.9133	3.5935	-0.1436
	4	s	50.69	25.35	2.373	0.1833	12.9504	3.5987	
	4	t	50.77	25.39	2.373	0.1838	12.9123	3.5934	-0.0478
	4	s	50.75	25.37	2.373	0.1836	12.9247	3.5951	
	4	t	50.73	25.37	2.373	0.1835	12.9318	3.5961	-0.2027
	4	s	50.62	25.31	2.373	0.1828	12.9844	3.6034	
	4	t	50.73	25.37	2.373	0.1835	12.9309	3.5960	-0.1990
	4	s	50.63	25.31	2.373	0.1828	12.9825	3.6031	

Table B-4. PWA 1480 (004) peak lattice misfit calculations.

	$h^2+k^2+l^2$	tall/short?	$2\theta$	$\theta$	$\lambda^2$	$\sin^2\theta$	$a^2$	$a$	$\delta$
<b>09113</b>	16	t	118.05	59.03	2.373	0.7351	12.9139	3.5936	0.2487
	16	s	118.53	59.26	2.373	0.7388	12.8499	3.5847	
	16	t	118.07	59.03	2.373	0.7353	12.9116	3.5933	0.2092
	16	s	118.47	59.23	2.373	0.7383	12.8577	3.5858	
	16	s	118.10	59.05	2.373	0.7355	12.9074	3.5927	0.0293
	16	t	118.04	59.02	2.373	0.7351	12.9150	3.5937	
	16	t	118.02	59.01	2.373	0.7349	12.9177	3.5941	0.2332
	16	s	118.47	59.23	2.373	0.7383	12.8576	3.5857	
	16	t	118.04	59.02	2.373	0.7350	12.9160	3.5939	0.2871
	16	s	118.59	59.29	2.373	0.7392	12.8420	3.5836	
	16	t	118.01	59.00	2.373	0.7348	12.9195	3.5944	0.2733
	16	s	118.53	59.27	2.373	0.7388	12.8491	3.5846	
<b>9114</b>	16	t	118.01	59.00	2.373	0.7348	12.9198	3.5944	0.2120
	16	s	118.41	59.21	2.373	0.7379	12.8651	3.5868	
	16	t	118.01	59.00	2.373	0.7348	12.9198	3.5944	0.2156
	16	s	118.42	59.21	2.373	0.7380	12.8642	3.5867	
	16	t	117.98	58.99	2.373	0.7346	12.9229	3.5948	0.0519
	16	s	118.08	59.04	2.373	0.7354	12.9095	3.5930	
	16	t	117.97	58.99	2.373	0.7345	12.9246	3.5951	0.2090
16	s	118.37	59.19	2.373	0.7376	12.8707	3.5876		
<b>09115</b>									
<b>09116</b>	16	t	117.85	58.92	2.373	0.7336	12.9415	3.5974	0.1719
	16	s	118.18	59.09	2.373	0.7361	12.8971	3.5912	
	16	t	117.96	58.98	2.373	0.7344	12.9259	3.5953	0.0541
	16	s	117.86	58.93	2.373	0.7336	12.9398	3.5972	
	16	t	117.82	58.91	2.373	0.7334	12.9446	3.5979	0.1118
	16	s	118.04	59.02	2.373	0.7350	12.9157	3.5938	
	16	t	117.83	58.91	2.373	0.7334	12.9443	3.5978	0.1055
	16	s	118.03	59.01	2.373	0.7349	12.9170	3.5940	
	16	t	118.05	59.02	2.373	0.7351	12.9143	3.5937	-0.1376
	16	s	117.79	58.89	2.373	0.7331	12.9499	3.5986	
	16	t	118.00	59.00	2.373	0.7347	12.9206	3.5945	-0.1963
	16	s	117.63	58.81	2.373	0.7319	12.9714	3.6016	
	16	t	118.00	59.00	2.373	0.7347	12.9211	3.5946	0.0740
	16	s	117.86	58.93	2.373	0.7336	12.9403	3.5973	
	16	t	117.83	58.91	2.373	0.7334	12.9442	3.5978	0.1275
	16	s	118.07	59.04	2.373	0.7353	12.9112	3.5932	
	16	t	118.09	59.05	2.373	0.7354	12.9084	3.5928	0.1643
	16	s	117.78	58.89	2.373	0.7330	12.9509	3.5987	
16	t	118.01	59.01	2.373	0.7348	12.9193	3.5943	-0.1831	
16	s	117.66	58.83	2.373	0.7321	12.9667	3.6009		

Table B-5. PWA 1480+ (004) peak lattice misfit calculations.

	$h^2+k^2+l^2$	tall/short?	$2\theta$	$\theta$	$\lambda^2$	$\sin^2\theta$	$a^2$	a	$\delta$
<b>12123</b>	16	t	118.10	59.05	2.373	0.7355	12.9069	3.5926	-0.0597
	16	s	117.99	58.99	2.373	0.7346	12.9223	3.5948	
	16	t	117.96	58.98	2.373	0.7344	12.9264	3.5953	0.0084
	16	s	117.97	58.99	2.373	0.7345	12.9242	3.5950	
	16	t	117.96	58.98	2.373	0.7345	12.9256	3.5952	-0.0718
	16	s	118.10	59.05	2.373	0.7355	12.9070	3.5926	
	16	t	117.98	58.99	2.373	0.7346	12.9238	3.5950	-0.0550
	16	s	118.08	59.04	2.373	0.7354	12.9096	3.5930	
<b>12124</b>	16	t	117.98	58.99	2.373	0.7346	12.9233	3.5949	0.2833
	16	s	118.52	59.26	2.373	0.7388	12.8503	3.5847	
	16	t	117.98	58.99	2.373	0.7346	12.9230	3.5949	0.0441
	16	s	117.90	58.95	2.373	0.7340	12.9344	3.5964	
	16	t	117.99	58.99	2.373	0.7347	12.9222	3.5947	
	16	s	118.66	59.33	2.373	0.7398	12.8326	3.5823	
	16	t	117.98	58.99	2.373	0.7346	12.9237	3.5950	0.0304
	16	s	118.04	59.02	2.373	0.7350	12.9158	3.5939	
	16	t	117.98	58.99	2.373	0.7346	12.9230	3.5949	
	16	s	118.37	59.19	2.373	0.7376	12.8707	3.5876	
	16	t	117.98	58.99	2.373	0.7346	12.9238	3.5950	0.0288
	16	s	118.03	59.02	2.373	0.7350	12.9164	3.5939	
	16	t	117.97	58.99	2.373	0.7345	12.9245	3.5951	0.0210
	16	s	118.01	59.01	2.373	0.7348	12.9191	3.5943	
	16	t	117.98	58.99	2.373	0.7346	12.9229	3.5948	0.0231
	16	s	118.03	59.01	2.373	0.7350	12.9169	3.5940	
	16	t	117.98	58.99	2.373	0.7346	12.9235	3.5949	0.0194
	16	s	118.02	59.01	2.373	0.7349	12.9185	3.5942	
	16	t	117.98	58.99	2.373	0.7346	12.9230	3.5949	0.0231
	16	s	118.03	59.01	2.373	0.7349	12.9170	3.5940	
16	t	118.02	59.01	2.373	0.7349	12.9183	3.5942	0.0205	
16	s	117.98	58.99	2.373	0.7346	12.9235	3.5949		
<b>12126</b>	16	t	118.11	59.05	2.373	0.7356	12.9062	3.5925	0.1055
	16	s	118.31	59.15	2.373	0.7371	12.8790	3.5887	
	16	t	118.06	59.03	2.373	0.7352	12.9130	3.5935	0.1603
	16	s	118.36	59.18	2.373	0.7375	12.8716	3.5877	
	16	t	118.13	59.07	2.373	0.7358	12.9026	3.5920	0.0267
	16	s	118.08	59.04	2.373	0.7354	12.9095	3.5930	
	16	t	118.10	59.05	2.373	0.7355	12.9074	3.5927	0.0236
	16	s	118.05	59.03	2.373	0.7351	12.9135	3.5935	
	16	t	118.10	59.05	2.373	0.7355	12.9076	3.5927	0.0230
	16	s	118.05	59.03	2.373	0.7351	12.9135	3.5935	
	16	t	118.13	59.06	2.373	0.7357	12.9034	3.5921	0.0277
	16	s	118.08	59.04	2.373	0.7353	12.9105	3.5931	
	16	t	118.06	59.03	2.373	0.7352	12.9126	3.5934	0.0100
	16	s	118.04	59.02	2.373	0.7351	12.9151	3.5938	
	16	t	118.06	59.03	2.373	0.7352	12.9126	3.5934	0.0100
	16	s	118.04	59.02	2.373	0.7351	12.9151	3.5938	

Table B-6. PWA 1484 (004) peak lattice misfit calculations.

	$h^2+k^2+l^2$	tall/short?	$2\theta$	$\theta$	$\lambda^2$	$\sin^2\theta$	$a^2$	a	$\delta$
<b>09223</b>	16	t	118.33	59.16	2.373	0.7373	12.8765	3.5884	0.2839
	16	s	118.88	59.44	2.373	0.7415	12.8036	3.5782	
<b>09224</b>									
<b>09225</b>									
<b>09226</b>	16	t	118.43	59.22	2.373	0.7381	12.8623	3.5864	-0.1606
	16	s	118.13	59.06	2.373	0.7357	12.9037	3.5922	
	16	t	118.50	59.25	2.373	0.7385	12.8541	3.5853	-0.0145
	16	s	118.47	59.23	2.373	0.7383	12.8579	3.5858	
	16	t	118.52	59.26	2.373	0.7387	12.8508	3.5848	0.1898
	16	s	118.89	59.44	2.373	0.7415	12.8021	3.5780	
	16	t	118.50	59.25	2.373	0.7386	12.8539	3.5852	0.1346
	16	s	118.76	59.38	2.373	0.7405	12.8193	3.5804	
	16	t	118.49	59.24	2.373	0.7385	12.8549	3.5854	0.2445
	16	s	118.96	59.48	2.373	0.7421	12.7922	3.5766	
	16	t	118.32	59.16	2.373	0.7372	12.8771	3.5885	-0.0952
	16	s	118.51	59.25	2.373	0.7386	12.8527	3.5851	
	16	t	118.30	59.15	2.373	0.7371	12.8797	3.5888	-0.0936
	16	s	118.48	59.24	2.373	0.7385	12.8556	3.5855	
	16	t	118.26	59.13	2.373	0.7367	12.8861	3.5897	-0.1109
	16	s	118.47	59.23	2.373	0.7383	12.8576	3.5857	
	16	t	118.24	59.12	2.373	0.7366	12.8888	3.5901	-0.1146
	16	s	118.46	59.23	2.373	0.7382	12.8593	3.5860	
	16	t	118.45	59.22	2.373	0.7382	12.8607	3.5862	-0.2271
	16	s	118.01	59.01	2.373	0.7348	12.9192	3.5943	
16	t	118.25	59.12	2.373	0.7366	12.8876	3.5899	0.1120	
16	s	118.46	59.23	2.373	0.7383	12.8588	3.5859		

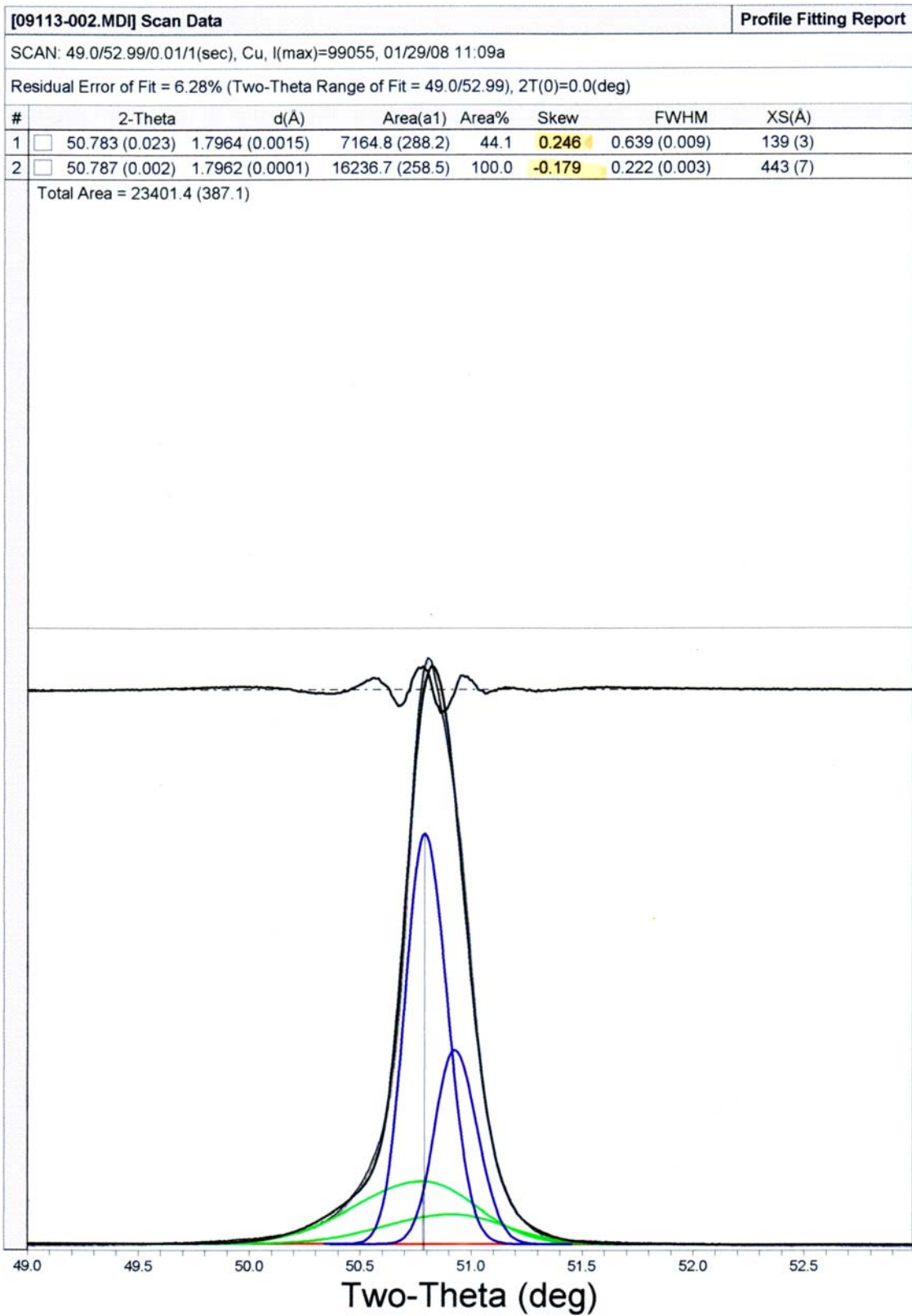


Figure B-1. XRD deconvolution of PWA 1480 (4hr. 1080°C, skewed, 6.28% error)

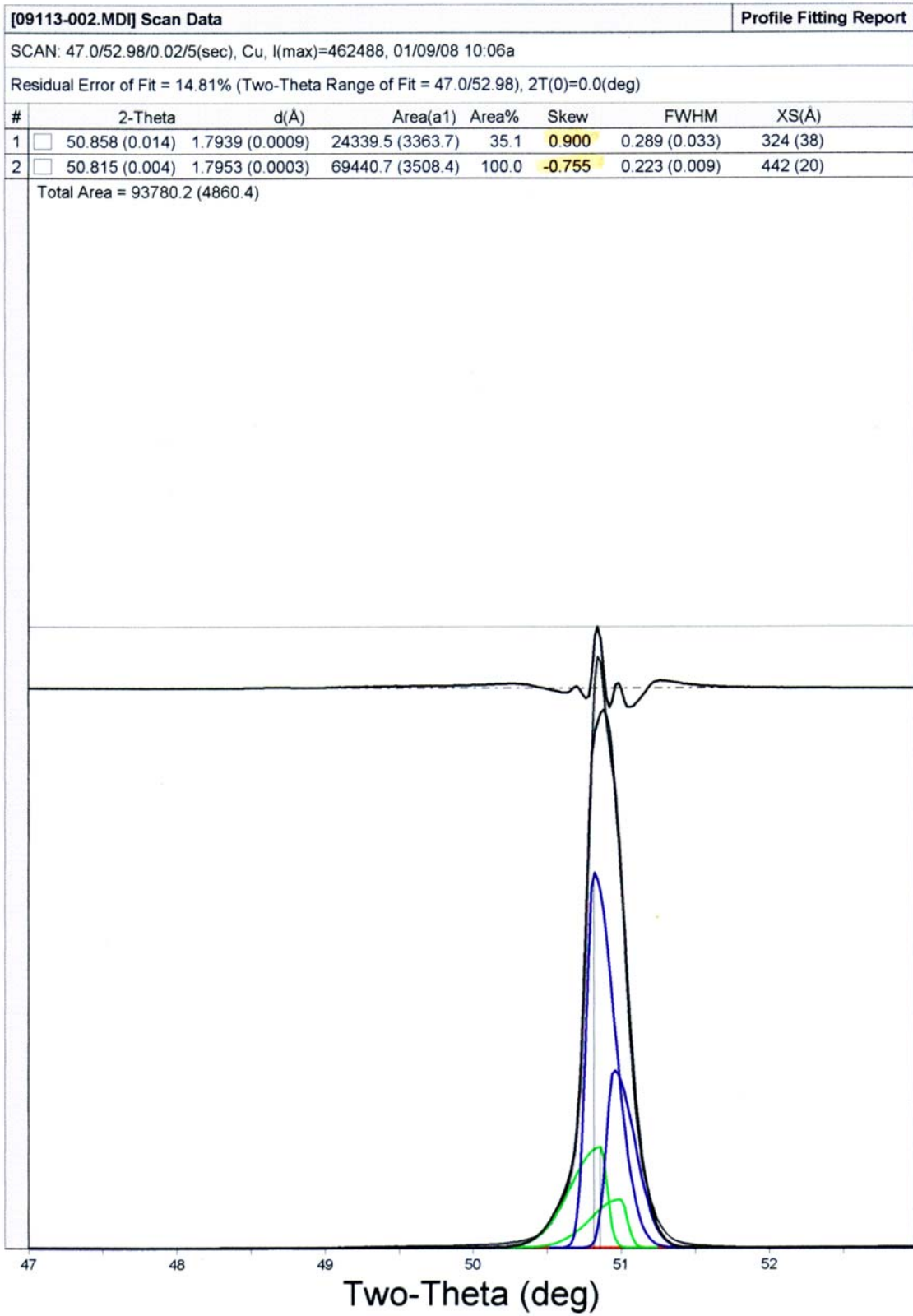


Figure B-2. XRD deconvolution of PWA 1480 (4hr. 1080°C, skewed, 14.81% error)

**[09113-002.MDI] Scan Data** **Profile Fitting Report**

SCAN: 49.0/52.99/0.01/1(sec), Cu, I(max)=99055, 01/29/08 11:09a

Residual Error of Fit = 6.63% (Two-Theta Range of Fit = 49.0/52.99), 2T(0)=0.0(deg)

#	2-Theta	d(Å)	Area(a1)	Area%	Skew	FWHM	XS(Å)
1	50.723 (0.005)	1.7984 (0.0003)	6136.2 (215.3)	35.5	0.000	0.692 (0.009)	128 (3)
2	50.800 (0.001)	1.7958 (0.0001)	17298.3 (200.2)	100.0	0.000	0.233 (0.002)	419 (5)

Total Area = 23434.5 (294.0)

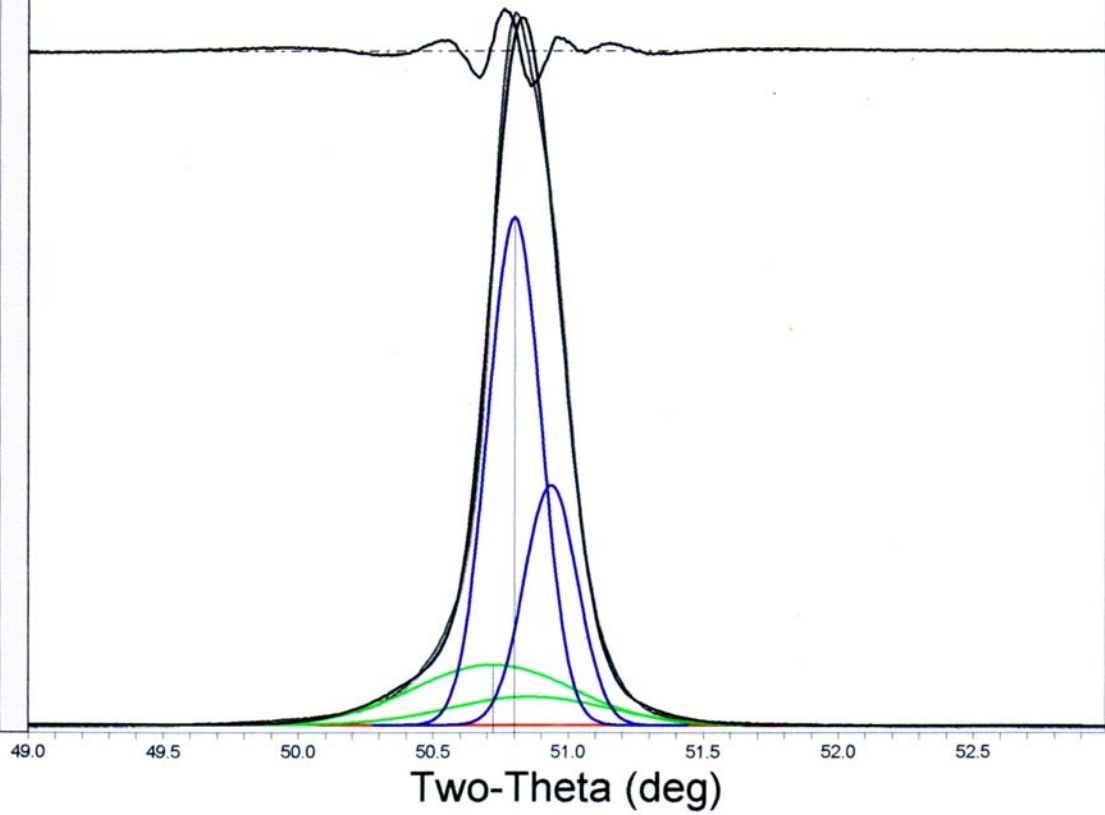


Figure B-3. XRD deconvolution of PWA 1480 (4hr. 1080°C, unskewed, 6.63% error)

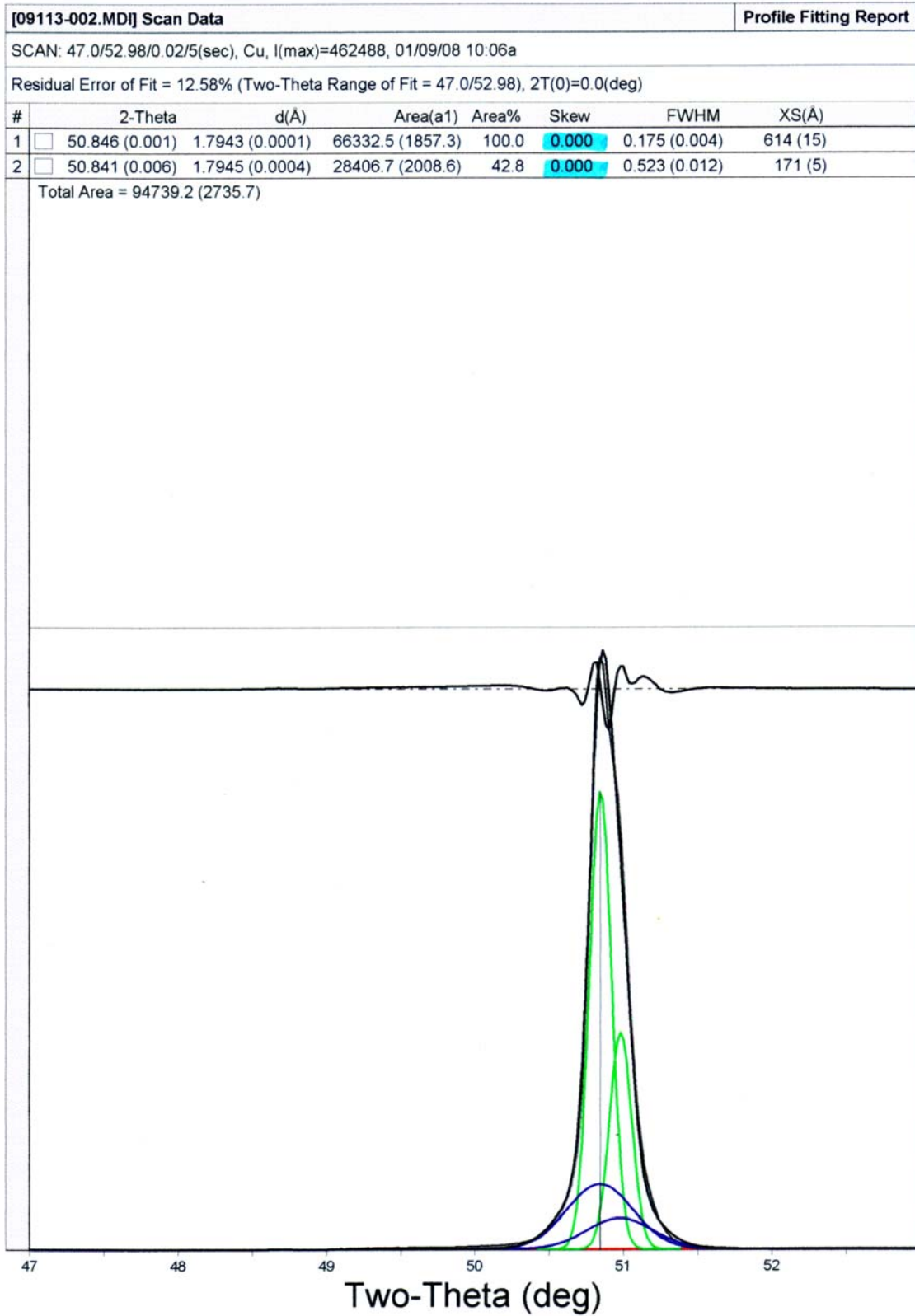


Figure B-4. XRD deconvolution of PWA 1480 (4hr. 1080°C, unskewed, 12.58% error)

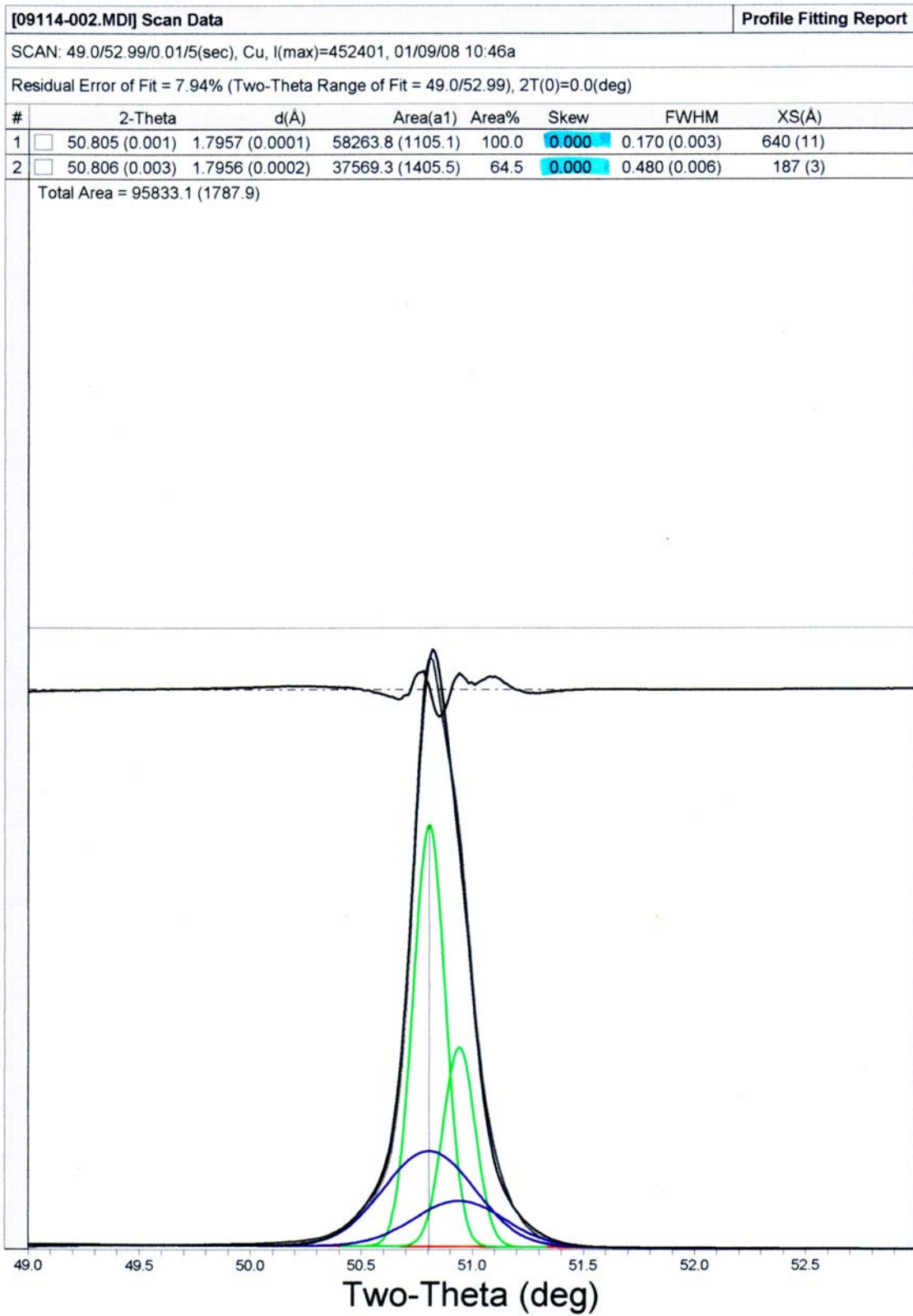


Figure B-5. XRD deconvolution of PWA 1480 (10hr. 1080°C, unskewed, 7.94% error)

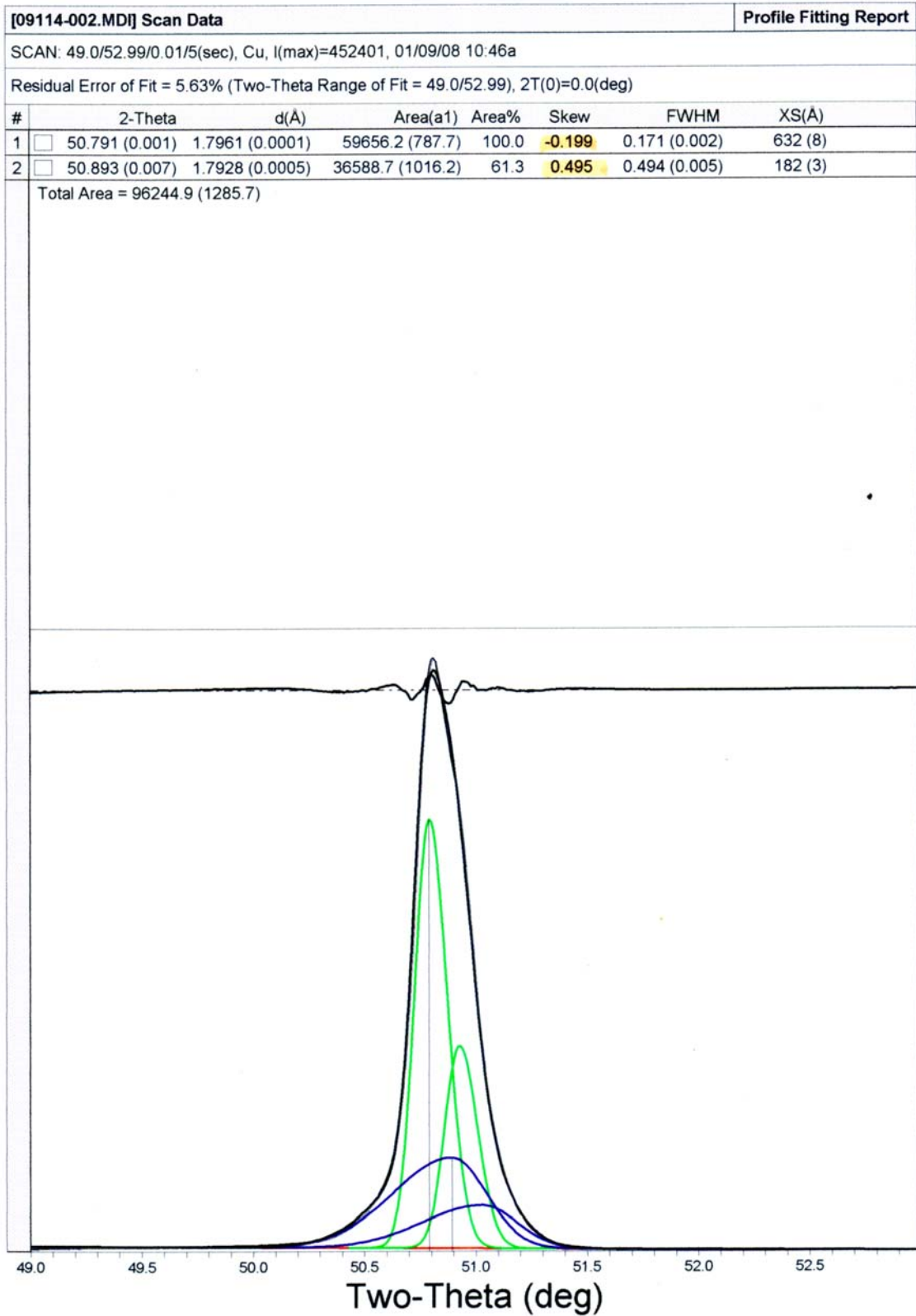


Figure B-6. XRD deconvolution of PWA 1480 (10hr. 1080°C, skewed, 5.63% error)

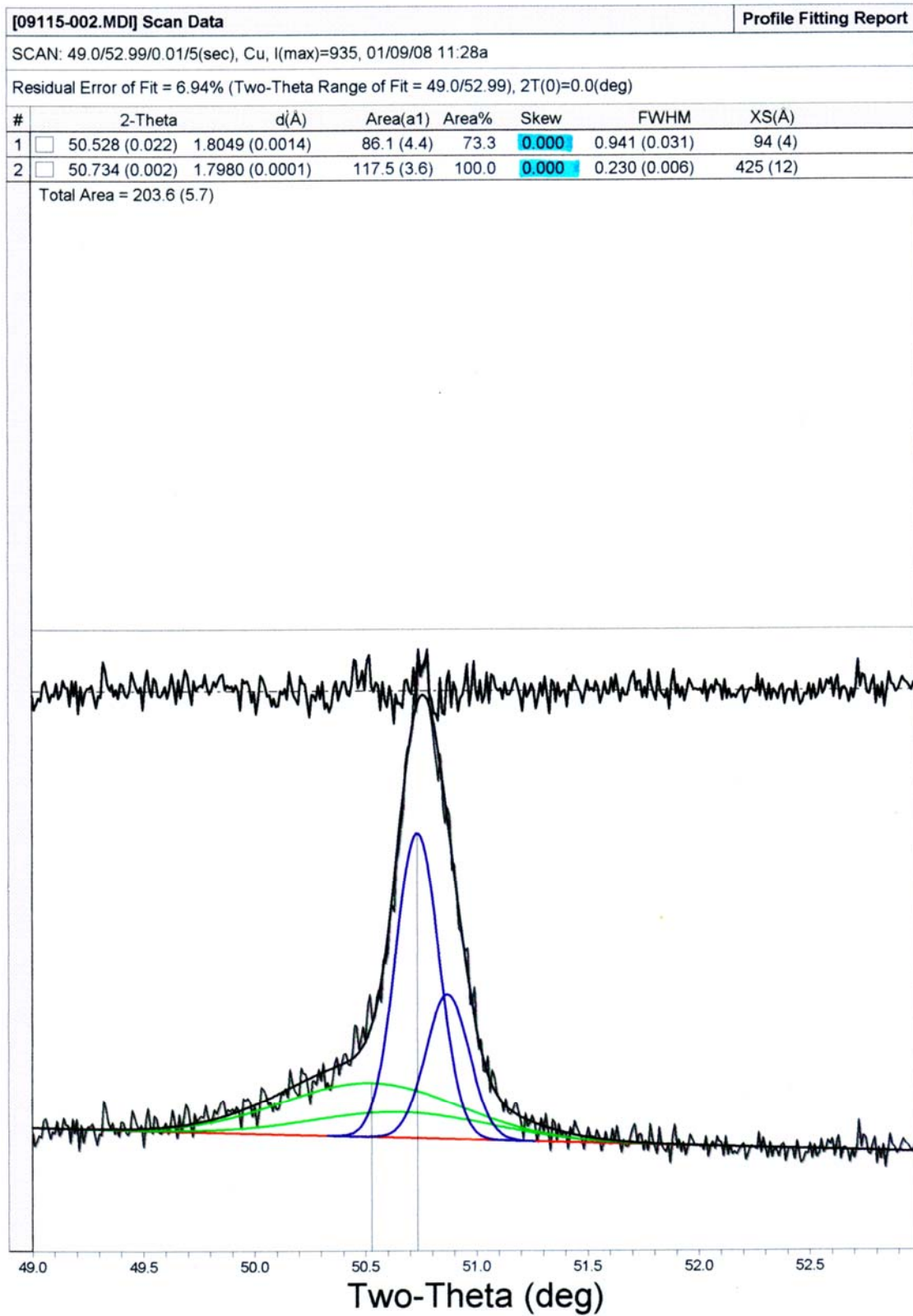


Figure B-7. XRD deconvolution of PWA 1480 (100hr. 1080°C, unskewed, 6.94% error)

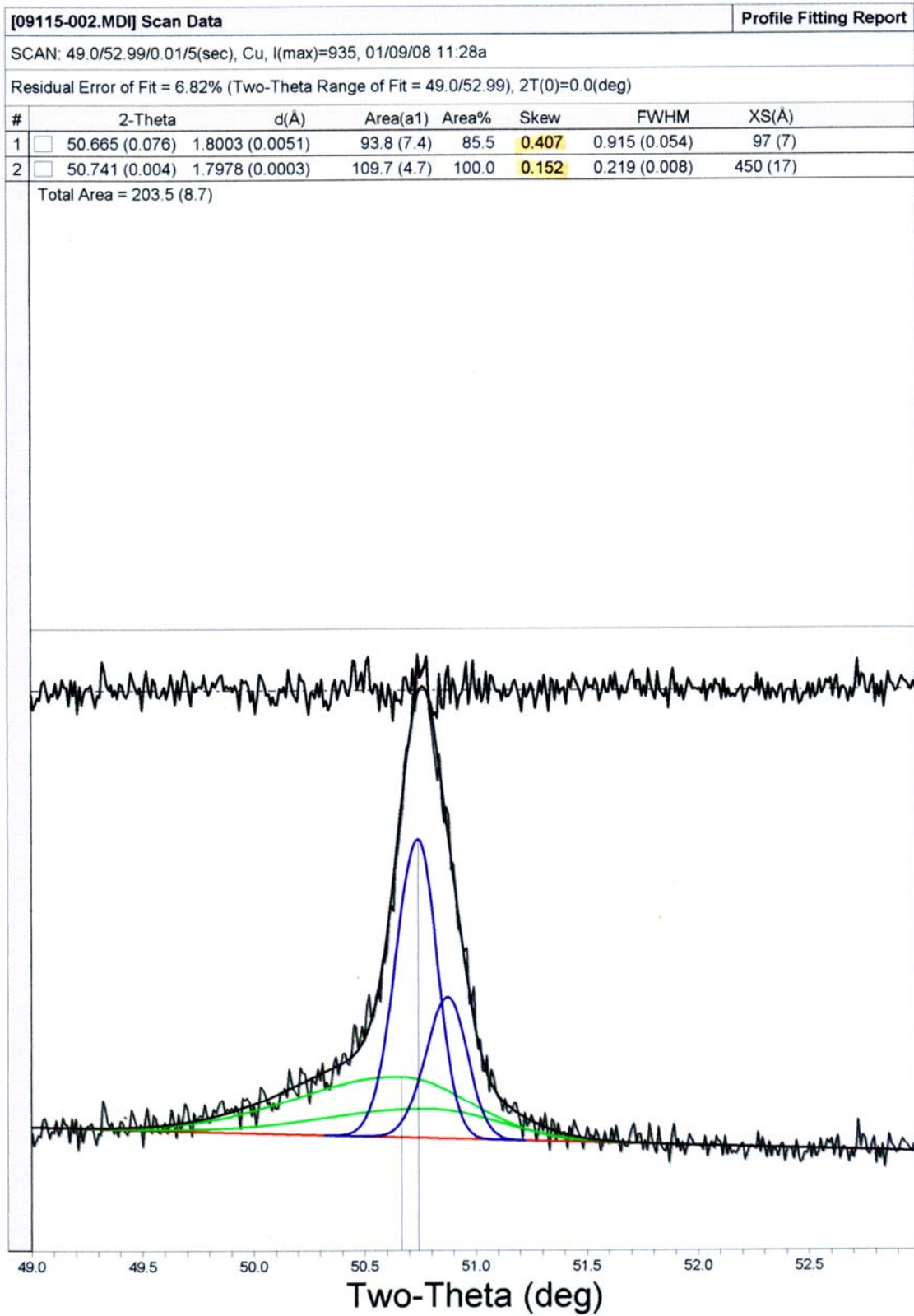


Figure B-8. XRD deconvolution of PWA 1480 (100hr. 1080°C, skewed, 6.82% error)

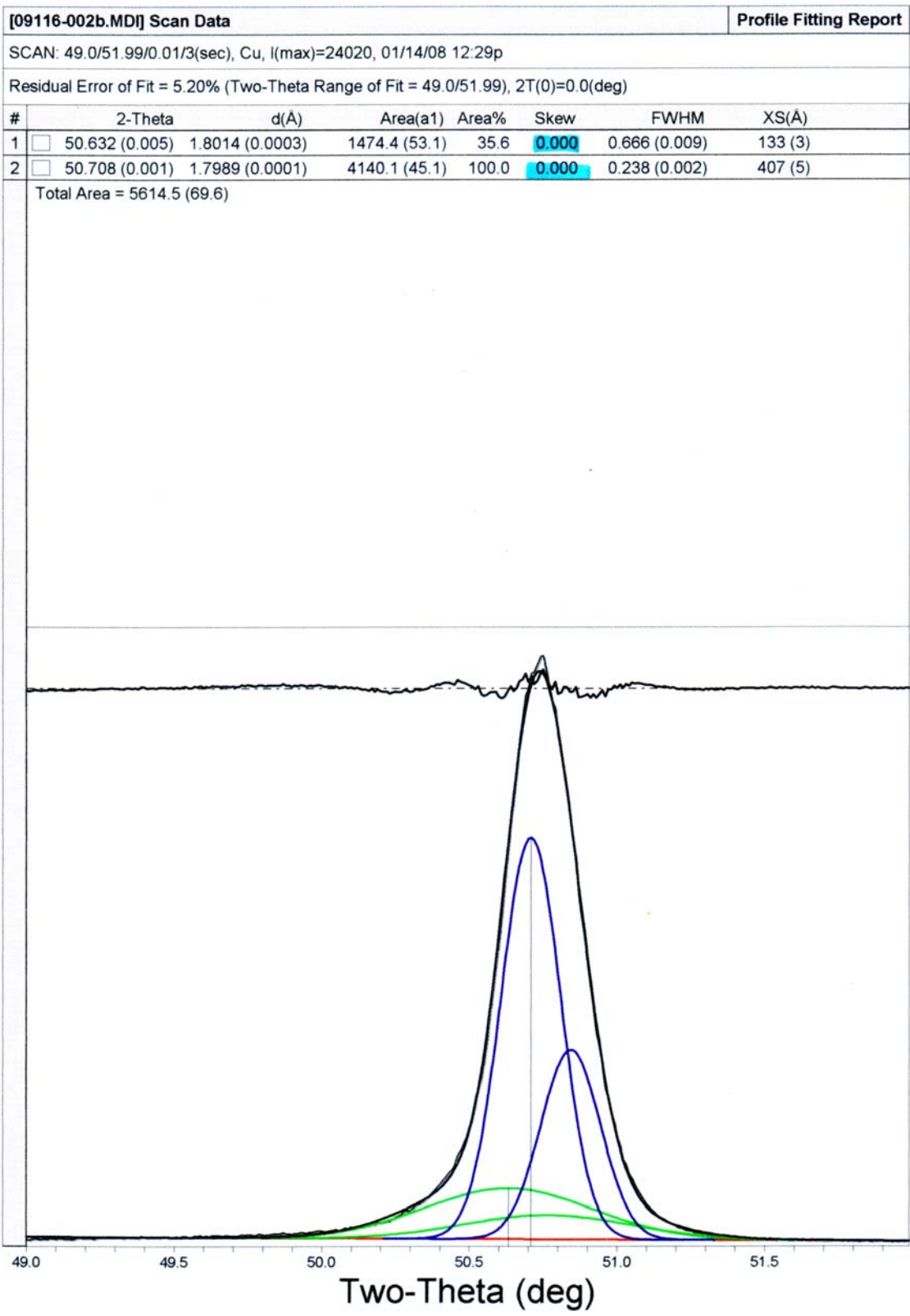


Figure B-9. XRD deconvolution of PWA 1480 (100hr. 1080°C, unskewed, 5.20% error)

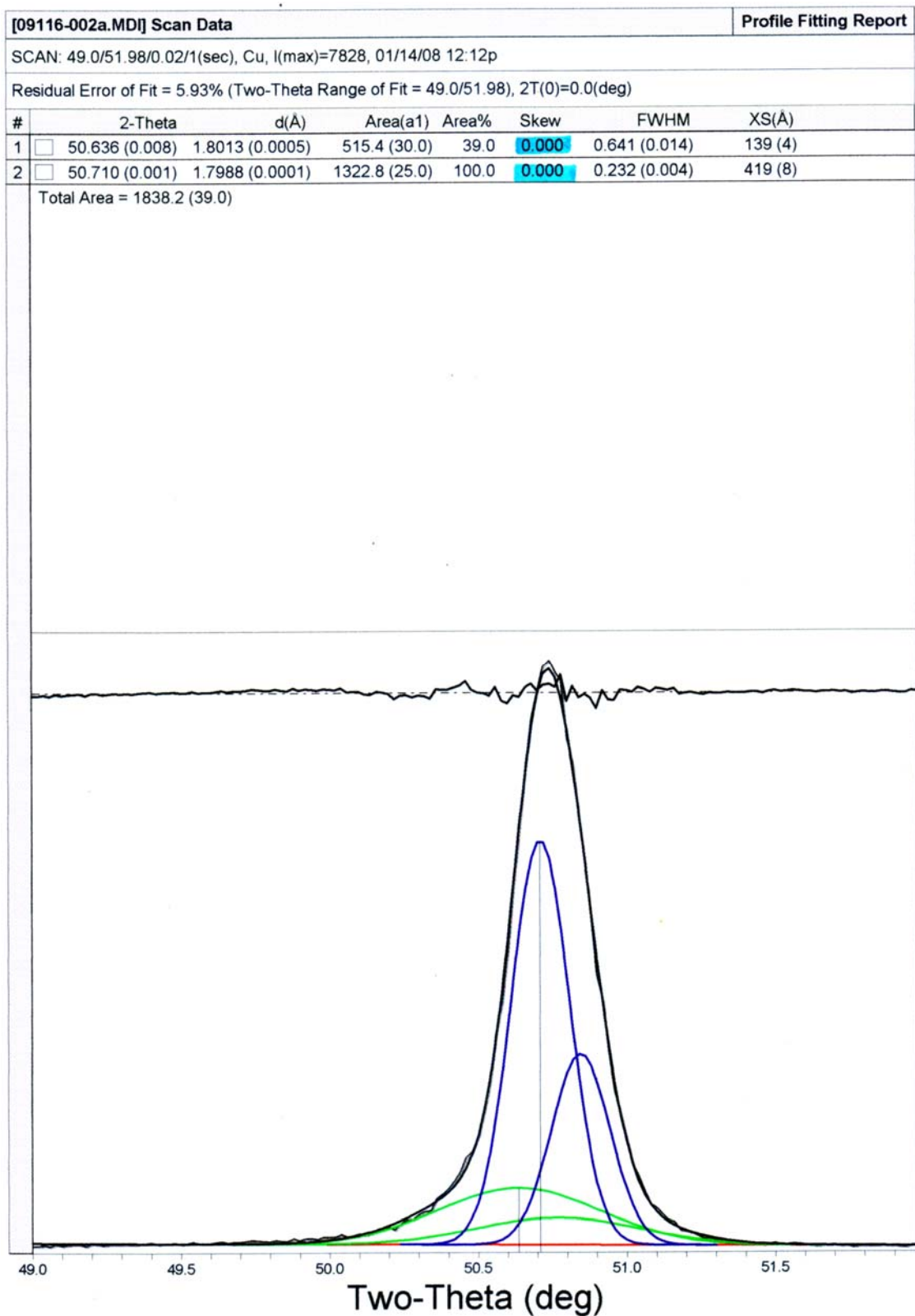


Figure B-10. XRD deconvolution of PWA 1480 (1000hr. 1080°C, unskewed, 5.93% error)

**[09116-002b.MD] Scan Data** **Profile Fitting Report**

SCAN: 49.0/51.99/0.01/3(sec), Cu, I(max)=24020, 01/14/08 12:29p

Residual Error of Fit = 4.61% (Two-Theta Range of Fit = 49.0/51.99), 2T(0)=0.0(deg)

#	2-Theta	d(Å)	Area(a1)	Area%	Skew	FWHM	XS(Å)
1	50.765 (0.016)	1.7970 (0.0011)	1613.7 (59.5)	40.3	0.486	0.658 (0.011)	135 (3)
2	50.719 (0.002)	1.7985 (0.0001)	4006.3 (48.9)	100.0	0.227	0.232 (0.002)	421 (5)

Total Area = 5620.0 (77.0)

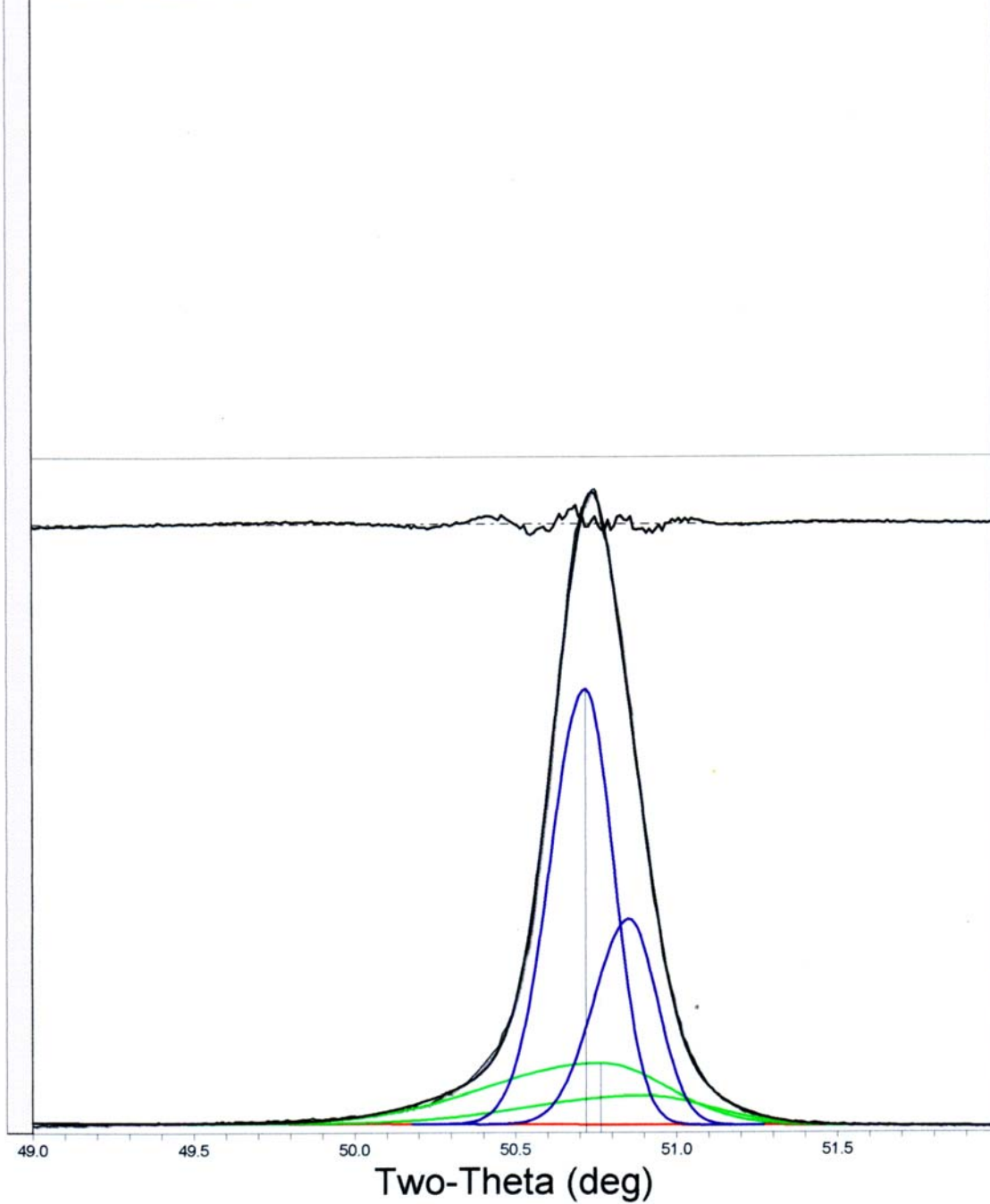


Figure B-11. XRD deconvolution of PWA 1480 (1000hr. 1080°C, skewed, 4.61% error)

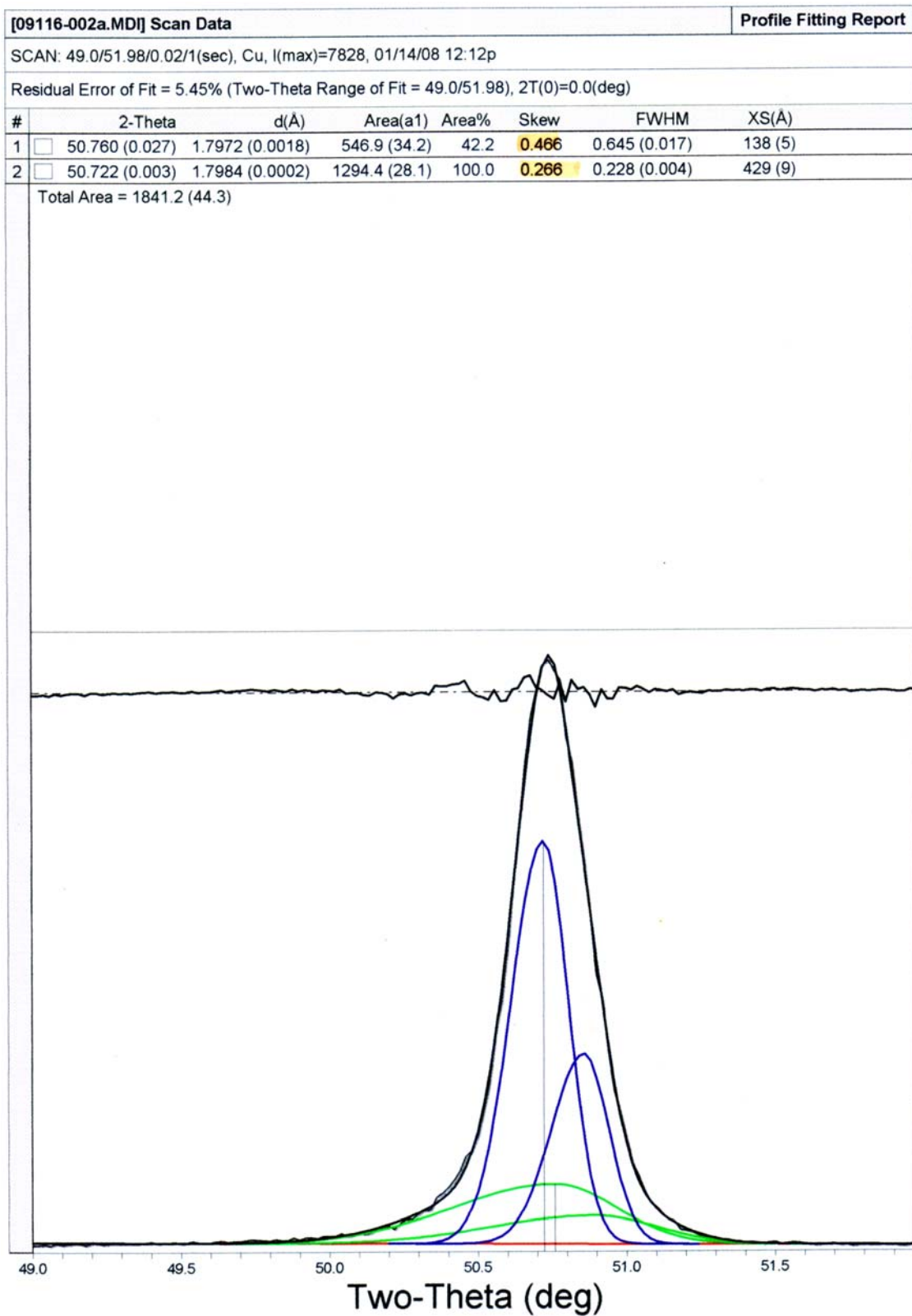


Figure B-12. XRD deconvolution of PWA 1480 (1000hr. 1080°C, skewed, 5.45% error)

[09113-004.MDI] Scan Data Profile Fitting Report

SCAN: 117.0/119.99/0.01/1(sec), Cu, I(max)=4727, 01/29/08 11:21a

Residual Error of Fit = 5.58% (Two-Theta Range of Fit = 117.0/119.99), 2T(0)=0.0(deg)

#	2-Theta	d(Å)	Area(a1)	Area%	Skew	FWHM	XS(Å)
1	118.009 (0.002)	0.8986 (0.0000)	1849.1 (19.9)	100.0	0.000	0.450 (0.004)	351 (4)
2	118.533 (0.014)	0.8962 (0.0001)	273.9 (17.3)	14.8	0.000	0.442 (0.024)	361 (21)

Total Area = 2123.0 (26.4)

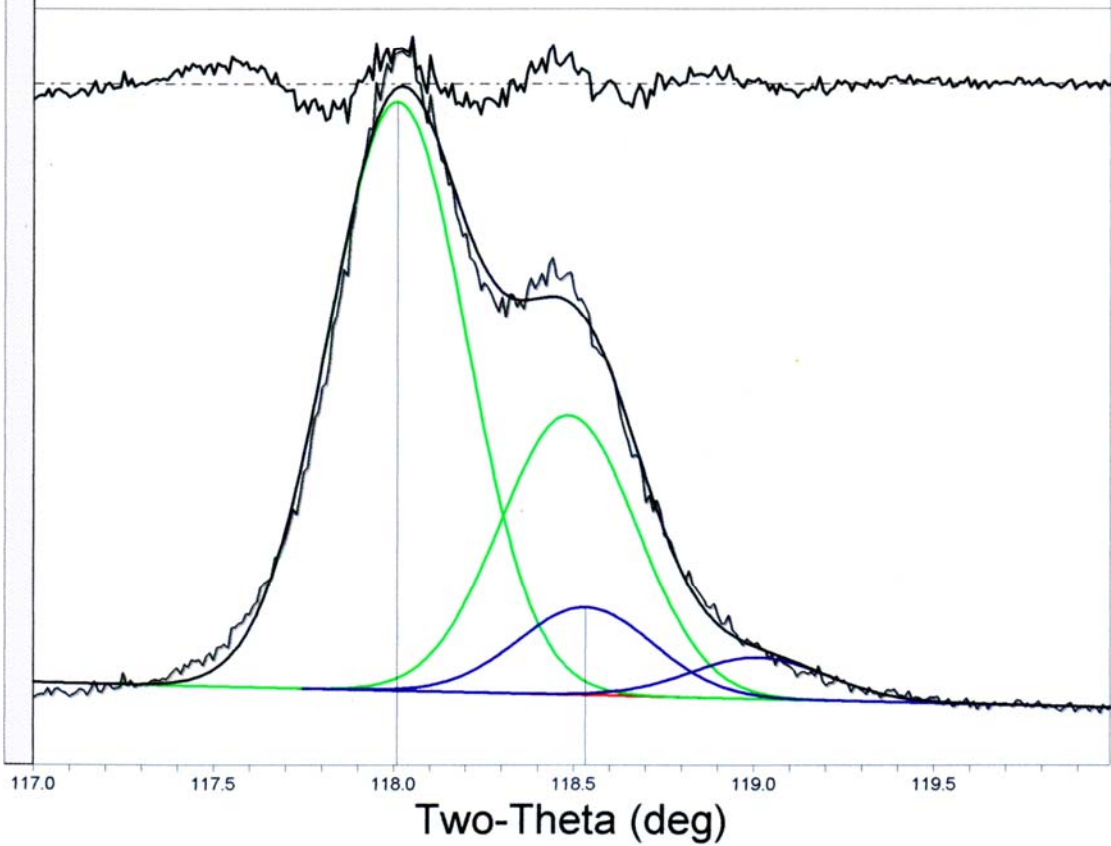


Figure B-13. XRD deconvolution of PWA 1480 (4hr. 1080°C, unskewed, 5.58% error)

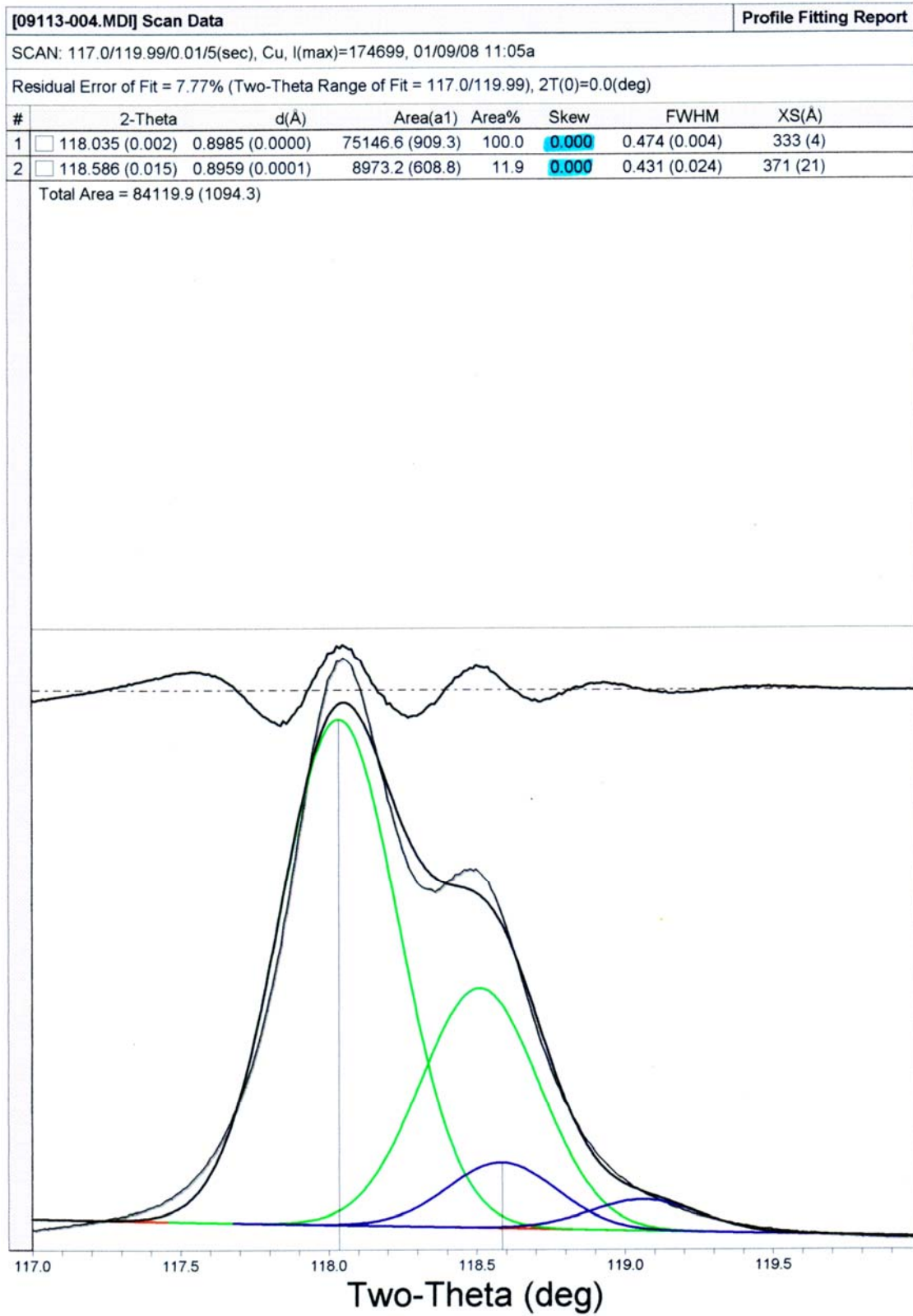


Figure B-14. XRD deconvolution of PWA 1480 (4hr. 1080°C, unskewed, 7.77% error)

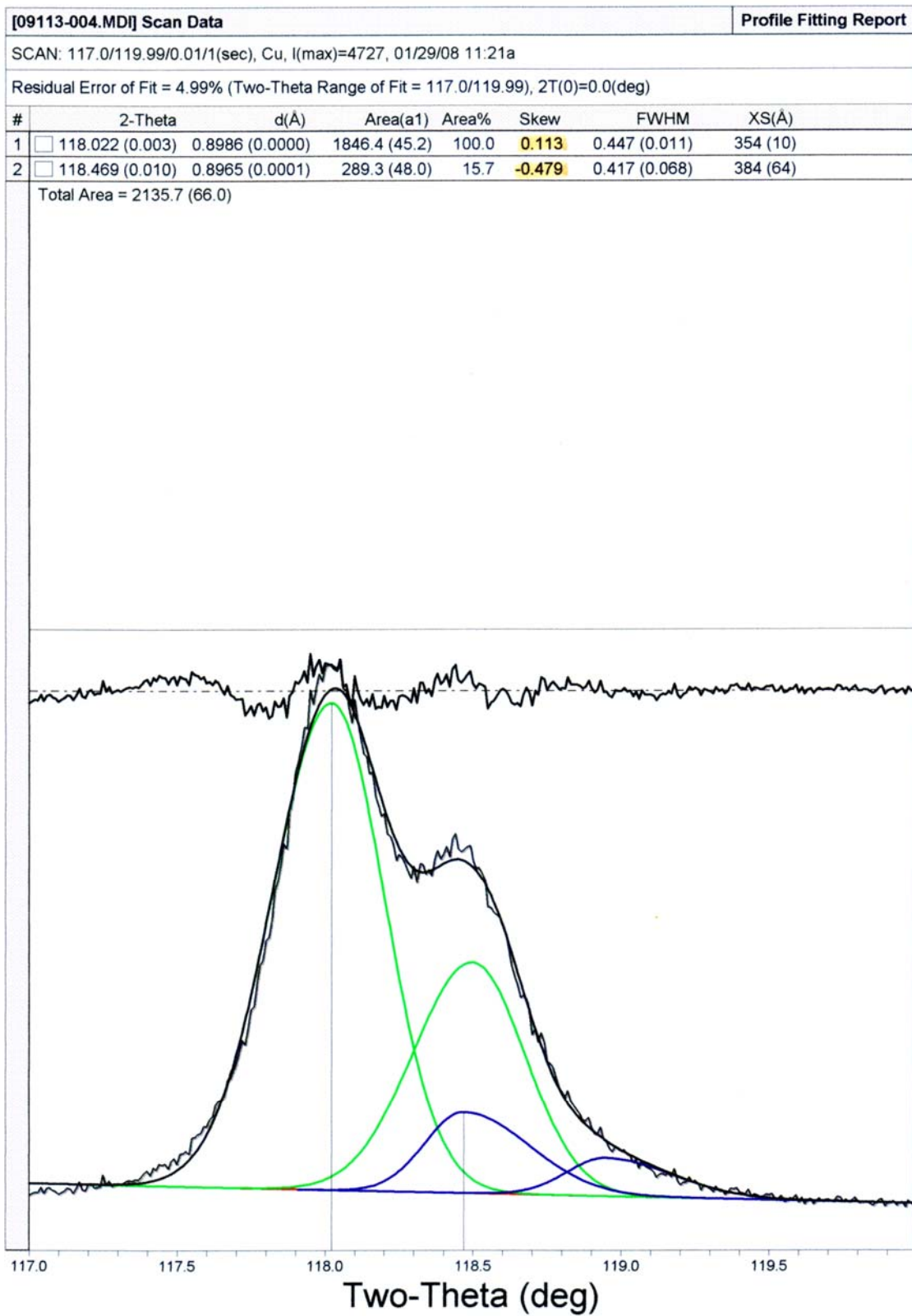


Figure B-15. XRD deconvolution of PWA 1480 (4hr. 1080°C, skewed, 4.99% error)

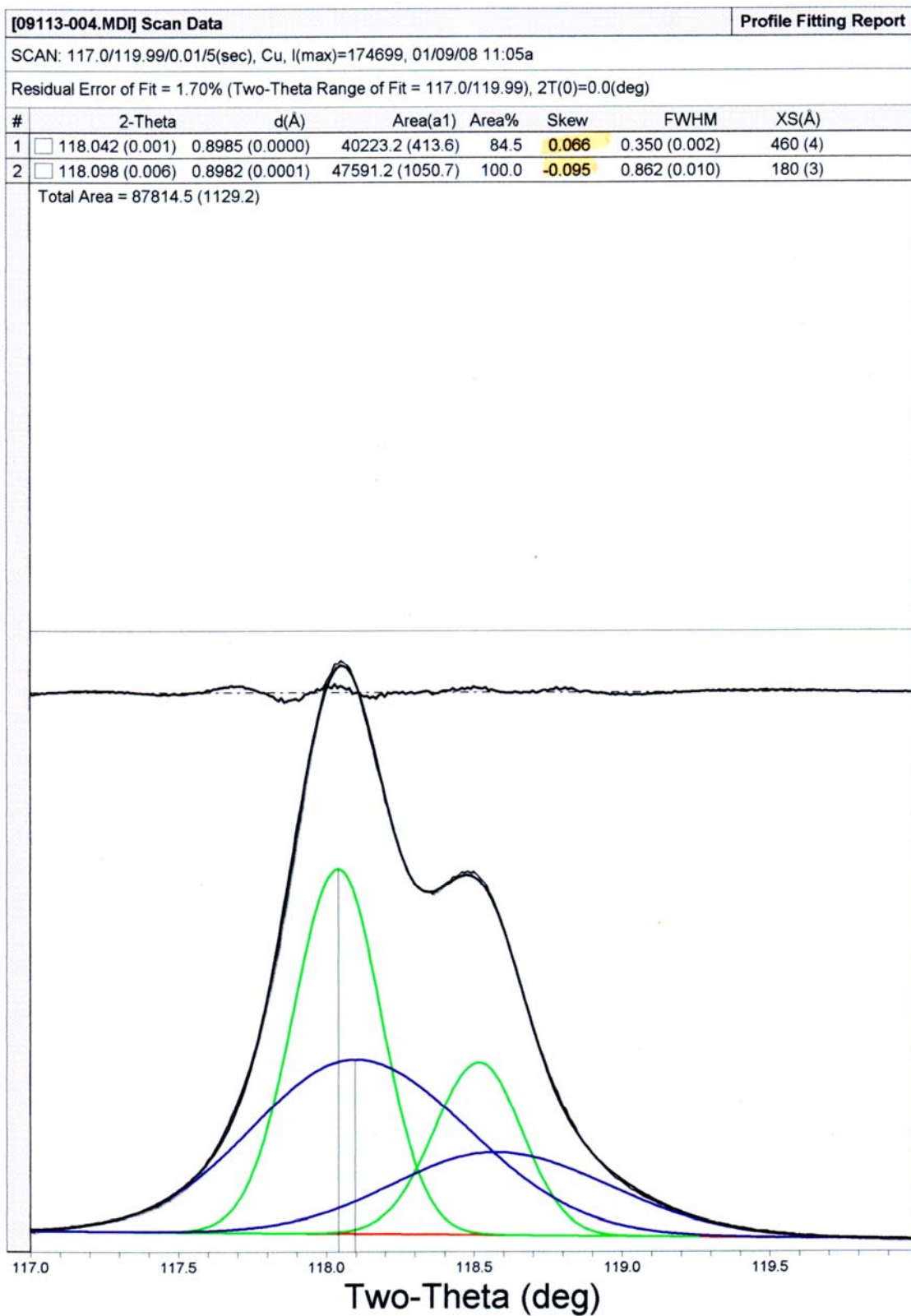


Figure B-16. XRD deconvolution of PWA 1480 (4hr. 1080°C, skewed, 1.70% error)

SCAN: 117.0/119.99/0.015(sec), Cu, I(max)=260171, 01/09/08 11:35a

Residual Error of Fit = 5.79% (Two-Theta Range of Fit = 117.0/119.99), 2T(0)=0.0(deg)

#	2-Theta	d(Å)	Area(a1)	Area%	Skew	FWHM	XS(Å)
1	117.971 (0.003)	0.8988 (0.0000)	105119.1 (2059.0)	100.0	0.000	0.464 (0.004)	340 (4)
2	118.371 (0.041)	0.8969 (0.0004)	29535.8 (3354.3)	28.1	0.000	0.761 (0.031)	206 (9)

Total Area = 134654.9 (3935.8)

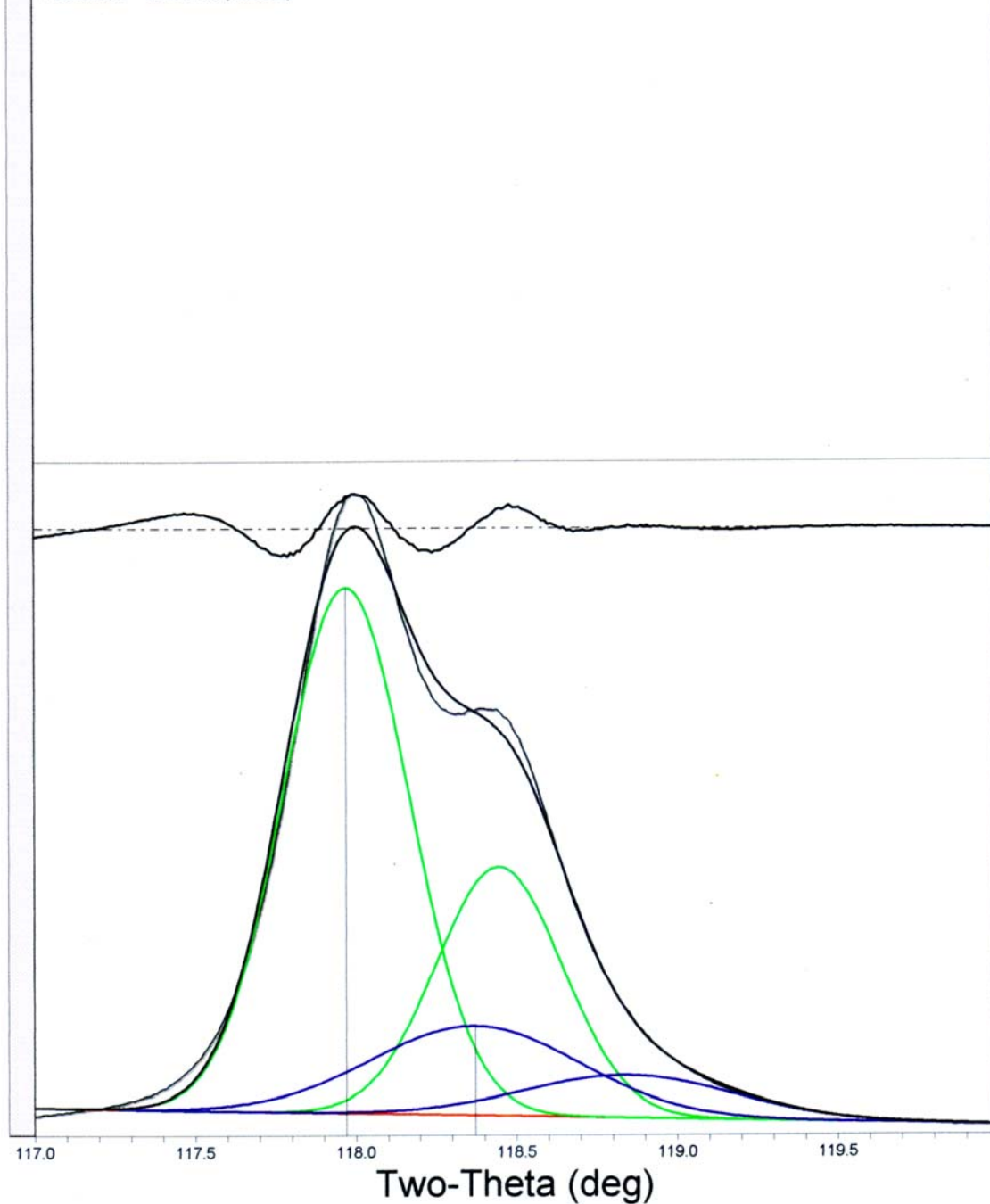


Figure B-17. XRD deconvolution of PWA 1480 (10hr. 1080°C, unskewed, 5.79% error)

SCAN: 117.0/119.99/0.015(sec), Cu, I(max)=260171, 01/09/08 11:35a

Residual Error of Fit = 1.41% (Two-Theta Range of Fit = 117.0/119.99), 2T(0)=0.0(deg)

#	2-Theta	d(Å)	Area(a1)	Area%	Skew	FWHM	XS(Å)
1	117.984 (0.001)	0.8987 (0.0000)	70017.1 (716.5)	100.0	0.038	0.387 (0.002)	413 (3)
2	118.083 (0.009)	0.8983 (0.0001)	68850.3 (1828.4)	98.3	-0.126	0.900 (0.013)	173 (3)

Total Area = 138867.5 (1963.8)

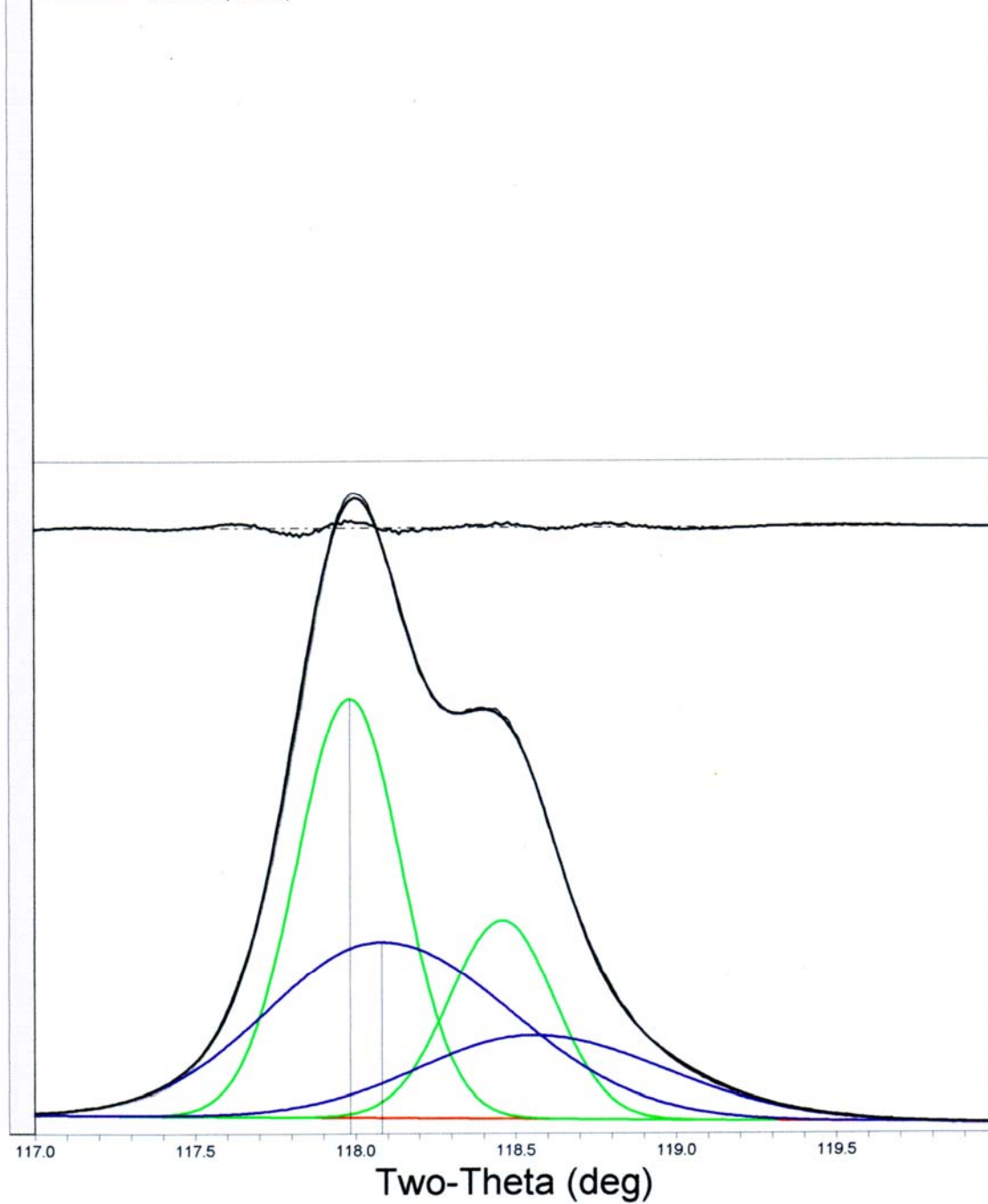


Figure B-18. XRD deconvolution of PWA 1480 (10hr. 1080°C, skewed, 1.41% error)

SCAN: 117.0/119.98/0.02/1(sec), Cu, I(max)=2510, 01/14/08 10:12a

Residual Error of Fit = 3.17% (Two-Theta Range of Fit = 117.0/119.98), 2T(0)=0.0(deg)

#	2-Theta	d(Å)	Area(a1)	Area%	Skew	FWHM	XS(Å)
1	117.856 (0.027)	0.8993 (0.0003)	562.4 (?)	58.5	0.000	0.796 (0.066)	195 (17)
2	117.997 (0.108)	0.8987 (0.0010)	961.7 (?)	100.0	0.000	1.020 (0.120)	152 (19)

Total Area = 1524.1 (0.0)

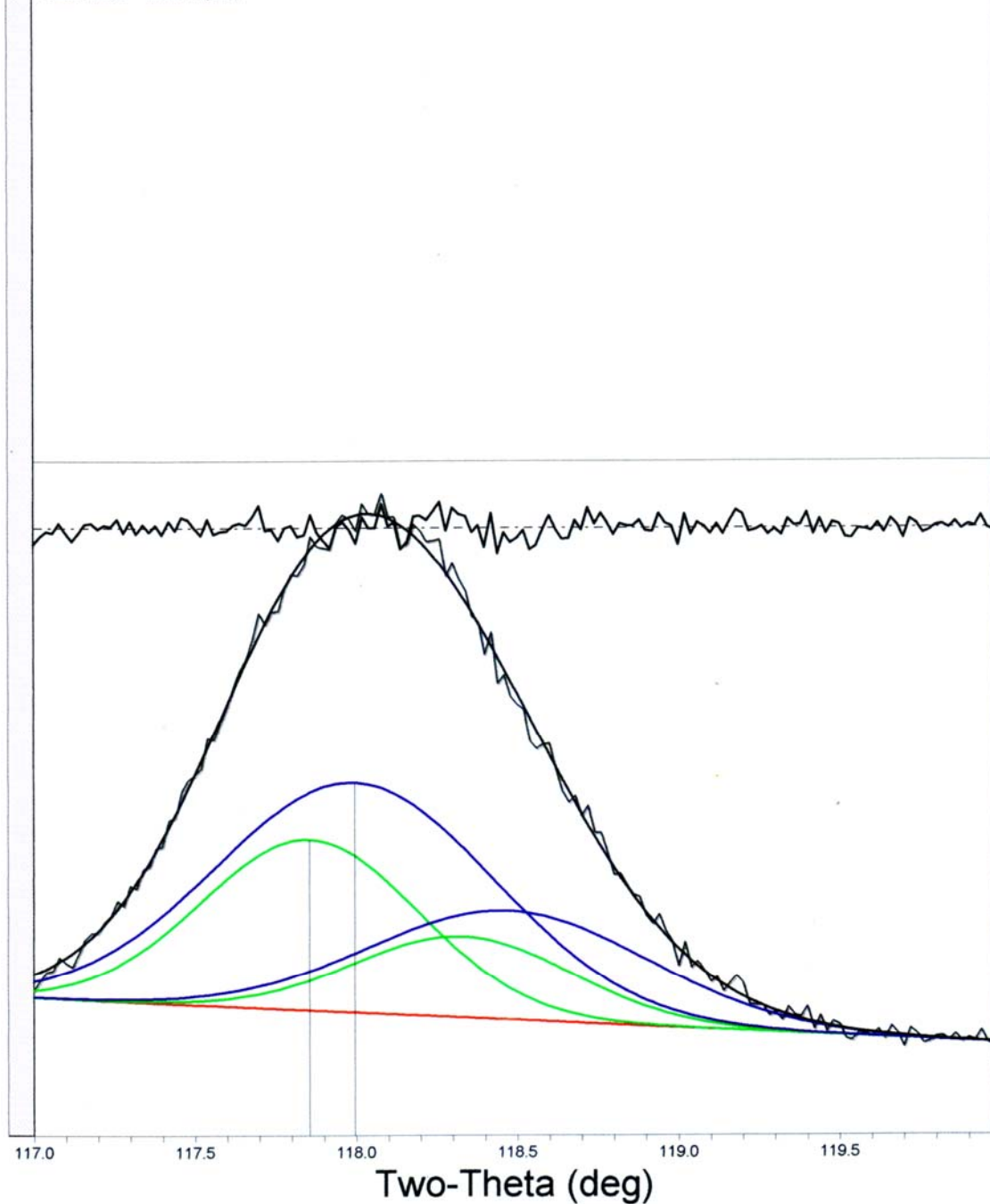


Figure B-19. XRD deconvolution of PWA 1480 (1000hr. 1080°C, unskewed, 3.17% error)

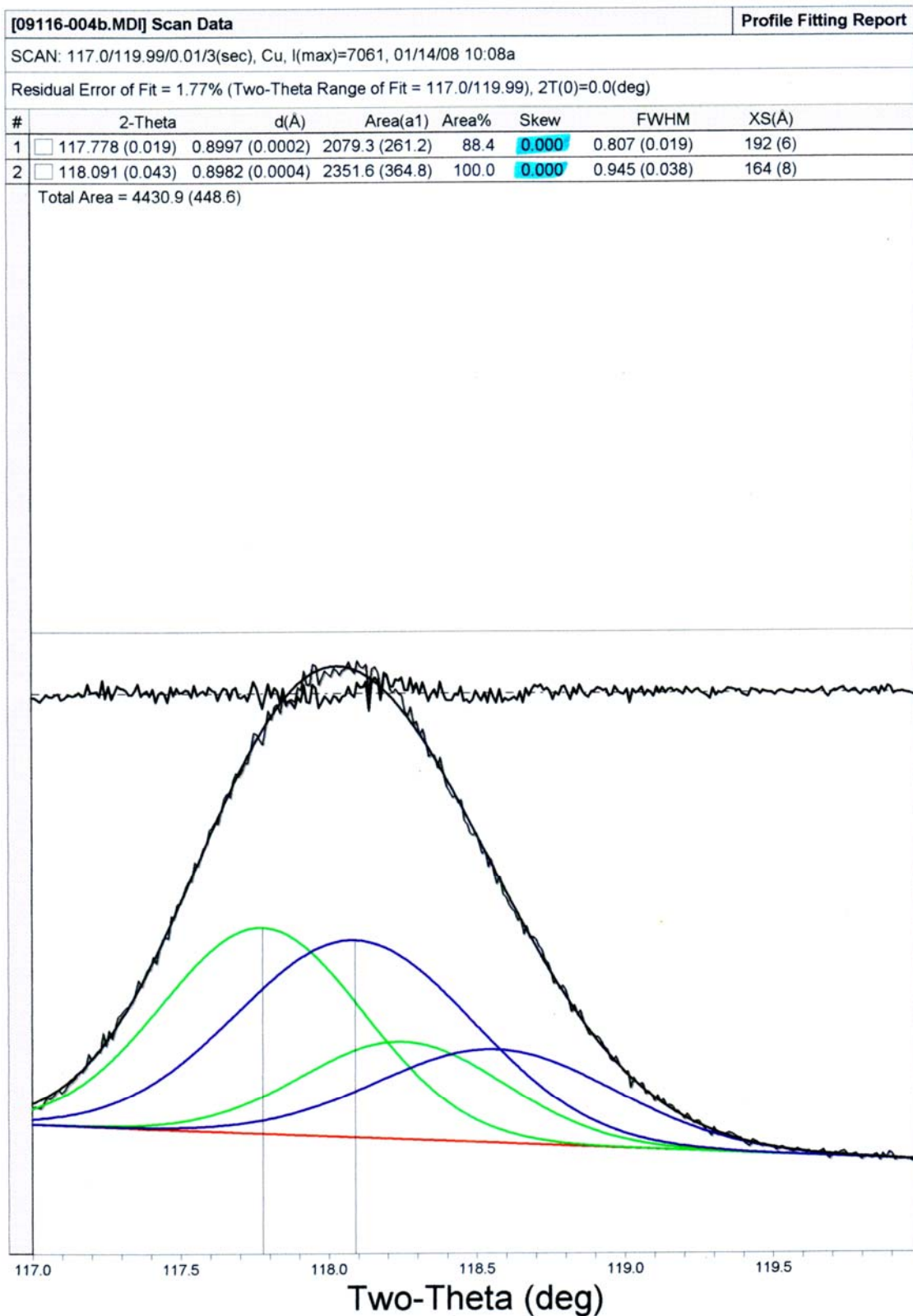


Figure B-20. XRD deconvolution of PWA 1480 (1000hr. 1080°C, unskewed, 1.77% error)

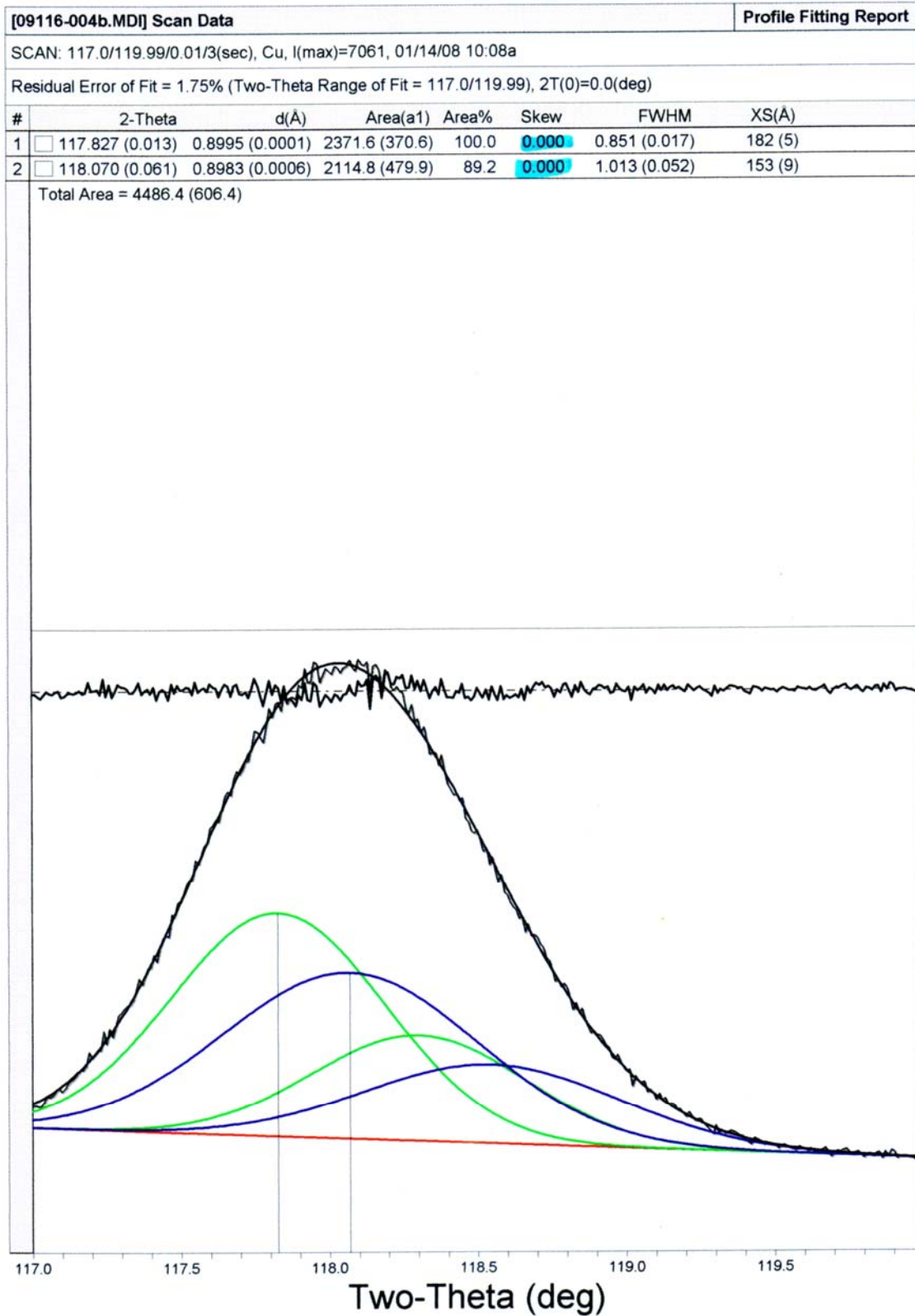


Figure B-21. XRD deconvolution of PWA 1480 (1000hr. 1080°C, unskewed, 1.75% error)

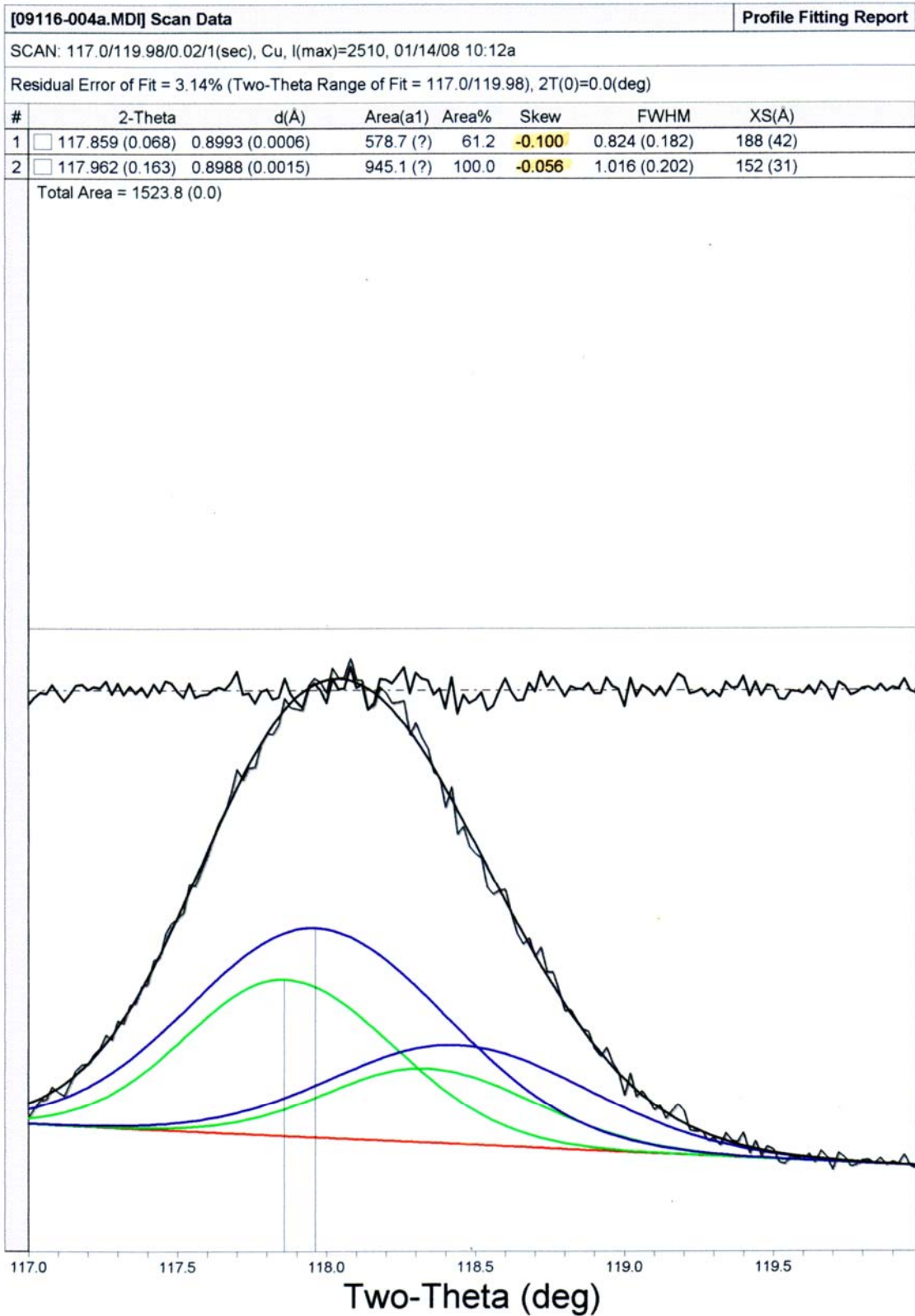


Figure B-22. XRD deconvolution of PWA 1480 (1000hr. 1080°C, skewed, 3.14% error)

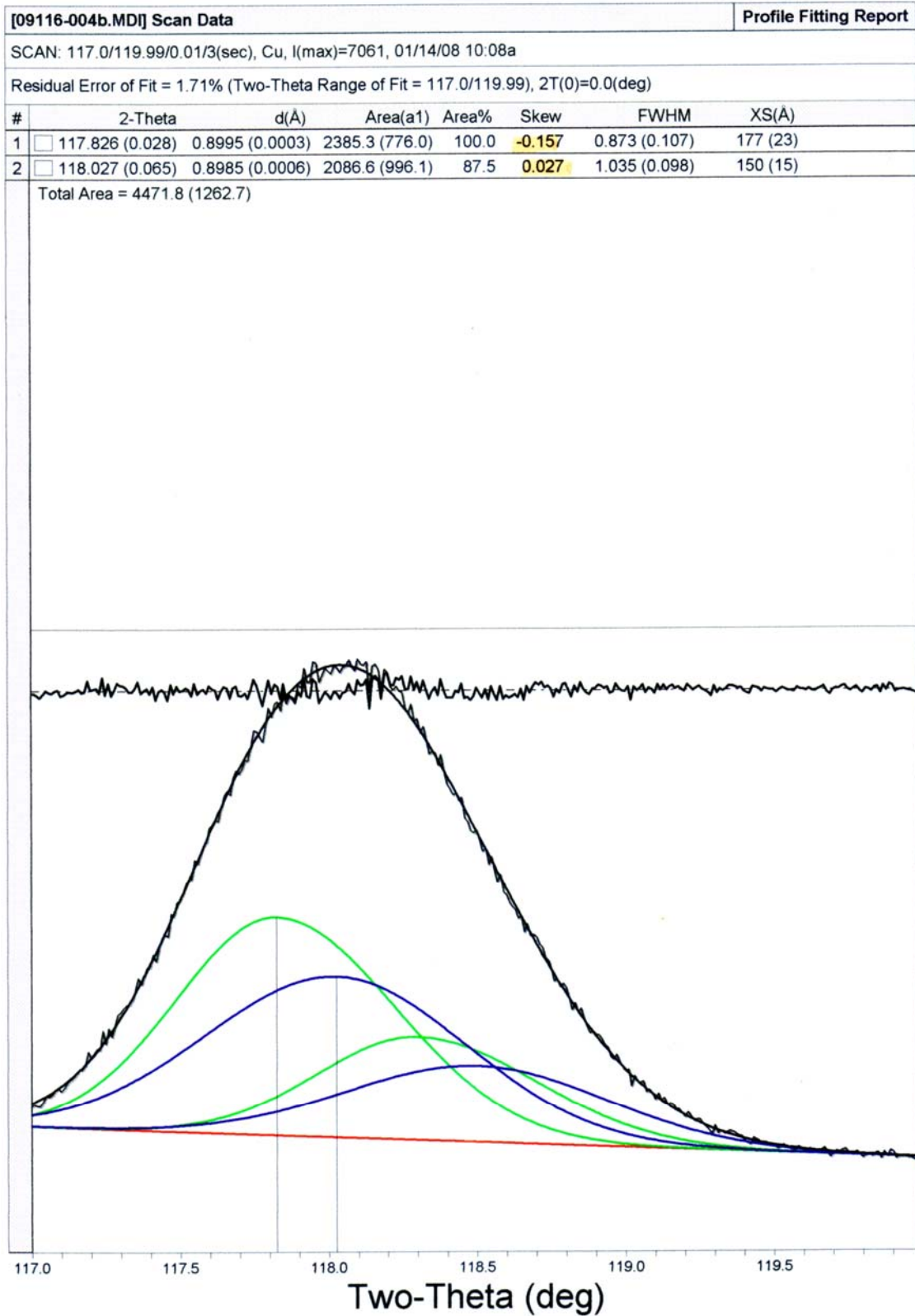


Figure B-23. XRD deconvolution of PWA 1480 (1000hr. 1080°C, skewed, 1.71% error)

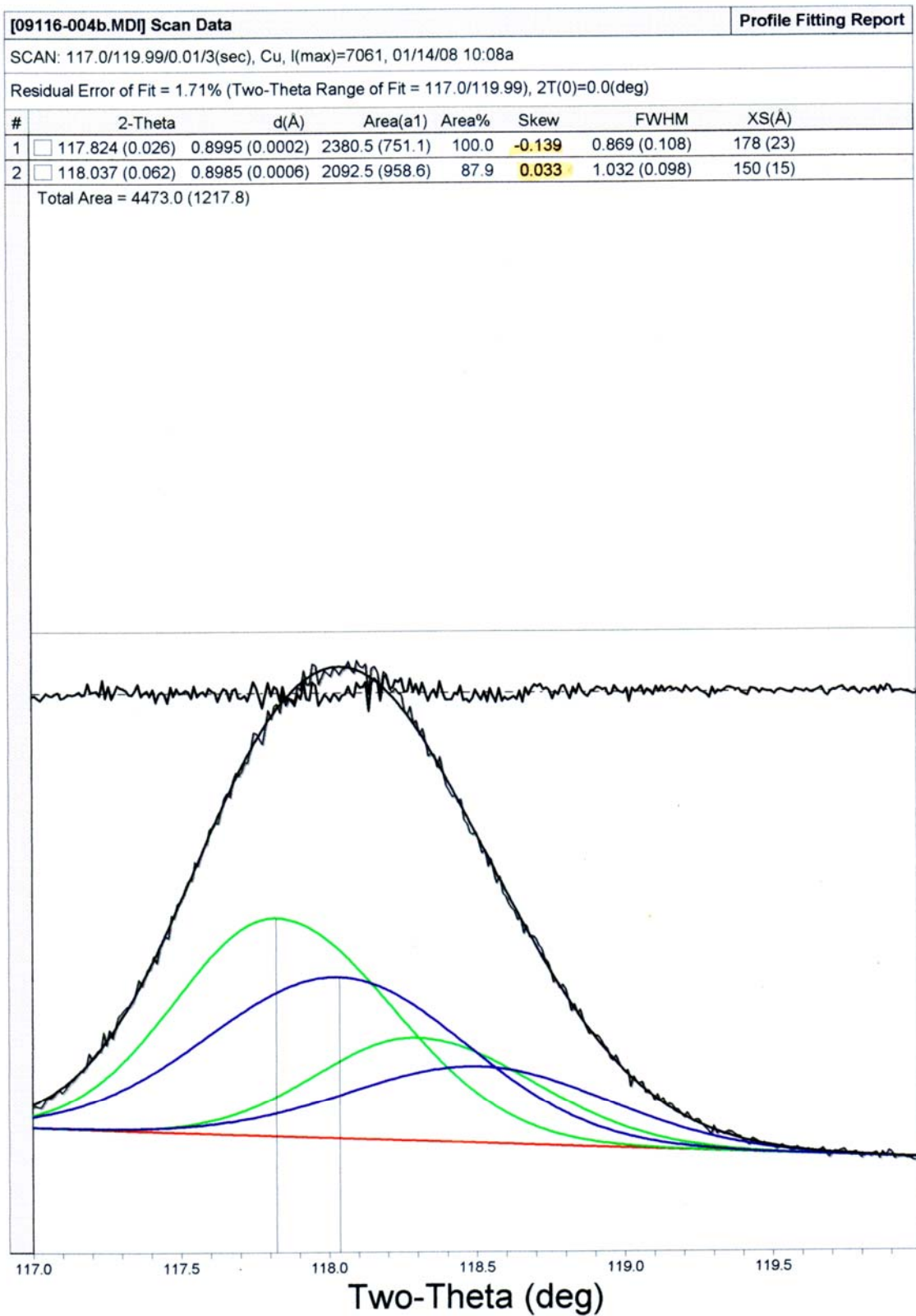


Figure B-24. XRD deconvolution of PWA 1480 (1000hr. 1080°C, skewed, 1.71% error)

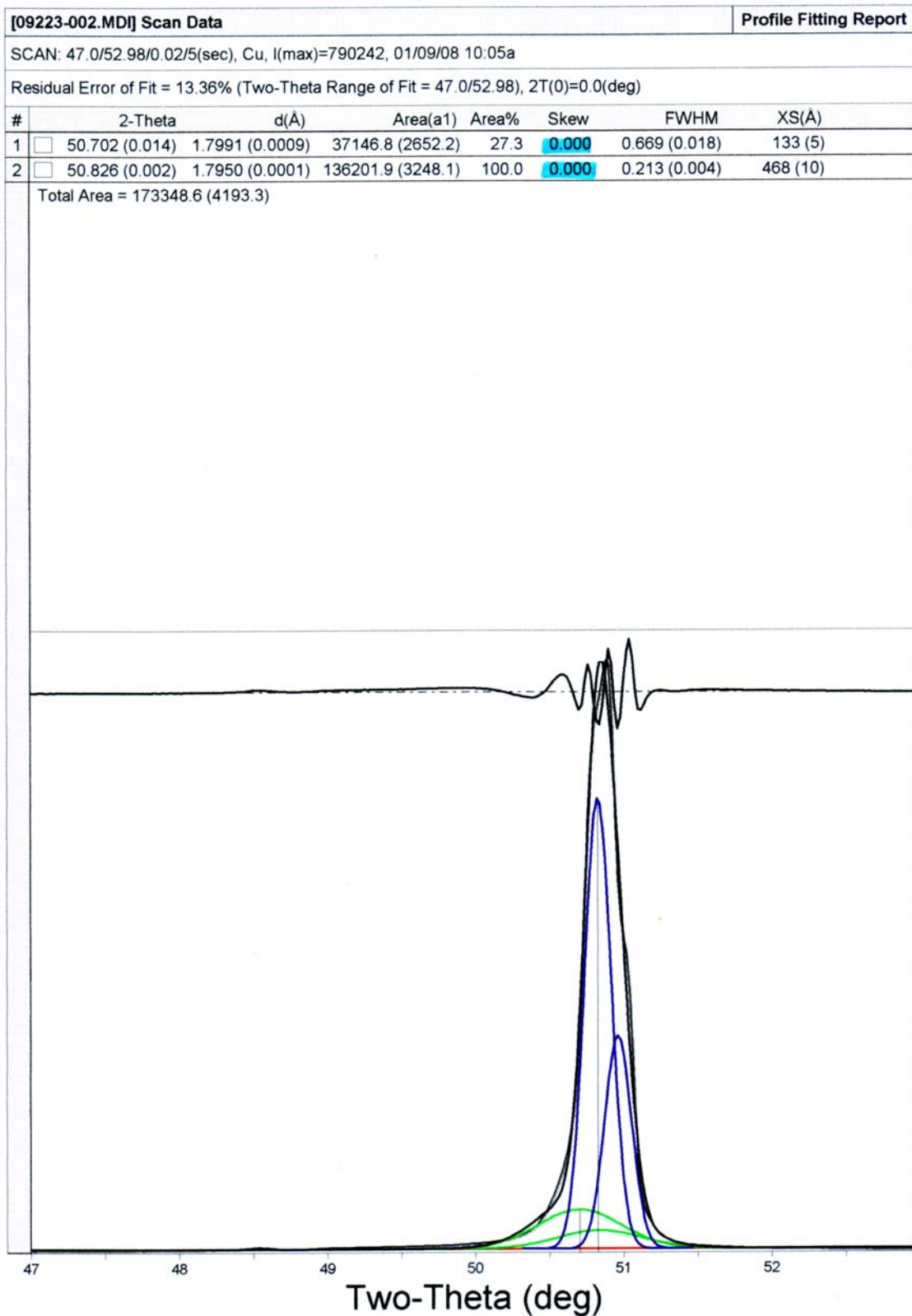


Figure B-25. XRD deconvolution of PWA 1484 (4hr. 1080°C, unskewed, 13.36% error)

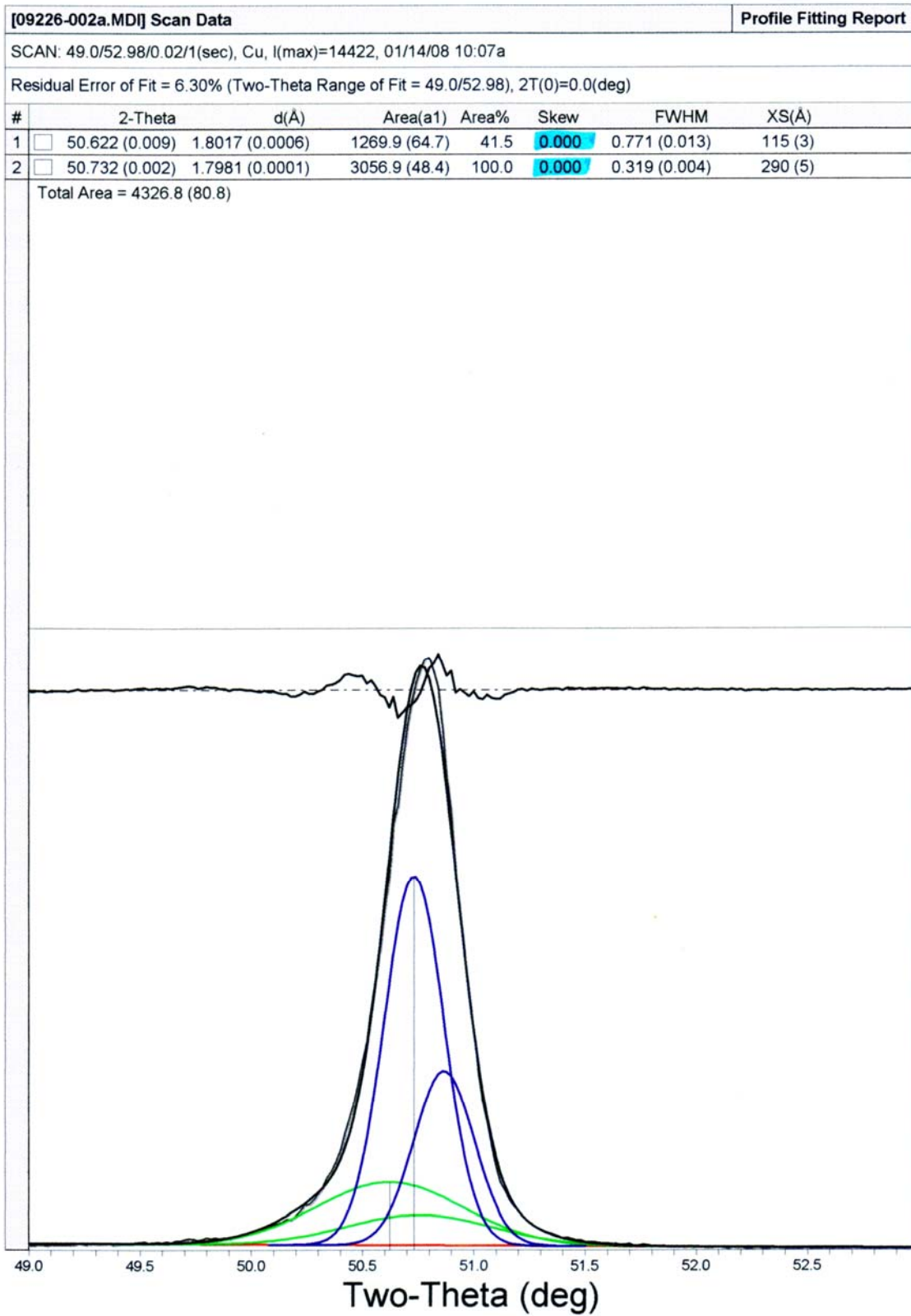


Figure B-26. XRD deconvolution of PWA 1484 (1000hr. 1080°C, unskewed, 6.30% error)

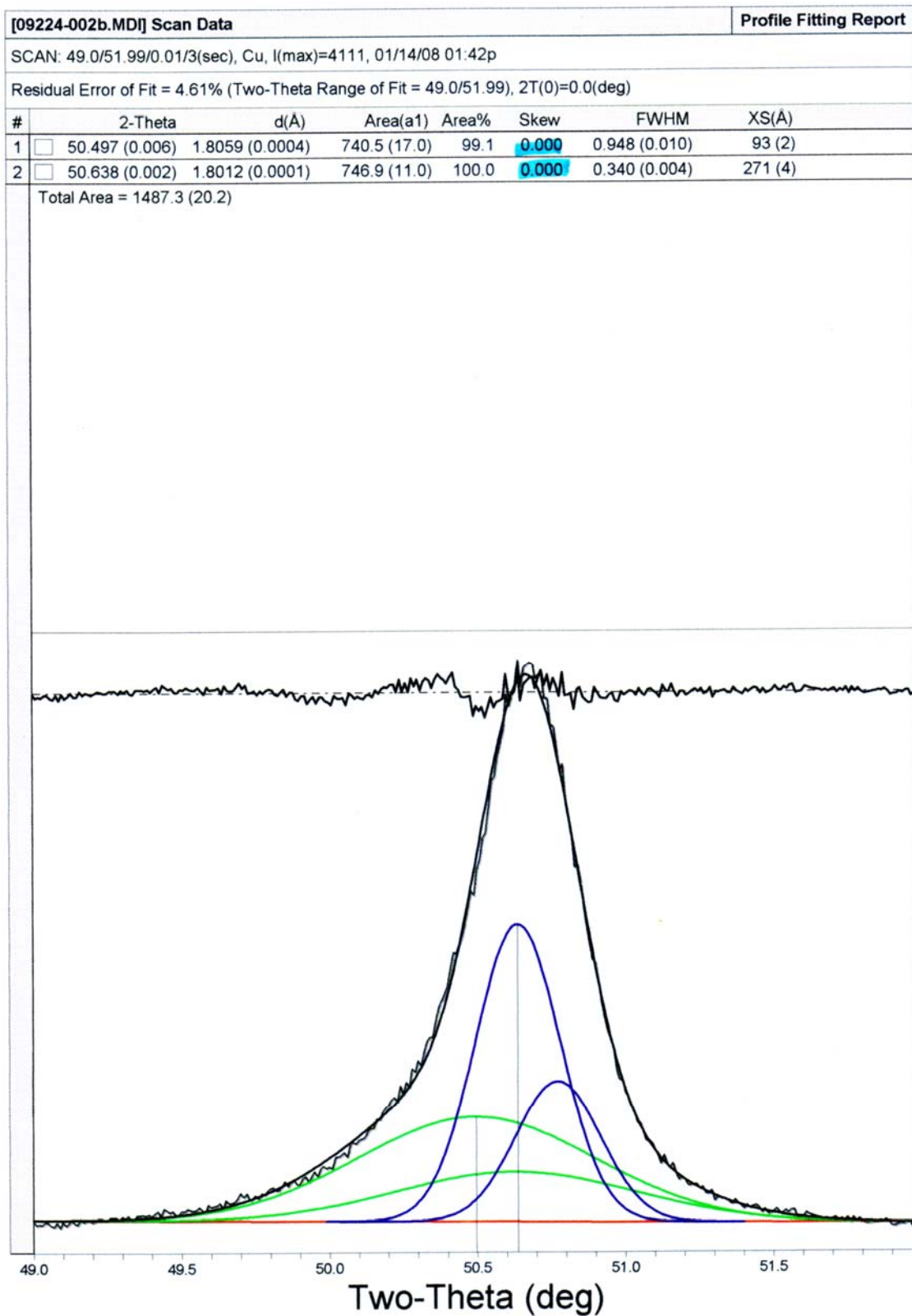


Figure B-27. XRD deconvolution of PWA 1484 (10hr. 1080°C, unskewed, 4.61% error)

SCAN: 49.0/51.99/0.01/3(sec), Cu, I(max)=44143, 01/14/08 10:24a

Residual Error of Fit = 5.85% (Two-Theta Range of Fit = 49.0/51.99), 2T(0)=0.0(deg)

#	2-Theta	d(Å)	Area(a1)	Area%	Skew	FWHM	XS(Å)
1	50.626 (0.006)	1.8016 (0.0004)	4322.3 (161.8)	49.8	0.000	0.703 (0.008)	126 (2)
2	50.734 (0.001)	1.7980 (0.0001)	8678.9 (118.6)	100.0	0.000	0.305 (0.003)	305 (4)

Total Area = 13001.3 (200.6)

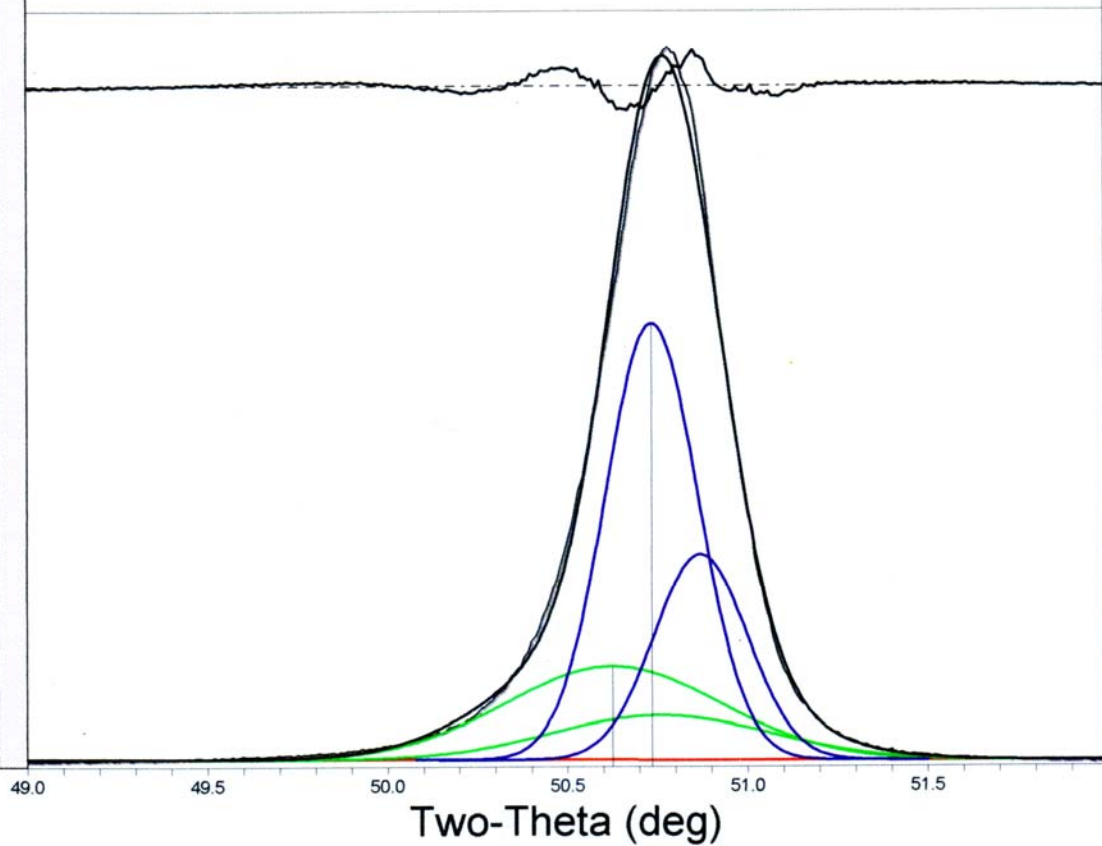


Figure B-28. XRD deconvolution of PWA 1484 (1000hr. 1080°C, unskewed, 5.85% error)

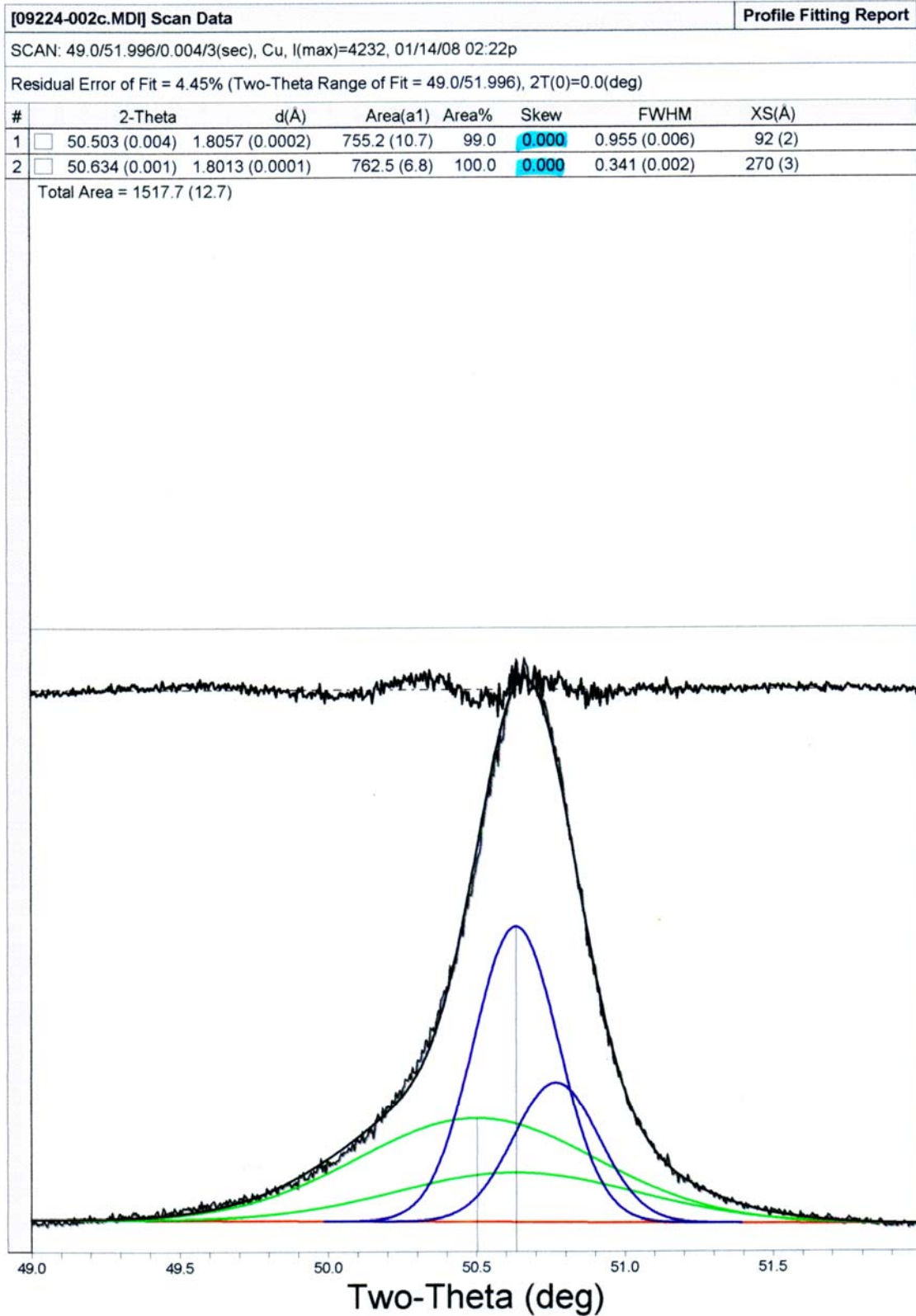


Figure B-29. XRD deconvolution of PWA 1484 (10hr. 1080°C, unskewed, 4.45% error)

SCAN: 47.0/52.98/0.02/5(sec), Cu, I(max)=790242, 01/09/08 10:05a

Residual Error of Fit = 11.71% (Two-Theta Range of Fit = 47.0/52.98), 2T(0)=0.0(deg)

#	2-Theta	d(Å)	Area(a1)	Area%	Skew	FWHM	XS(Å)
1	50.881 (0.049)	1.7932 (0.0032)	30441.2 (2490.7)	21.0	0.630	0.864 (0.043)	103 (6)
2	50.862 (0.003)	1.7938 (0.0002)	144712.7 (3193.9)	100.0	0.566	0.224 (0.004)	438 (9)

Total Area = 175154.0 (4050.3)

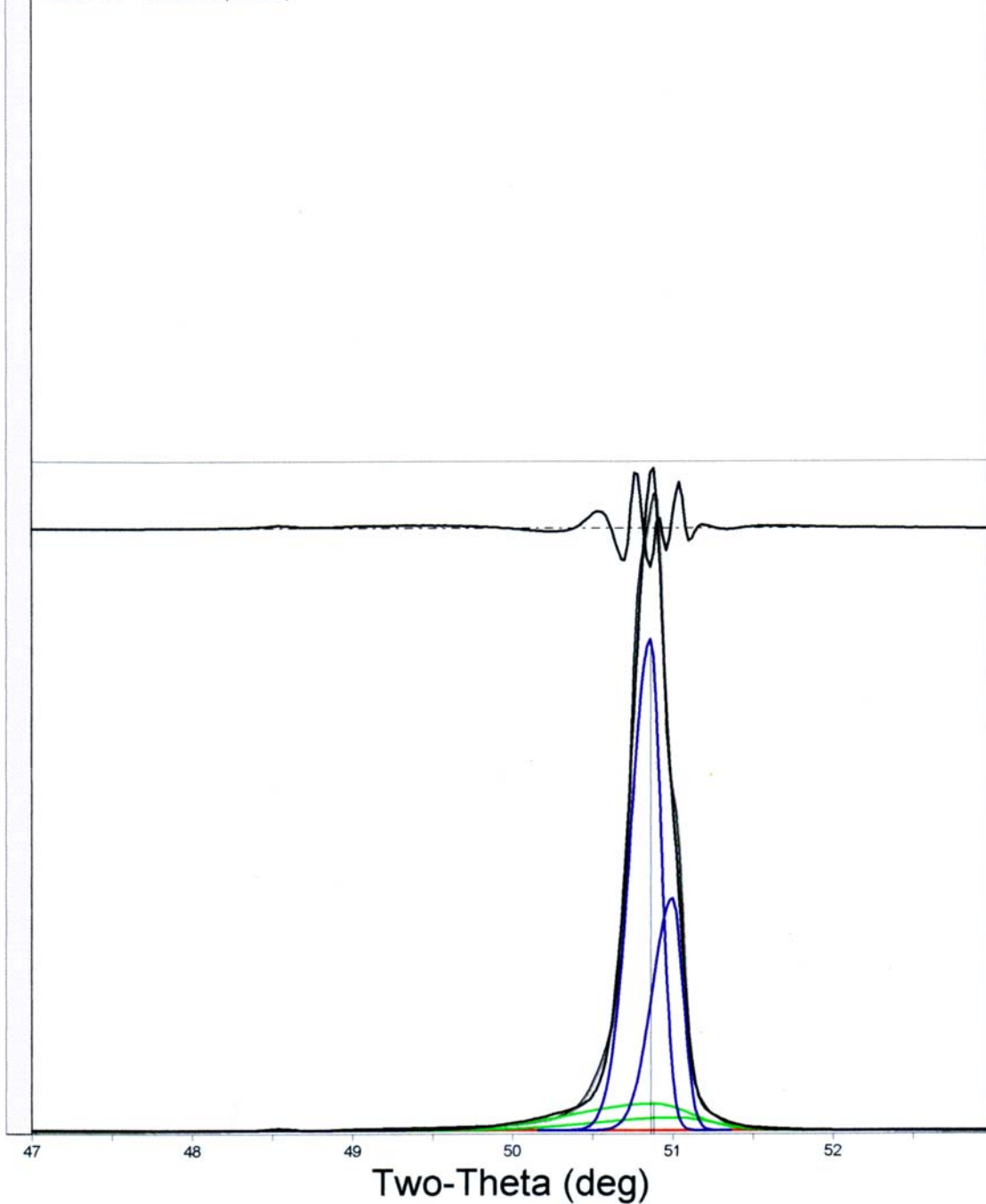


Figure B-30. XRD deconvolution of PWA 1484 (4hr. 1080°C, skewed, 11.71% error)

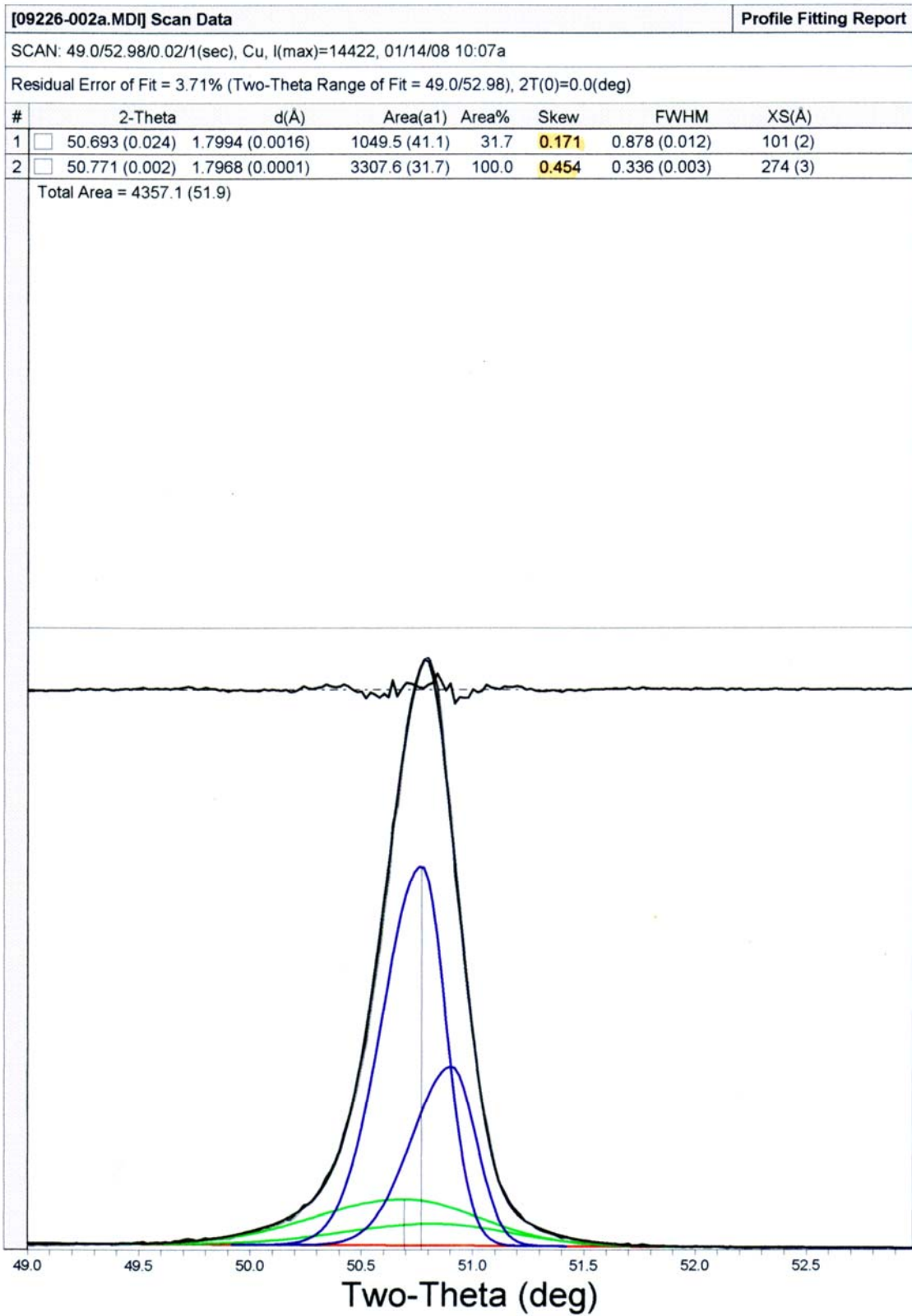


Figure B-31. XRD deconvolution of PWA 1484 (1000hr. 1080°C, skewed, 3.71% error)

**[09226-002b.MD] Scan Data** **Profile Fitting Report**

SCAN: 49.0/51.99/0.01/3(sec), Cu, I(max)=44143, 01/14/08 10:24a

Residual Error of Fit = 3.20% (Two-Theta Range of Fit = 49.0/51.99), 2T(0)=0.0(deg)

#	2-Theta	d(Å)	Area(a1)	Area%	Skew	FWHM	XS(Å)
1	50.747 (0.016)	1.7976 (0.0011)	3452.3 (102.4)	35.7	0.353	0.823 (0.010)	108 (2)
2	50.773 (0.001)	1.7967 (0.0001)	9670.4 (76.0)	100.0	0.508	0.328 (0.002)	282 (3)

Total Area = 13122.7 (127.5)

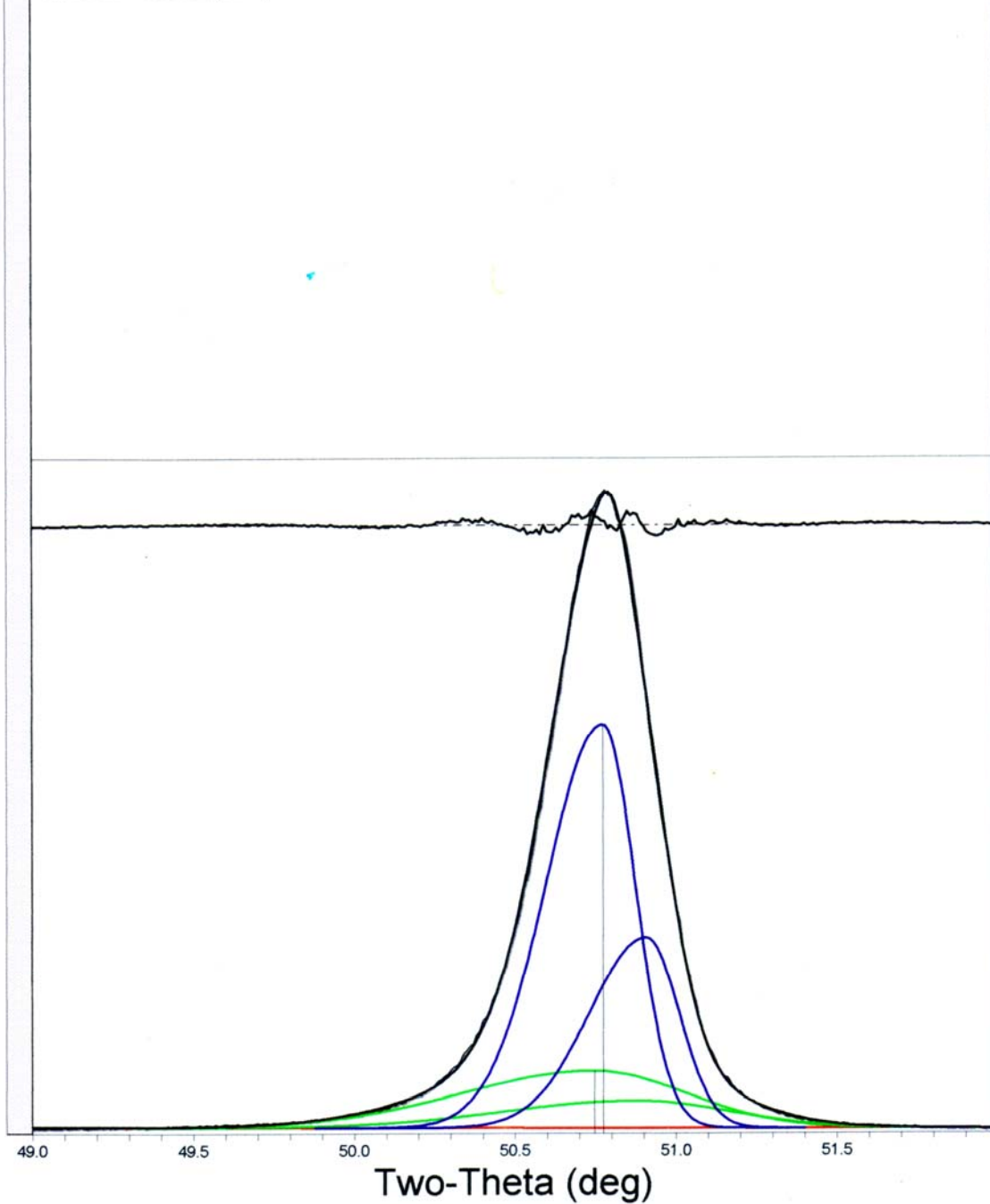


Figure B-32. XRD deconvolution of PWA 1484 (1000hr. 1080°C, skewed, 3.20% error)

SCAN: 49.0/51.99/0.01/3(sec), Cu, I(max)=4111, 01/14/08 01:42p

Residual Error of Fit = 4.07% (Two-Theta Range of Fit = 49.0/51.99), 2T(0)=0.0(deg)

#	2-Theta	d(Å)	Area(a1)	Area%	Skew	FWHM	XS(Å)
1	50.553 (0.025)	1.8040 (0.0017)	736.5 (20.6)	96.5	0.146	0.987 (0.014)	89 (2)
2	50.664 (0.003)	1.8003 (0.0002)	763.4 (13.2)	100.0	0.344	0.348 (0.005)	264 (4)

Total Area = 1499.9 (24.4)

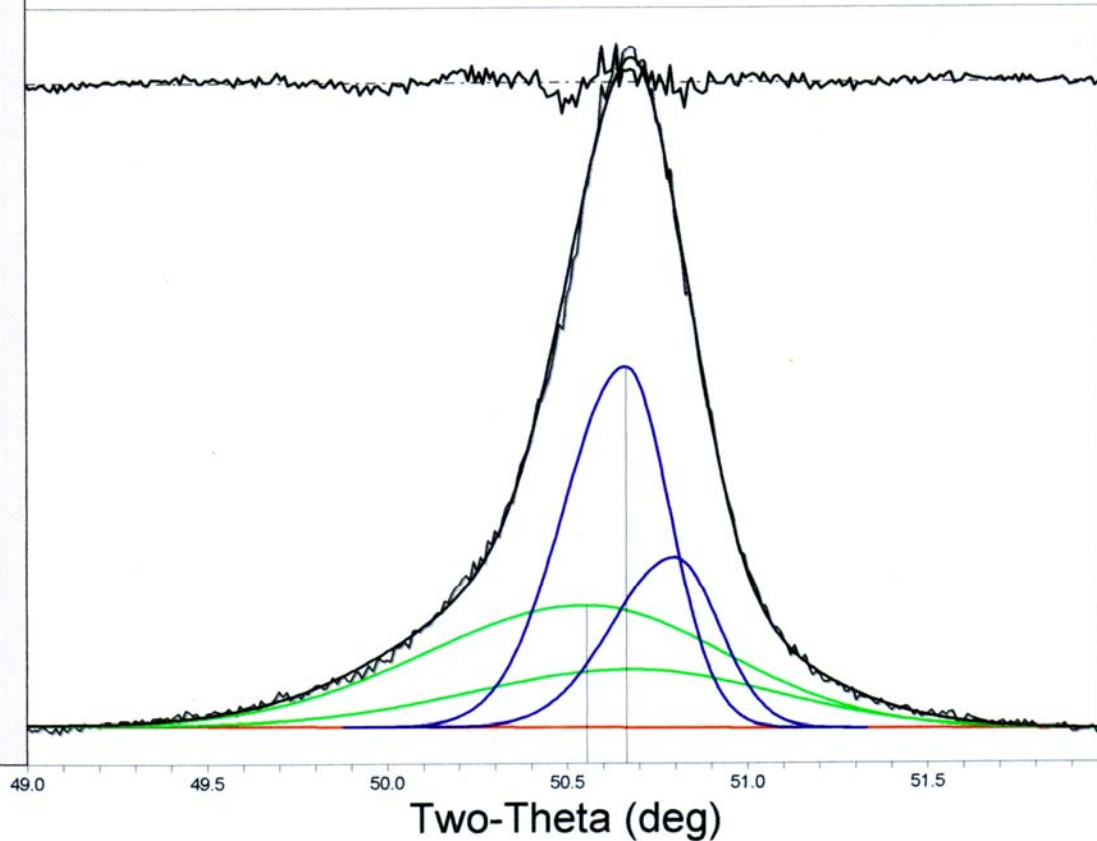


Figure B-33. XRD deconvolution of PWA 1484 (10hr. 1080°C, skewed, 4.07% error)

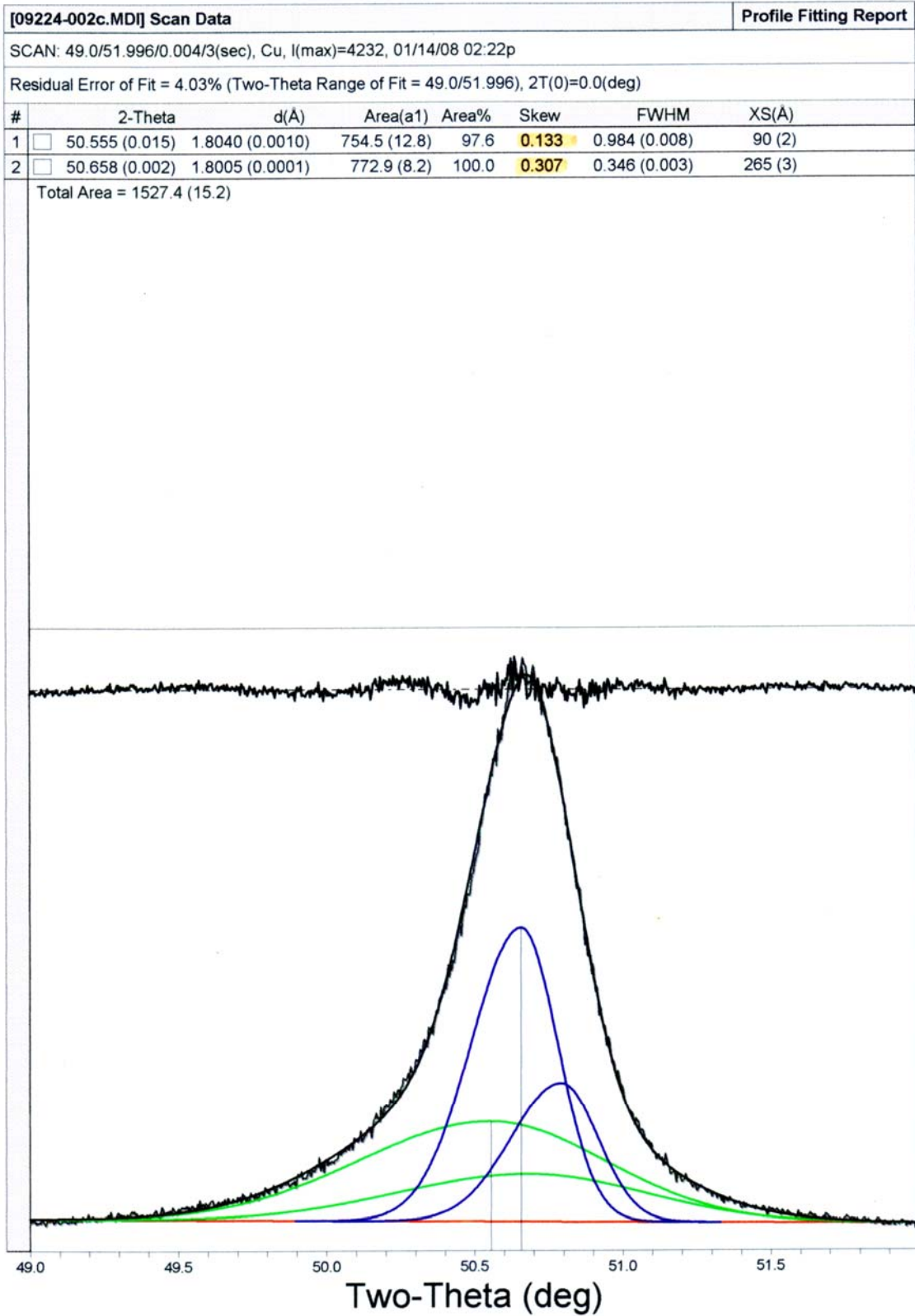


Figure B-34. XRD deconvolution of PWA 1484 (10hr. 1080°C, skewed, 4.03% error)

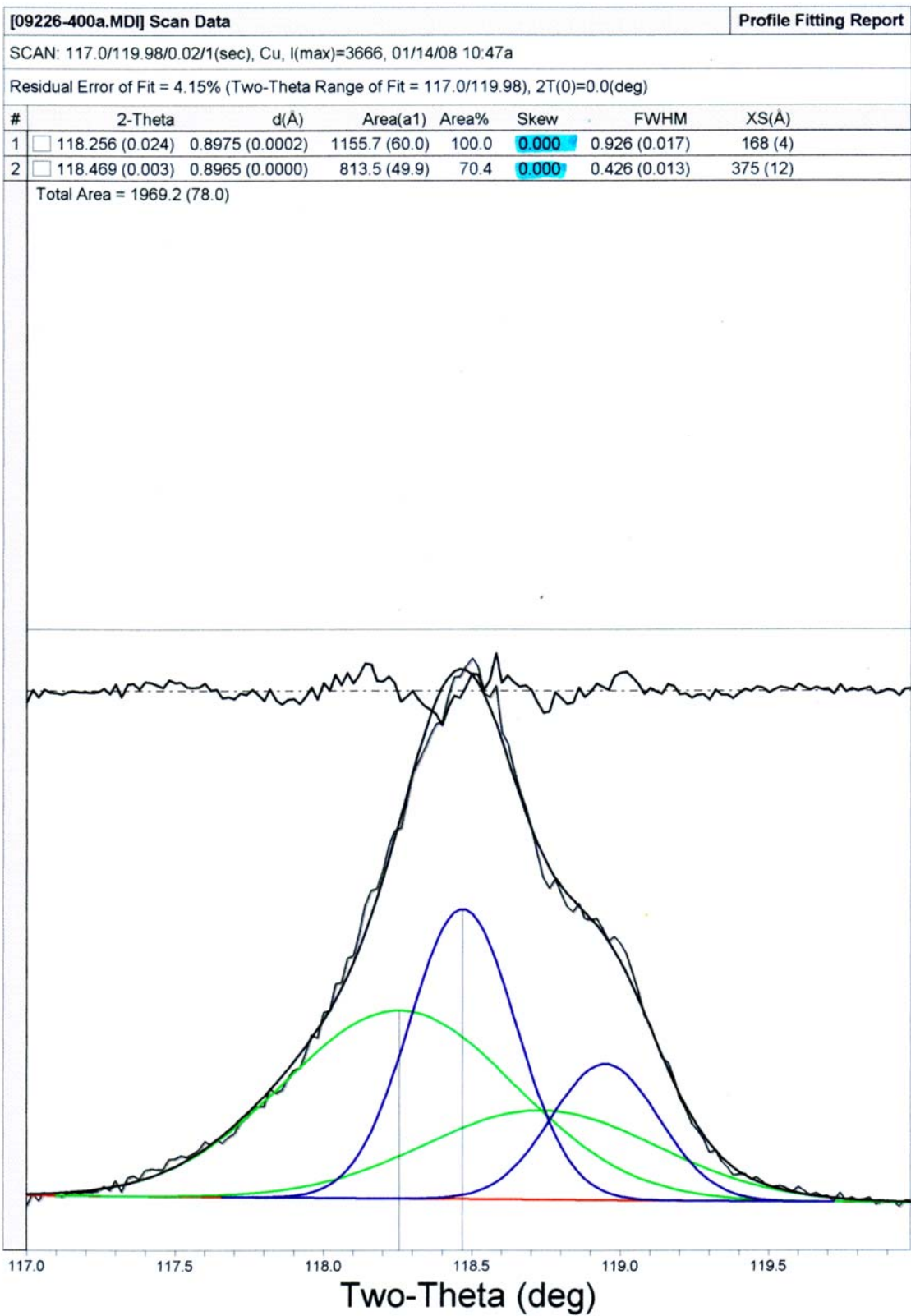


Figure B-35. XRD deconvolution of PWA 1484 (1000hr. 1080°C, unskewed, 4.15% error)

SCAN: 117.0/119.99/0.01/3(sec), Cu, I(max)=10386, 01/14/08 11:05a

Residual Error of Fit = 3.24% (Two-Theta Range of Fit = 117.0/119.99), 2T(0)=0.0(deg)

#	2-Theta	d(Å)	Area(a1)	Area%	Skew	FWHM	XS(Å)
1	118.236 (0.013)	0.8975 (0.0001)	3281.2 (91.8)	100.0	0.000	0.916 (0.010)	170 (3)
2	118.456 (0.002)	0.8965 (0.0000)	2301.9 (77.7)	70.2	0.000	0.418 (0.007)	382 (7)

Total Area = 5583.2 (120.3)

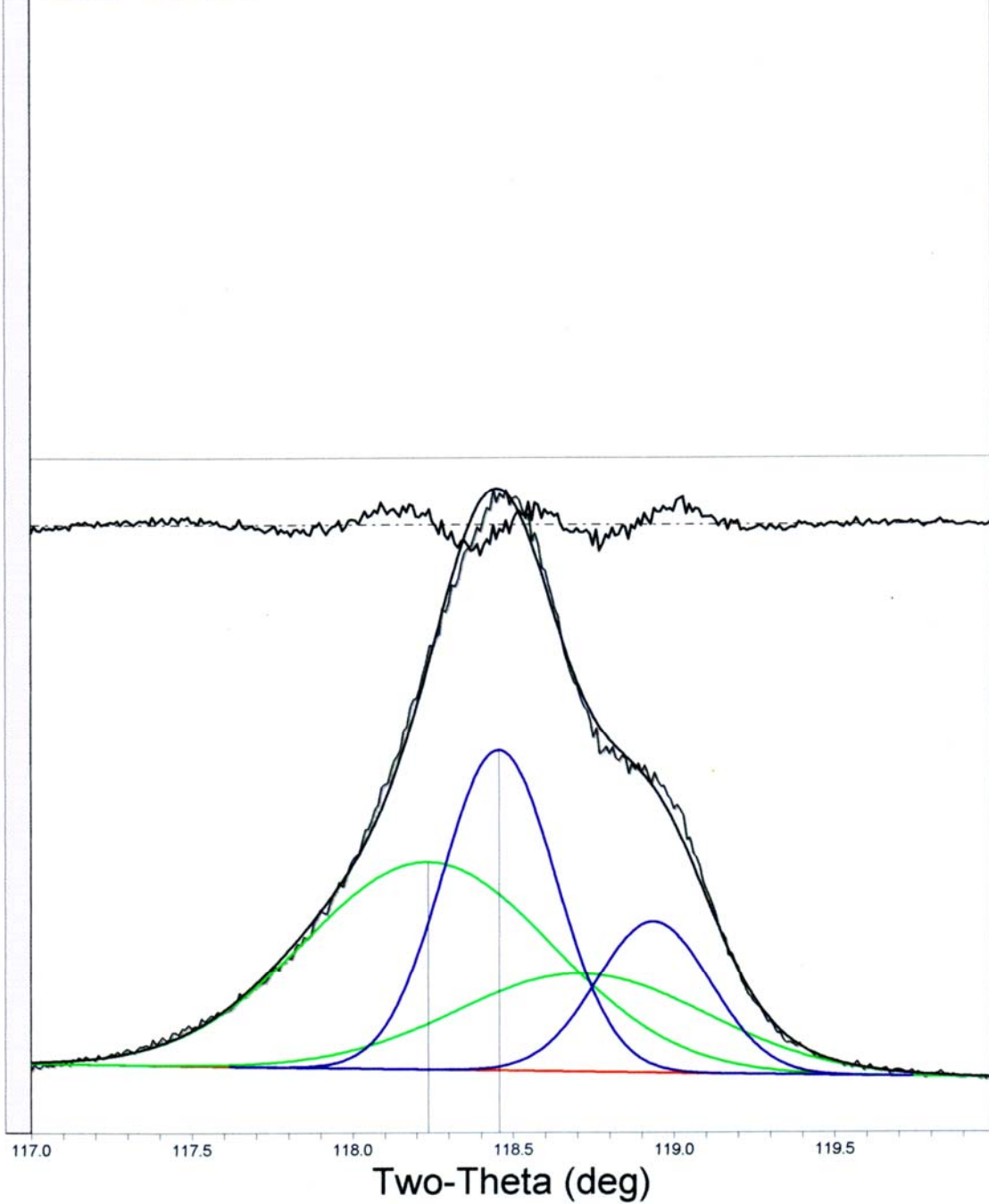


Figure B-36. XRD deconvolution of PWA 1484 (1000hr. 1080°C, unskewed, 3.24% error)

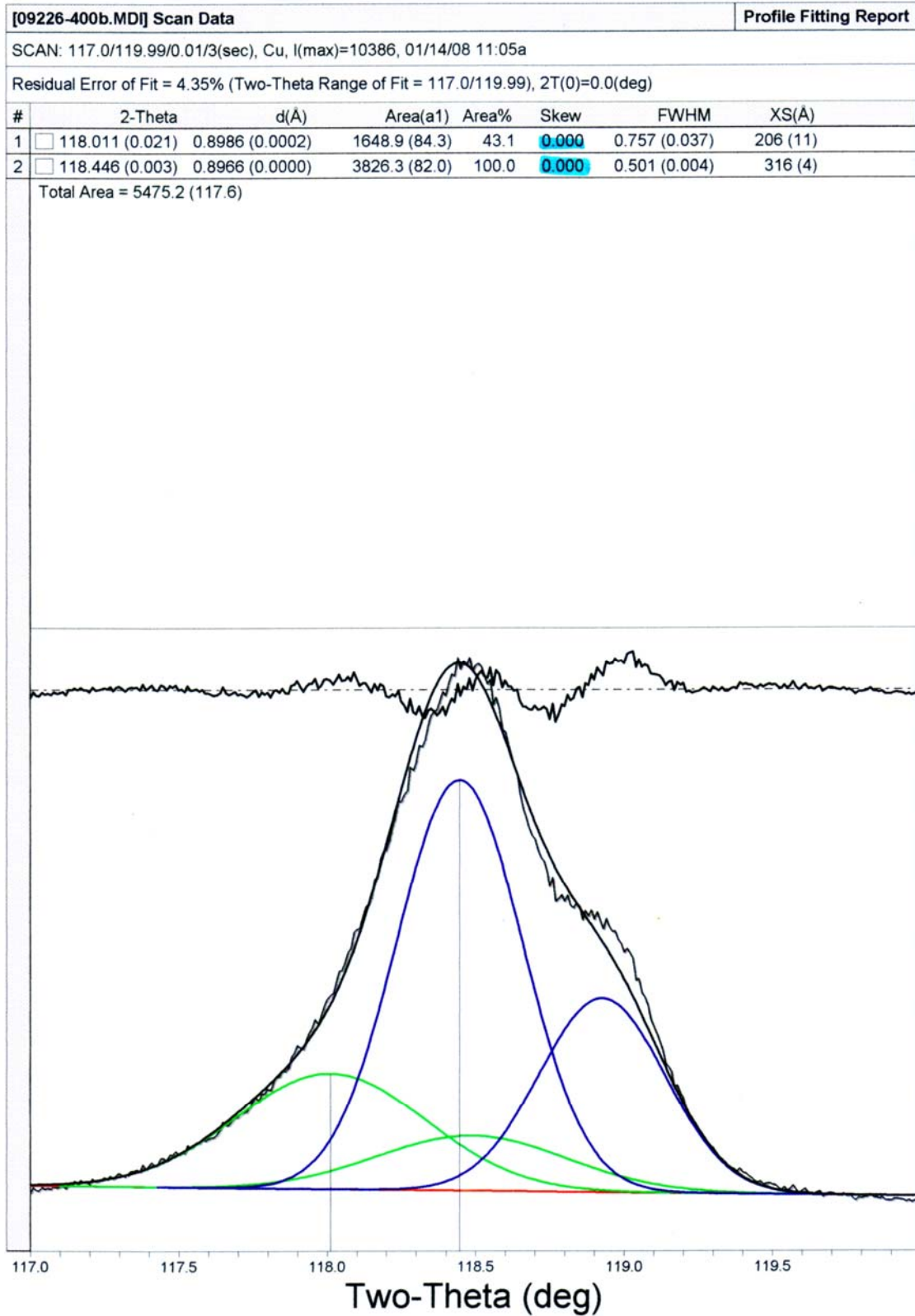


Figure B-37. XRD deconvolution of PWA 1484 (1000hr. 1080°C, unskewed, 4.35% error)

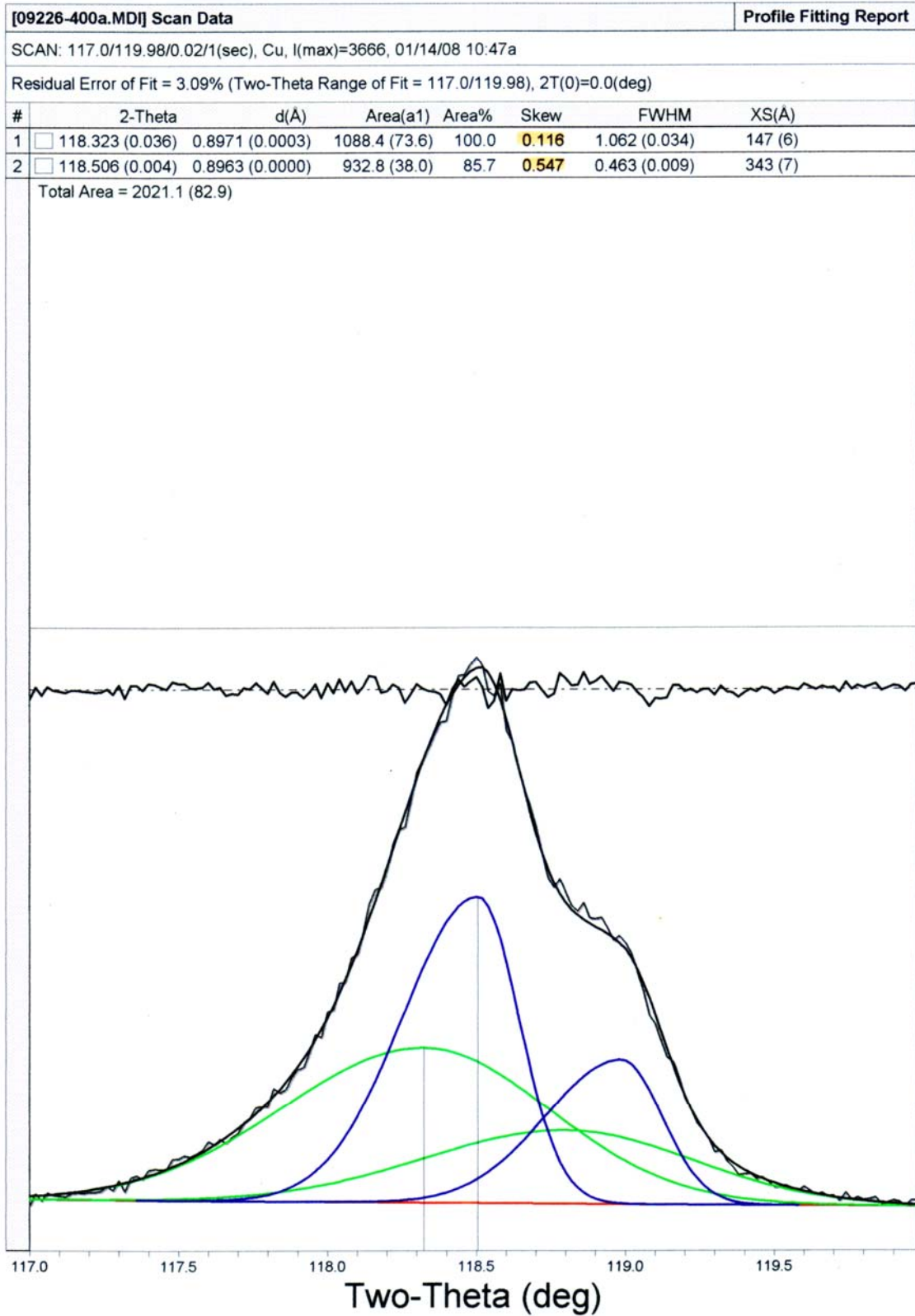


Figure B-38. XRD deconvolution of PWA 1484 (1000hr. 1080°C, skewed, 3.09% error)

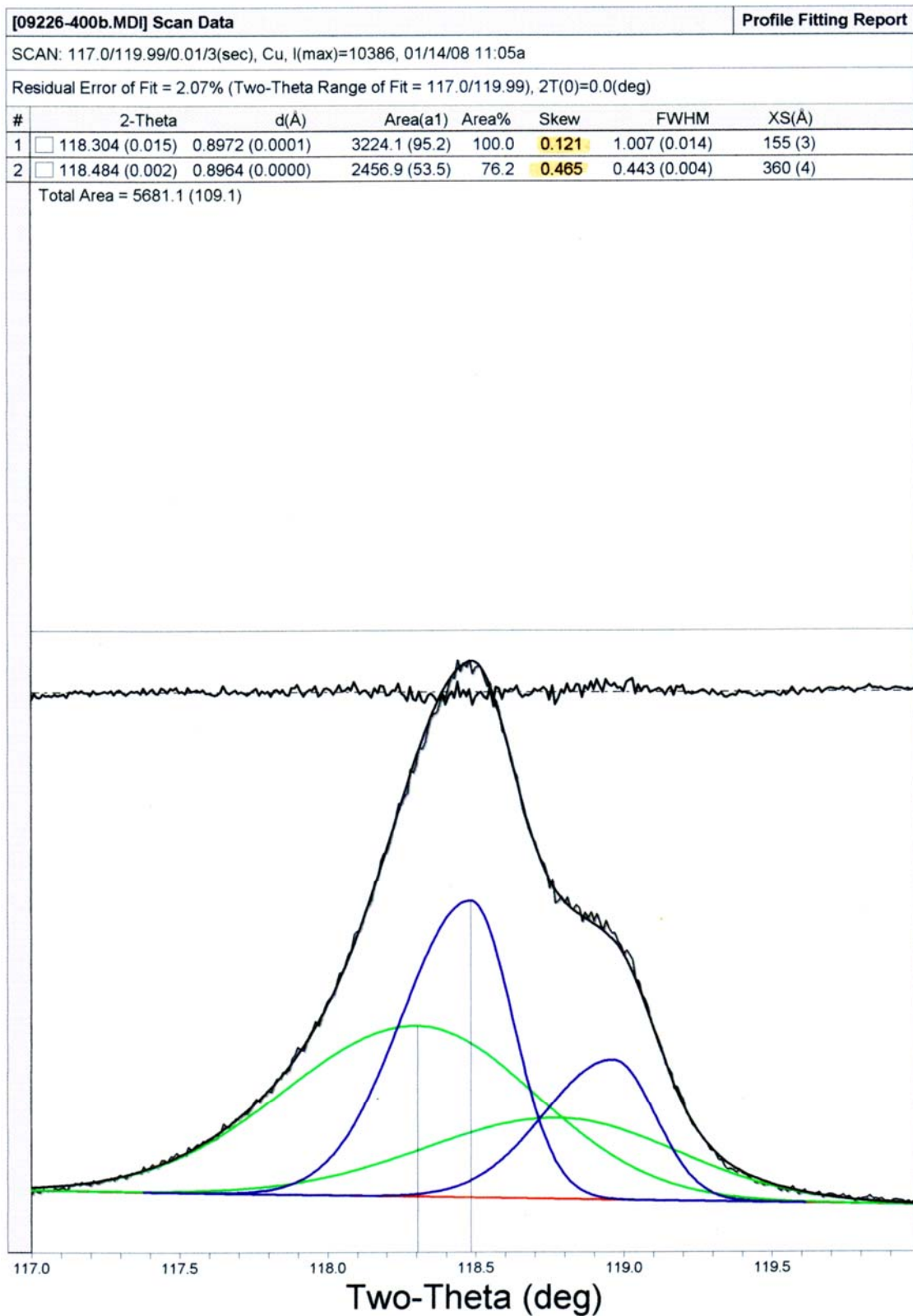


Figure B-39. XRD deconvolution of PWA 1484 (1000hr. 1080°C, skewed, 2.07% error)

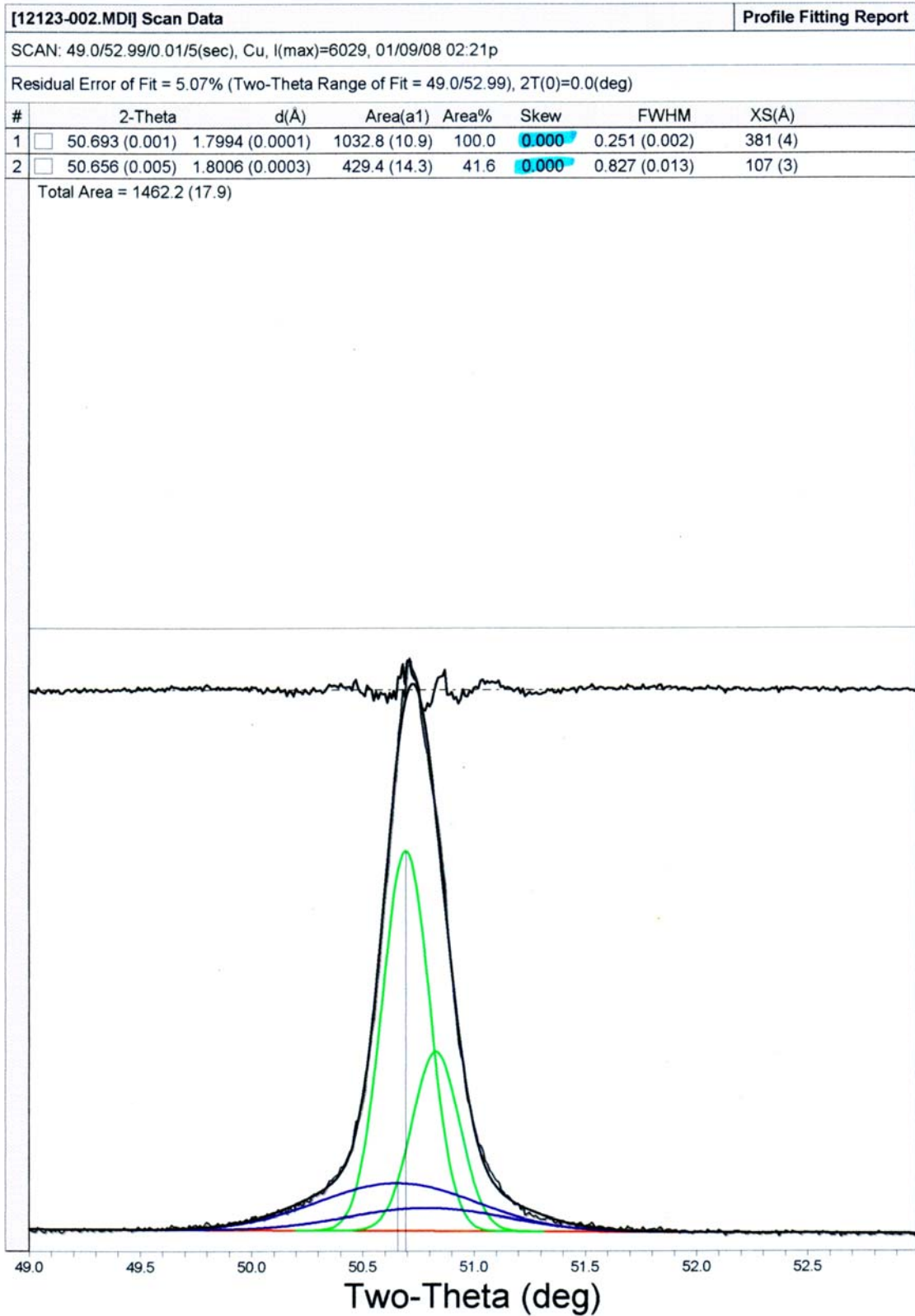


Figure B-40. XRD deconvolution of PWA 1480+ (4hr. 1080°C, unskewed, 5.07% error)

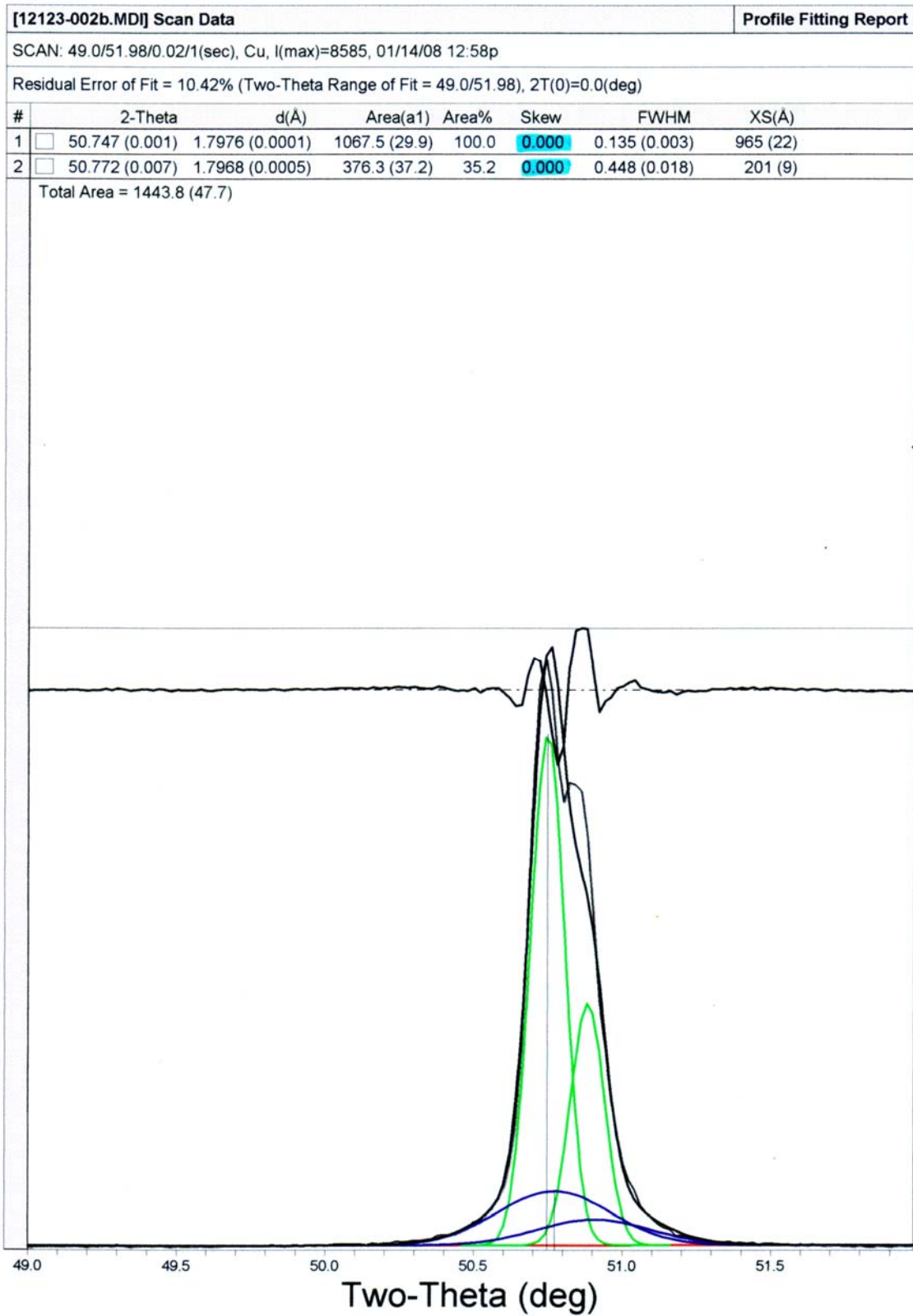


Figure B-41. XRD deconvolution of PWA 1480+ (4hr. 1080°C, unskewed, 10.42% error)

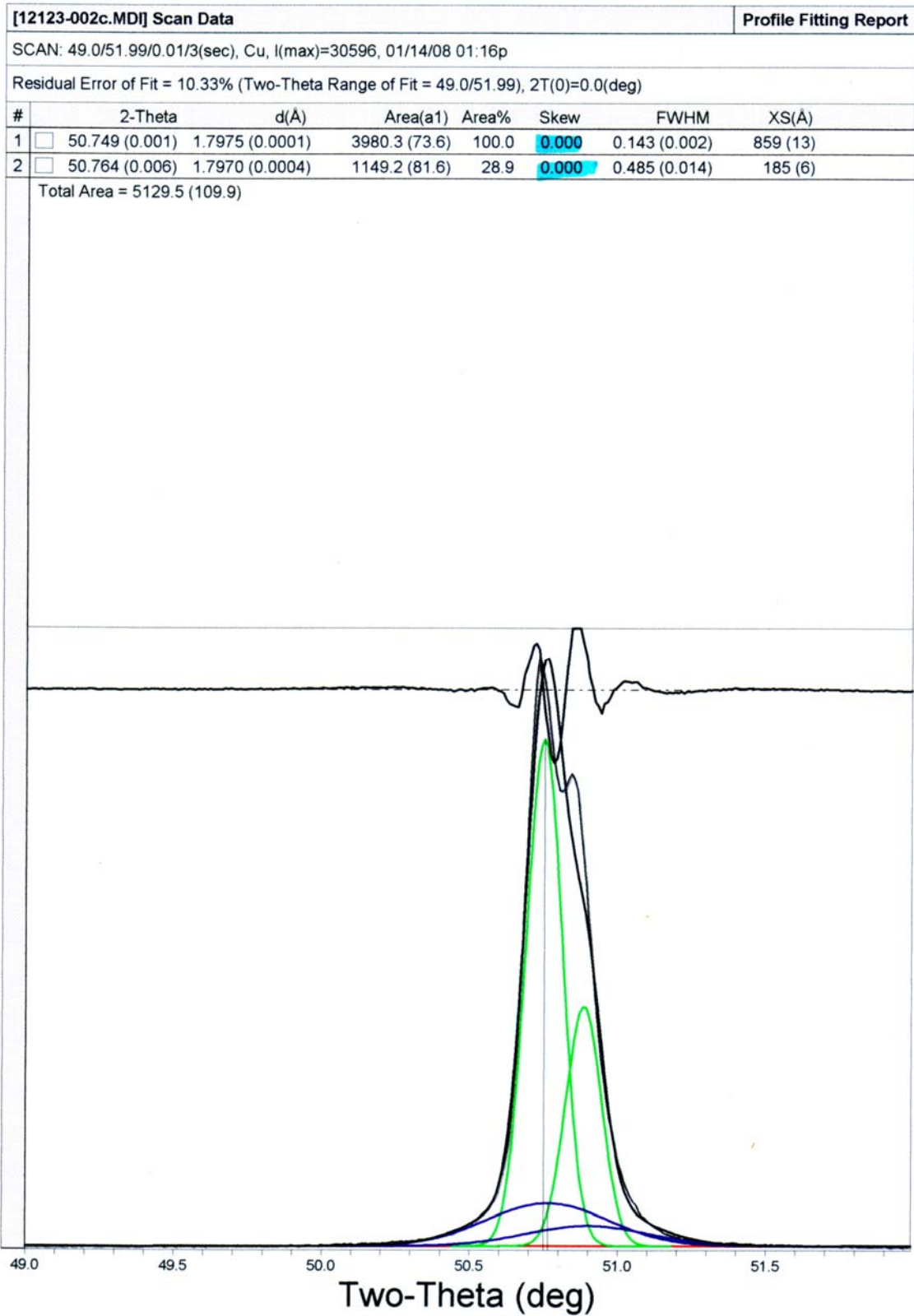


Figure B-42. XRD deconvolution of PWA 1480+ (4hr. 1080°C, unskewed, 10.33% error)

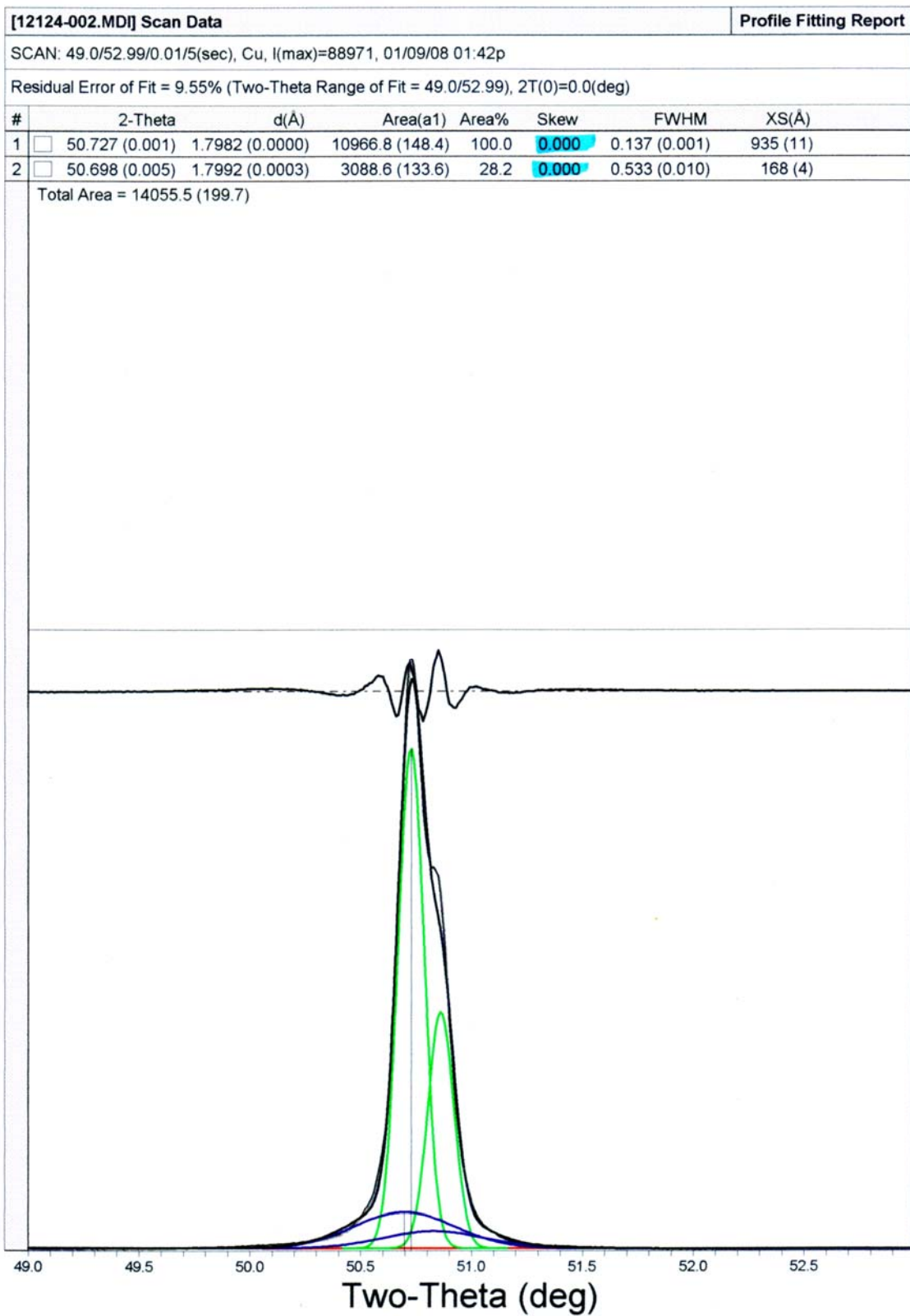


Figure B-43. XRD deconvolution of PWA 1480+ (10hr. 1080°C, unskewed, 9.55% error)

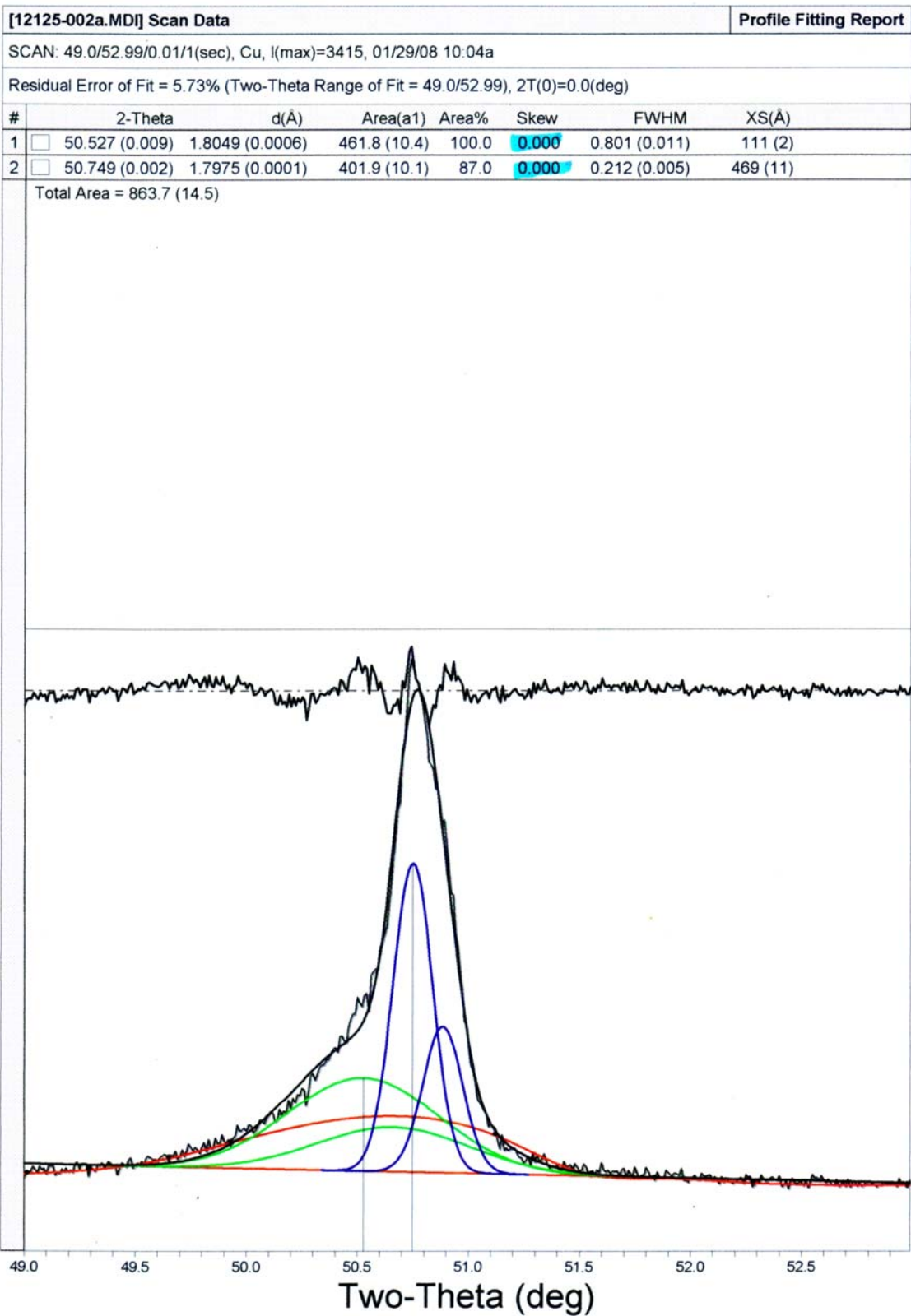


Figure B-44. XRD deconvolution of PWA 1480+ (10hr. 1080°C, unskewed, 5.73% error)

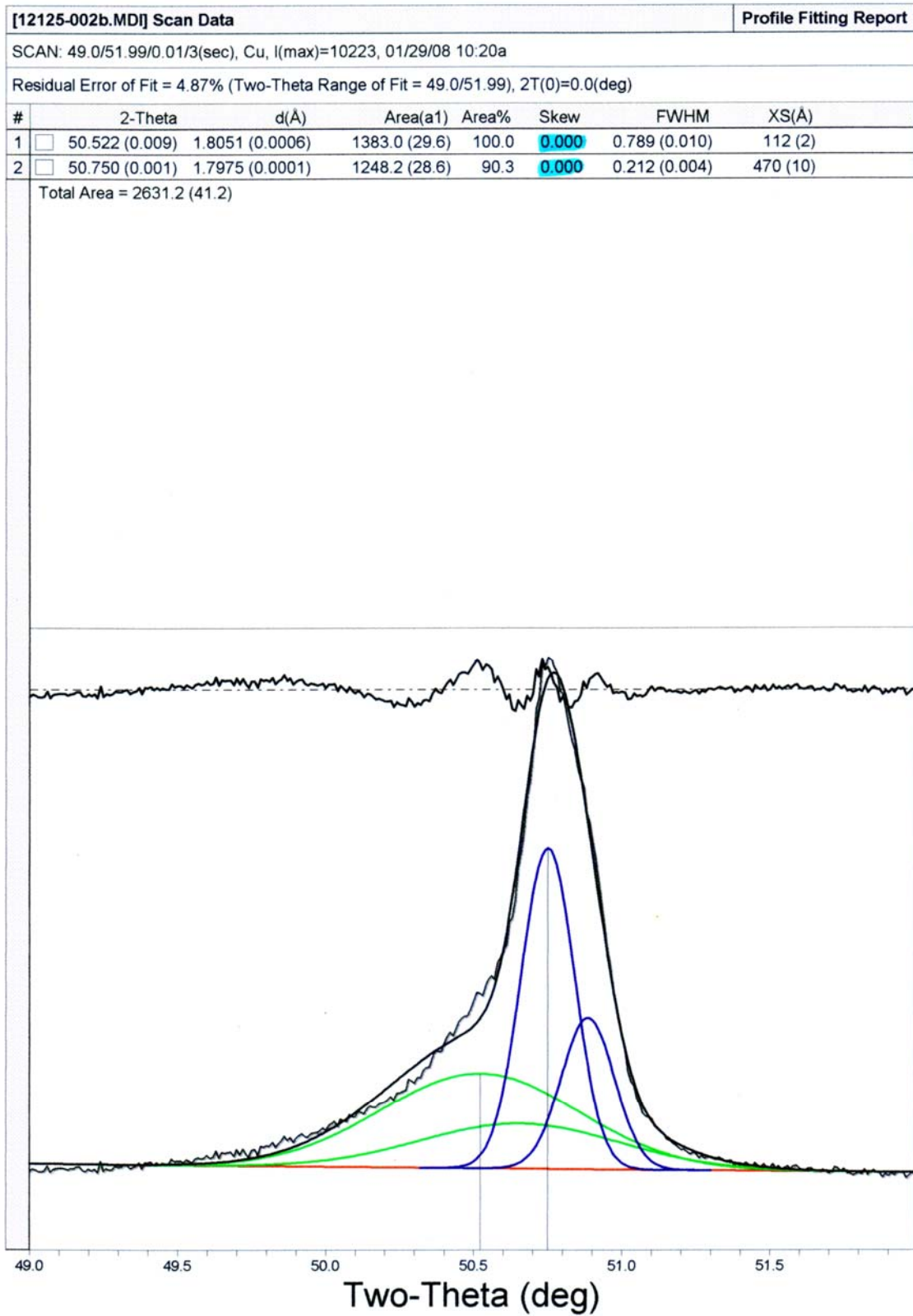


Figure B-45. XRD deconvolution of PWA 1480+ (10hr. 1080°C, unskewed, 4.87% error)

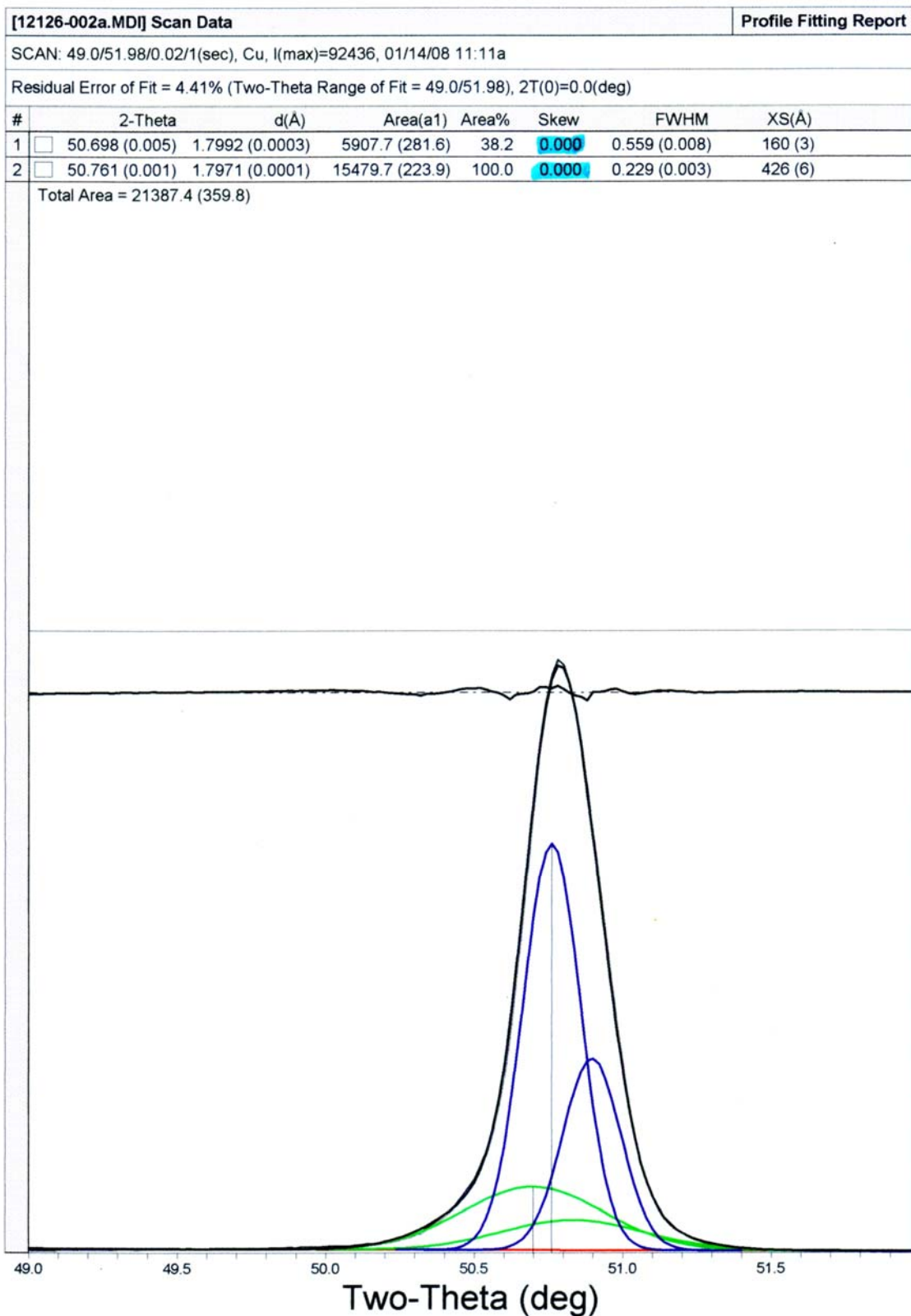


Figure B-46. XRD deconvolution of PWA 1480+ (1000hr. 1080°C, unskewed, 4.41% error)

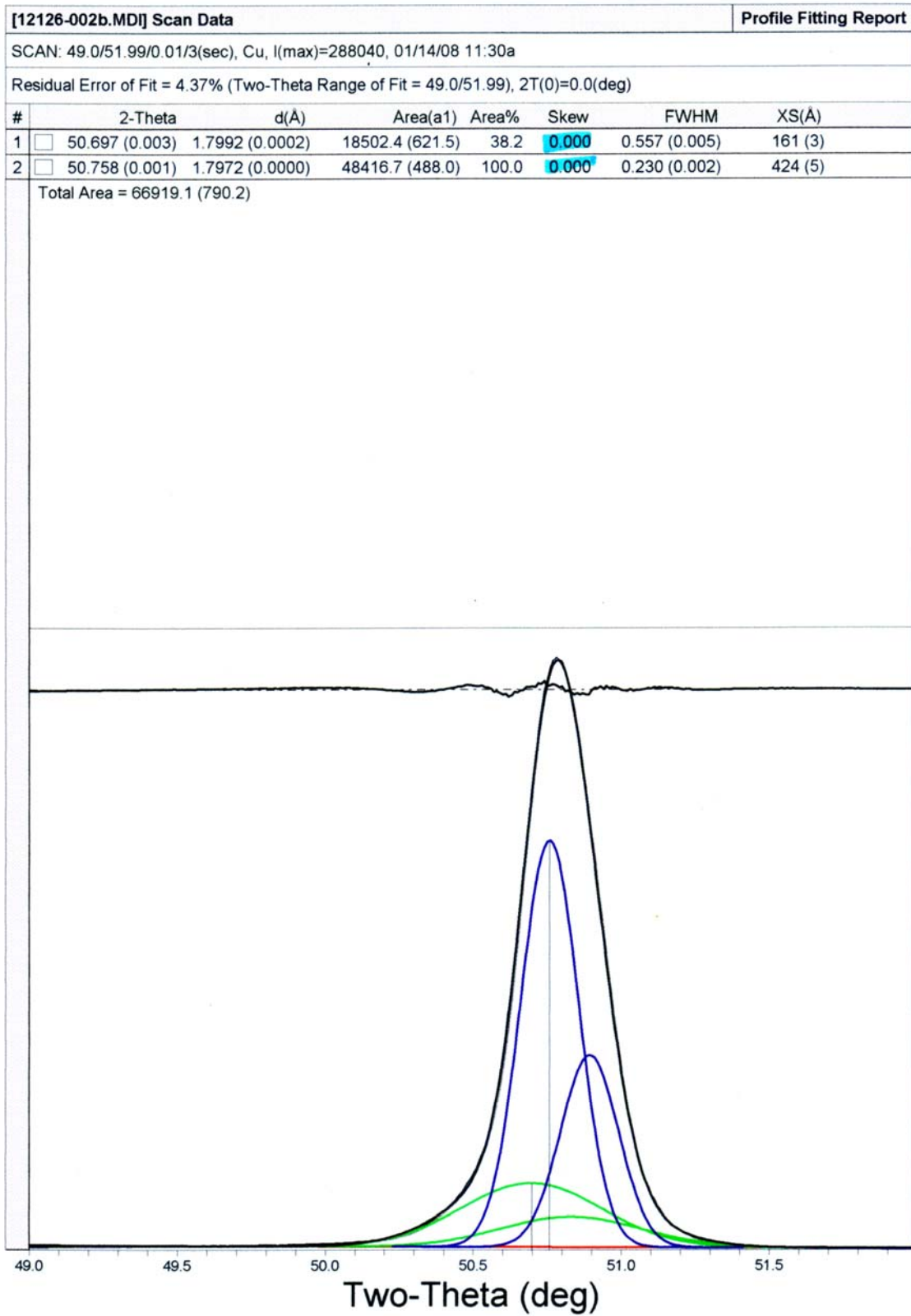


Figure B-47. XRD deconvolution of PWA 1480+ (1000hr. 1080°C, unskewed, 4.37% error)

[12123-002.MDI] Scan Data Profile Fitting Report

SCAN: 49.0/52.99/0.01/5(sec), Cu, I(max)=6029, 01/09/08 02:21p

Residual Error of Fit = 5.05% (Two-Theta Range of Fit = 49.0/52.99), 2T(0)=0.0(deg)

#	2-Theta	d(Å)	Area(a1)	Area%	Skew	FWHM	XS(Å)
1	50.695 (0.002)	1.7993 (0.0001)	1026.0 (12.3)	100.0	0.034	0.250 (0.002)	384 (5)
2	50.686 (0.022)	1.7996 (0.0015)	435.7 (14.8)	42.5	0.107	0.820 (0.013)	108 (3)

Total Area = 1461.6 (19.2)

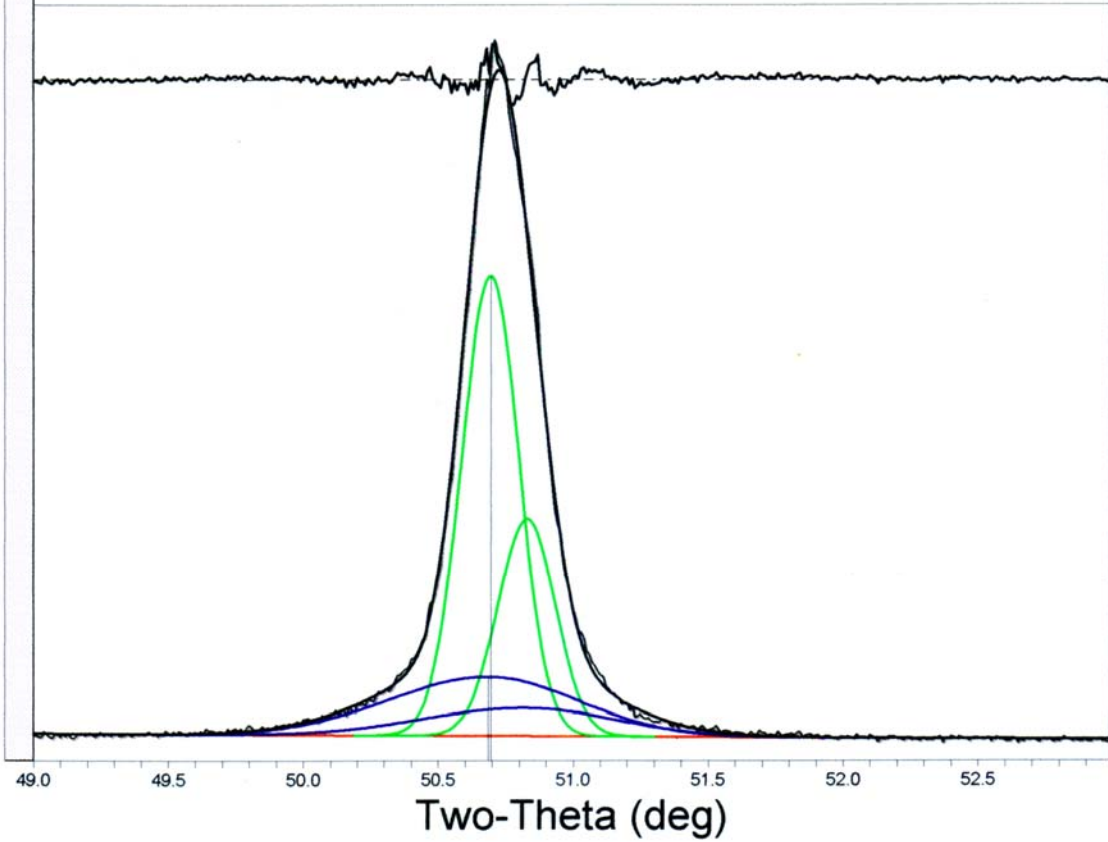


Figure B-48. XRD deconvolution of PWA 1480+ (4hr. 1080°C, skewed, 5.05% error)

[12123-002b.MD] Scan Data Profile Fitting Report

SCAN: 49.0/51.98/0.02/1(sec), Cu, I(max)=8585, 01/14/08 12:58p

Residual Error of Fit = 6.91% (Two-Theta Range of Fit = 49.0/51.98), 2T(0)=0.0(deg)

#	2-Theta	d(Å)	Area(a1)	Area%	Skew	FWHM	XS(Å)
1	50.730 (0.001)	1.7982 (0.0001)	1107.7 (21.0)	100.0	-0.468	0.141 (0.002)	885 (14)
2	50.752 (0.027)	1.7974 (0.0018)	347.4 (24.3)	31.4	-0.026	0.469 (0.013)	192 (6)

Total Area = 1455.2 (32.1)

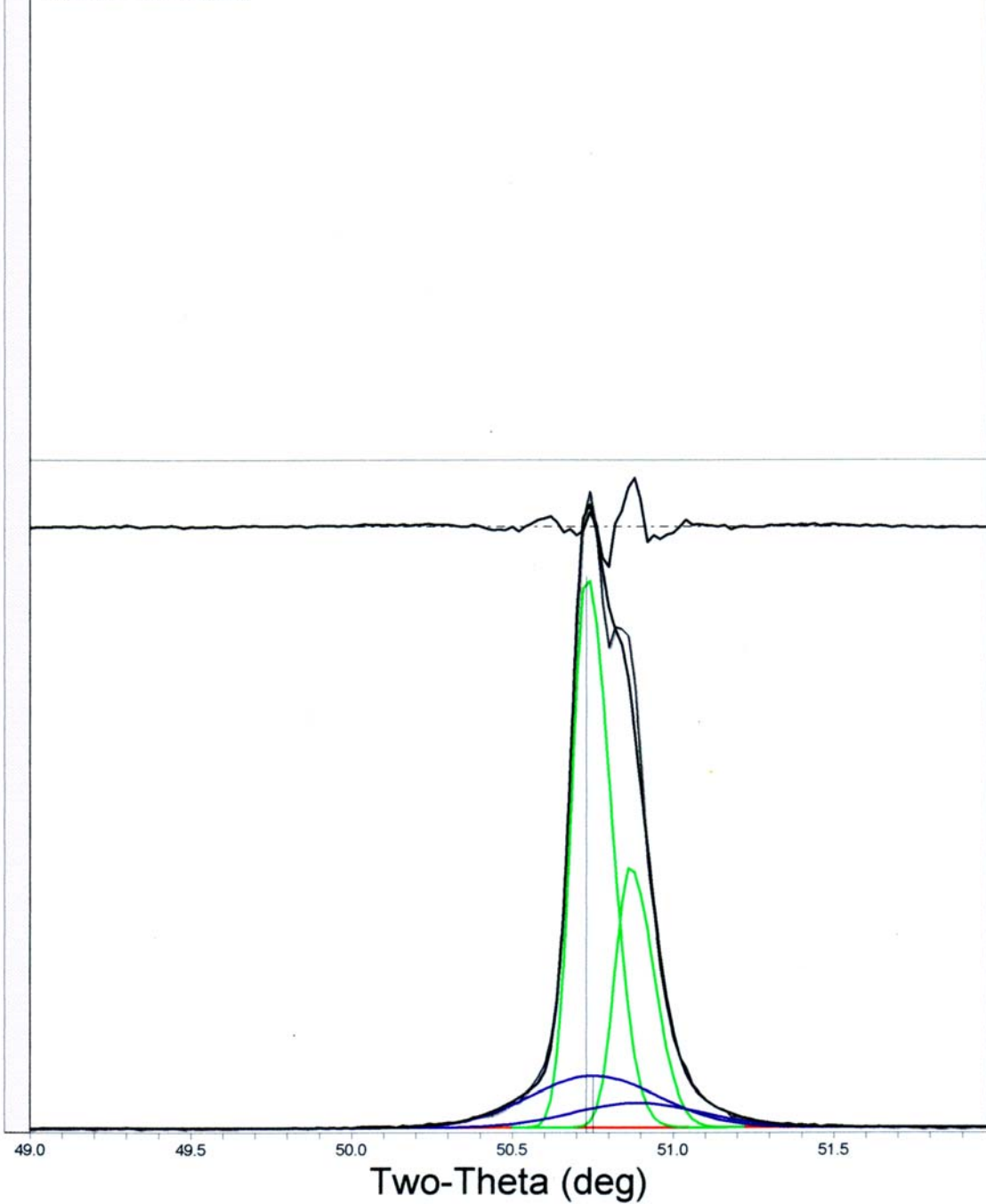


Figure B-49. XRD deconvolution of PWA 1480+ (4hr. 1080°C, skewed, 6.91% error)

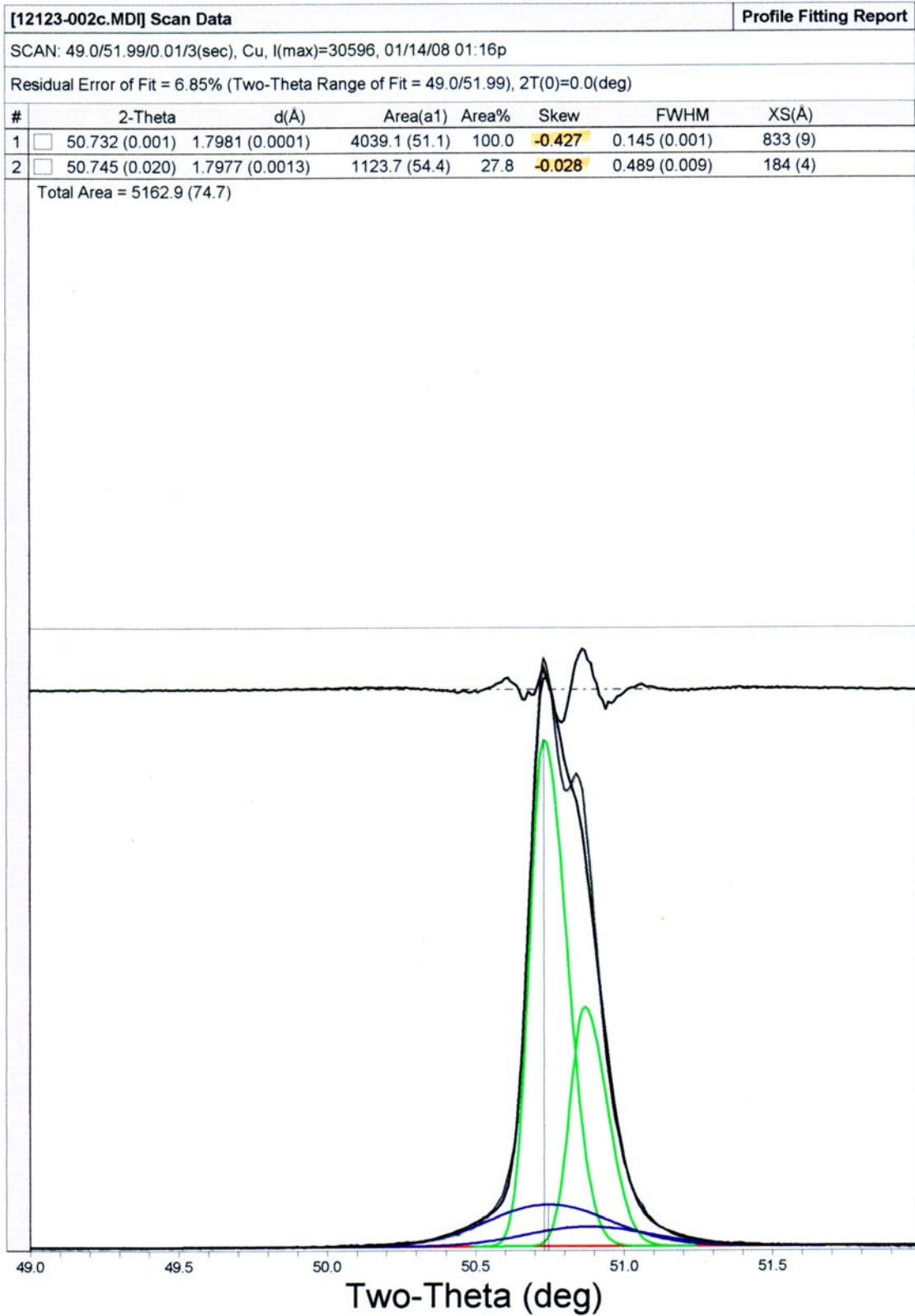


Figure B-50. XRD deconvolution of PWA 1480+ (4hr. 1080°C, skewed, 6.85% error)

**[12124-002.MDI] Scan Data** **Profile Fitting Report**

SCAN: 49.0/52.99/0.01/5(sec), Cu, I(max)=88971, 01/09/08 01:42p

Residual Error of Fit = 9.54% (Two-Theta Range of Fit = 49.0/52.99), 2T(0)=0.0(deg)

#	2-Theta	d(Å)	Area(a1)	Area%	Skew	FWHM	XS(Å)
1	50.727 (0.001)	1.7982 (0.0001)	10963.1 (152.6)	100.0	0.010	0.137 (0.001)	936 (11)
2	50.699 (0.021)	1.7992 (0.0014)	3091.8 (139.0)	28.2	0.005	0.533 (0.010)	168 (4)

Total Area = 14055.0 (206.4)

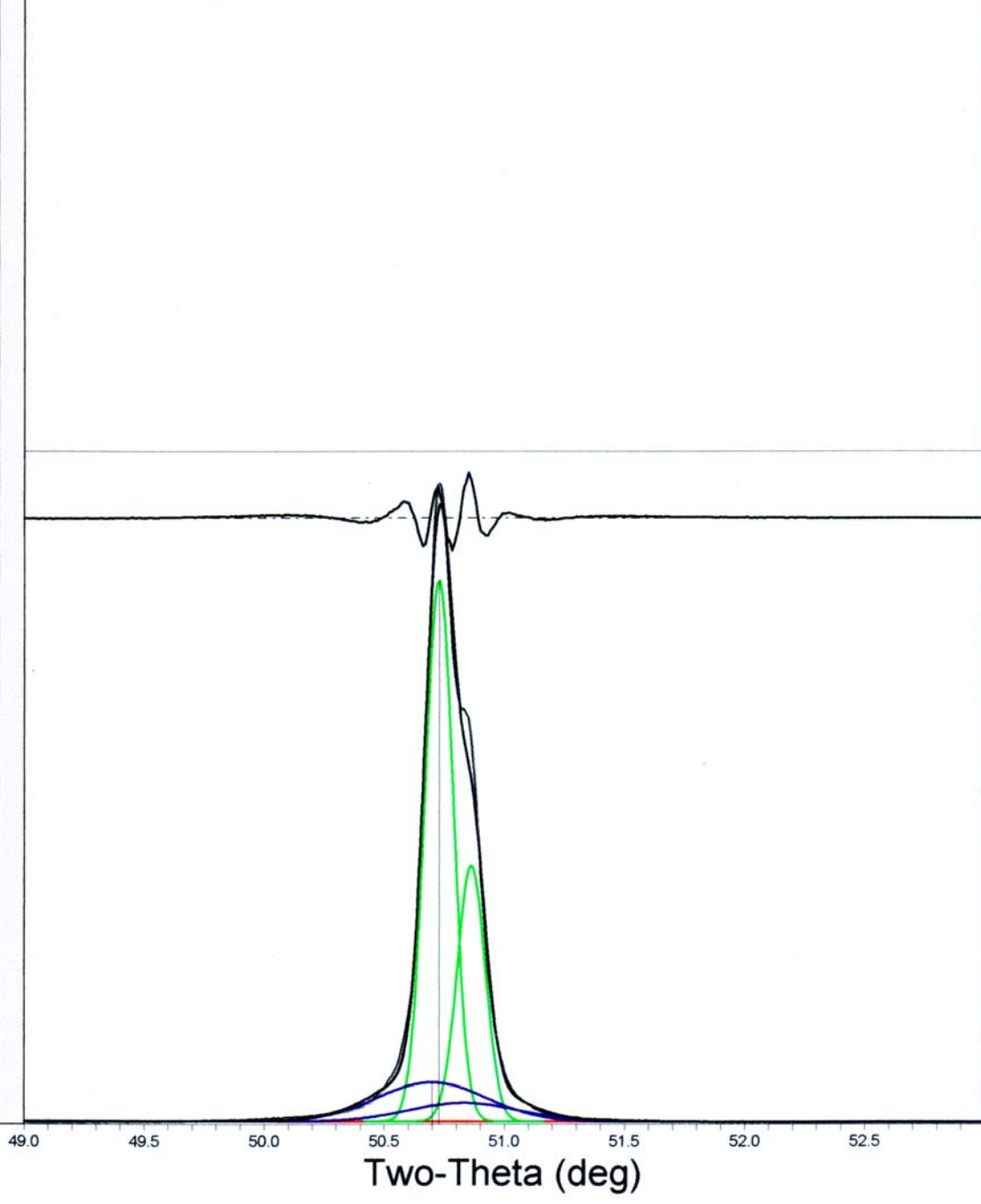


Figure B-51. XRD deconvolution of PWA 1480+ (10hr. 1080°C, skewed, 9.54% error)

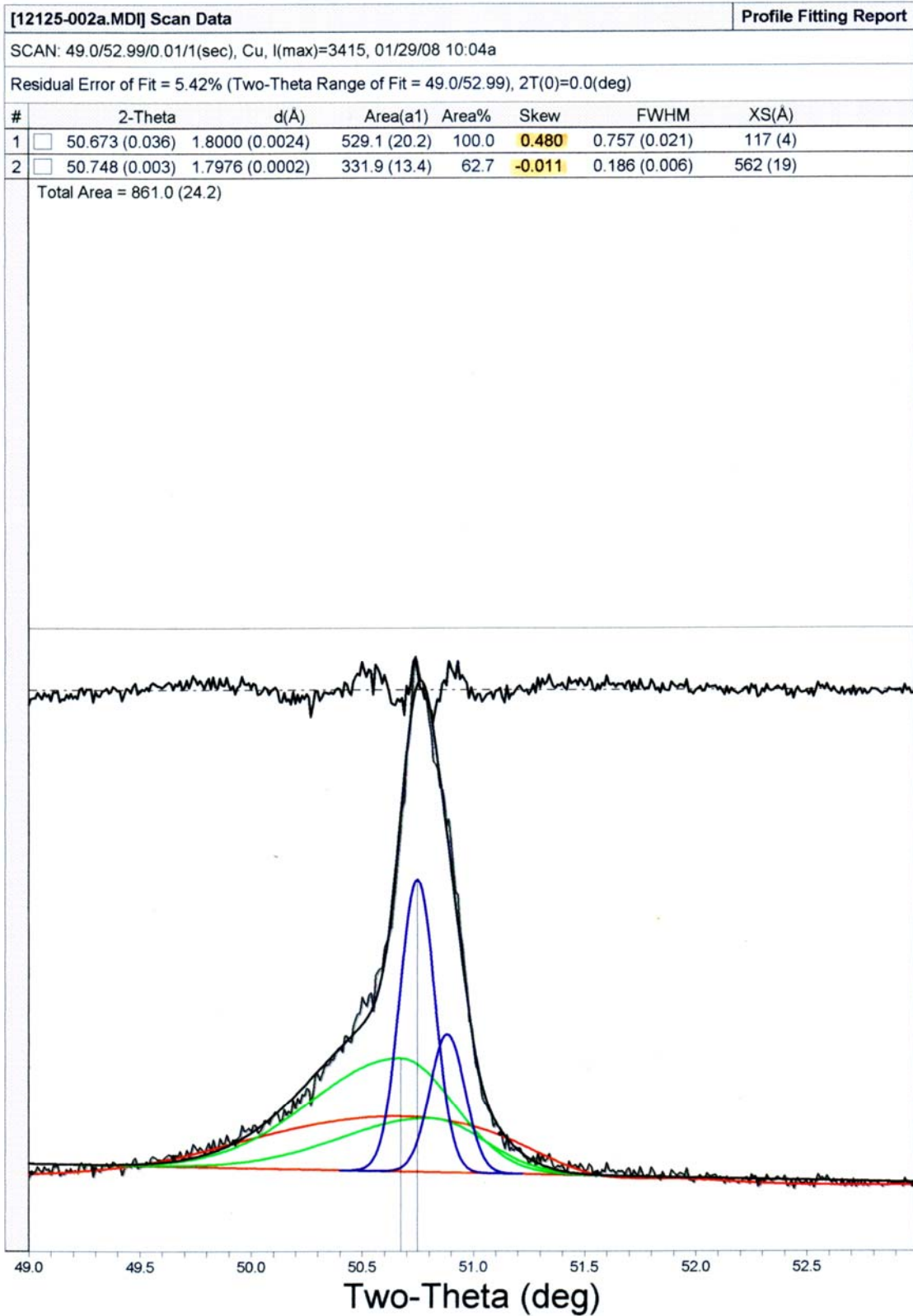


Figure B-52. XRD deconvolution of PWA 1480+ (100hr. 1080°C, skewed, 5.42% error)

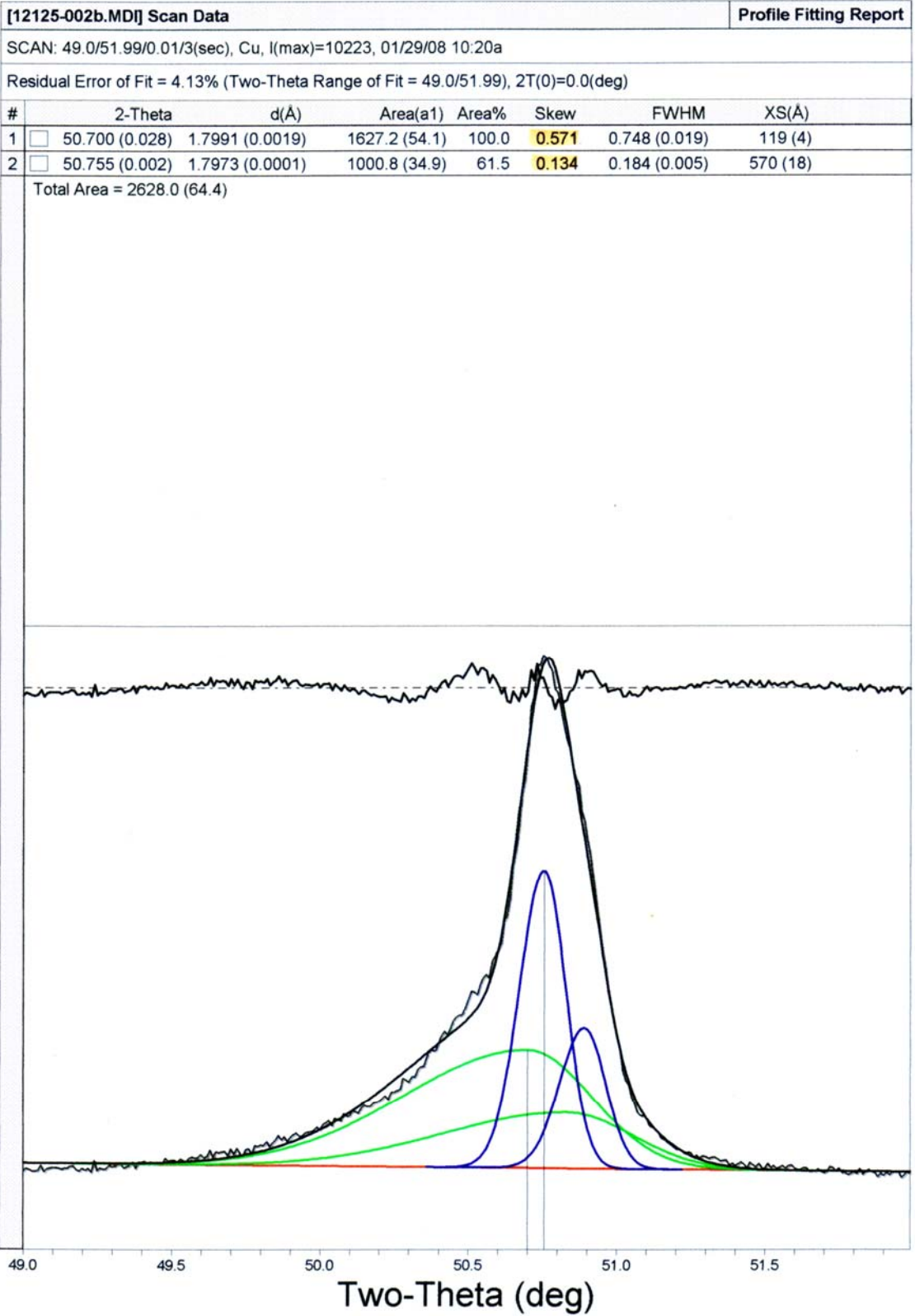


Figure B-53. XRD deconvolution of PWA 1480+ (100hr. 1080°C, skewed, 4.13% error)

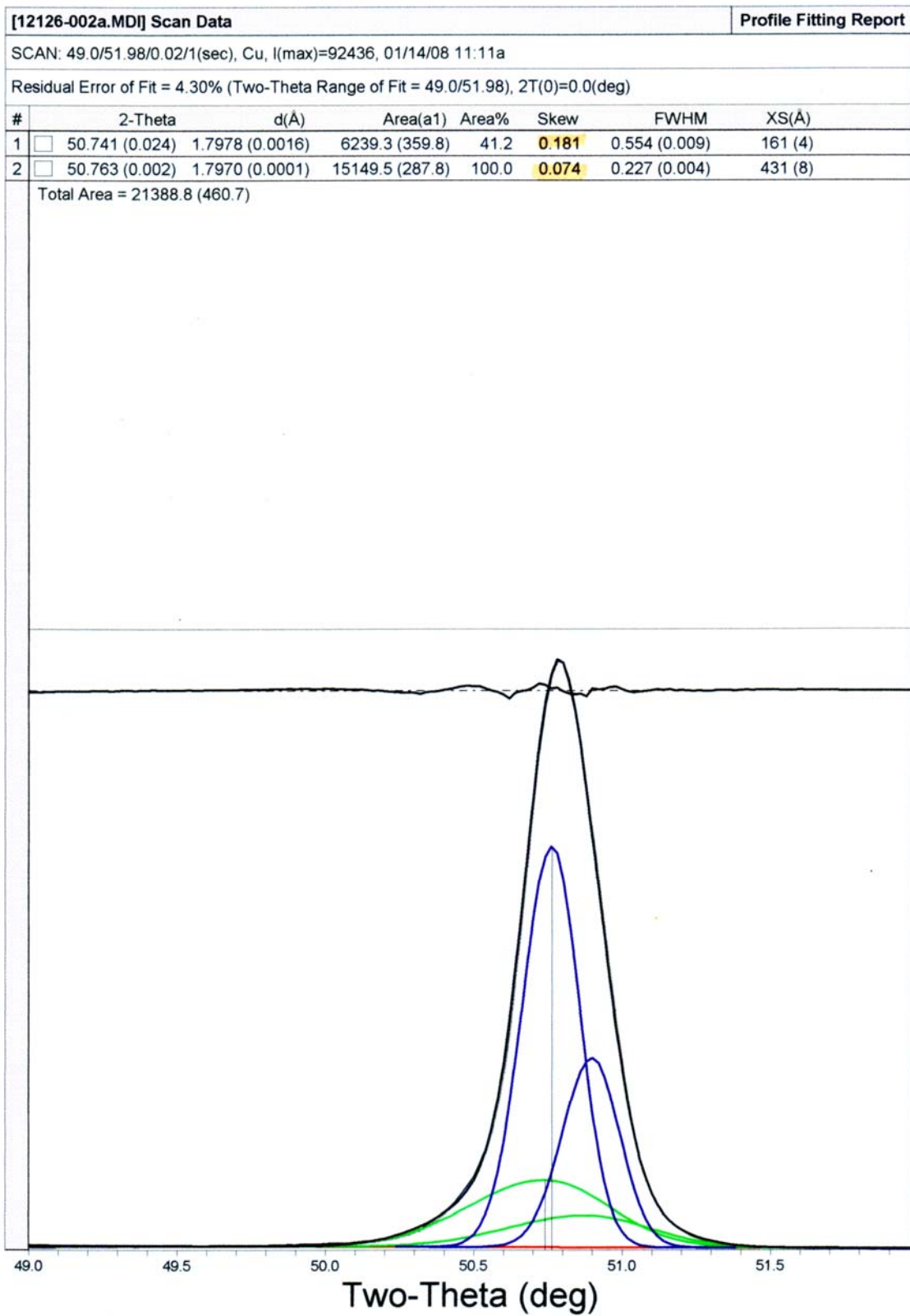


Figure B-54. XRD deconvolution of PWA 1480+ (1000hr. 1080°C, skewed, 4.30% error)

**[12126-002b.MD] Scan Data** **Profile Fitting Report**

SCAN: 49.0/51.99/0.01/3(sec), Cu, I(max)=288040, 01/14/08 11:30a

Residual Error of Fit = 4.28% (Two-Theta Range of Fit = 49.0/51.99), 2T(0)=0.0(deg)

#	2-Theta	d(Å)	Area(a1)	Area%	Skew	FWHM	XS(Å)
1	50.736 (0.017)	1.7979 (0.0011)	19504.5 (788.8)	41.1	0.164	0.551 (0.006)	162 (3)
2	50.759 (0.001)	1.7972 (0.0001)	47415.8 (629.9)	100.0	0.050	0.228 (0.002)	429 (6)

Total Area = 66920.4 (1009.5)

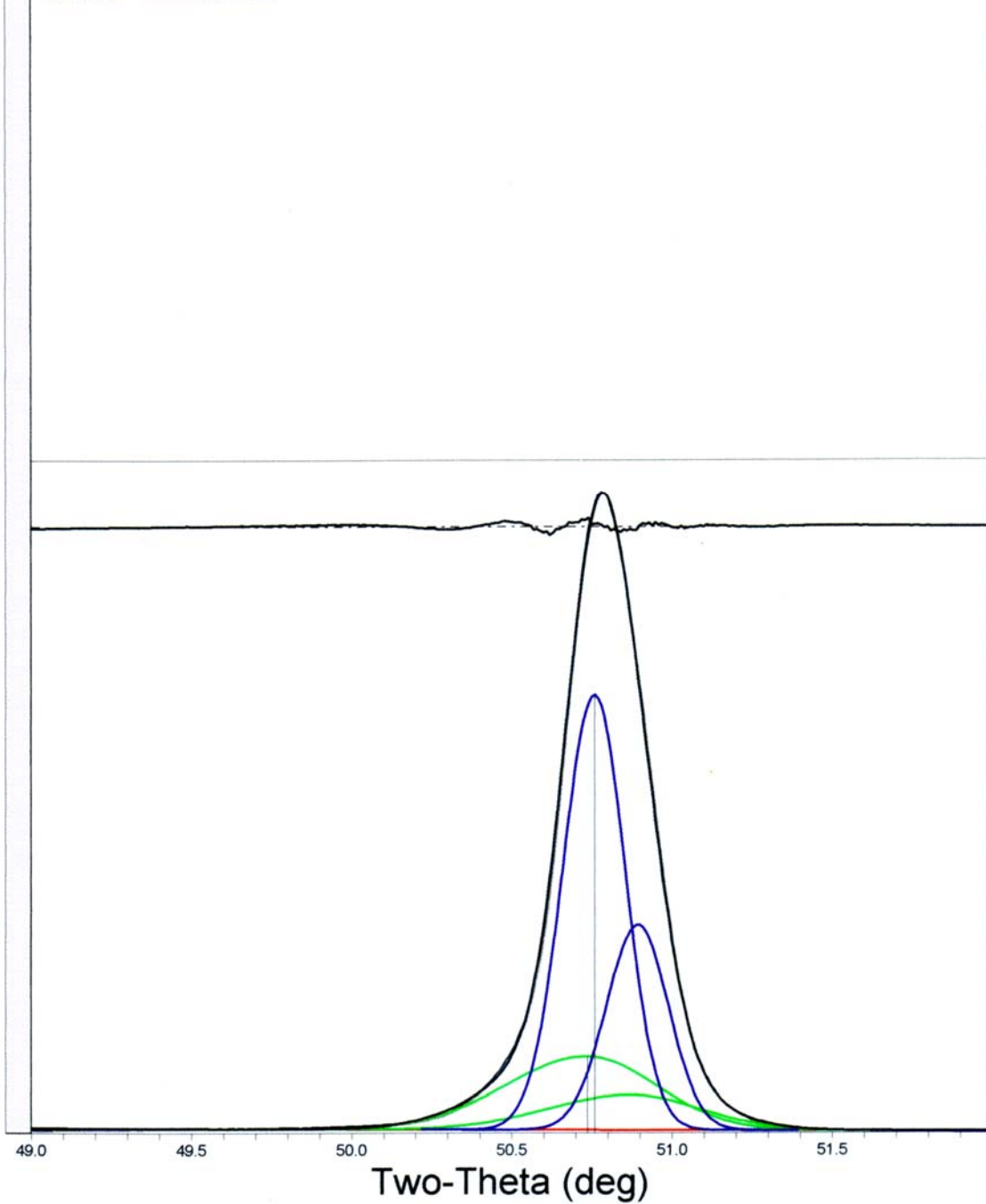


Figure B-55. XRD deconvolution of PWA 1480+ (1000hr. 1080°C, skewed, 4.28% error)

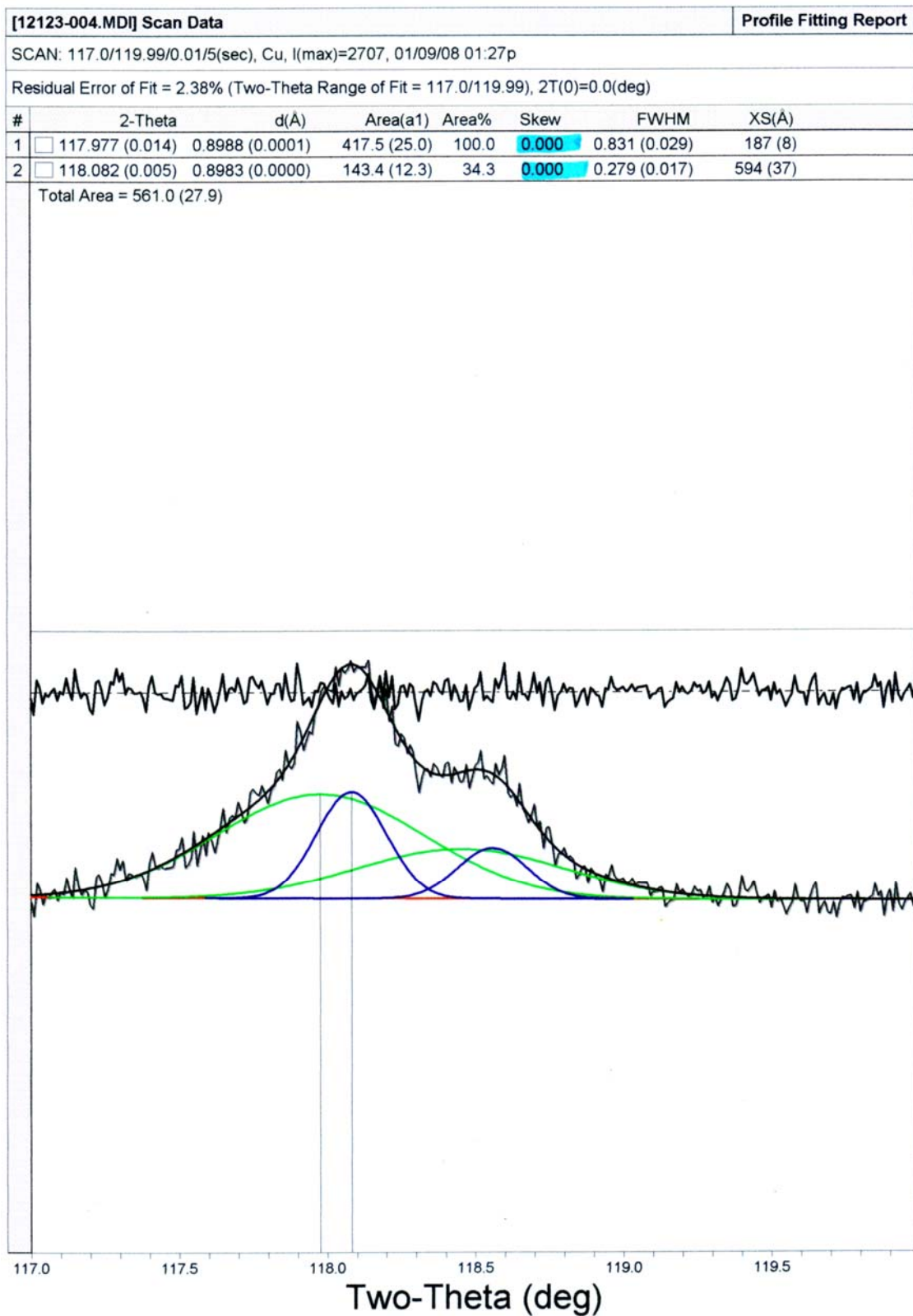


Figure B-56. XRD deconvolution of PWA 1480+ (4hr. 1080°C, unskewed, 2.38% error)

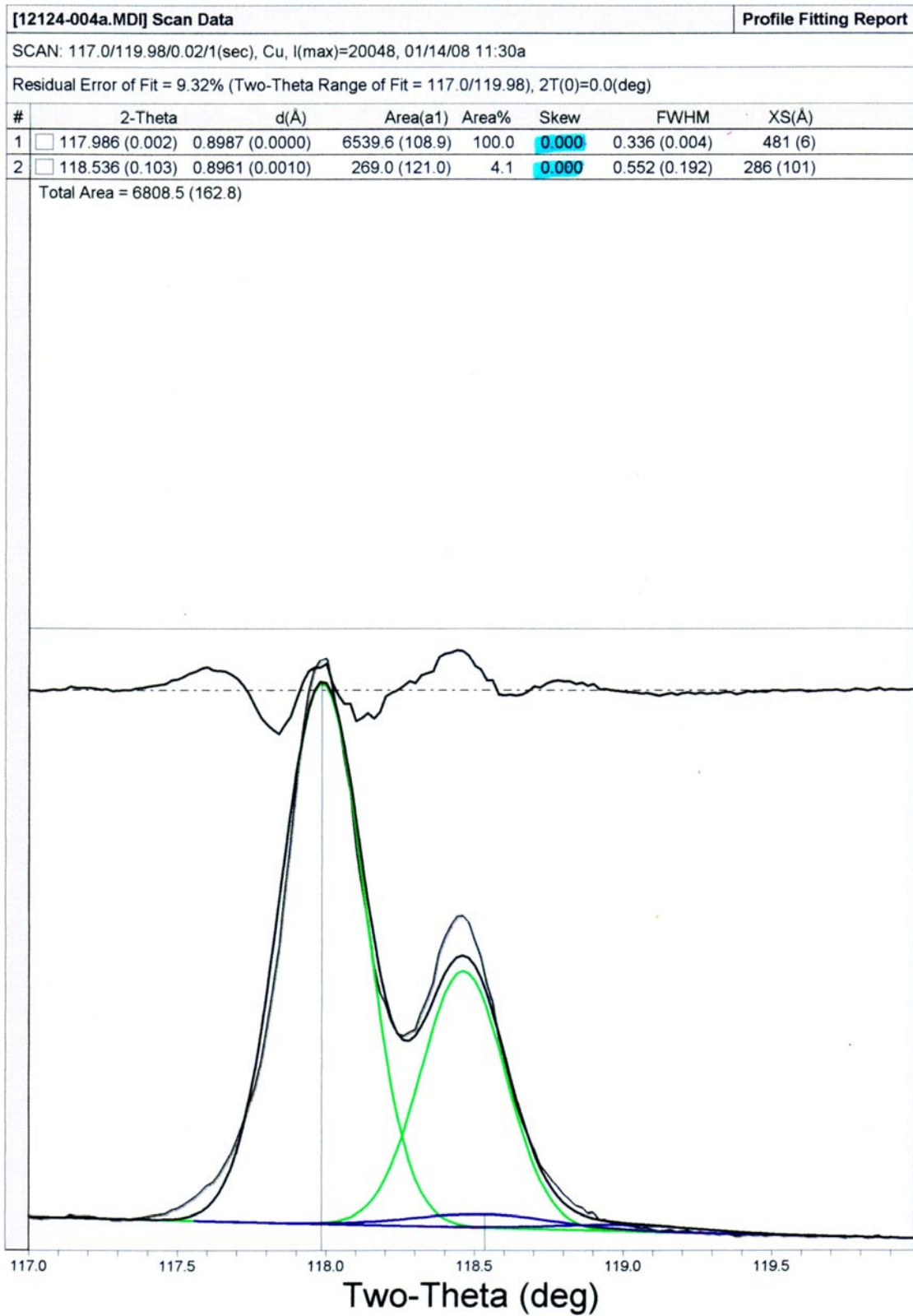


Figure B-57. XRD deconvolution of PWA 1480+ (10hr. 1080°C, unskewed, 9.32% error)

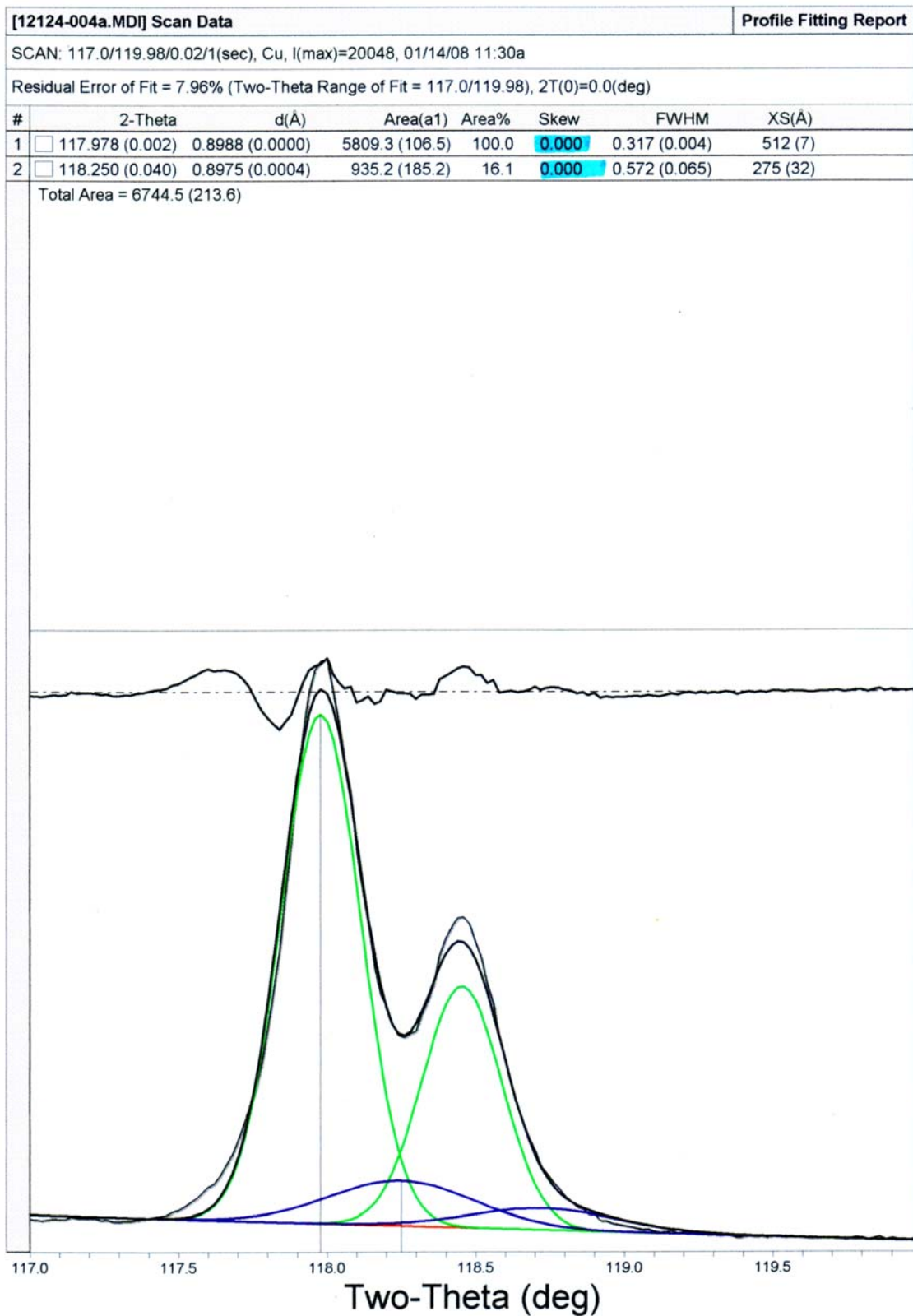


Figure B-58. XRD deconvolution of PWA 1480+ (10hr. 1080°C, unskewed, 7.96% error)

**[12124-004a.MDI] Scan Data** **Profile Fitting Report**

SCAN: 117.0/119.98/0.02/1(sec), Cu, I(max)=20048, 01/14/08 11:30a

Residual Error of Fit = 3.84% (Two-Theta Range of Fit = 117.0/119.98), 2T(0)=0.0(deg)

#	2-Theta	d(Å)	Area(a1)	Area%	Skew	FWHM	XS(Å)
1	117.979 (0.001)	0.8988 (0.0000)	3221.4 (98.1)	87.0	0.000	0.238 (0.005)	714 (16)
2	118.018 (0.003)	0.8986 (0.0000)	3703.3 (205.7)	100.0	0.000	0.530 (0.011)	297 (7)

Total Area = 6924.7 (227.9)

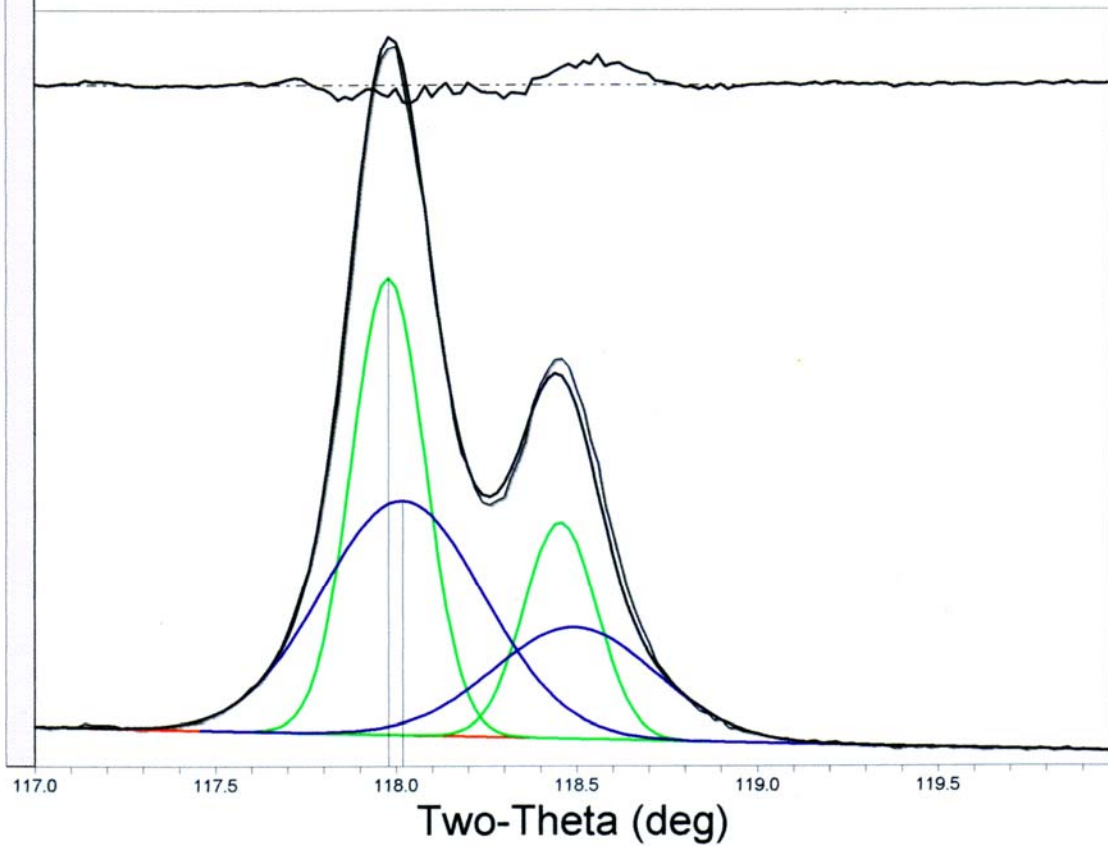


Figure B-59. XRD deconvolution of PWA 1480+ (10hr. 1080°C, unskewed, 3.84% error)

[12124-004a.MDI] Scan Data Profile Fitting Report

SCAN: 117.0/119.98/0.02/1(sec), Cu, I(max)=20048, 01/14/08 11:30a

Residual Error of Fit = 3.89% (Two-Theta Range of Fit = 117.0/119.98), 2T(0)=0.0(deg)

#	2-Theta	d(Å)	Area(a1)	Area%	Skew	FWHM	XS(Å)
1	117.979 (0.001)	0.8988 (0.0000)	3092.2 (97.9)	80.9	0.000	0.234 (0.005)	730 (17)
2	118.016 (0.003)	0.8986 (0.0000)	3823.0 (204.5)	100.0	0.000	0.520 (0.011)	302 (7)

Total Area = 6915.2 (226.8)

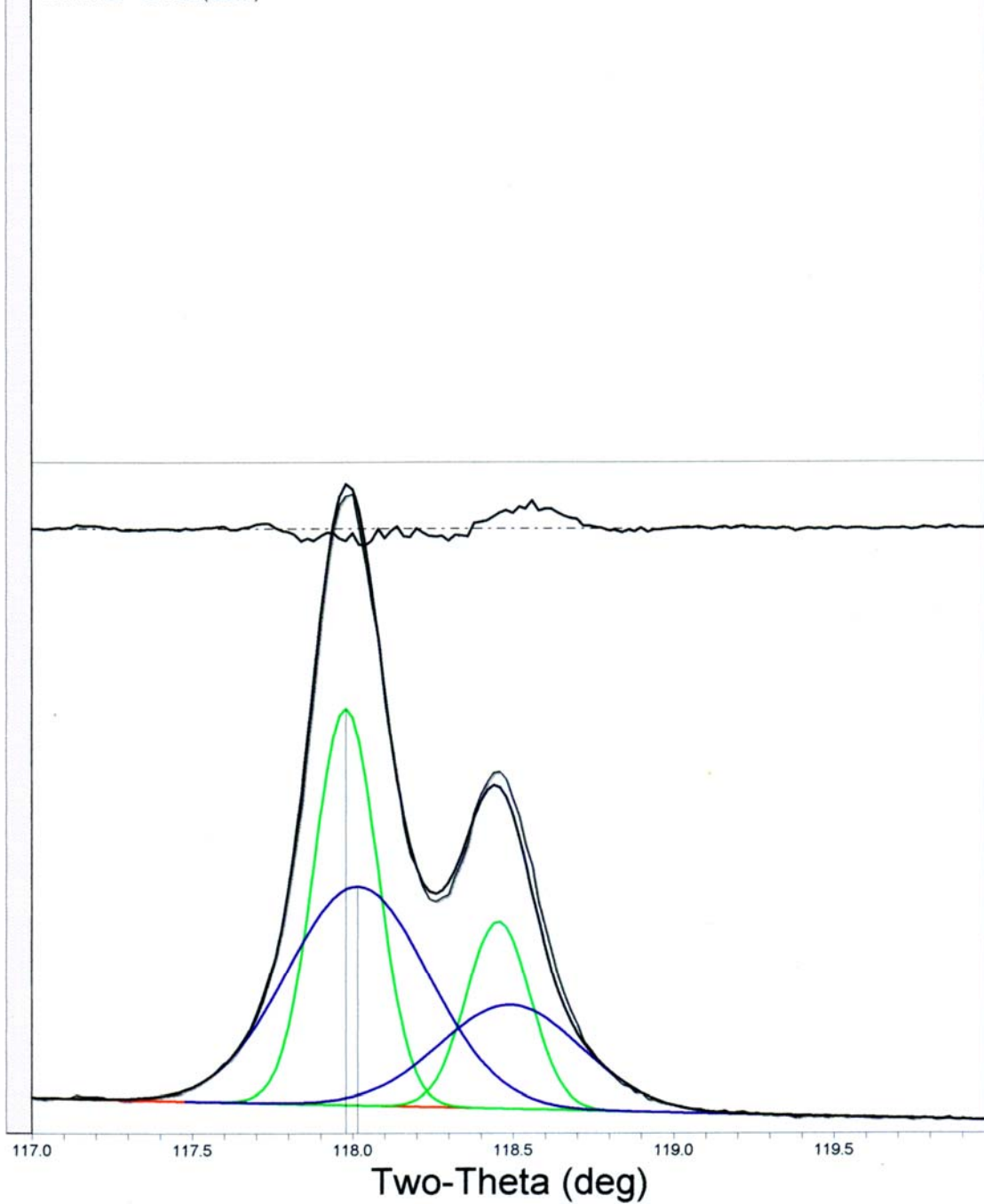


Figure B-60. XRD deconvolution of PWA 1480+ (10hr. 1080°C, unskewed, 3.89% error)

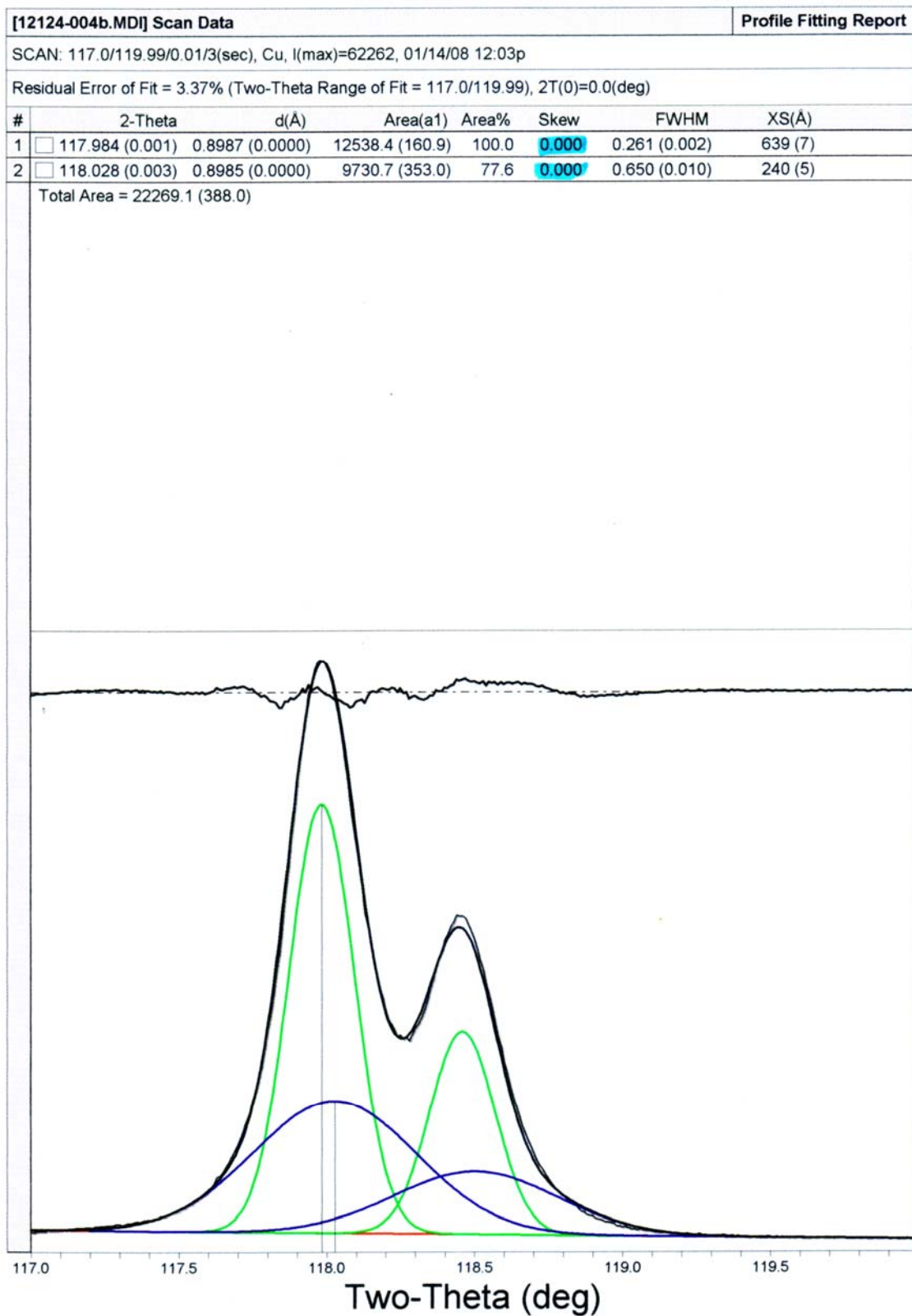


Figure B-61. XRD deconvolution of PWA 1480+ (10hr. 1080°C, unskewed, 3.37% error)

[12124-004b.MD] Scan Data Profile Fitting Report

SCAN: 117.0/119.99/0.01/3(sec), Cu, I(max)=62262, 01/14/08 12:03p

Residual Error of Fit = 3.38% (Two-Theta Range of Fit = 117.0/119.99), 2T(0)=0.0(deg)

#	2-Theta	d(Å)	Area(a1)	Area%	Skew	FWHM	XS(Å)
1	117.983 (0.001)	0.8987 (0.0000)	12151.6 (163.4)	100.0	0.000	0.257 (0.002)	650 (7)
2	118.027 (0.003)	0.8985 (0.0000)	10052.3 (357.9)	82.7	0.000	0.633 (0.010)	247 (5)

Total Area = 22203.9 (393.4)

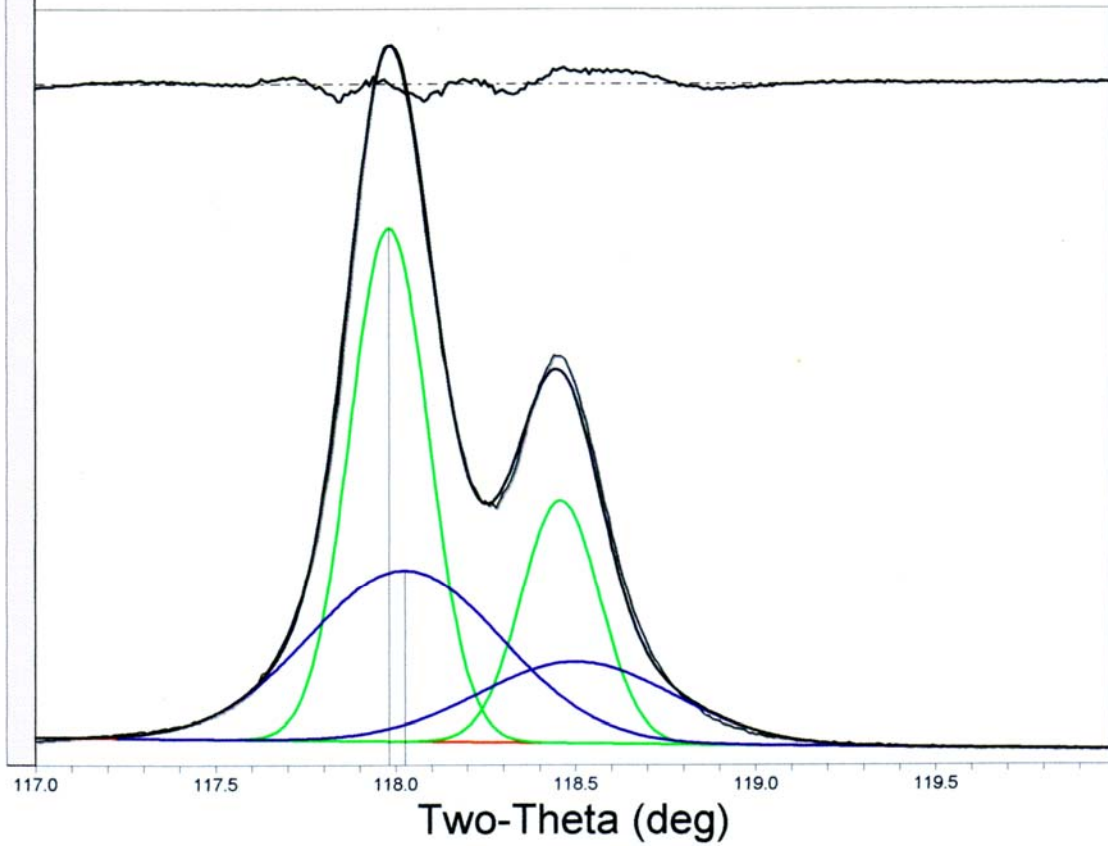


Figure B-62. XRD deconvolution of PWA 1480+ (10hr. 1080°C, unskewed, 3.38% error)

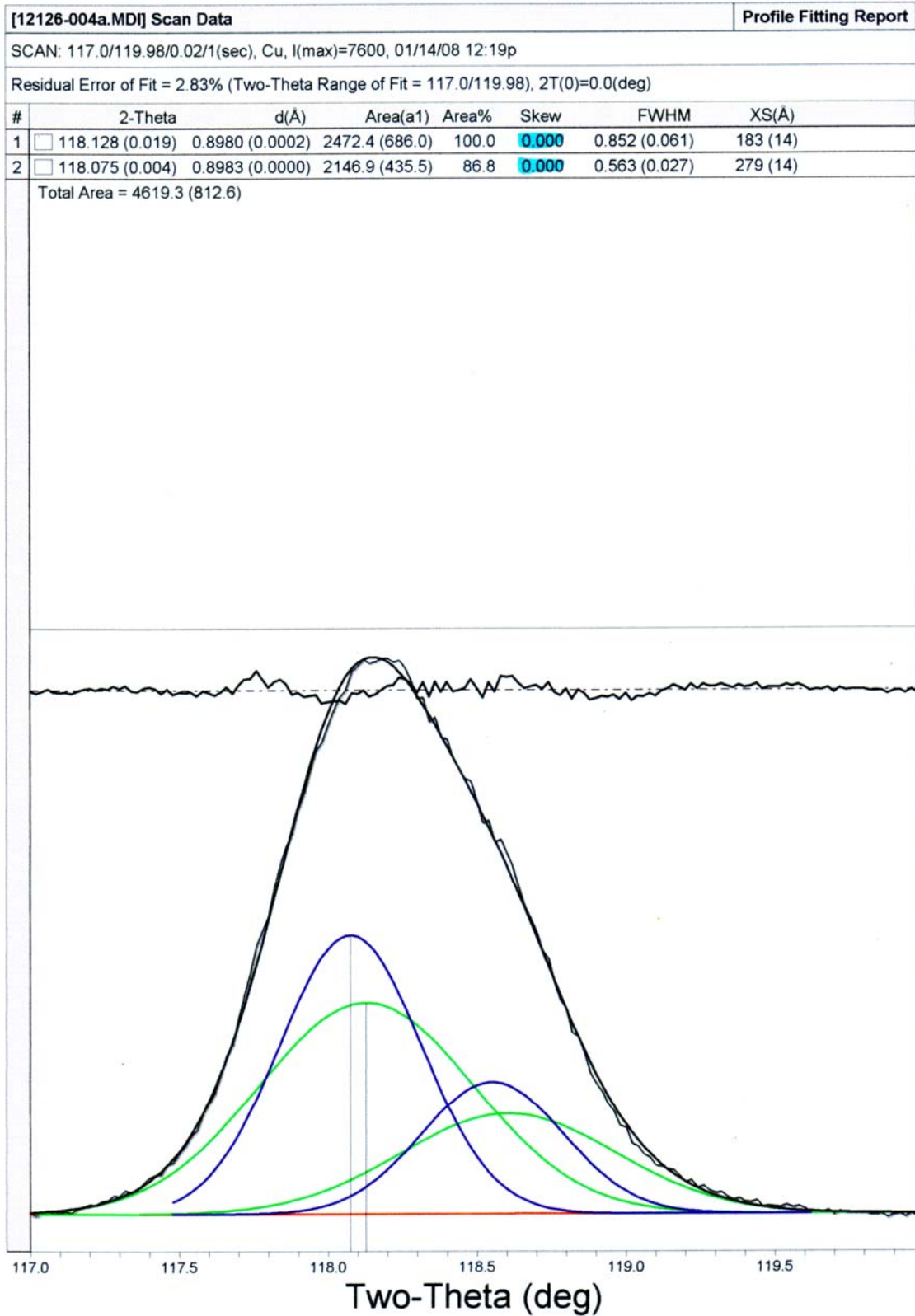


Figure B-63. XRD deconvolution of PWA 1480+ (1000hr. 1080°C, unskewed, 2.83% error)

**[12126-004b.MDI] Scan Data** **Profile Fitting Report**

SCAN: 117.0/119.99/0.01/3(sec), Cu, I(max)=27376, 01/14/08 12:36p

Residual Error of Fit = 1.49% (Two-Theta Range of Fit = 117.0/119.99), 2T(0)=0.0(deg)

#	2-Theta	d(Å)	Area(a1)	Area%	Skew	FWHM	XS(Å)
1	118.060 (0.002)	0.8984 (0.0000)	9385.0 (457.0)	100.0	0.000	0.939 (0.015)	165 (4)
2	118.041 (0.001)	0.8985 (0.0000)	7222.8 (263.8)	77.0	0.000	0.527 (0.007)	298 (5)

Total Area = 16607.8 (527.7)

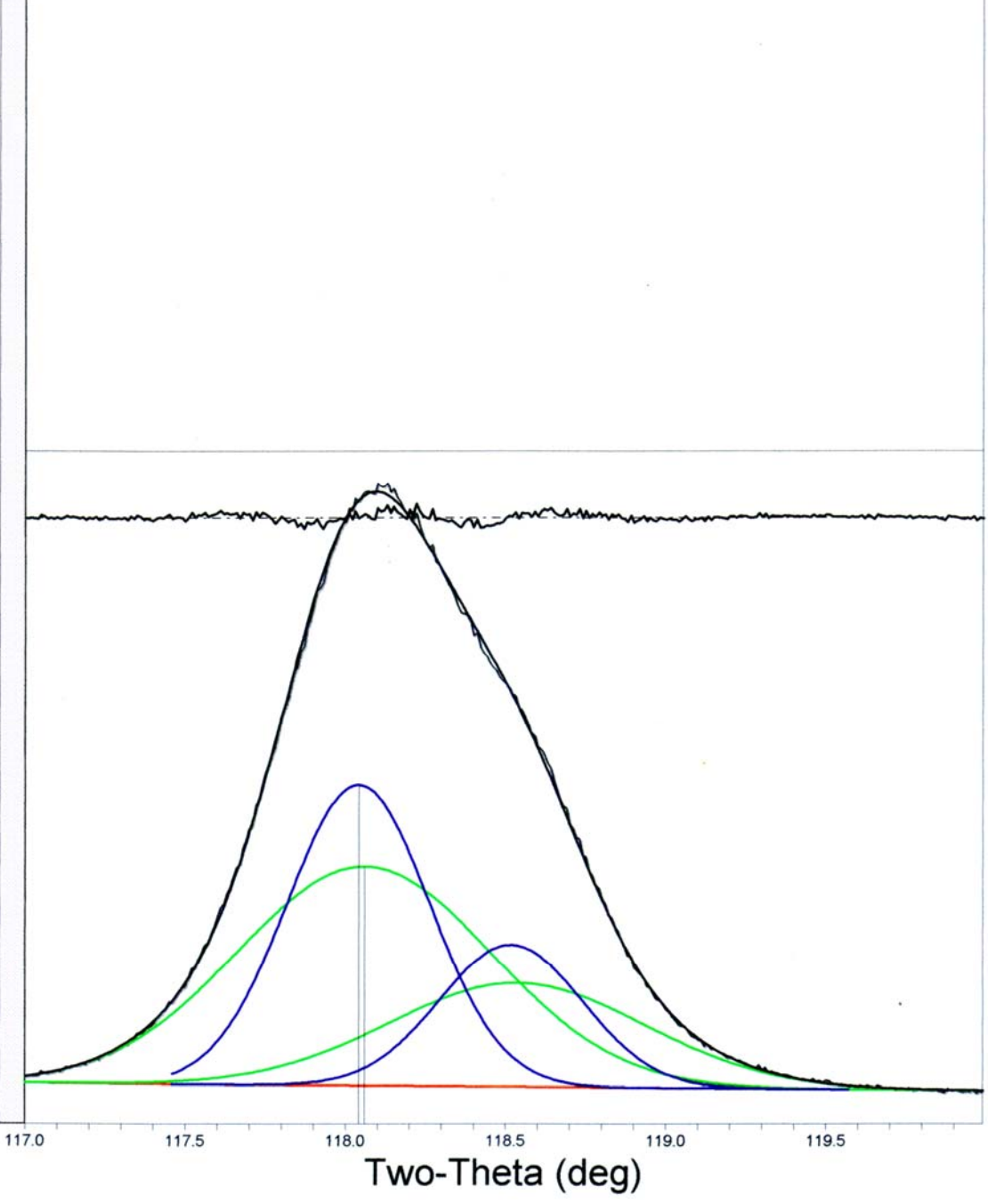


Figure B-64. XRD deconvolution of PWA 1480+ (1000hr. 1080°C, unskewed, 1.49% error)

**[12126-004b.MDI] Scan Data** **Profile Fitting Report**

SCAN: 117.0/119.99/0.01/3(sec), Cu, I(max)=27376, 01/14/08 12:36p

Residual Error of Fit = 1.49% (Two-Theta Range of Fit = 117.0/119.99), 2T(0)=0.0(deg)

#	2-Theta	d(Å)	Area(a1)	Area%	Skew	FWHM	XS(Å)
1	118.041 (0.001)	0.8985 (0.0000)	7219.2 (264.1)	76.9	0.000	0.527 (0.007)	298 (5)
2	118.060 (0.002)	0.8984 (0.0000)	9386.9 (457.3)	100.0	0.000	0.939 (0.015)	165 (4)

Total Area = 16606.1 (528.0)

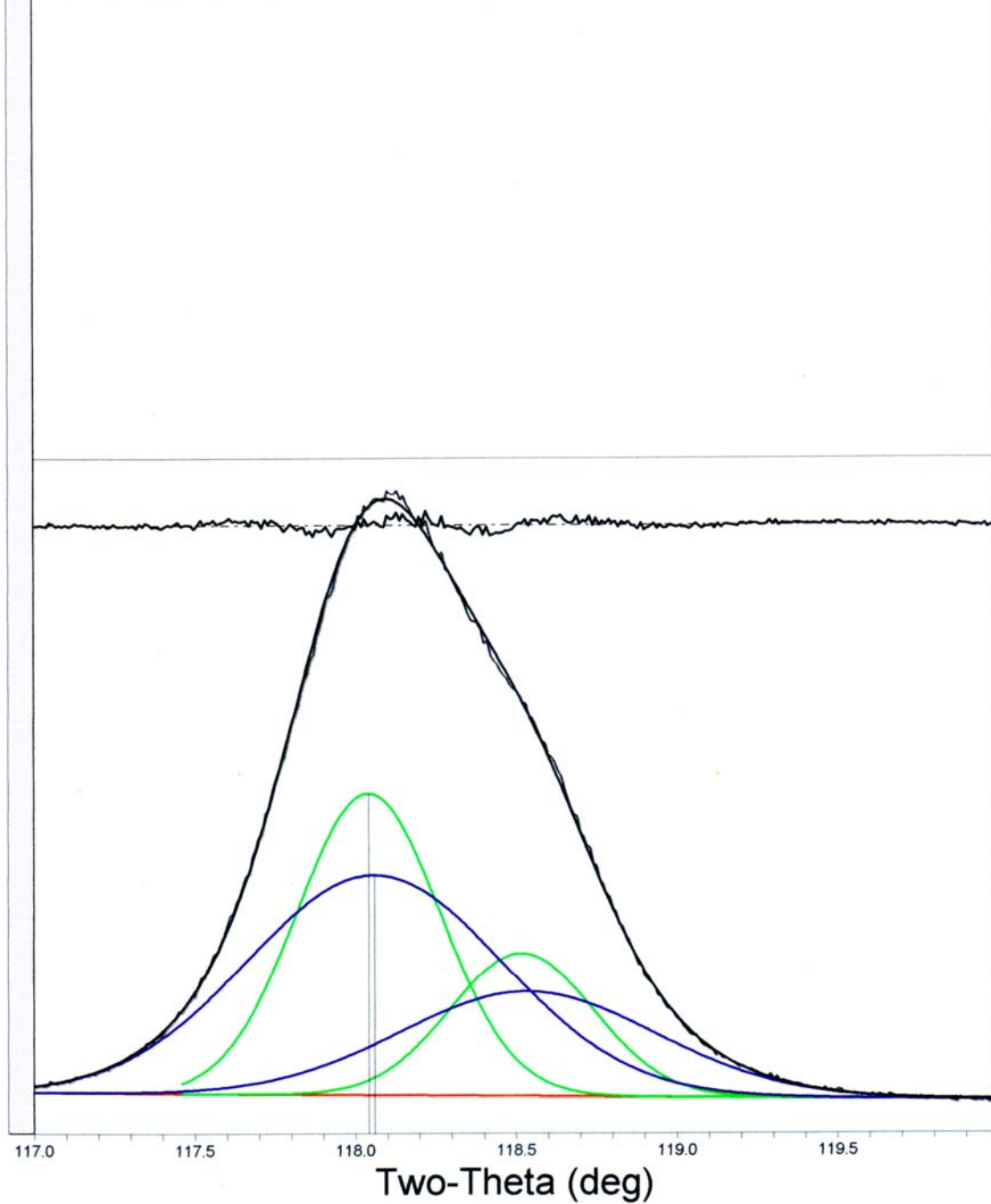


Figure B-65. XRD deconvolution of PWA 1480+ (1000hr. 1080°C, unskewed, 1.49% error)

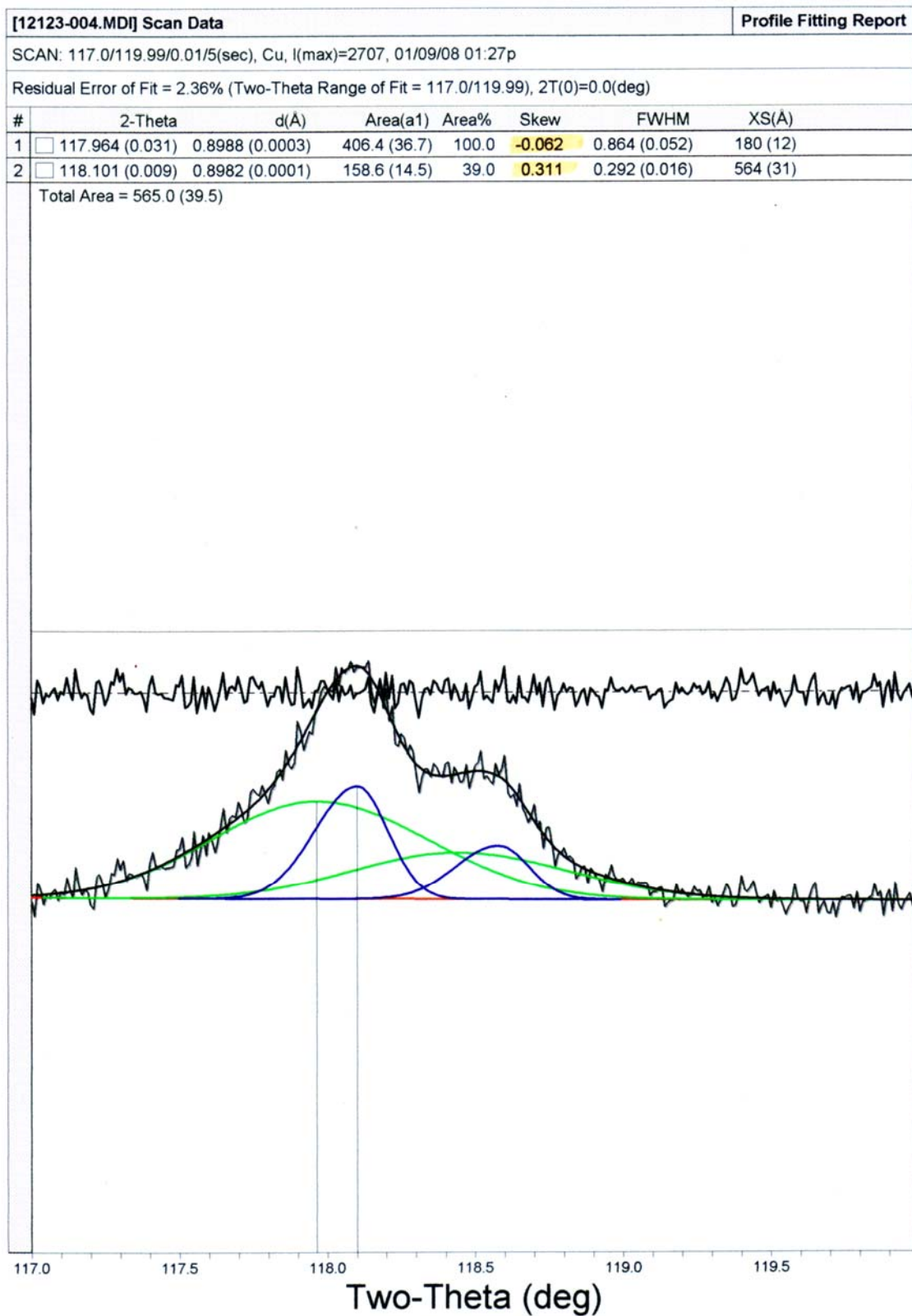


Figure B-66. XRD deconvolution of PWA 1480+ (4hr. 1080°C, skewed, 2.36% error)

**[12124-004a.MDI] Scan Data** **Profile Fitting Report**

SCAN: 117.0/119.98/0.02/1(sec), Cu, I(max)=20048, 01/14/08 11:30a

Residual Error of Fit = 3.77% (Two-Theta Range of Fit = 117.0/119.98), 2T(0)=0.0(deg)

#	2-Theta	d(Å)	Area(a1)	Area%	Skew	FWHM	XS(Å)
1	117.972 (0.002)	0.8988 (0.0000)	3222.4 (105.1)	86.8	-0.141	0.239 (0.005)	711 (17)
2	118.012 (0.005)	0.8986 (0.0000)	3711.3 (217.0)	100.0	-0.022	0.532 (0.012)	295 (8)

Total Area = 6933.6 (241.1)

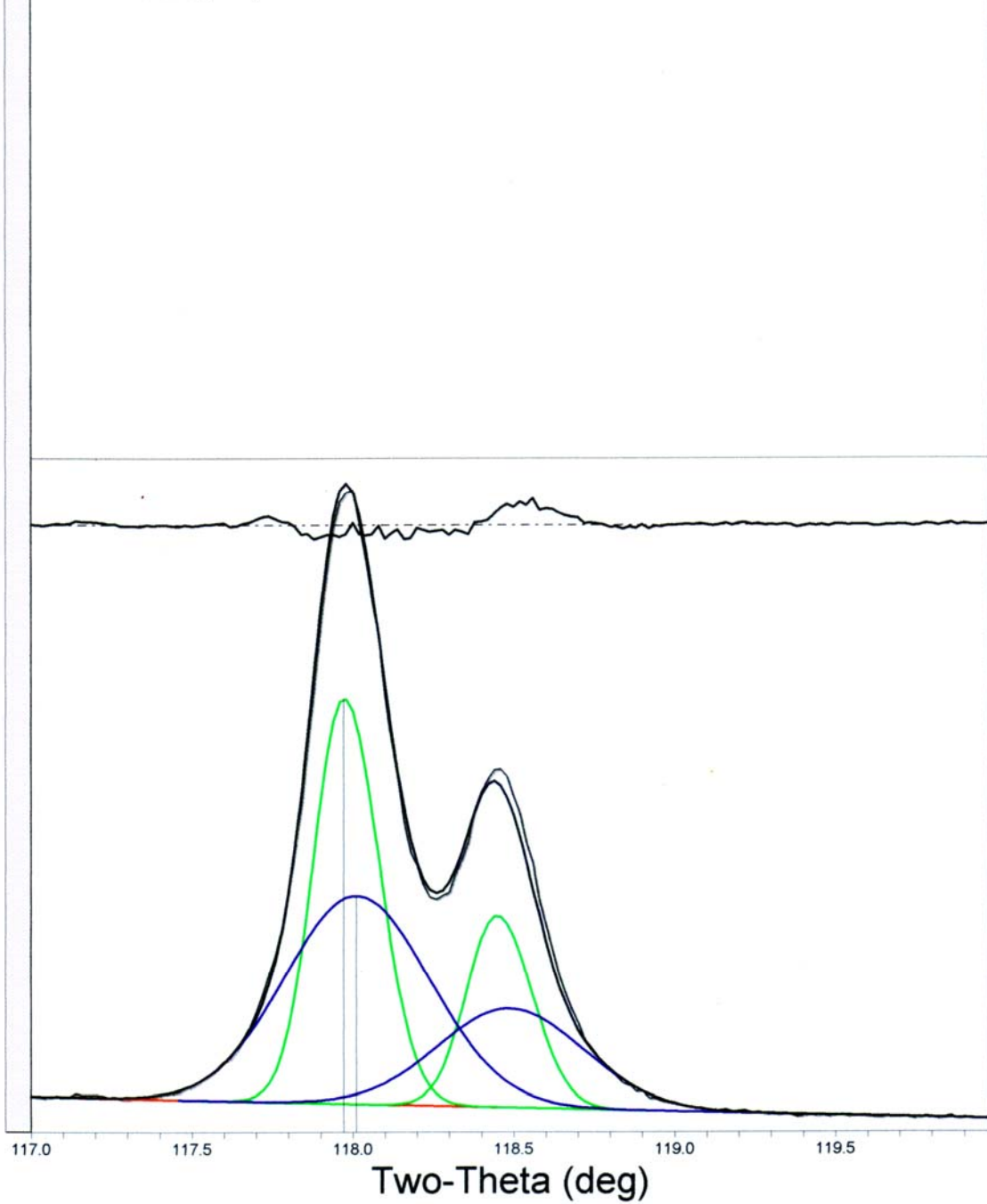


Figure B-67. XRD deconvolution of PWA 1480+ (10hr. 1080°C, skewed, 3.77% error)

[12124-004a.MDI] Scan Data Profile Fitting Report

SCAN: 117.0/119.98/0.02/1(sec), Cu, I(max)=20048, 01/14/08 11:30a

Residual Error of Fit = 7.19% (Two-Theta Range of Fit = 117.0/119.98), 2T(0)=0.0(deg)

#	2-Theta	d(Å)	Area(a1)	Area%	Skew	FWHM	XS(Å)
1	117.899 (0.009)	0.8991 (0.0001)	2572.3 (272.9)	61.2	0.133	0.311 (0.018)	524 (31)
2	117.983 (0.004)	0.8987 (0.0000)	4201.8 (353.4)	100.0	-0.679	0.305 (0.013)	535 (25)

Total Area = 6774.1 (446.5)

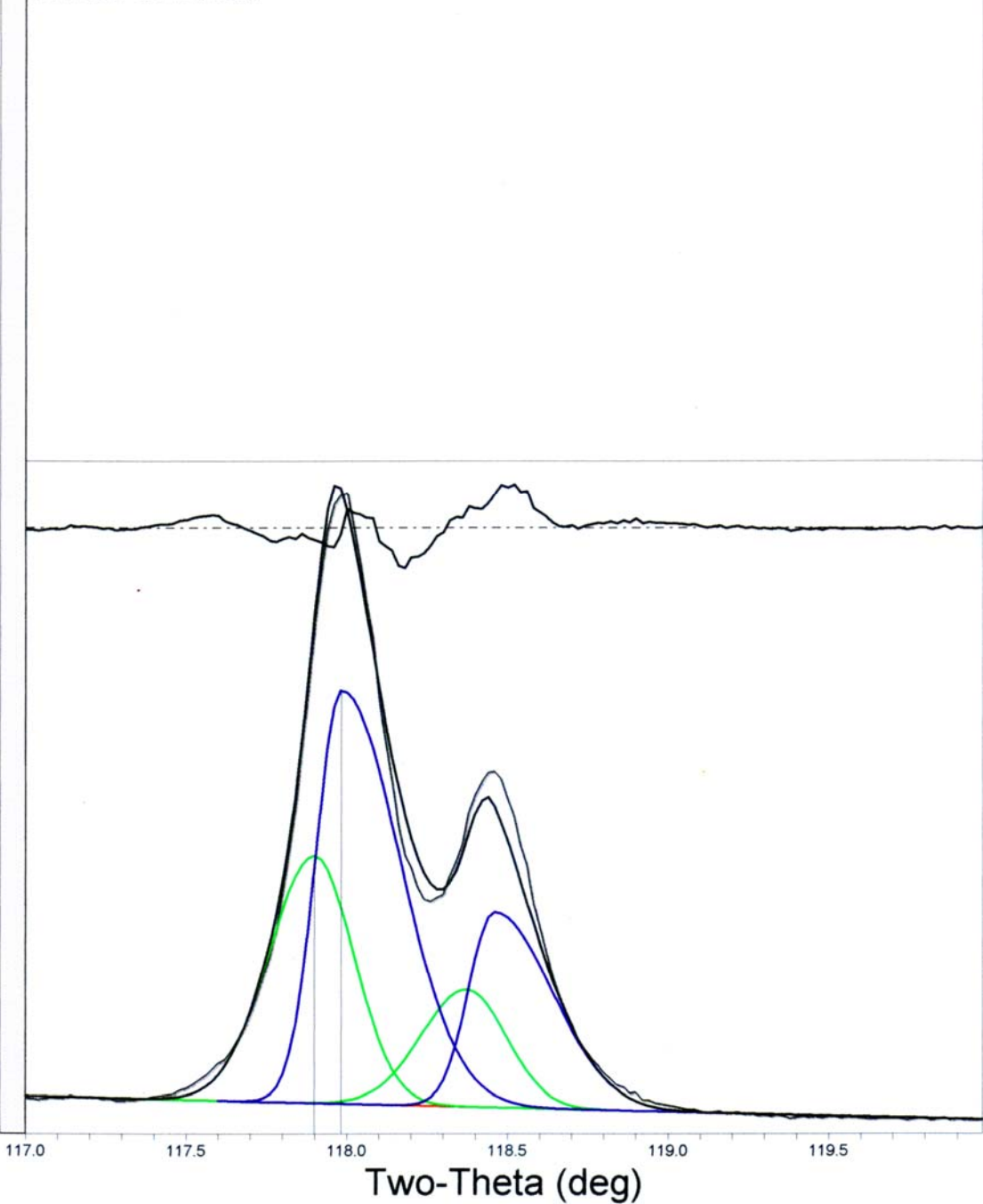


Figure B-68. XRD deconvolution of PWA 1480+ (10hr. 1080°C, skewed, 7.19% error)

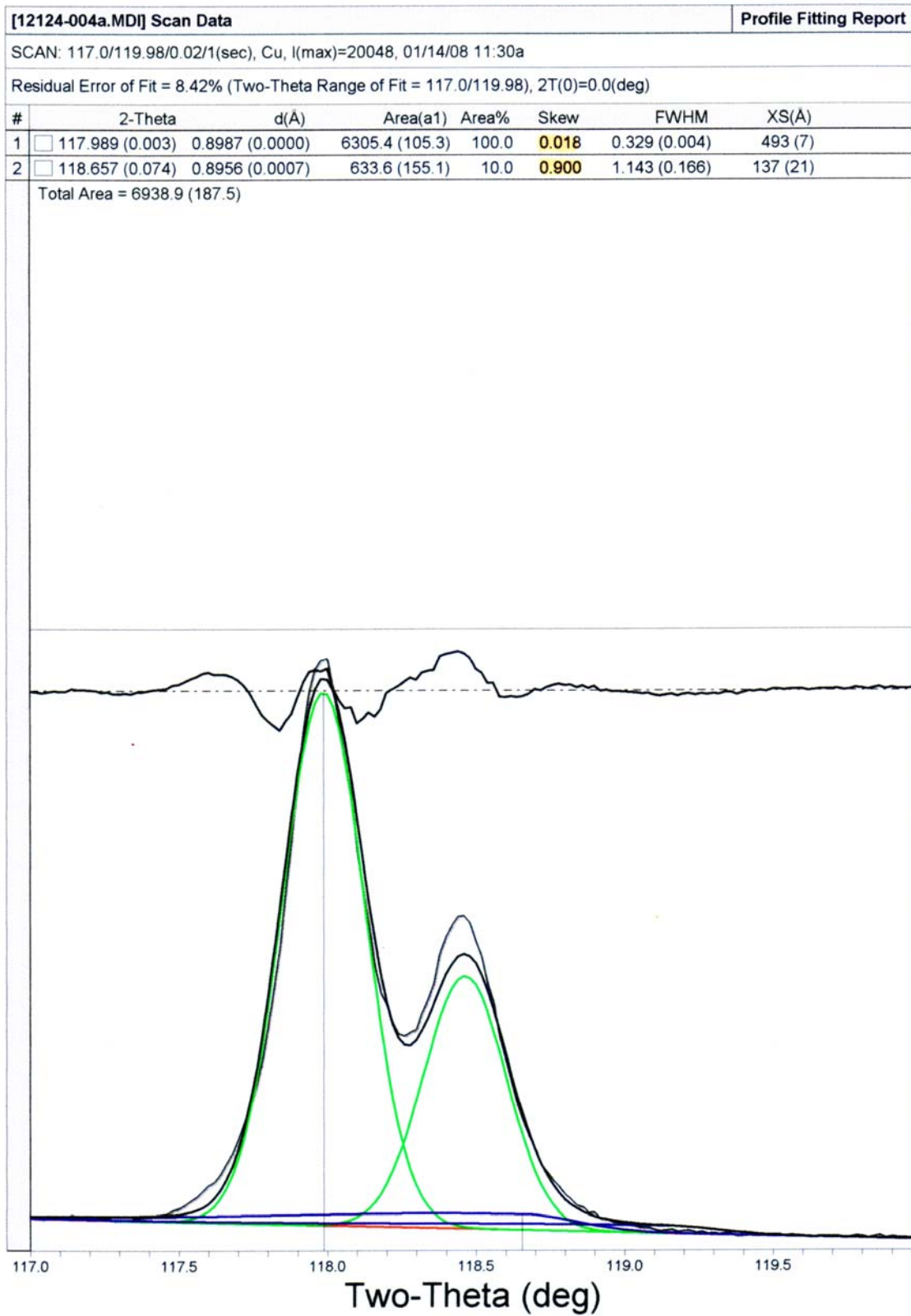


Figure B-69. XRD deconvolution of PWA 1480+ (10hr. 1080°C, skewed, 8.42% error)

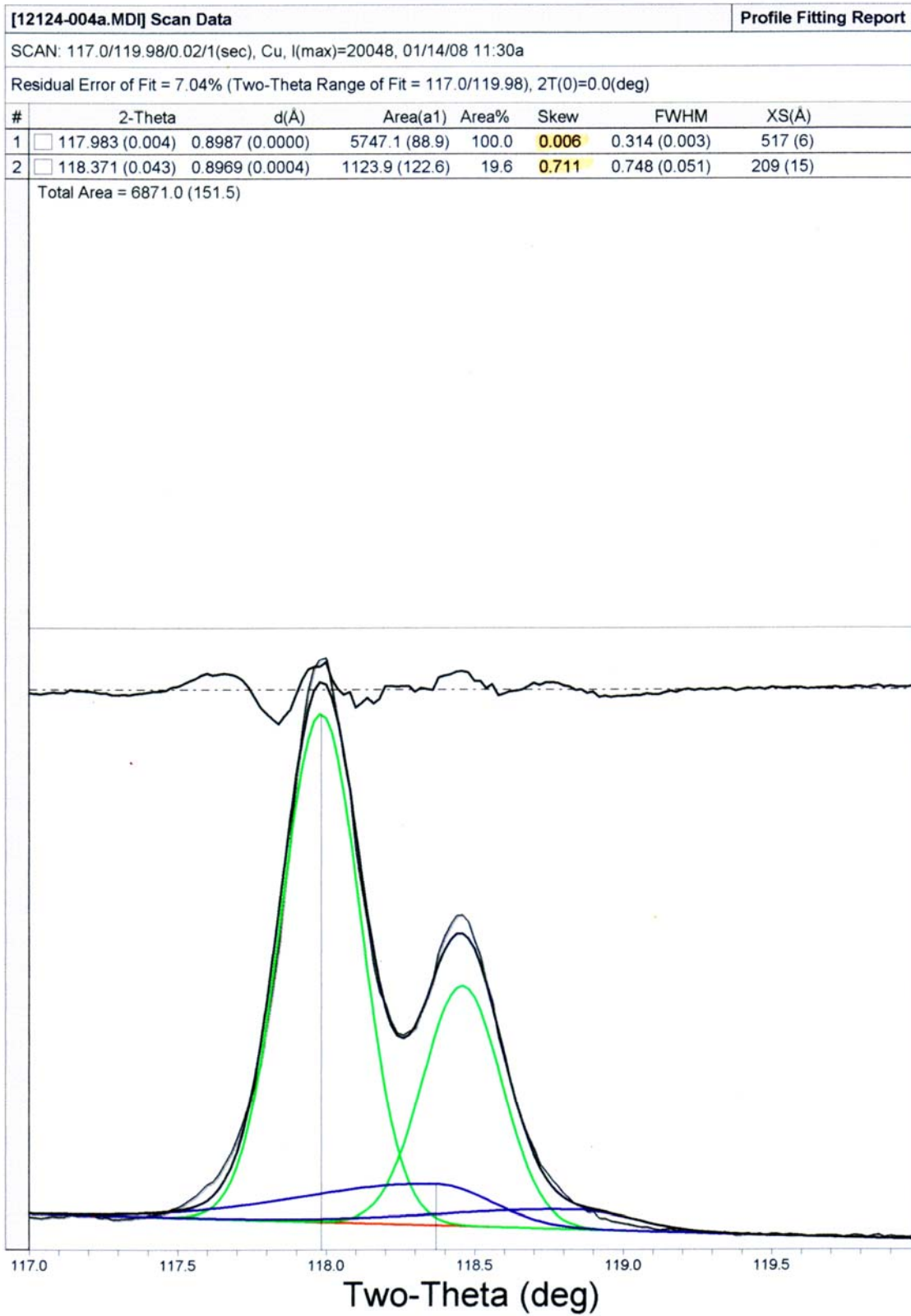


Figure B-70. XRD deconvolution of PWA 1480+ (10hr. 1080°C, skewed, 7.04% error)

[12124-004b.MD] Scan Data Profile Fitting Report

SCAN: 117.0/119.99/0.01/3(sec), Cu, I(max)=62262, 01/14/08 12:03p

Residual Error of Fit = 3.28% (Two-Theta Range of Fit = 117.0/119.99), 2T(0)=0.0(deg)

#	2-Theta	d(Å)	Area(a1)	Area%	Skew	FWHM	XS(Å)
1	117.978 (0.001)	0.8988 (0.0000)	12497.7 (162.3)	100.0	-0.091	0.261 (0.002)	640 (7)
2	118.036 (0.005)	0.8985 (0.0000)	9774.2 (351.3)	78.2	0.065	0.649 (0.010)	240 (5)

Total Area = 22271.9 (386.9)

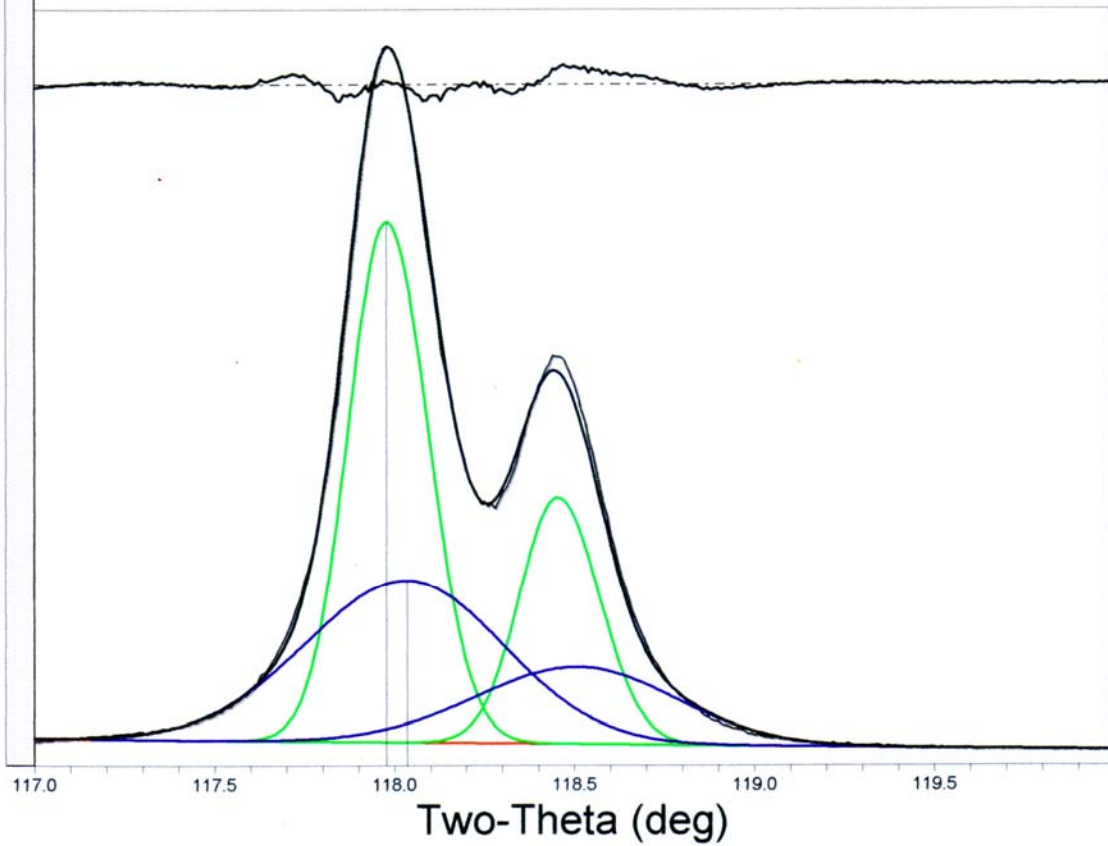


Figure B-71. XRD deconvolution of PWA 1480+ (10hr. 1080°C, skewed, 3.28% error)

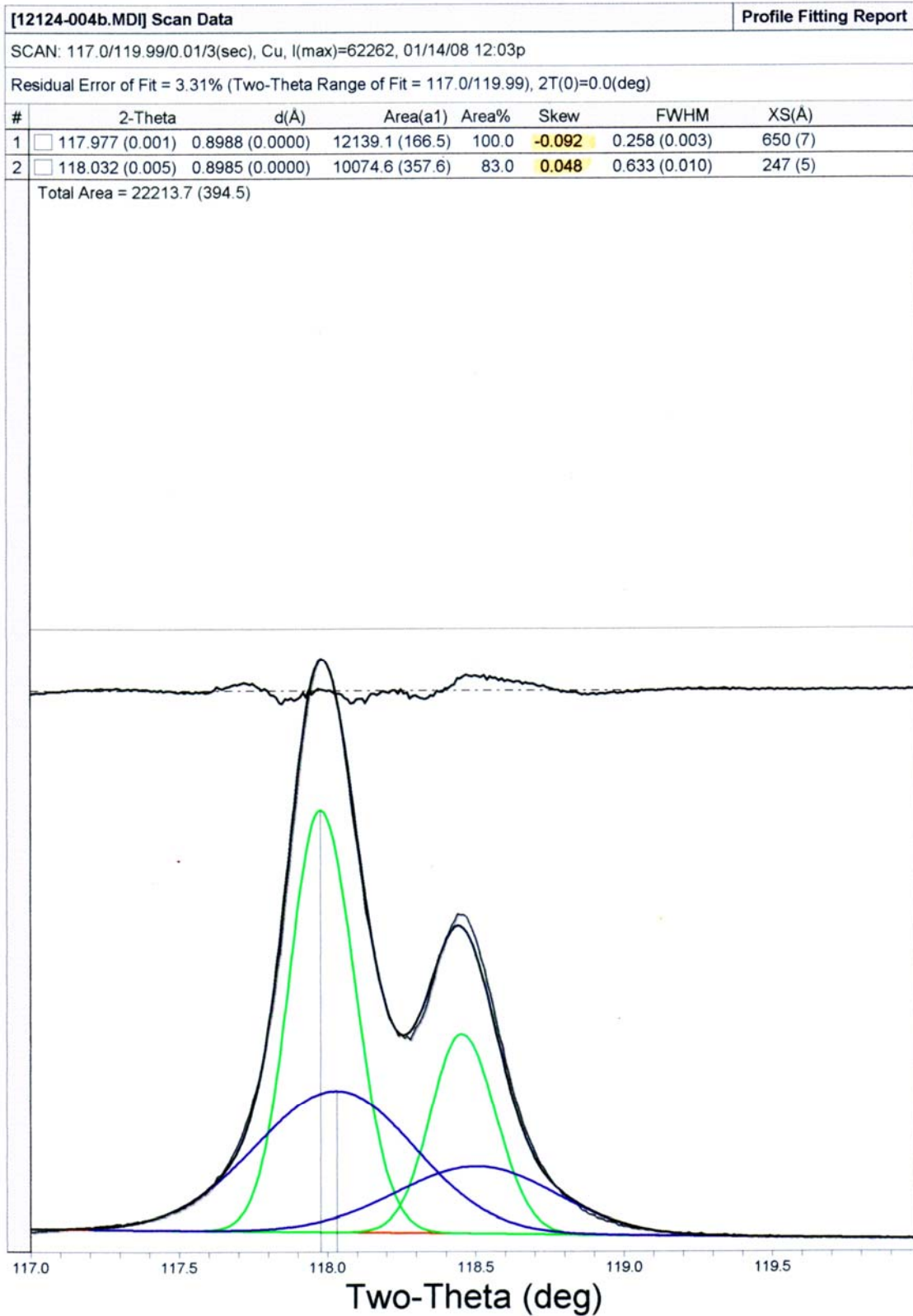


Figure B-72. XRD deconvolution of PWA 1480+ (10hr. 1080°C, skewed, 3.31% error)

SCAN: 117.0/119.98/0.02/1(sec), Cu, I(max)=7600, 01/14/08 12:19p

Residual Error of Fit = 2.79% (Two-Theta Range of Fit = 117.0/119.98), 2T(0)=0.0(deg)

#	2-Theta	d(Å)	Area(a1)	Area%	Skew	FWHM	XS(Å)
1	118.134 (0.029)	0.8980 (0.0003)	2465.6 (741.5)	100.0	-0.002	0.852 (0.067)	183 (15)
2	118.083 (0.006)	0.8983 (0.0001)	2152.8 (471.5)	87.3	0.078	0.562 (0.029)	279 (16)

Total Area = 4618.4 (878.7)

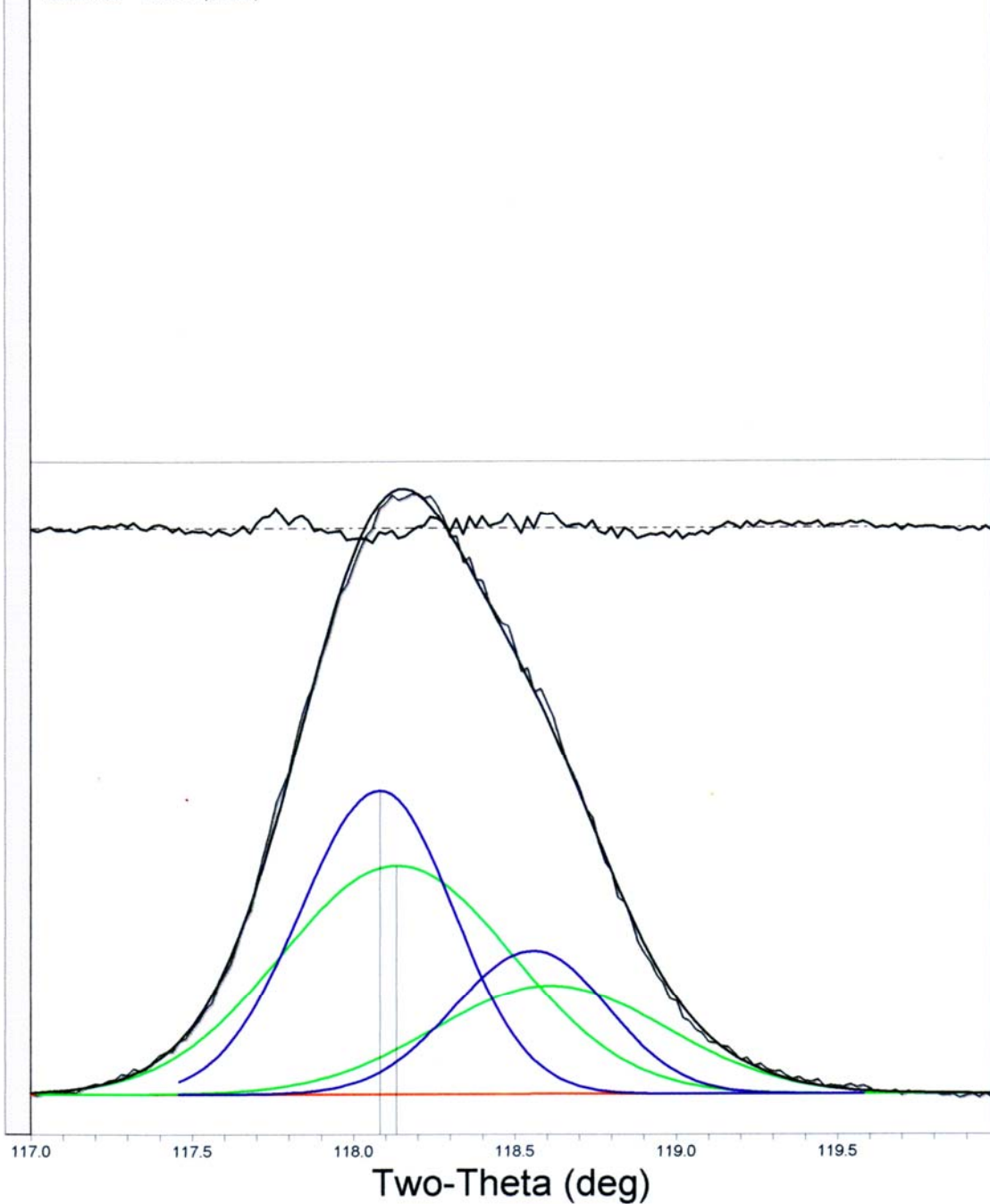


Figure B-73. XRD deconvolution of PWA 1480+ (1000hr. 1080°C, skewed, 2.79% error)

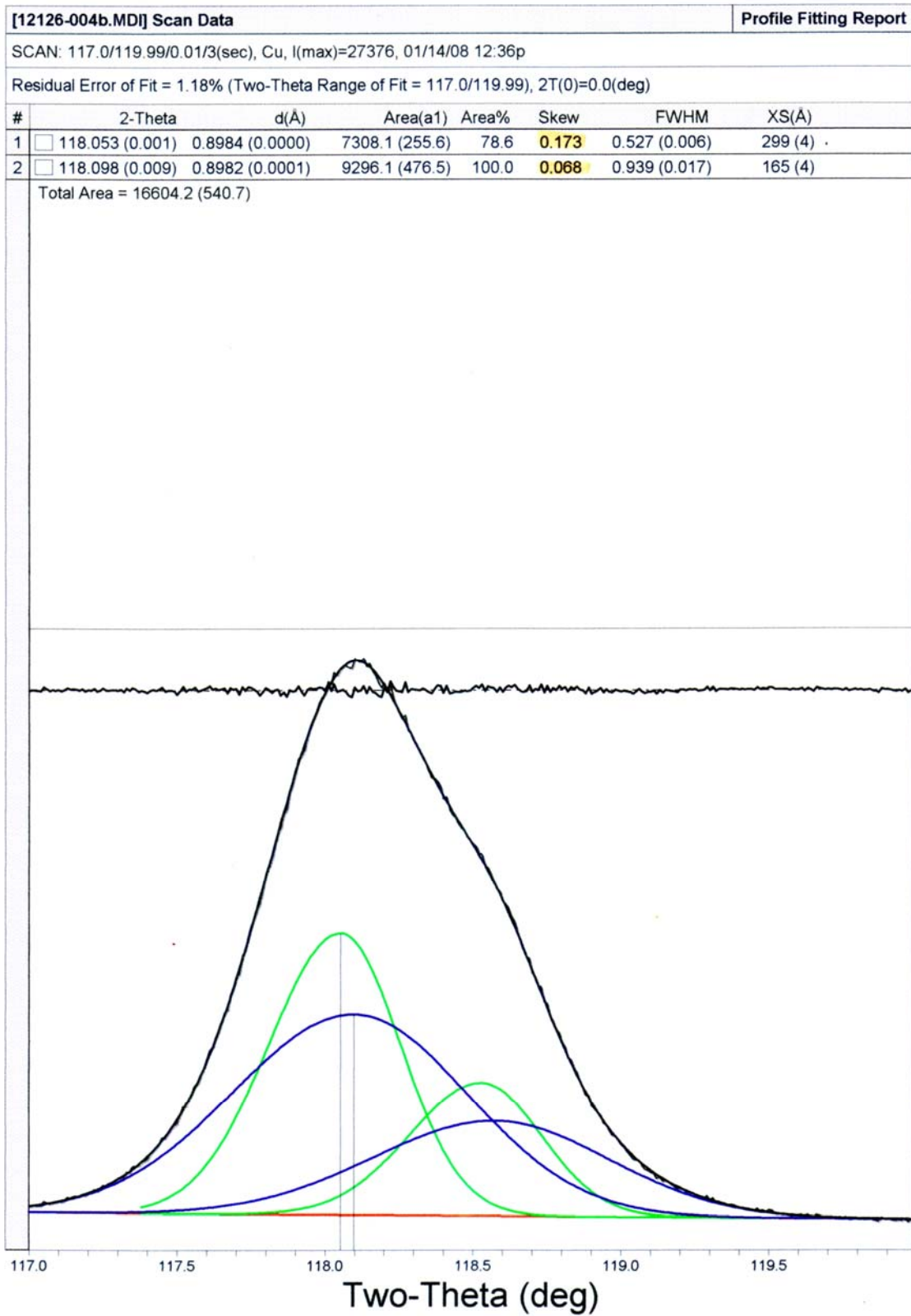


Figure B-74. XRD deconvolution of PWA 1480+ (1000hr. 1080°C, skewed, 1.18% error)

[12126-004b.MDI] Scan Data Profile Fitting Report

SCAN: 117.0/119.99/0.01/3(sec), Cu, I(max)=27376, 01/14/08 12:36p

Residual Error of Fit = 1.18% (Two-Theta Range of Fit = 117.0/119.99), 2T(0)=0.0(deg)

#	2-Theta	d(Å)	Area(a1)	Area%	Skew	FWHM	XS(Å)
1	118.097 (0.009)	0.8982 (0.0001)	9300.0 (478.4)	100.0	0.065	0.939 (0.017)	165 (4)
2	118.053 (0.001)	0.8984 (0.0000)	7307.1 (256.6)	78.6	0.171	0.527 (0.006)	299 (4)

Total Area = 16607.1 (542.9)

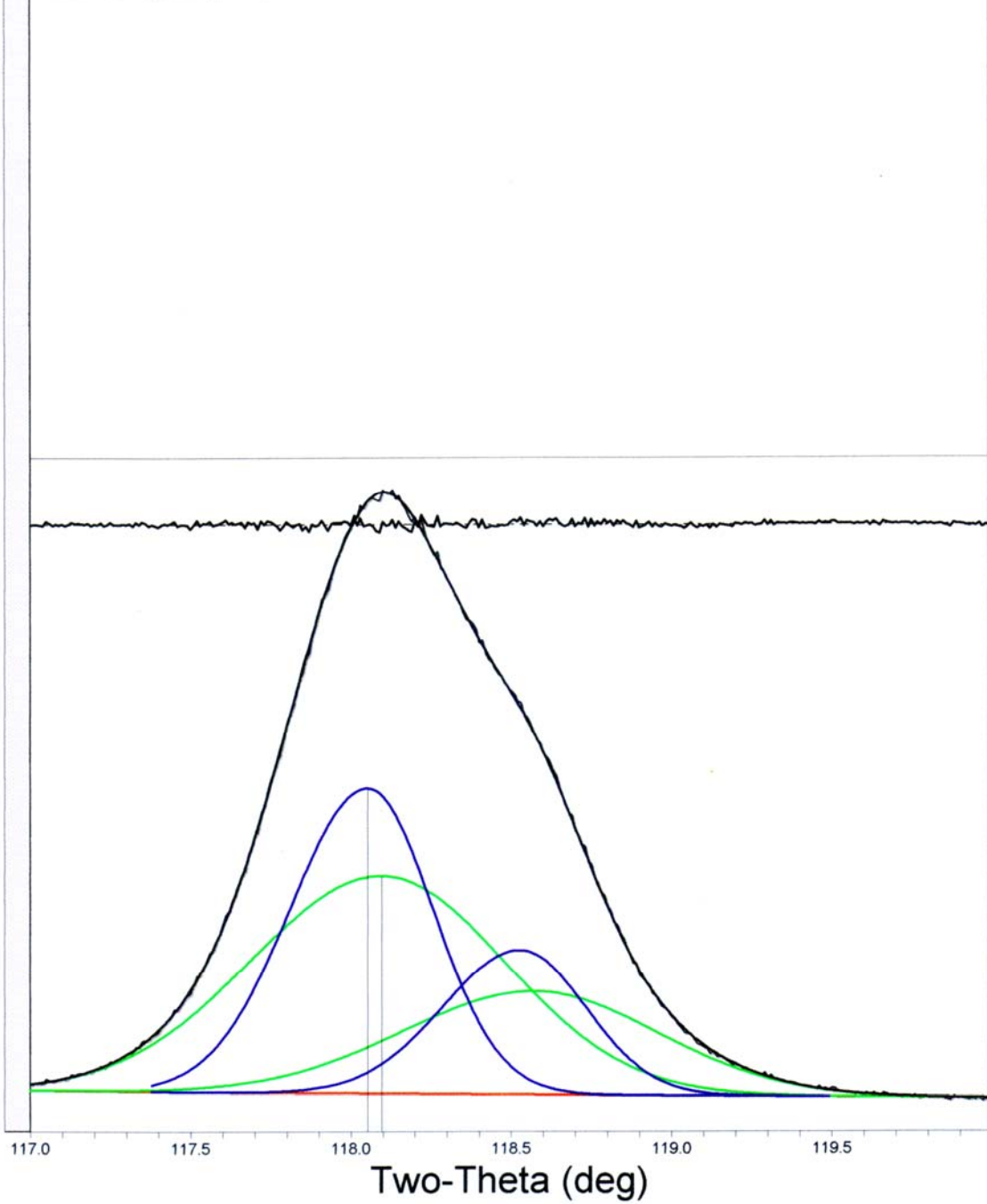


Figure B-75. XRD deconvolution of PWA 1480+ (1000hr. 1080°C, skewed, 1.18% error)

## LIST OF REFERENCES

1. A.D. Cetel and D.N. Duhl. in *Superalloys 1988*. Seven Springs, PA: TMS, 1988, p. 235-244.
2. Erickson, G.L. in *Critical Issues in the Development of High Temperature Structural Materials*: TMS, 1993, p. 87-105.
3. Erickson, G.L. in *Superalloys 1996*. Seven Springs, PA: TMS, 1996, p. 35-44.
4. Harris, K., et al., *Journal of Materials Engineering and Performance*, 1993. 2(4): p. 481-487.
5. Reed, R.C., *The Superalloys: Fundamentals and Applications*. New York: Cambridge Press. 2006, pp. 372.
6. Dimiduk, D.M. and R. Dutton, a presentation by Air Force Research Laboratory, 2004. [http://www.darpa.mil/dso/thrusts/matdev/aim/images/projects/AIM\\_airforcelab.pdf](http://www.darpa.mil/dso/thrusts/matdev/aim/images/projects/AIM_airforcelab.pdf) accessed 26 July 2007.
7. Energy, D.o., a presentation by U.S. Department of Energy, 2000. [http://www.netl.doe.gov/publications/brochures/pdfs/scng/ATS\\_Brochure.pdf](http://www.netl.doe.gov/publications/brochures/pdfs/scng/ATS_Brochure.pdf) accessed March 15, 2008.
8. Giamei, A.F. and D.L. Anton, *Metallurgical Transactions A*, 1985. 16A(November 1985): p. 1997-2005.
9. K. Harris, et al. in *Superalloys 1996*. Seven Springs, PA: TMS, 1992, p. 297-306.
10. Blavette, D., P. Caron, and T. Khan, *Scripta Metallurgica*, 1986. 20(10): p. 1395-1400.
11. Blavette, D., P. Caron, and T. Khan. in *Superalloys 1988*. Seven Springs, PA: TMS, 1988, p. 305-314.
12. Knowles, D.M. and S. Gunturi, *Materials Science and Engineering*, 2002. A328(2002): p. 223-237.
13. Chen, Q.Z. and D.M. Knowles, *Materials Science and Engineering A*, 2003. 356(1-2): p. 352-367.
14. Matan, N., et al., *Acta Materialia*, 1999. 47(5): p. 1549-1563.
15. Sass, V., U. Glatzel, and M. Feller-Kniepmeier, *Acta Materialia*, 1996. 44(5): p. 1967-1977.
16. Rae, C.M.F. and R.C. Reed, *Acta Materialia*, 2006. 55: p. 1067-1081.

17. Rae, C.M.F., N. Matan, and R.C. Reed, *Materials Science and Engineering A*, 2001. 300(1-2): p. 125-134.
18. Dilip M. Shah, et al. in *Superalloys 2004*. Seven Springs, PA: TMS, 2004, p. 197-206.
19. Sugui, T., et al., *Materials Science and Engineering*, 1998. A262: p. 271-278.
20. Kakehi, K., *Materials Science and Engineering A*, 1999. 278(1-2): p. 135-141.
21. Caron, P., et al. in *Superalloys 1988*. Seven Springs, PA: TMS, 1988, p. 215-224.
22. Nathal, M.V., *Metallurgical Transactions A*, 1987. 18A: p. 1961-1970.
23. Viswanathan, G.B., et al., *Acta Materialia*, 2005. 53(10): p. 3041-3057.
24. Viswanathan, G.B., et al., *Materials Science and Engineering A*, 2005. 400-401: p. 489-495.
25. MacKay, R.A. and L.J. Ebert. in *Superalloys 1984*. Seven Springs, PA: TMS, 1984, p. 135-144.
26. Pearson, D.D., F.D. Lemkey, and B.H. Kear. in *Superalloys 1980*. Seven Springs, PA: TMS, 1980, p. 513-520.
27. Zhang, J.X., et al., *Acta Materialia*, 2005. 53(2005): p. 4623-4633.
28. Koizumi, Y., et al. in *Superalloys 2004*. Seven Springs, PA: TMS, 2004, p. 35-44.
29. Walston, S., et al. in *Superalloys 2004*. Seven Springs, PA: TMS, 2004, p. 15-24.
30. Brooks, C.R., *Heat Treatment: Structure and Properties of Nonferrous Alloys*. Metals Park, OH: ASM International. 1982, pp. 420.
31. Dieter, G.E., *Mechanical Metallurgy*. New York: McGraw-Hill. 1986, pp. 751.
32. Nathal, M.V. and L.J. Ebert. in *Superalloys 1984*. Seven Springs, PA: TMS, 1984, p. 125-133.
33. Link, T. and M. Feller-Kniepmeier, *Metallurgical and Materials Transactions A*, 1992. 23(1): p. 99-105.
34. Sengupta, A., et al., *Journal of Materials Engineering and Performance*, 1994. 3(1): p. 73-81.
35. Darolia, R., D.F. Lahrman, and R.D. Field. in *Superalloys 1988*. Seven Springs, PA: TMs, 1988, p. 255-264.

36. Caron, P. and T. Khan, *Materials Science and Engineering*, 1983. 61(2): p. 173-184.
37. Copley, S.M. and B.H. Kear, *Transactions of the Metallurgical Society of AIME*, 1967. 239: p. 984-992.
38. Wlodek, S. in *Long-Term Stability of High Temperature Materials*, G.E. Fuchs, K.A. Dannemann, and T.A. Deragon, Editors. TMS: Warrendale, PA. 1999.
39. He, L.Z., et al., *Materials Science and Engineering*, 2005. A397(2005): p. 297-304.
40. Lee, J.K. in *Superalloys 1996*. Seven Springs, PA: TMS, 1996, p. 211-220.
41. Keefe, P.W., S.O. Mancuso, and G.E. Maurer. in *Superalloys 1992*. Seven Springs, PA: TMS, 1992, p. 487-496.
42. Dilip M. Shah and A. Cetel. in *Superalloys 1996*. Seven Springs, PA: TMS, 1996, p. 273-282.
43. Maldini, M., G. Angella, and V. Lupinc, *Materials Science and Engineering*, 2007. A462(1-2): p. 436-440.
44. Fuchs, G.E., *Journal of Materials Engineering and Performance*, 2002. 11(1): p. 19-25.
45. Sponseller, D.L. in *Superalloys 1996*. Seven Springs, PA: TMS, 1996, p. 259-270.
46. Lahrman, D.F., et al., *Acta Materialia*, 1988. 36(5): p. 1309-1320.
47. Shah, D.M., et al. in *Superalloys 2004*. Seven Springs, PA: TMS, 2004, p. 197-206.
48. Copley, S.M. and B.H. Kear, *Transactions of the Metallurgical Society of AIME*, 1967. 239: p. 977-984.
49. Caron, P., et al., *Scripta Metallurgica*, 1986. 20(6): p. 875-880.
50. Durand-Charre, M. in *The Microstructure of Superalloys*. Overseas Publishers Association: London. 1997, p. 75-81.
51. Blum, F., J.M. Benson, and C.M. Stander, *Journal of Materials Science Letters*, 1994. 13(16): p. 1213-1214.
52. Kelly, T.F. and D.J. Larson, *Materials Characterization*, 2000. 44(1-2): p. 59-85.
53. Fuchs, G.E., *Materials Science and Engineering*, 2000. A300(1-2): p. 52-60.

54. Cetel, A.D. and D.N. Duhl. in *Superalloys 1992*. Seven Springs, PA: TMS, 1992, p. 287-296.
55. McLean, M., et al. in *Superalloys 1992*. Seven Springs, PA: TMS, 1992, p. 609-618.
56. Zhang, J.X., et al. in *Superalloys 2004*. Seven Springs, PA: TMS, 2004, p. 189-195.
57. Sugui, T., et al., *Materials Science and Engineering*, 1999. A279: p. 160-165.
58. Viswanathan, G.B., et al. in *Superalloys 2004*. Seven Springs, PA: TMS, 2004, p. 173-178.
59. Link, T., et al., *Acta Materialia*, 2000. 48(2000): p. 1981-1994.
60. Royer, A., et al., *Materials Science and Engineering A*, 2001. 319-321: p. 800-804.
61. Royer, A. and P. Bastie. in *Superalloys 1996*. Seven Springs, PA: TMS, 1996, p. 221-228.
62. Mughrabi, H., H. Biermann, and T. Ungar. in *Superalloys 1992*. Seven Springs, PA: TMS, 1992, p. 599-608.
63. Ma, A., D. Dye, and R.C. Reed, *Acta Materialia*. In Press, Corrected Proof: p. 220.
64. Knowles, D.M. and Q.Z. Chen, *Materials Science and Engineering A*, 2003. 340(1-2): p. 88-102.
65. Ma, S., et al., *Materials Science and Engineering*, 2005. A399: p. 141-153.
66. Kamaraj, M., et al., *Materials Science and Engineering A*, 2001. 319-321: p. 796-799.
67. Serin, K., G. Gobekli, and G. Eggeler, *Materials Science and Engineering A*, 2004. 387-389: p. 133-137.
68. Sarosi, P.M., et al., *Ultramicroscopy*, 2005. 103(1): p. 83-93.
69. Miller, M.K., et al., *Applied Surface Science*, 1994. 76-77: p. 172-176.
70. Epishin, A., et al., *Acta Materialia*, 2001. 49(2001): p. 4017-4023.
71. Epishin, A., et al., *Acta Materialia*, 2000. 48(16): p. 4169-4177.
72. Yoon, K.E., R.D. Noebe, and D.N. Seidman, *Acta Materialia*, 2007. 55(4): p. 1145-1157.
73. Sudbrack, C.K., et al., *Acta Materialia*, 2008. 56(3): p. 448-463.

74. Pollock, T.M. and A.S. Argon. in *Superalloys 1988*. Seven Springs, PA: TMS, 1988, p. 285-294.
75. Wang, W.Z., et al., *Materials Science and Engineering: A*, 2008. 479(1-2): p. 148-156.
76. Su, C.H. and P.W. Voorhees, *Acta Materialia*, 1996. 44(5): p. 1987-1999.
77. Cetel, A.D. and D.N. Duhl. in *Superalloys 1988*: TMS, 1988, p. 235-244.
78. Al-Jarba, K.A. and G.E. Fuchs, *Materials Science and Engineering A*, 2004. 373(1-2): p. 255-267.
79. Cutler, E.R., A.J. Wasson, and G.E. Fuchs, *Scripta Materialia*, 2008. 58(2): p. 146-149.
80. Grose, D. and G. Ansell, *Metallurgical and Materials Transactions A*, 1981. 12(9): p. 1631-1645.
81. Westbrooke, E.F., L.E. Forero, and F. Ebrahimi, *Acta Materialia*, 2005. 53(7): p. 2137-2147.
82. Eggeler, G. and A. Dlouhy, *Acta Materialia*, 1997. 45(10): p. 4251-4262.
83. Nategh, S. and S.A. Sajjadi, *Materials Science and Engineering A*, 2003. 339(1-2): p. 103-108.
84. McCabe, R. and M. Fine, *JOM*, 2000. 52(6): p. 33-35.
85. Bruckner, U., et al., *Materials Science and Engineering*, 1998. A247: p. 23-31.

## BIOGRAPHICAL SKETCH

Brandon Wilson was born and raised in the heart of horse country around Ocala, FL. At a young age he joined the Cub Scouts of America and later the Boy Scouts of America and achieved the highest rank of Eagle at the age of 17. Brandon graduated with honors from Vanguard High School (Ocala, FL) in 1998 and enrolled in college at Central Florida Community College (Ocala, FL). Originally intending to attend film school at the University of Central Florida (Orlando, FL), he made the decision to attend the University of Florida (Gainesville, FL) instead and entered the mechanical engineering program. Following his first materials course, Introduction to Materials, taught by Dr. Dow Whitney and Dr. John Ambrose, he made the decision to enter the materials science and engineering program with a metals specialization.

Shortly after entering the materials science and engineering department, he applied for the University Scholars Program organized by the University of Florida. The University Scholars Program is an opportunity for undergraduate students to learn about research in a laboratory setting. Upon being accepted into the program, he was partnered with Dr. Gerhard Fuchs who became his eventual graduate advisor and mentor. Graduating cum laude with his bachelors degree in May 2003, Brandon went on to marry Krista Renner three weeks later. He then entered the graduate program in materials science and engineering in August 2003. He continued working with Dr. Fuchs on the research presented herein. Upon graduating he plans to take an engineering position working with nickel and titanium alloys for aerospace and power generation applications.